

Dating Magmatism on Mars: Application of *In-Situ* and Microsampling Techniques for Shergottite
Geochronology

by

Alex I-Fan Sheen

A thesis submitted in partial fulfilment of the requirements for the degree of

Doctor of Philosophy

Department of Earth and Atmospheric Sciences

University of Alberta

© Alex I-Fan Sheen, 2022

ABSTRACT

Establishing an absolute time scale of Mars is critical to understanding the planet's geological evolution. Currently, martian meteorites are the only samples of the planet available for radiometric geochronology analysis in terrestrial laboratory settings. The record of known martian absolute ages is dominated by shergottites, the largest group of martian meteorites, which represent mafic to ultramafic extrusive to hypabyssal bodies. Shergottites are conventionally dated using isochron methods (e.g., Rb–Sr, Sm–Nd, Lu–Hf) involving mineral separation and chemical chromatography. On the other hand, advances in secondary ion mass spectrometry (SIMS) analysis have enabled *in-situ* U–Pb baddeleyite (ZrO_2) geochronology, which has the potential not only to preserve the petrographic context but also to overcome challenges of resolving igneous versus secondary signatures in the major minerals and of the bulk rock. *In-situ* radiometric chronology of shergottites is therefore crucial for refining the martian meteorite age record as well as developing strategies for dating future returned samples from Mars. This dissertation presents three studies aimed at 1) investigating constraints associated with SIMS U–Pb baddeleyite geochronology and 2) assessing the feasibility of micromill extraction as a less destructive alternative to bulk crushing for Rb–Sr and Sm–Nd geochronology of shergottites.

A comprehensive survey of petrography, mineralogy, and geochemistry in a suite of eight basaltic shergottites confirms an igneous origin of baddeleyite, which crystallized in association with evolved late-stage melts. Pyroxene major element compositions demonstrate that baddeleyite crystallization in these shergottites is controlled primarily by fractional crystallization; samples with pyroxene compositions evolving beyond the stability boundary at 1-bar pressure generally contain more abundant baddeleyite than those with pyroxene compositions terminating at or before the stability boundary. These observations demonstrate that pyroxene composition can be a useful proxy for evaluating baddeleyite distribution in unknown shergottite samples, enabling a preliminary feasibility assessment for SIMS U–Pb analysis prior to conducting detailed baddeleyite search.

Electron backscatter diffraction (EBSD) analysis of baddeleyite microstructures in the enriched basaltic shergottites Jiddat al Harasis (JaH) 479, Northwest Africa (NWA) 10299, and NWA 12919 reveals widespread phase transformation to high-pressure orthogonal polymorphs (α -ZrO₂) before reverting to the monoclinic structure (m -ZrO₂). A larger proportion of grains preserving magmatic orientations in JaH 479 suggests it experienced lower bulk shock pressure compared to NWA 10299 and NWA 12919.

SIMS U–Pb baddeleyite analysis yields igneous crystallization ages of 210 ± 9 Ma (JaH 479; 2σ), 196 ± 11 Ma (NWA 10299), and 188 ± 11 Ma (NWA 12919). The results show no resolvable Pb loss in the analyzed shergottites, indicating that post-shock heating associated with the observed microstructures was insufficient to drive significant Pb diffusion in baddeleyite.

The minimum volumes of olivine, pyroxene, plagioclase, and merrillite that need to be micromilled for an isotopic analysis (ID-TIMS or ICP-MS) are estimated to be between 10^5 and 10^7 μm^3 for Sr and between 10^5 and 10^9 μm^3 for Nd. Physical characteristics of shergottites, including grain size, morphology, compositional zoning, inclusions, and shock features, present significant limitations for obtaining pure mineral fractions using the maximum micromill sampling resolution of ~ 40 μm (at a drilling depth of 20 μm). In addition, variations in mineral composition may result in realistic sample volumes several orders of magnitude greater than these minimum estimates. These technical and physical constraints make micromill sampling unsuitable for conducting Rb–Sr or Sm–Nd geochronology of shergottites.

The findings presented in this dissertation demonstrate that the physical characteristics of shergottites present unique challenges that must be considered when applying analytical methods that have been developed for terrestrial analogs, especially with respect to preserving the samples and resolving igneous signatures from secondary effects such as impact shock and alteration. SIMS U–Pb baddeleyite dating benefits from the use of pyroxene composition trends for assessing baddeleyite distribution and of EBSD microstructural analysis for constraining U–Pb isotope systematics under shock

metamorphism. Although micromill sampling is not currently feasible for shergottite Rb–Sr and Sm–Nd geochronology, the identified technical and physical limitations provide guidelines for designing future analytical strategies. The findings presented in this dissertation contribute to a refined approach for applying *in-situ* and microanalysis techniques to dating shergottites and potentially future returned samples, with wider implications for expanding the absolute time scale of Mars.

PREFACE

This Ph.D. thesis is an original work by A. Sheen and includes scientific work produced by research collaborators Dr. James Darling (University of Portsmouth), Jarret Hamilton (University of Alberta), Dr. Leanne Staddon (University of Portsmouth), and the late Dr. Erin Walton (MacEwan University, University of Alberta), with assistance from Dr. D. Graham Pearson (University of Alberta), Dr. Winfried Schwarz (Heidelberg University), and Dr. Sarah Woodland (University of Alberta). Alex Sheen was the lead researcher and author for all chapters in this thesis. Dr. Christopher Herd was the supervisory author and was involved with concept formation of all chapters and associated manuscripts. All studies presented in this thesis were funded by Natural Sciences and Engineering Research Council of Canada (NSERC) CGS-D scholarship to A. Sheen, with additional funding sources particular to each study specified below.

Chapter 2 was published as Sheen A.I., Herd C.D.K., Hamilton J., and Walton E.L. (2021) Petrographic controls on baddeleyite occurrence in a suite of eight basaltic shergottites. *Meteoritics & Planetary Science* 56, 1502–1530 (doi: 10.1111/maps.13726). Funding was partly supported by NSERC Grant RGPIN-2018-04902 to C. Herd, and NSERC Discovery Grant 04073 to E. Walton. A. Sheen performed petrographic examinations, EPMA data collection, EPMA baddeleyite survey, reduction and interpretation of EPMA and ICP-MS data. J. Hamilton and E.L. Walton performed petrographic examinations of shock features and contributed writing on description of shock features as well as interpretation of bulk shock pressure estimates. Analytical assistance was provided by Dr. Andrew Locock (EPMA) and Dr. Guangcheng Chen (ICP-MS). Sample preparation was conducted by Mark Labbe (University of Alberta), A. Sheen, and C. Herd. This manuscript includes WDS compositional data previously collected by Dr. Nicholas Castle during his Ph.D. research at the University of Alberta. Valuable comments from reviewers Dr. Tom Lapen (University of Houston), Dr. Takafumi Niihara (University of Tokyo), and Associate Editor Cyrena Goodrich (Lunar and Planetary Institute) contributed to significant improvements of the original manuscript during the peer-review process. Samples were provided by Dr. Tony Irving at the University of Washington (NWA

11057, 11073, 11255, and 12266) and Dr. Julia Roszjar at the Natural History Museum Vienna (KG 002). University of Alberta specimens used in this study were MET11619/TEP1 and TEP2 (JaH 479), MET11774/2 (NWA 10299), and MET11776/3/TEP (NWA 12919).

Chapter 3 is planned to be submitted for publication in *Meteoritic & Planetary Science* as Sheen A.I., Herd C.D.K., Staddon L.G., Darling J.R., and Schwarz W.H. Baddeleyite microstructural response to shock metamorphism in enriched shergottites: SIMS U–Pb baddeleyite geochronology of Jiddat al Harasis (JaH) 479, Northwest Africa (NWA) 10299, and NWA 12919. Funding was supported by NSERC Grant RGPIN-2018-04902 to C. Herd and UK Science and Technology Facilities Council grant [ST/S000291/1] to J. Darling. Travel funding for the study was supported by the NSERC Michael Smith Foreign Study Supplement (MSFSS) to A. Sheen. Data processing and interpretation were performed by A. Sheen with guidance from L. Staddon, J. Darling, and W. Schwarz. SEM imaging and EBSD analysis was carried out by L. Staddon with analytical assistance from Dr. Joseph Dunlop (University of Portsmouth). SIMS U–Pb baddeleyite analysis was performed by W. Schwarz. Sample preparation was supported by Mark Labbe, Dr. Patrick Hill (University of Alberta), L. Staddon, and Geoff Long (University of Portsmouth). Dr. Richard Stern (University of Alberta) provided valuable guidance on coordinating sample preparation and analytical steps. The manuscript constituting this chapter has benefited from valuable comments from co-author L. Staddon on scientific writing. University of Alberta specimens used in this study were MET11619/TEP1 (JaH 479), MET11774/2 (NWA 10299), and MET11776/4 (NWA 12919). Lisa Budney (University of Alberta) provided administrative and logistic support for the loan of specimens.

Chapter 4 is planned to be submitted for publication as Sheen A.I. and Herd C.D.K. A feasibility assessment of micromill sampling for Rb–Sr and Sm–Nd geochronology of shergottites. Funding was supported by NSERC Grant RGPIN-2018-04902 and NSERC Grant RTI-2018-00043 to C. Herd. A. Sheen performed micromill sample collection, data processing and interpretation. The micromill protocol specific to the study was developed and implemented by A. Sheen with guidance from D.G. Pearson on

analytical design and logistic support from S. Woodland, Dr. Chiranjeeb Sarkar, and M. Labbe (University of Alberta). ICP-MS analysis was performed by S. Woodland. LA-ICP-MS data acquisition was performed by Dr. Andy DuFrane (University of Alberta). Sample preparation was supported by M. Labbe and C. Herd. Synthetic glasses used in this study were previously prepared by Alexandra Blinova and C. Herd for Blinova A. and Herd C.D.K. (2009) Experimental study of polybaric REE partitioning between olivine, pyroxene and melt of the Yamato 980459 composition: Insights into the petrogenesis of depleted shergottites. *Geochimica et Cosmochimica Acta* 73, 3471–3492. The manuscript constituting this chapter has benefited from valuable comments from Dr. Balz Kamber, Associate Editor at *Chemical Geology*.

ACKNOWLEDGEMENTS

To my family, thank you for always being there for me.

I would like to thank my supervisor, Dr. Chris Herd, for the incredible opportunity to undertake the research presented herein, at a time when Mars science is catapulted into the spotlight (once again!) with the launch of the Mars 2020 mission. I am forever grateful for your tireless guidance and constant enthusiasm, as well as for the countless wonderful scientific discussions that helped me make the (at time frightening) leap from terrestrial geology to space.

Thank you to my thesis committee members, Drs. Graham Pearson and Richard Stern, for thoughtful and constructive feedback for this dissertation, as well as guidance and logistics support for research design. Additional thanks go to members of the candidacy examination and the final examination committees, Drs. Rob Creaser and T. Mark Harrison, for constructive feedback that resulted in significant improvement of this dissertation.

To the wonderful team at the University of Portsmouth, Drs. James Darling and Leanne Staddon, thank you for the opportunity to undertake and collaborate on EBSD and SIMS research. It has been an unforgettable and immensely rewarding experience to work with you despite all the wrenches the pandemic threw at us.

Thank you to the Natural Sciences and Engineering Research Council of Canada for funding my studies, as well as travel to the U.K. I am very grateful for the program officers who made efforts to ensure the pandemic caused as little impact as possible to the award processes.

Lastly, thank you to all the unsung heroes who has kept the world going during the pandemic. Wherever you be, whatever your role, however big or small the challenges you faced, you did not fight alone.

Alex Sheen

Aug. 2022

TABLE OF CONTENTS

ABSTRACT.....	ii
PREFACE	v
ACKNOWLEDGEMENTS.....	viii
TABLE OF CONTENTS.....	ix
LIST OF TABLES.....	xii
LIST OF FIGURES.....	xiii
CHAPTER 1: INTRODUCTION	1
1.2 Martian meteorites.....	2
1.3 Shergottites and the shergottite conundrum.....	3
1.3.1 Evidence for an ancient surface on Mars.....	4
1.3.2 Young or old shergottites: the question of U–Pb ages	5
1.3.3 SIMS U–Pb baddeleyite geochronology and Pb isotopic evolution of martian reservoirs ...	7
1.4 <i>In-situ</i> methods for shergottite geochronology.....	10
1.4.1 Baddeleyite as an igneous geochronometer	11
1.5 Microsampling methods of meteoritic samples	13
1.6 Motivations and objectives.....	13
1.7 Dissertation structure	15
1.8 References	17
CHAPTER 2: PETROGRAPHIC CONTROLS ON BADDELEYITE OCCURRENCE IN A SUITE OF EIGHT BASALTIC SHERGOTTITES	27
2.1 Abstract.....	27
2.2 Introduction	27
2.3 Background	28
2.4 Methodology.....	30
2.4.1 Samples	30
2.4.2 ICP-MS bulk chemistry	31
2.4.3 EPMA petrographic characterization.....	31
2.4.4 Oxygen fugacity calculation	33
2.4.5 Baddeleyite identification and petrographic characterization	33
2.5 Results.....	34
2.5.1 Sample petrography.....	34
2.5.2 Pyroxene composition trends	43
2.5.3 Bulk chemical composition	44

2.5.4	Oxygen fugacity.....	44
2.5.5	Baddeleyite size distribution and petrographic associations	45
2.6	Discussion.....	47
2.6.1	Baddeleyite as a late-stage igneous mineral	47
2.6.2	Shock pressure estimates and implications for baddeleyite paragenesis	48
2.6.3	Controls on baddeleyite occurrence in shergottites.....	49
2.6.4	Variation in baddeleyite grain size and morphology	53
2.6.5	Implications for baddeleyite characterization in shergottites and other martian meteorite groups	55
2.6.6	Towards a streamlined methodology for assessing shergottite samples for <i>in-situ</i> U–Pb baddeleyite analysis.....	58
2.7	Summary	59
2.8	References	80
CHAPTER 3:	Baddeleyite microstructural response to shock metamorphism in enriched shergottites: SIMS U–Pb baddeleyite geochronology of Jiddat al Harasis (JaH) 479, Northwest Africa (NWA) 10299, and NWA 12919	85
3.1	Abstract.....	85
3.2	Introduction	86
3.3	Baddeleyite petrography and microstructural response to shock	89
3.4	Samples.....	90
3.4.1	JaH 479	91
3.4.2	NWA 10299	91
3.4.3	NWA 12919	92
3.4.4	Shock features and bulk shock pressure estimates	92
3.5	Methodology.....	93
3.5.1	EBSD baddeleyite microstructure analysis.....	93
3.5.2	SIMS U–Pb analysis	94
3.6	Results.....	96
3.6.1	EBSD baddeleyite microstructures.....	96
3.6.2	SIMS U–Pb isotopic analysis.....	98
3.7	Discussion.....	101
3.7.1	Baddeleyite microstructure and shock history	101
3.7.2	Baddeleyite petrography and shock response.....	104
3.7.3	Baddeleyite microstructures and U–Pb isotope systematics	105
3.7.4	Implications for shergottite magmatism and ejection	108
3.7.5	Implications for Mars sample return missions.....	110

3.8	Conclusions	111
3.9	References	128
CHAPTER 4: A feasibility assessment of micromill sampling for Rb–Sr and Sm–Nd geochronology of shergottites.....		138
4.1	Abstract.....	138
4.2	Introduction	139
4.3	Methodology.....	142
4.3.1	The micromill sample method (wet-based).....	142
4.3.2	Determining the micromill sampling resolution and drilling geometry.....	144
4.3.3	Evaluating trace element composition of total procedural blank	144
4.3.4	Trace element LA-ICPMS of NWA 10299	146
4.4	Results.....	147
4.4.1	Geometry of micromill drill bits	147
4.4.2	Trace element composition of total procedural blanks.....	148
4.4.3	Trace elements LA-ICPMS of NWA 10299 major minerals	148
4.4.4	Minimum required micromilling volumes for Sr, Nd isotopic analyses.....	149
4.5	Discussion.....	149
4.5.1	Micromill blank contribution	149
4.5.2	Required drilling volume.....	152
4.5.3	Effects of encountering non-target phases	157
4.5.4	Realistic required mass and sampling time	158
4.5.5	Current limits on micromill sampling for mineral Sr, Nd isotopic analysis	160
4.5.6	Alternative applications	161
4.6	Conclusions	161
4.7	References	171
CHAPTER 5: CONCLUSIONS.....		180
BIBLIOGRAPHY		184
APPENDIX 1		206
APPENDIX 2		246

LIST OF TABLES

Table 2.1. Modal abundance of major phases based on EPMA X-ray element maps	61
Table 2.2. Statistical results of the baddeleyite survey	62
Table 2.3. Results of ICP-MS analysis of bulk major, minor, and trace elements.....	63
Table 2.4. Oxygen fugacity (f_{O_2}) of the studied samples.....	65
Table 2.5. Number of documented baddeleyite grains, mean length, maximum length, and mean aspect ratio in each petrographic association category.....	66
Table 3.1. Instrument parameters for EBSD baddeleyite microstructure analysis.....	114
Table 3.2. Baddeleyite microstructures determined by EBSD analysis	115
Table 3.3. Distribution of baddeleyite microstructural groups in the studied samples	117
Table 3.4. SIMS U–Pb isotopic analysis of baddeleyite in JaH 479, NWA 10299, and NWA 12919.....	118
Table 4.1. HR-ICPMS trace element analysis of bulk synthetic basaltic glass SGY, micromilled powder, and procedural blanks	163
Table 4.2. Results of LA-ICPMS trace element analysis of pyroxene and plagioclase glass in NWA 10299	164
Table 4.3. The range of Sr and Nd concentrations in major minerals in shergottite literature, with minimum volume required for analysis based on 0.250 ng Sr and 1 ng Nd for isotopic analysis	165
Table 4.4. Minimum required sampling area, in μm^2 , for Sr and Nd isotopic analyses assuming a drilling depth of 20 μm	165

LIST OF FIGURES

Fig. 2.1. Maps of baddeleyite occurrences in the surveyed shergottites	67
Fig. 2.2. BSE images of representative baddeleyite occurrences in JaH 479	68
Fig. 2.3. Examples of baddeleyite occurrences in KG 002.....	69
Fig. 2.4. Representative baddeleyite occurrences in NWA 10299.....	69
Fig. 2.5. Representative baddeleyite occurrences in NWA 11057.....	70
Fig. 2.6. Representative baddeleyite occurrences in NWA 11073.....	71
Fig. 2.7. Representative baddeleyite occurrences in NWA 11255.....	72
Fig. 2.8. Representative baddeleyite occurrences in NWA 12262.....	73
Fig. 2.9. Representative baddeleyite occurrences in NWA 12919.....	74
Fig. 2.10. Pyroxene compositions plotted in En-Fs-Dp-Hd quadrilateral space.....	75
Fig. 2.11. Bulk REE normalized to CI chondrite	77
Fig. 2.12. Frequency distribution histogram and cumulative percentage of baddeleyite grain length	74
Fig. 2.13. Cumulative percentage of baddeleyite grain length in subsection maps of NWA 10299	78
Fig. 2.14. Relative proportion of baddeleyite grains in each petrographic association	78
Fig. 2.15. Frequency of baddeleyite grains, at $\geq 1 \mu\text{m}$ and $\geq 4 \mu\text{m}$ populations, plotted against TiO ₂ and Yb	79
Fig. 3.1. BSE images of sample sections examined in this study, with baddeleyite targets for EBSD and SIMS analyses labeled.....	120
Fig. 3.2. Electron backscatter diffraction (EBSD) maps and pole figures of Group 1, 2, 3, and mixed group baddeleyite microstructures.....	121
Fig. 3.3. Tera-Wasserburg plots of U-Pb isotopic analysis of baddeleyite in JaH 479, NWA 10299, and NWA 12919	125
Fig. 3.4. Schematic diagram illustrating baddeleyite microstructural response to varying shock conditions	126
Fig. 4.1. Breakdown of the feasibility assessment for applying micromill sampling to mineral Sr, Nd isotopic analyses in shergottites.....	166
Fig. 4.2. Photograph of the Merchantek/New Wave Research MicroMill instrument used in this study	166
Fig. 4.3. Secondary electron SEM images of carbide drill bits used in this study	167
Fig. 4.4. BSE images of test patterns performed by bit 001B on synthetic basaltic glass SGY	168

Fig. 4.5. BSE image of a representative area of NWA 10299 annotated with equivalent schematic sampling area sizes for obtaining the minimum required volume for Sr isotopic analysis	169
Fig. 4.6. Estimated drilling time for obtaining the minimum required Sr and Nd mass (0.250 ng and 1 ng, respectively) in a target of known Sr or Nd concentration.....	170

CHAPTER 1: INTRODUCTION

1.1 Overview

The planetary evolution of Mars bears striking contrasts with that of the Earth, characterized by the present-day absence of a substantial atmosphere, crustal recycling, and dynamo-generated global magnetic field (e.g., [Jakosky et al., 1994](#); [Pepin et al., 1994](#); [Borg et al., 1997](#); [Acuña et al., 1998](#); [Foley et al., 2005](#)). The additional contrast between modern Mars and inferred conditions of ancient Mars, with a thicker atmosphere and surface and near-surface water, has continued to intrigue researchers and fuel exploration missions searching for evidence of past habitability (e.g., [Bibring et al., 2006](#); [Ehlmann et al., 2011](#)). From the first fly-by photographs returned by Mariner 4 in 1965 to the ongoing collection of geological samples by the Perseverance rover for future sample return missions, our understanding of the Red Planet has evolved far beyond Huygens' sketch of Syrtis Major Planum and Schiaparelli's illusory *canali*.

A major source of uncertainty in interpreting the geological history of Mars is the lack of precise absolute time constraints on surface features. Currently, the ages of martian surface units are determined using crater counting chronology, a method that is sensitive to the extrapolation of the lunar radiometric age vs. cratering frequency curve for calibrating the Mars cratering record ([Neukum et al., 2001](#); [Hartmann, 2005](#)). This extrapolation is in turn based on assumptions on the Moon-to-Mars ratio in cratering rate, as well as dynamic models for the bombardment history of the inner solar system (e.g., [Hartmann and Neukum, 2001](#); [Brasser et al., 2020](#); [Marchi, 2021](#) and references therein). Although *in-situ* K-Ar measurements have been achieved by the Curiosity rover on sedimentary units in the Gale crater (e.g., [Farley et al., 2014](#); [Vasconcelos et al., 2016](#)), the small dataset and associated large uncertainties preclude the construction of an absolute time scale with a precision approaching that of the Earth or the Moon (e.g., [Geiss and Rossi, 2013](#)). A geological framework constrained by radiometric dating is therefore crucial to understanding the evolution of Mars.

1.2 Martian meteorites

Martian meteorites are currently the only samples of Mars that are directly available for study in terrestrial laboratory settings. Initially termed “SNC meteorites” after the three major groups identified at the time—shergottites, nakhrites, and chassignites (named after the Shergotty, Nakhla and Chassigny meteorites, respectively)—these meteorites were demonstrated to be martian in origin based on multiple lines of evidence from mineralogy, petrography, geochemistry, and isotopic compositions (e.g., Treiman et al., 2000 and references therein). Notably, a bulk rock FeO/MnO ratio of ~35–40 distinguishes these meteorites from terrestrial and lunar igneous rocks (FeO/MnO of 60 and 70–75, respectively; Treiman et al., 2000). The wide composition range of isotopic reservoirs inferred from these meteorites further indicates a parent body large enough to support complex igneous processes (Jagoutz, 1989; Jones, 1989; Treiman et al., 2000). Furthermore, trapped gas within impact melt glass in these meteorites shares similar volatile isotopic compositions as those measured in the present-day Martian atmosphere (e.g., Bogard and Johnson, 1983; Wieler et al., 2016; Walton et al., 2008). Lastly, chemical and mineralogical evidence for extraterrestrial hydrous alteration (e.g., Treiman et al., 1993) is consistent with the presence of water at or near the Martian surface, both now and in the geologic past as inferred from geomorphological features identified by orbiters and surface rovers (e.g., Clifford et al., 1993; Baker, 2001).

A key development which lent further support to a Martian origin of these meteorites is the recognition that rock fragments can survive ejection from planetary bodies during an impact event. The mechanical model presented by Melosh (1985) identified the free surface, where the compressive stress wave from the incoming impact is largely cancelled out by the near simultaneous tensile wave reflected off the planetary surface. Rocks at the free surface may be spalled off as a thin layer at velocities exceeding the escape velocity (5 km/s for Mars; Head et al., 2002). A crucial consideration in this model is that the target rock must be competent enough to survive the spallation process and be ejected into space. This

mechanical requirement has implications for the sampling bias in the martian meteorite age record discussed below.

Since [Treiman et al. \(2000\)](#) summarized the lines of evidence supporting the martian origin of the SNC meteorites, the inventory of martian meteorites has grown from 21 to 333 specimens as of July 2022 (*The Meteoritical Bulletin*). These are subdivided into five groups: shergottites (n=283), nakhlites (n=28), chassignites (n=3), polymict regolith breccia (n=18), and orthopyroxenite (n=1). The oldest martian igneous ages are represented by the 4.09 ± 0.03 Ga Allan Hill (ALH) 84001 orthopyroxenite ([Lapen et al., 2010](#)) and 4.5–4.3 Ga igneous clasts in the polymict regolith breccia Northwest Africa (NWA) 7034 and pairs (e.g., [Goodwin et al., 2022](#)). Nakhlites and chassignites, representing cumulate clinopyroxenites and dunites respectively, share a common ~1.3 Ga igneous age (e.g., [Borg and Drake, 2005; Park et al., 2014; Udry and Day, 2018](#)). Shergottites, the most prevalent type of martian meteorites, define distinct age populations of 2.40–2.37 Ga and 716–157 Ma (e.g., [Nyquist et al., 2001; Borg and Drake, 2005; Park et al., 2014; Herd et al., 2017; Lapen et al., 2017; Udry et al., 2020](#)).

1.3 Shergottites and the shergottite conundrum

Shergottites are divided by petrographic characteristics into three major subgroups: basaltic, olivine-phyric, poikilitic ([Goodrich, 2002](#)). Basaltic shergottites are basalts containing pyroxene and plagioclase and are interpreted to have crystallized from near-surface flows and/or conduits (e.g., [McCoy et al., 1992; McSween et al., 1996; Lentz and McSween, 2000](#)). Olivine-phyric shergottites are characterized by megacrystic olivine and minor orthopyroxene in a fine-grained groundmass of olivine, pyroxene, and plagioclase (e.g., [Goodrich, 2003](#)). Poikilitic shergottites (historically termed “Iherzolitic”) are olivine-pyroxene cumulates (e.g., [Ikeda, 1994; Howarth et al., 2014](#)). In addition, two minor petrographic subgroups have been recently recognized: gabbroic shergottites, which represent feeder systems to basaltic shergottites (e.g., [Filiberto et al., 2018](#)), and augite-rich shergottites, which are basalts with augite as the only pyroxene present (e.g., [Herd et al., 2017; Lapen et al., 2017](#)).

By far, radiometric igneous ages of martian meteorites are dominated by shergottites (49 out of 64 dated), which apart from the augite-rich shergottites 2.40–2.37 Ga age group fall within a late-Amazonian age range of 716–157 Ma ([Udry et al., 2020](#) and references therein). The prevalence of young igneous ages in the martian meteorite record strongly contrasts with ancient, >3 Ga ages inferred for most of Mar’s surface. This apparent paradox, combined with a general paucity of understanding of isotopic behavior under surficial and near-surface secondary processes on Mars, led to debates over the interpretation of shergottite radiometric ages, also known as the “shergottite conundrum” (e.g., [Bouvier et al., 2007, 2008; Moser et al., 2013](#)).

1.3.1 Evidence for an ancient surface on Mars

Based on crater density, impact rates, and crater retention ages, [Hartmann \(1973\)](#) proposed the Martian southern highlands to be ca. 3–4 Ga, with younger, ca. 0.3 Ga volcanic centres at Tharsis. The antiquity of the southern highlands was supported by chronologic studies by [Söderblom et al. \(1974\)](#), [Neukum and Wise \(1976\)](#), and [Neukum and Hiller \(1981\)](#). On the other hand, volcanic flows in Elysium Planitia have been estimated to be younger than 100 Ma ([Plescia, 1990; Hartmann and Berman, 2000](#)). The restricted extent of young terranes reflects the relative scarcity of volcanic activity on Mars in recent geologic history.

Independent of crater counting methods, isotopic systematics of extinct nuclides in Martian meteorites provide insights into the preservation of ancient terranes across most the planet’s surface. Shergottites, nakhlites, and the Chassigny meteorite display initial $\varepsilon^{142}\text{Nd}$ values ranging from –0.22 to +0.92, with predominantly positive values indicating that the mantle source for these meteorites became enriched in Nd (relative to Sm) during the differentiation of Mars within the first 300 m.y. after the formation of the solar system ([Borg et al., 1997; Foley et al., 2005; Harper et al., 1995](#)). Similarly, [Foley et al. \(2005\)](#) reported positive initial $\varepsilon^{182}\text{W}$ values for shergottites and nakhlites, reflecting a major silicate differentiation event at ca. 4.5 Ga. Comparison of initial $\varepsilon^{142}\text{Nd}$ and $\varepsilon^{182}\text{W}$ values further suggests that

shergottites and nakhrites were derived from long-lived, compositionally distinct mantle reservoirs (Foley et al., 2005). An isotopic signature involving extinct nuclides is easily obscured if mixing occurs among the different early-formed reservoirs (as is the case for most terrestrial rocks due to crustal recycling). Therefore, the preservation of ^{142}Nd and ^{182}W anomalies in Martian meteorites suggests a planetary evolution devoid of significant plate tectonics soon after the planet's formation (Borg et al., 1997; Foley et al., 2005; cf. Yin, 2012), consistent with crater counting evidence for widespread ancient terranes on Mars.

1.3.2 Young or old shergottites: the question of U–Pb ages

As the inventory of martian meteorites grew throughout the 1980s and 1990s, so did the number of dating studies. Although Rb–Sr and Sm–Nd systems yielded generally similar ages for the same shergottites, the interpretation of U–Pb isotopic data was more nuanced. The first investigation of U–(Th–)Pb isotopic systematics in shergottites was carried out by Chen and Wasserburg (1986), who reported slightly older ages for both Shergotty (>200 Ma) and Zagami (230 ± 5 Ma) than those previously determined by Rb–Sr (Shergotty: 165 ± 11 Ma; Zagami: 180 ± 4 Ma) and Sm–Nd (Shergotty: 147 ± 20 Ma) methods (Shih et al., 1982; Jagoutz and Wänke, 1986). Evolved, non-radiogenic initial Pb isotopic compositions led the authors to conclude that U/Pb fractionation occurred early in Mars' history, and that shergottites originated from evolved ($\mu < 5$), long-lived mantle sources with distinct Pb isotopic compositions. This was followed by analyses of Lewis Cliff (LEW) 88516 and Yamato (Y) 793605, which yielded similar, ~200 Ma ages (Chen and Wasserburg, 1993; Misawa et al., 1997). At the time, scatter observed in the U–Pb data precluded definitive characterization of these ages with respect to igneous crystallization history and the ~200 Ma ages for Shergotty, Zagami, LEW 88516, and Y-793605 were interpreted to reflect disturbance events which resulted in Pb loss and U–Pb isotopic reset (Chen and Wasserburg, 1986, 1993; Misawa et al., 1997). A U–Pb upper intercept date of 4439 ± 9 Ma for Y-793605 was interpreted as evidence for long-lived U–Pb reservoirs (Misawa et al., 1997).

To arrive at more precise constraints on U–Pb isotopic systematics in Martian meteorites, [Borg et al. \(2005\)](#) interpreted U–Pb data of Zagami in the context of Rb–Sr and Sm–Nd analyses conducted on the same whole rock and mineral fractions used for U–Pb analysis. Despite observed disturbances of U–Pb systematics, the purest silicate mineral fractions yielded a 156 ± 6 Ma ^{238}U – ^{206}Pb isochron age concordant with Rb–Sr (166 ± 6 Ma) and Sm–Nd (166 ± 12 Ma) results. Addressing the issue that ~200 Ma U–Pb ages in previous studies are consistently older than Rb–Sr and/or Sm–Nd ages, [Borg et al. \(2005\)](#) attributed some of the data scatter to U–Pb fractionation during leaching procedures ([Misawa et al., 1997](#)). Most significantly, the authors suggested the analyzed fractions were contaminated by two distinct components with high radiogenic Pb, which causes analyses to trend along discordia and yield <4 Ga upper intercepts. A terrestrial contaminant was identified in leachate analyses and also in data reported by [Chen and Wasserburg \(1986\)](#). A second contaminant associated with impact melt glass suggested a Martian origin, with high ^{207}Pb / ^{206}Pb ratios consistent with derivation from a reservoir (at least before 0.18 Ga) which underwent fractionation of U from Pb early in Mars' history (ca. 4.56 Ga), possibly through fluid-based surface weathering ([Borg et al., 2005](#)).

A contrasting picture was put forth by [Bouvier et al. \(2005, 2008\)](#), who interpreted a ca. 4.1 Ga whole-rock Pb–Pb date as the igneous crystallization age for Shergotty, Zagami, Los Angeles, and Elephant Moraine (EET) A79001. These authors argued that <600 Ma shergottite ages (the known age range at the time) determined from U–Pb, Rb–Sr, Sm–Nd, and Lu–Hf systems reflect alteration events which reset isotopic systematics. The case for ancient shergottite crystallization drew its main support from a consistent, collinear trend displayed by Pb–Pb data along the analyses of [Chen and Wasserburg \(1986\)](#). The interpretation of this Pb–Pb array as an isochron rested on the lack of evidence for terrestrial and martian contamination. In the mixing model of [Bouvier et al. \(2008\)](#), contamination by a radiogenic martian Pb reservoir was deemed unlikely as data scatter do not appear to deviate significantly from the proposed 4.1 Ga Pb–Pb isochron (c.f., [Borg et al., 2005](#)). Young ages obtained by other isotopic systems

were attributed to the presence of disseminated phosphate inclusions, which the authors argued to have undergone open-system behaviour during acidic fluid alteration events, hence resetting the Rb–Sr, Nd–Sm, Lu–Hf, and U–Pb isotopic systems ([Bouvier et al., 2005, 2008, 2009](#)).

[Nyquist et al. \(2009\)](#) challenged the [Bouvier et al. \(2005, 2008\)](#) model based on the diversity in lithology, geochemistry, and CRE ages, which suggests that shergottites originated from more than one distinct locality on Mars. For the young ages to reflect acidic fluid alteration, such events must have occurred at a high frequency during the Amazonian and at extensive spatial scales to affect the source rocks of shergottites. A young, Amazonian 346 ± 16 Ma age determined from concordant Rb–Sr, Sm–Nd, and ^{40}Ar – ^{39}Ar analyses of NWA 1460, which lacks petrographic evidence for secondary alteration minerals, further argues against this model ([Nyquist et al., 2009](#)). Likewise, an in-depth investigation of Ar isotope systematics by [Walton et al. \(2008\)](#) yielded evidence against ancient igneous crystallization.

1.3.3 SIMS U–Pb baddeleyite geochronology and Pb isotopic evolution of martian reservoirs

Advancement in *in-situ* secondary ion mass spectrometry (SIMS) U–Pb analysis led to a breakthrough in the shergottite conundrum in 2013, when [Moser et al. \(2013\)](#) and [Zhou et al. \(2013\)](#) respectively reported the first baddeleyite U–Pb ages of NWA 5298 (187 ± 33 Ma) and Zagami (182.7 ± 6.9 Ma). Critically, the baddeleyite U–Pb age of Zagami is within uncertainty of previous Rb–Sr and Sm–Nd isochron ages, lending support to the interpretation of young shergottite igneous crystallization. Although the origin of baddeleyite in shergottites was initially questioned, multiple studies ([Niihara et al., 2012; Darling et al., 2016; Herd et al., 2018a; Staddon et al., 2021](#); discussed in more detail in Chapter 3) have since confirmed that baddeleyite U–Pb systematics in shergottites record igneous signatures and yield robust (i.e. resistant to secondary processes) crystallization age data. The sampling bias towards young ages in the martian meteorite record was further demonstrated to be consistent with the ejection model of [Melosh \(1985\)](#); mechanical requirements for surviving impact and ejection favors young igneous lithologies which are more rheologically competent compared to old crusts heavily reworked by impact-

driven regolith-forming processes ([Walton et al., 2008](#)). This is reflected in the under-representation of the latter lithology in the martian meteorite inventory (the polymict regolith breccia NWA 7034 and pairs; e.g., [McCubbin et al., 2016](#); [Goodwin et al., 2022](#)). Shock condition constraints from mineralogical observations by [Fritz et al. \(2005\)](#) further support the preferential ejection of shergottites from restricted locations on Mars.

Whereas baddeleyite U–Pb geochronology provided an unambiguous solution to the young shergottite igneous ages, the apparent inconsistency with ancient whole-rock Pb–Pb isochrons was resolved by constraints on the evolution of Pb isotopic reservoirs on Mars. Early studies indicated an unfractionated U–Pb composition for the Martian mantle with a μ -value ($^{238}\text{U}/^{204}\text{Pb}$ ratio) constraint of 1–5 (e.g., [Chen and Wasserburg, 1986](#); [Borg et al., 2005](#); [Bouvier et al., 2005, 2008](#); [Gaffney et al., 2007](#)), whereas a long-lived, differentiated crustal U–Pb reservoir ($\mu > 13.4$) was inferred from the martian regolith breccia NWA 7533 ([Bellucci et al., 2015](#)). Scattering in shergottite U–Pb data has been postulated to be a result of contamination by distinct terrestrial and/or Martian reservoirs (e.g., [Borg et al., 2005](#); [Bouvier et al., 2008](#)). ^{207}Pb – ^{206}Pb data of altered baddeleyites and other igneous minerals measured by [Moser et al. \(2013\)](#) indicate mixing between terrestrial Pb and a primitive, U-depleted Martian reservoir. Following the *in-situ* approach, [Bellucci et al. \(2016\)](#) reported radiogenic Pb of secondary origin in olivine crystals in Chassigny, the type meteorite of chassignites, with a similar mixing trend as shergottites. As terrestrial contamination was ruled out based on extensive textural characterizations, a Martian origin was proposed for the radiogenic Pb contaminant, consistent with the differentiated crustal U–Pb reservoir identified by [Bellucci et al. \(2015\)](#). These findings therefore indicate that the >4 Ga apparent ages determined from shergottite Pb–Pb data reflect contamination by a long-lived, evolved martian Pb reservoir and do not date shergottite crystallization. The presence of this crustal-derived contaminant in Pb isotope data of shergottites, nakhrites (e.g., [Bouvier et al., 2009](#)), and chassignites indicates that it is widespread across the Martian surface. [Bellucci et al. \(2016\)](#) further postulated that the contaminant may

have been introduced into the meteorite source rocks via fluid activity before impact and ejection, which resulted in isotopic mixing within the igneous minerals. This Pb evolution model is consistent with the lack of evidence for effective crustal recycling on Mars (e.g., [Borg et al., 1997](#); [Foley et al., 2005](#); [Walton et al., 2008](#)) and the extensive regolith formation from pre-3.8 Ga Noachian crust hypothesized by [Taylor \(2013\)](#). The findings of [Bellucci et al. \(2015, 2016\)](#) provided the last piece of puzzle to solving the shergottite conundrum.

The shergottite conundrum highlights an important frontier in martian meteorite research—the importance of *in-situ* analytical methods for obtaining isotopic information at the micrometre or sub-micrometre resolution while preserving the overall sample. Measurement of radiogenic isotope systematics (e.g., Rb–Sr, Sm–Nd, Lu–Hf, U–Pb) in shergottites is typically conducted by dissolving mineral fractions separated from a crushed bulk sample. However, like all martian meteorites, shergottites have undergone shock metamorphism during ejection from Mars which creates a variety of secondary features crosscutting the igneous texture (e.g., [Fritz et al., 2005](#); [Walton et al., 2008](#)). These include (but are not limited to) planar deformation, fractures, mosaicism, transformation of igneous plagioclase to maskelynite or vesiculated glass, the formation of shock melt pockets and/or veins, and the formation of high-pressure polymorphs (e.g., [Fritz et al., 2005](#); [Walton et al., 2008](#); [Baziotis et al., 2013](#)). Shock features can act as pathways for terrestrial alteration, as inferred from fractures infilled by secondary minerals (carbonates, sulfates, etc.), the remobilization of Ce in silicates in cold desert meteorites, and LREE contamination with a terrestrial crustal signature in hot desert meteorites ([Crozaz and Wadhwa, 2001](#); [Crozaz et al., 2003](#)). On the other hand, shock melt pockets and veins represent a mix of melted whole-rock components with fractionated parent/daughter nuclides and are more susceptible than the bulk rock to terrestrial weathering ([Jagoutz, 1989](#); [Zipfel et al., 2000](#); [Wadhwa et al., 2001](#)). In addition to terrestrial weathering, some martian meteorites also exhibit geochemical and isotopic evidence of secondary processes at or near the surface of Mars, such as low-temperature alteration signature preserved in shock

melt pockets in the shergottite Tissint ([Kuchka et al., 2017](#)) and unsupported radiogenic Pb in olivine in Chassigny ([Bellucci et al., 2016](#)). As these secondary features occur on mm- to μm -scales throughout the bulk rock, excluding these phases during analysis is crucial to resolving undisturbed igneous geochemical and isotopic signatures. In radiogenic isotopic analysis involving chemical chromatography, this is typically achieved by intensive mineral separation protocols, careful handpicking, and acid cleaning and/or leaching steps. Nevertheless, in some cases contamination cannot be completely excluded (e.g., [Ferdous et al., 2017](#)), reflecting the complexity of secondary modifications in martian meteorites.

Similar complex processes affecting isotopic systematics limit the application of the K–Ar and Ar–Ar systems for shergottite geochronology relative to Rb–Sr, Sm–Nd, Lu–Hf, and U–Pb. The assumption that there was no initial radiogenic argon is often not satisfied in shergottite systems, with excess ^{40}Ar originating from shock-implanted atmospheric gas or other surface reservoirs, and/or inherited from the magma or assimilated crustal material (e.g., [Bogard and Park, 2008](#); [Walton et al., 2008](#); [Park et al., 2013, 2014](#)). Resolving the origin of such isotopic signatures involves modeling Ar diffusivity and thermal history of the rock, which are outside the scope of this dissertation. For the remainder of this dissertation, discussions on radiometric geochronology of shergottites will focus on the Rb–Sr, Sm–Nd, and U–Pb systems.

1.4 *In-situ* methods for shergottite geochronology

A key advantage of *in-situ* techniques is the ability to be combined with additional characterization of the surrounding petrographic context (e.g., SEM images, chemical maps) to carry out targeted, spatially informed analyses. This enables analysis at high spatial resolution (from μm - down to the nm-scale depending on the type of analysis) while the overall specimen is broadly preserved. The application of *in-situ* SIMS U–Pb baddeleyite geochronology proved a turning point in resolving in the shergottite conundrum ([Moser et al., 2013](#); [Zhou et al., 2013](#)) and the combination with electron back scatter diffraction (EBSD) analysis of shock microstructure further demonstrated the igneous origin of

baddeleyite in shergottites ([Moser et al., 2013](#); [Darling et al., 2016](#)). The development of *in-situ* geochronology methods is influenced by the priority of sample preservation in meteoritic research. For terrestrial mafic igneous rocks such as gabbro, diabase, and basalt—the closest petrological analogs to shergottites—isotope dilution thermal ionization mass spectrometry (ID-TIMS) U–Pb analysis of accessory mineral separates is generally the preferred technique for high-accuracy, high-precision (1–2 Myr 2σ for Phanerozoic ages) igneous geochronology (e.g., [Heaman and LeCheminant, 1993](#)). However, in terrestrial applications, the use of accessory minerals for TIMS analysis typically involves crushing sample mass on the order of at least 100's of grams, which makes the method unsuitable for shergottites; shergottites analyses that involve bulk crushing (e.g., trace elements ICP-MS, Rb–Sr, Sm–Nd, Lu–Hf geochronology) typically do not exceed 1 g crushed mass for the sake of sample preservation. The use of *in-situ* techniques is therefore crucial for investigating shergottite radiometric chronology and for assessing the effects of secondary processes on radiogenic isotope systematics at the between-grain and within-grain scales.

1.4.1 Baddeleyite as an igneous geochronometer

In shergottites, baddeleyite (monoclinic ZrO_2) is the preferred target phase for SIMS U–Pb analysis. Baddeleyite occurs as an accessory late-stage mineral most commonly found in mesostasis pockets, a petrographic setting parallel to the association with highly fractionated late-stage melts in terrestrial diabase and gabbro ([Heaman and LeCheminant, 1993](#)). The chief advantages of baddeleyite as an igneous geochronometer are its ability to incorporate U (up to 100's of ppm) and exclude Pb during crystallization and resistance against Pb loss up to amphibolite facies metamorphism ([Heaman and LeCheminant, 1993](#); [Millonig et al., 2013](#)). Although baddeleyite is commonly used for dating terrestrial mafic bodies *via* ID-TIMS techniques, the *in-situ* SIMS U–Pb analytical protocols for baddeleyite was not widely applied until the late 2000's when the oxygen flooding technique was developed to suppress the orientation-dependent Pb/U fractionation of baddeleyite ([Li et al., 2010](#); [Schmitt et al., 2010](#)); this reduced the relative

uncertainty of SIMS U–Pb baddeleyite analysis to 1–3% for Phanerozoic samples (<539 Ma, a range which includes most dated shergottites; [Li et al., 2010](#); [Schmitt et al., 2010](#)).

The application of SIMS U–Pb baddeleyite analysis to shergottite geochronology (and other baddeleyite-bearing meteorites) faced the unique challenge of interpreting U–Pb data with respect to ubiquitous shock metamorphism in these rocks. [Bouvier et al. \(2008\)](#) argued a secondary origin of baddeleyite in shergottites based on 1) observations of baddeleyite forming from the breakdown of zircon in terrestrial impact structures (e.g., [El Goresy, 1965](#); [Wittmann et al., 2006](#); see also [Timms et al., 2017](#)) and 2) evidence for baddeleyite phase transformation in kimberlites which formed under pressure conditions (inferred by extrapolation from experimental results at ambient pressure) exceeded by those estimated for shergottites ([Kerschhofer et al., 2000](#)). This interpretation was countered by [Niihara et al. \(2011\)](#), who reported SHRIMP baddeleyite U–Pb data for Roberts Massif (RBT) 04262 which were concordant with analyses obtained from other igneous mineral fractions and thus suggesting an igneous origin of the baddeleyite. Shock-loading experiments conducted by [Niihara et al. \(2012\)](#) further indicated that neither phase transformation nor complete U–Pb isotopic reset occurs in baddeleyite at pressures up to 57 GPa. Likewise, experiments on lunar basalts led [Gaffney et al. \(2011\)](#) to conclude that shock metamorphism either imparts no effect on isotopic age information (both in the whole rock and in mineral fractions) or causes it to degrade, instead of resetting the isotopic systematics completely. Both [Niihara et al. \(2012\)](#) and [Gaffney et al. \(2011\)](#) concluded that impact shock is unlikely to cause isotopic reset in such a way that preserves a concordant alteration age.

These experimental findings were confirmed by SIMS U–Pb analysis of the shergottite NWA 5298; highly shocked, granular baddeleyite associated with shock melt pockets exhibits up to 80% radiogenic Pb loss and yield common-Pb-corrected $^{206}\text{Pb}/^{238}\text{U}$ ages as young as 22 ± 2 Ma, whereas the least shocked baddeleyite grains yield an igneous crystallization age of 175 ± 30 Ma ([Moser et al., 2013](#); [Darling et al., 2016](#)). Further examination of three additional shergottites by [Staddon et al. \(2021\)](#) revealed complex

baddeleyite microstructural response to varying conditions of shock metamorphism, characterized by widespread phase transformation to high-pressure polymorphs followed by reversion. Unlike NWA 5298, however, these shergottites show no resolvable link between baddeleyite microstructures and U–Pb isotope systematics. Although open-system U–Pb behavior in baddeleyite in NWA 5298 remains to be further constrained by observations in additional shergottites, these studies demonstrate that baddeleyite is a robust U–Pb geochronometer for dating shergottite igneous crystallization.

1.5 Microsampling methods of meteoritic samples

In addition to *in-situ* methods for conducting spatially guided geochemical and isotopic analysis, microsampling techniques have also seen increasing application in meteoritic research (e.g., [Nakanishi et al., 2018](#); [White et al., 2020](#); [Darling et al., 2021](#)). Microsampling physically extracts small, mm³- to nm³-volumes from the sample surface by means of mechanic tools (e.g., micromill; [Charlier et al., 2006](#); [Hoffmann et al., 2009](#)) or focused ion beams (FIB; [Volkert and Minor, 2007](#)). As the extracted material can be subjected to digestion and chemical chromatography, microsampling bypasses analytical uncertainties typically introduced in *in-situ* methods by elemental fractionation, matrix mismatch, and interference from isobaric and polyatomic species (e.g., [Košler et al., 2002](#); [Storey et al., 2006](#); [Fisher et al., 2011](#); [Zack and Hogmalm, 2016](#)). With respect to the need for sample preservation in meteoritic studies, microsampling thus presents an alternative for conducting spatially informed microanalysis where *in-situ* analysis offers lower precision and/or resolution.

1.6 Motivations and objectives

The research presented in this dissertation is motivated by the growing significance of *in-situ* techniques in martian geology, a trend not only fueled by decades of direct observations of the martian surface by landers and rovers, but made all the more relevant in the last few years by the ongoing sample collection by the Mars 2020 Perseverance rover in preparation for a future sample-return mission. The returned samples present the unprecedented opportunity to perform analysis in terrestrial laboratory

settings on martian samples with known field contexts, which carries far-reaching implications for bridging the gap between our knowledge of Mars based on martian meteorites research and that based on exploration missions. Indeed, ongoing efforts to identify the source craters of martian meteorites (e.g., Tornabene et al., 2006; Herd et al., 2018b; Hamilton et al., 2020; Lagain et al., 2021) reflect the gradual convergence of meteorite-based and field-based Mars research. As illustrated by the shergottite conundrum, radiometric geochronology plays a key role in linking martian meteorites with the surface of Mars. As the martian meteorite age record continues to be updated and refined with new data (e.g., the discovery of the ~2.4 Ga augite-rich shergottites by Herd et al., 2017, and Lapen et al., 2017), the advantages of spatially informed analytical techniques present potential solutions where secondary processes preclude precise resolution of igneous isotopic signatures by bulk sampling methods. *In-situ* techniques will also be the dominant method for studying future returned samples, as the small sampling volume relative to chemical chromatography techniques enables optimal sample preservation while maximizing scientific information. Motivated by these considerations, the research presented in this dissertation seeks to refine the petrological, technical, and analytical limitations on conducting spatially informed radiometric geochronology of shergottites through examinations of SIMS U–Pb baddeleyite analysis and micromill sampling, with the aim of answering the following questions:

1. What are the petrological, mineralogical, and geochemical controls on baddeleyite petrogenesis in shergottites?
2. How do baddeleyite U–Pb isotope systematics respond to shock metamorphism in shergottites? What factors caused the difference between observed baddeleyite Pb-loss in NWA 5298 and the lack thereof in other shergottites, such as NWA 7257, NWA 8679, and Zagami?
3. Is *in-situ* U–Pb baddeleyite analysis feasible for all shergottites? If not, how do factors identified in 1) and 2) apply to assessing the feasibility of additional undated shergottites for future studies?

4. Where SIMS U–Pb baddeleyite analysis is not feasible, does micromill sampling provide a suitable alternative for chemical chromatography (e.g., ICP-MS, ID-TIMS) radiometric geochronology of shergottites? What are the analytical and physical limits of such an application?

1.7 Dissertation structure

This dissertation presents three research studies in the form of journal manuscripts (published or to be submitted), each constituting a chapter.

Chapter 2 details the investigation into the controls on baddeleyite crystallization through a petrological survey of baddeleyite occurrence in a suite of eight basaltic shergottites using electron probe microanalysis (EPMA), combined with wavelength-dispersive spectrometry (WDS) mineralogy analysis, petrography, and ICP-MS trace-element geochemistry. Results indicate that, of the petrogenetic and geochemical factors identified by [Herd et al. \(2018a\)](#), fractional crystallization exerts the strongest control on baddeleyite crystallization in shergottites by concentrating Zr in late-stage melts. The major element composition of pyroxenes, particularly FeO content with respect to the stability boundary at 1 bar, discriminates between shergottites that are relatively baddeleyite-rich and those that are relatively poor. There is further link between pyroxene major element trends and the phases with which baddeleyite is associated, suggesting that pyroxene composition is a useful proxy for assessing baddeleyite abundance and distribution in shergottites.

Chapter 3 presents the SIMS U–Pb baddeleyite geochronology of the enriched shergottites Jiddat al Harasis (JaH 479), NWA 10299, and NWA 12919 (also examined in the petrological survey), evaluated in the context of EBSD microstructural constraints on the response of the baddeleyite grains to shock metamorphism. SIMS analysis yields three new crystallization ages for enriched shergottites, further highlighting the relatively restricted age range of enriched shergottites compared to intermediate and depleted shergottites; this contrast suggests that magmatic processes responsible for forming enriched shergottites may have been operative over a shorter duration versus those which produced the

intermediate and depleted shergottites. Results of baddeleyite microstructural analysis indicate that, despite the prevalence of phase transformation into high-pressure polymorphs (followed by reversion), post-shock heating was insufficient to cause significant Pb volume diffusion. This study demonstrates that the lack of resolvable Pb-loss from baddeleyite in shergottites extends to a bulk shock pressure of ~55 GPa, higher than the previous estimate (~30 GPa; [Staddon et al., 2021](#)). As the studied samples are representative of shock levels experienced by the bulk of shergottites, this study illustrates that baddeleyite U–Pb geochronology is more widely applicable to shergottites than previously envisioned.

Chapter 4 reports a feasibility assessment of micromill extraction of igneous minerals (pyroxene, plagioclase, olivine, and merrillite) in shergottites for conducting Rb–Sr and Sm–Nd geochronology. ICP-MS trace element analysis of a synthetic glass sample, both as micromilled powder and as a whole piece, suggest negligible contamination of Sr and Nd from the micromilling procedure. The volumes required for micromill extraction were calculated based on a literature survey of mineral trace element content in addition to LA-ICPMS analysis of NWA 10299. The study identified significant limitations in shergottite petrography and mineralogy that precludes efficient extraction of the estimated required sample volumes with respect to the maximum drilling resolution of the micromill instrument. These technical and physical factors limit the application of micromill sampling for Rb–Sr and Sm–Nd geochronology of shergottites.

1.8 References

- Acuña, M. H., Connerney, J. E. P., Wasilewski, P., Lin, R. P., Anderson, K. A., Carlson, C. W., McFadden, J., Curtis, D. W., Mitchell, D., Reme, H., Mazelle, C., Sauvaud, J. A., d'Uston, C., Cros, A., Medale, J. L., Bauer, S. J., Cloutier, P., Mayhew, M., Winterhalter, D. & Ness, N. F. (1998) Magnetic Field and Plasma Observations at Mars: Initial Results of the Mars Global Surveyor Mission. *Science* **279**: 1676-1680.
- Baker, V. R. (2001) Water and the martian landscape. *Nature* **412**: 228-236.
- Baziotis, I. P., Liu, Y., DeCarli, P. S., Jay Melosh, H., McSween, H. Y., Bodnar, R. J. & Taylor, L. A. (2013) The Tissint Martian meteorite as evidence for the largest impact excavation. *Nature Communications* **4**: 1404.
- Bellucci, J. J., Nemchin, A. A., Whitehouse, M. J., Humayun, M., Hewins, R. & Zanda, B. (2015) Pb-isotopic evidence for an early, enriched crust on Mars. *Earth and Planetary Science Letters* **410**: 34-41.
- Bellucci, J. J., Nemchin, A. A., Whitehouse, M. J., Snape, J. F., Kielman, R. B., Bland, P. A. & Benedix, G. K. (2016) A Pb isotopic resolution to the Martian meteorite age paradox. *Earth and Planetary Science Letters* **433**: 241-248.
- Bibring, J., Langevin, Y., Mustard, J. F., François Poulet, Arvidson, R., Gendrin, A., Gondet, B., Mangold, N., Pinet, P., Forget, F., Michel Berthé, Jean-Pierre Bibring, Gendrin, A., Cécile Gomez, Gondet, B., Jouplet, D., François Poulet, Soufflot, A., Vincendon, M., Combes, M., Drossart, P., Thérèse Encrenaz, Fouchet, T., Merchiorri, R., Belluci, G., Altieri, F., Formisano, V., Capaccioni, F., Cerroni, P., Coradini, A., Fonti, S., Koralev, O., Kottsov, V., Ignatiev, N., Moroz, V., Titov, D., Zasova, L., Loiseau, D., Mangold, N., Pinet, P., Sylvain Douté, Schmitt, B., Sotin, C., Hauber, E., Hoffmann, H., Jaumann, R., Keller, U., Arvidson, R., Mustard, J. F., Duxbury, T., François Forget & Neukum, G. (2006) Global Mineralogical and Aqueous Mars History Derived from OMEGA/Mars Express Data. *Science* **312**: 400-404.
- Bogard, D. D. & Johnson, P. (1983) Martian Gases in an Antarctic Meteorite? *Science* **221**: 651-654.
- Bogard, D. D. & Park, J. (2008) 39Ar-40Ar dating of the Zagami Martian shergottite and implications for magma origin of excess 40Ar. *Meteoritics & Planetary Science* **43**: 1113-1126.
- Borg, L. & Drake, M. J. (2005) A review of meteorite evidence for the timing of magmatism and of surface or near-surface liquid water on Mars. *Journal of Geophysical Research: Planets* **110**.
- Borg, L. E., Edmunson, J. E. & Asmerom, Y. (2005) Constraints on the U-Pb isotopic systematics of Mars inferred from a combined U-Pb, Rb-Sr, and Sm-Nd isotopic study of the Martian meteorite Zagami. *Geochimica et Cosmochimica Acta* **69**: 5819-5830.

- Borg, L. E., Nyquist, L. E., Taylor, L. A., Wiesmann, H. & Shih, C. (1997) Constraints on Martian differentiation processes from Rb/Sr and Sm/Nd isotopic analyses of the basaltic shergottite QUE 94201. *Geochimica et Cosmochimica Acta* **61**: 4915-4931.
- Bouvier, A., Blichert-Toft, J., Vervoort, J. D. & Albarède, F. (2005) The age of SNC meteorites and the antiquity of the Martian surface. *Earth and Planetary Science Letters* **240**: 221-233.
- Bouvier, A., Blichert-Toft, J., Vervoort, J. D. & Albarède, F. (2007) The Conundrum of the Age of Shergottites. *38th Annual Lunar and Planetary Science Conference*: 1683.
- Bouvier, A., Blichert-Toft, J., Vervoort, J. D., Gillet, P. & Albarède, F. (2008) The case for old basaltic shergottites. *Earth and Planetary Science Letters* **266**: 105-124.
- Bouvier, A., Blichert-Toft, J. & Albarède, F. (2009) Martian meteorite chronology and the evolution of the interior of Mars. *Earth and Planetary Science Letters* **280**: 285-295.
- Brasser, R., Werner, S. C. & Mojzsis, S. J. (2020) Impact bombardment chronology of the terrestrial planets from 4.5 Ga to 3.5 Ga. *Icarus* **338**: 113514.
- Charlier, B. L. A., Ginibre, C., Morgan, D., Nowell, G. M., Pearson, D. G., Davidson, J. P. & Ottley, C. J. (2006) Methods for the microsampling and high-precision analysis of strontium and rubidium isotopes at single crystal scale for petrological and geochronological applications. *Chemical Geology* **232**: 114-133.
- Chen J. H., and Wasserburg G. J. 1993. LEW88516 and SNC Meteorites. pp. 275.
- Chen, J. H. & Wasserburg, G. J. (1986) Formation ages and evolution of Shergotty and its parent planet from U-Th-Pb systematics. *Geochimica et Cosmochimica Acta* **50**: 955-968.
- Clifford, S. M. (1993) A model for the hydrologic and climatic behavior of water on Mars. *Journal of Geophysical Research: Planets* **98**: 10973-11016.
- Crozaz, G. & Wadhwa, M. (2001) The terrestrial alteration of saharan shergottites dar al gani 476 and 489: a case study of weathering in a hot desert environment. *Geochimica et Cosmochimica Acta* **65**: 971-977.
- Crozaz, G., Floss, C. & Wadhwa, M. (2003) Chemical alteration and REE mobilization in meteorites from hot and cold deserts. *Geochimica et Cosmochimica Acta* **67**: 4727-4741.
- Darling, J. R., White, L. F., Kizovski, T., Černok, A., Moser, D. E., Tait, K. T., Dunlop, J., Langelier, B., Douglas, J. O., Zhao, X., Franchi, I. A. & Anand, M. (2021) The shocking state of apatite and merrillite in shergottite Northwest Africa 5298 and extreme nanoscale chlorine isotope variability revealed by atom probe tomography. *Geochimica et Cosmochimica Acta* **293**: 422-437.

- Darling, J. R., Moser, D. E., Barker, I. R., Tait, K. T., Chamberlain, K. R., Schmitt, A. K. & Hyde, B. C. (2016) Variable microstructural response of baddeleyite to shock metamorphism in young basaltic shergottite NWA 5298 and improved U–Pb dating of Solar System events. *Earth and Planetary Science Letters* **444**: 1-12.
- Ehlmann, B. L., Mustard, J. F., Murchie, S. L., Bibring, J., Meunier, A., Fraeman, A. A. & Langevin, Y. (2011) Subsurface water and clay mineral formation during the early history of Mars. *Nature* **479**: 53-60.
- El Goresy, A., Gillet, P., Miyahara, M., Ohtani, E., Ozawa, S., Beck, P. & Montagnac, G. (2013) Shock-induced deformation of Shergottites: Shock-pressure and perturbations of magmatic ages on Mars. *Geochimica et Cosmochimica Acta* **101**: 233-262.
- Farley, K. A., Malespin, C., Mahaffy, P., Grotzinger, J. P., Vasconcelos, P. M., Milliken, R. E., Malin, M., Edgett, K. S., Pavlov, A. A., Hurowitz, J. A., Grant, J. A., Miller, H. B., Arvidson, R., Beegle, L., Calef, F., Conrad, P. G., Dietrich, W. E., Eigenbrode, J., Gellert, R., Gupta, S., Hamilton, V., Hassler, D. M., Lewis, K. W., McLennan, S. M., Ming, D., Navarro-González, R., Schwenger, S. P., Steele, A., Stolper, E. M., Sumner, D. Y., Vaniman, D., Vasavada, A., Williford, K., Wimmer-Schweingruber, R., null, n., Blake, D. F., Bristow, T., DesMarais, D., Edwards, L., Haberle, R., Hoehler, T., Hollingsworth, J., Kahre, M., Keely, L., McKay, C., Wilhelm, M. B., Bleacher, L., Brinckerhoff, W., Choi, D., Dworkin, J. P., Floyd, M., Freissinet, C., Garvin, J., Glavin, D., Harpold, D., Martin, D. K., McAdam, A., Raaen, E., Smith, M. D., Stern, J., Tan, F., Trainer, M., Meyer, M., Posner, A., Voytek, M., Anderson, R. C., Aubrey, A., Behar, A., Blaney, D., Brinza, D., Christensen, L., Crisp, J. A., DeFlores, L., Feldman, J., Feldman, S., Flesch, G., Hurowitz, J., Jun, I., Keymeulen, D., Maki, J., Mischna, M., Morookian, J. M., Parker, T., Pavri, B., Schoppers, M., Sengstacken, A., Simmonds, J. J., Spanovich, N., Juarez, Manuel de la Torre, Webster, C. R., Yen, A., Archer, P. D., Cucinotta, F., Jones, J. H., Morris, R. V., Niles, P., Rampe, E., Nolan, T., Fisk, M., Radziemski, L., Barracough, B., Bender, S., Berman, D., Dobrea, E. N., Tokar, R., Williams, R. M. E., Yingst, A., Leshin, L., Cleghorn, T., Huntress, W., Manhès, G., Hudgins, J., Olson, T., Stewart, N., Sarrazin, P., Vicenzi, E., Wilson, S. A., Bullock, M., Ehresmann, B., Peterson, J., Rafkin, S., Zeitlin, C., Fedosov, F., Golovin, D., Karpushkina, N., Kozyrev, A., Litvak, M., Malakhov, A., Mitrofanov, I., Mokrousov, M., Nikiforov, S., Prokhorov, V., Sanin, A., Tretyakov, V., Varenikov, A., Vostrukhin, A., Kuzmin, R., Clark, B., Wolff, M., Botta, O., Drake, D., Bean, K., Lemmon, M., Anderson, R. B., Herkenhoff, K., Lee, E. M., Sucharski, R., Hernández, M. Á, de Pablo, Ávalos, J. J. B., Ramos, M., Kim, M., Plante, I., Muller, J., Ewing, R., Boynton, W., Downs, R., Fitzgibbon, M., Harshman, K., Morrison, S., Kortmann, O., Palucis, M., Williams, A., Lugmair, G., Wilson, M. A., Rubin, D., Jakosky, B., Balic-Zunic, T., Frydenvang, J., Jensen, J. K., Kinch, K., Koefoed,

A., Madsen, M. B., Stipp, S. L. S., Boyd, N., Campbell, J. L., Perrett, G., Pradler, I., VanBommel, S., Jacob, S., Owen, T., Rowland, S., Savijärvi, H., Boehm, E., Böttcher, S., Burmeister, S., Guo, J., Köhler, J., García, C. M., Mueller-Mellin, R., Bridges, J. C., McConnochie, T., Benna, M., Franz, H., Bower, H., Brunner, A., Blau, H., Boucher, T., Carmosino, M., Atreya, S., Elliott, H., Halleaux, D., Rennó, N., Wong, M., Pepin, R., Elliott, B., Spray, J., Thompson, L., Gordon, S., Newsom, H., Ollila, A., Williams, J., Bentz, J., Nealson, K., Popa, R., Kah, L. C., Moersch, J., Tate, C., Day, M., Kocurek, G., Hallet, B., Sletten, R., Francis, R., McCullough, E., Cloutis, E., ten Kate, I. L., Kuzmin, R., Fraeman, A., Scholes, D., Slavney, S., Stein, T., Ward, J., Berger, J. & Moores, J. E. (2014) In Situ Radiometric and Exposure Age Dating of the Martian Surface. *Science* **343**: 1247166.

Ferdous, J., Brandon, A. D., Peslier, A. H. & Pirotte, Z. (2017) Evaluating crustal contributions to enriched shergottites from the petrology, trace elements, and Rb-Sr and Sm-Nd isotope systematics of Northwest Africa 856. *Geochimica et Cosmochimica Acta* **211**: 280-306.

Filiberto, J., Gross, J., Udry, A., Trella, J., Wittmann, A., Cannon, K. M., Penniston-Dorland, S., Ash, R., Hamilton, V. E., Meado, A. L., Carpenter, P., Jolliff, B. & Ferré, E. C. (2018) Shergottite Northwest Africa 6963: A Pyroxene-Cumulate Martian Gabbro. *Journal of Geophysical Research: Planets* **123**: 1823-1841.

Fisher, C. M., McFarlane, C. R. M., Hanchar, J. M., Schmitz, M. D., Sylvester, P. J., Lam, R. & Longerich, H. P. (2011) Sm–Nd isotope systematics by laser ablation-multicollector-inductively coupled plasma mass spectrometry: Methods and potential natural and synthetic reference materials. *Chemical Geology* **284**: 1-20.

Foley, C. N., Wadhwa, M., Borg, L. E., Janney, P. E., Hines, R. & Grove, T. L. (2005) The early differentiation history of Mars from 182W-142Nd isotope systematics in the SNC meteorites. *Geochimica et Cosmochimica Acta* **69**: 4557-4571.

Fritz, J., Greshake, A. & Stöffler, D. (2005) Micro-Raman spectroscopy of plagioclase and maskelynite in Martian meteorites: Evidence of progressive shock metamorphism. *Antarctic Meteorite Research* **18**: 96.

Gaffney, A. M., Borg, L. E. & Connelly, J. N. (2007) Uranium–lead isotope systematics of Mars inferred from the basaltic shergottite QUE 94201. *Geochimica et Cosmochimica Acta* **71**: 5016-5031.

Gaffney, A. M., Borg, L. E., Asmerom, Y., Shearer, C. K. & Burger, P. V. (2011) Disturbance of isotope systematics during experimental shock and thermal metamorphism of a lunar basalt with implications for Martian meteorite chronology. *Meteoritics & Planetary Science* **46**: 35-52.

- Geiss, J. & Rossi, A. P. (2013) On the chronology of lunar origin and evolution. *The Astronomy and Astrophysics Review* **21**: 68.
- Goodrich, C. A. (2002) Olivine-phyric martian basalts: A new type of shergottite. *Meteoritics & Planetary Science* **37**: B31-B34.
- Goodrich, C. A. (2003) Petrogenesis of olivine-phyric shergottites Sayh al Uhaymir 005 and Elephant Moraine A79001 lithology A. *Geochimica et Cosmochimica Acta* **67**: 3735-3772.
- Goodwin, A., Garwood, R. J. & Tartèse, R. (2022) A Review of the “Black Beauty” Martian Regolith Breccia and Its Martian Habitability Record. *Astrobiology* **22**: 755-767.
- Hamilton J. S., Herd C. D. K., Walton E. L., and Tornabene L. L. 2020. Prioritizing Candidate Source Craters for Martian Meteorites. pp. 2607.
- Harper, C. L., Nyquist, L. E., Bansal, B., Wiesmann, H. & Chi-Yu Shih (1995) Rapid Accretion and Early Differentiation of Mars Indicated by $^{142}\text{Nd}/^{144}\text{Nd}$ in SNC Meteorites. *Science* **267**: 213-217.
- Hartmann, W. K. (2005) Martian cratering 8: Isochron refinement and the chronology of Mars. *Icarus* **174**: 294-320.
- Hartmann, W. K. (1973) Martian Cratering, 4, Mariner 9 initial analysis of cratering chronology. *Journal of Geophysical Research (1896-1977)* **78**: 4096-4116.
- Hartmann W. K., and Neukum G. 2001. Cratering Chronology and the Evolution of Mars. Chronology and Evolution of. pp. 165-194.
- Hartmann, W. K. & Berman, D. C. (2000) Elysium Planitia lava flows: Crater count chronology and geological implications. *Journal of Geophysical Research: Planets* **105**: 15011-15025.
- Head, J. N., Jay Melosh, H. & Ivanov, B. A. (2002) Martian Meteorite Launch: High-Speed Ejecta from Small Craters. *Science* **298**: 1752-1756.
- Heaman, L. M. & LeCheminant, A. N. (1993) Paragenesis and U-Pb systematics of baddeleyite (ZrO_2). *Chemical Geology; Geochemistry of Accessory Minerals* **110**: 95-126.
- Herd, C. D. K., Walton, E. L., Agee, C. B., Muttik, N., Ziegler, K., Shearer, C. K., Bell, A. S., Santos, A. R., Burger, P. V., Simon, J. I., Tappa, M. J., McCubbin, F. M., Gattaccea, J., Lagroix, F., Sanborn, M. E., Yin, Q., Cassata, W. S., Borg, L. E., Lindvall, R. E., Kruijer, T. S., Brennecka, G. A., Kleine, T., Nishiizumi, K. & Caffee, M. W. (2017) The Northwest Africa 8159 martian meteorite: Expanding the martian sample suite to the early Amazonian. *Geochimica et Cosmochimica Acta* **218**: 1-26.
- Herd, C. D. K., Moser, D. E., Tait, K., Darling, J. R., Shaulis, B. J. & McCoy, T. J. (2018a) Crystallization of Baddeleyite in Basaltic Rocks from Mars, and Comparisons with the Earth, Moon, and Vesta. *Microstructural Geochronology*: 137-166.

- Herd C. D. K., Tornabene L. L., Bowling T. J., Walton E. L., Sharp T. G., Melosh H. J., Hamilton J. S., Viviano C. E., and Ehlmann B. L. (2018b). Constraining the Source Craters of the Martian Meteorites: Implications for Prioritization of Returned Samples from Mars. pp. 6097.
- Hoffmann, D. L., Spötl, C. & Mangini, A. (2009) Micromill and in situ laser ablation sampling techniques for high spatial resolution MC-ICPMS U-Th dating of carbonates. *Chemical Geology* **259**: 253-261.
- Howarth, G. H., Pernet-Fisher, J., Balta, J. B., Barry, P. H., Bodnar, R. J. & Taylor, L. A. (2014) Two-stage polybaric formation of the new enriched, pyroxene-oikocrystic, Iherzolitic shergottite, NWA 7397. *Meteoritics & Planetary Science* **49**: 1812-1830.
- Ikeda, Y. (1994) Petrography and petrology of the ALH-77005 shergottite. *Antarctic Meteorite Research* **7**: 9.
- Jagoutz, E. (1989) Sr and Nd isotopic systematics in ALHA 77005: Age of shock metamorphism in shergottites and magmatic differentiation on Mars. *Geochimica et Cosmochimica Acta* **53**: 2429-2441.
- Jagoutz, E. & Wänke, H. (1986) Sr and Nd isotopic systematics of Shergotty meteorite. *Geochimica et Cosmochimica Acta* **50**: 939-953.
- Jakosky, B. M., Pepin, R. O., Johnson, R. E. & Fox, J. L. (1994) Mars Atmospheric Loss and Isotopic Fractionation by Solar-Wind-Induced Sputtering and Photochemical Escape. *Icarus* **111**: 271-288.
- Jones, J. H. (1989) Isotopic relationships among the shergottites, the nakhlites and Chassigny. *Lunar and Planetary Science Conference Proceedings* **19**: 465-474.
- Kerschhofer, L., Schärer, U. & Deutsch, A. (2000) Evidence for crystals from the lower mantle: baddeleyite megacrysts of the Mbuji Mayi kimberlite. *Earth and Planetary Science Letters* **179**: 219-225.
- Košler, J., Fonneland, H., Sylvester, P., Tubrett, M. & Pedersen, R. (2002) U-Pb dating of detrital zircons for sediment provenance studies—a comparison of laser ablation ICPMS and SIMS techniques. *Chemical Geology* **182**: 605-618.
- Kuchka, C. R., Herd, C. D. K., Walton, E. L., Guan, Y. & Liu, Y. (2017) Martian low-temperature alteration materials in shock-melt pockets in Tissint: Constraints on their preservation in shergottite meteorites. *Geochimica et Cosmochimica Acta* **210**: 228-246.
- Lagain, A., Benedix, G. K., Servis, K., Baratoux, D., Doucet, L. S., Rajšić, A., Devillepoix, H. A. R., Bland, P. A., Towner, M. C., Sansom, E. K. & Miljković, K. (2021) The Tharsis mantle source of depleted shergottites revealed by 90 million impact craters. *Nature Communications* **12**: 6352.

- Lapen, T. J., Righter, M., Brandon, A. D., Debaille, V., Beard, B. L., Shafer, J. T. & Peslier, A. H. (2010) A Younger Age for ALH84001 and Its Geochemical Link to Shergottite Sources in Mars. *Science* **328**: 347-351.
- Lapen, T. J., Righter, M., Andreasen, R., Irving, A. J., Satkoski, A. M., Beard, B. L., Nishiizumi, K., Timothy Jull, A. J. & Caffee, M. W. (2017) Two billion years of magmatism recorded from a single Mars meteorite ejection site. *Science Advances* **3**: e1600922.
- Lentz, R. C. F. & McSween Jr., H. Y. (2000) Crystallization of the basaltic shergottites: Insights from crystal size distribution (CSD) analysis of pyroxenes. *Meteoritics & Planetary Science* **35**: 919-927.
- Li, Q., Li, X., Liu, Y., Tang, G., Yang, J. & Zhu, W. (2010) Precise U-Pb and Pb-Pb dating of Phanerozoic baddeleyite by SIMS with oxygen flooding technique. *Journal of Analytical Atomic Spectrometry* **25**: 1107-1113.
- Marchi, S. (2021) A New Martian Crater Chronology: Implications for Jezero Crater. *The Astronomical Journal* **161**: 187.
- McCoy, T. J., Taylor, G. J. & Keil, K. (1992) Zagami: Product of a two-stage magmatic history. *Geochimica et Cosmochimica Acta* **56**: 3571-3582.
- McSween, H. Y., Eisenhour, D. D., Taylor, L. A., Wadhwa, M. & Crozaz, G. (1996) QUE94201 shergottite: Crystallization of a Martian basaltic magma. *Geochimica et Cosmochimica Acta* **60**: 4563-4569.
- Melosh, H. J. (1985) Ejection of rock fragments from planetary bodies. *Geology* **13**: 144-148.
- Millonig, L. J., Gerdes, A. & Groat, L. A. (2013) The effect of amphibolite facies metamorphism on the U-Th-Pb geochronology of accessory minerals from meta-carbonatites and associated meta-alkaline rocks. *Chemical Geology* **353**: 199-209.
- Misawa, K., Nakamura, N., Premo, W. R. & Tatsumoto, M. (1997) U-Th-Pb isotopic systematics of Iherzolitic shergottite Yamato-793605. *Antarctic Meteorite Research* **10**: 95.
- Moser, D. E., Chamberlain, K. R., Tait, K. T., Schmitt, A. K., Darling, J. R., Barker, I. R. & Hyde, B. C. (2013) Solving the Martian meteorite age conundrum using micro-baddeleyite and launch-generated zircon. *Nature* **499**: 454-457.
- Nakanishi, N., Yokoyama, T., Okabayashi, S., Iwamori, H. & Hirata, T. (2022) Geochemical constraints on the formation of chondrules: Implication from Os and Fe isotopes and HSE abundances in metals from CR chondrites. *Geochimica et Cosmochimica Acta* **319**: 254-270.
- Neukum, G. & Hiller, K. (1981) Martian ages. *Journal of Geophysical Research: Solid Earth* **86**: 3097-3121.
- Neukum, G. & Wise, D. U. (1976) Mars: A Standard Crater Curve and Possible New Time Scale. *Science* **194**: 1381-1387.

- Neukum G., Ivanov B. A., and Hartmann W. K. 2001. Cratering Records in the Inner Solar System in Relation to the Lunar Reference System. *Chronology and Evolution of*. pp. 55-86.
- Niihara, T. (2011) Uranium-lead age of baddeleyite in shergottite Roberts Massif 04261: Implications for magmatic activity on Mars. *Journal of Geophysical Research: Planets* **116**.
- Niihara, T., Kaiden, H., Misawa, K., Sekine, T. & Mikouchi, T. (2012) U-Pb isotopic systematics of shock-loaded and annealed baddeleyite: Implications for crystallization ages of Martian meteorite shergottites. *Earth and Planetary Science Letters* **341-344**: 195-210.
- Nyquist, L. E., Bogard, D. D., Shih, C. -, Park, J., Reese, Y. D. & Irving, A. J. (2009) Concordant Rb-Sr, Sm-Nd, and Ar-Ar ages for Northwest Africa 1460: A 346Ma old basaltic shergottite related to "Iherzolitic" shergottites. *Geochimica et Cosmochimica Acta* **73**: 4288-4309.
- Nyquist L. E., Bogard D. D., Shih C. -, Greshake A., Stöffler D., and Eugster O. 2001. Ages and Geologic Histories of Martian Meteorites. *Chronology and Evolution of*. pp. 105-164.
- Park, J., Bogard, D. D., Nyquist, L. E., Garrison, D. H. & Mikouchi, T. (2013) Ar-Ar ages and trapped Ar components in Martian shergottites RBT 04262 and LAR 06319. *Geochimica et Cosmochimica Acta* **121**: 546-570.
- Park, J., Bogard Donald, D., Nyquist Laurence, E. & Herzog, G. F. (2014) Issues in dating young rocks from another planet: Martian shergottites. *Geological Society, London, Special Publications* **378**: 297-316.
- Pepin, R. O. (1994) Evolution of the Martian Atmosphere. *Icarus* **111**: 289-304.
- Plescia, J. B. (1990) Recent flood lavas in the Elysium region of Mars. *Icarus* **88**: 465-490.
- Schmitt, A. K., Chamberlain, K. R., Swapp, S. M. & Harrison, T. M. (2010) In situ U-Pb dating of micro-baddeleyite by secondary ion mass spectrometry. *Chemical Geology* **269**: 386-395.
- Shih, C. -, Nyquist, L. E., Bogard, D. D., McKay, G. A., Wooden, J. L., Bansal, B. M. & Wiesmann, H. (1982) Chronology and petrogenesis of young achondrites, Shergotty, Zagami, and ALHA77005: late magmatism on a geologically active planet. *Geochimica et Cosmochimica Acta* **46**: 2323-2344.
- Soderblom, L. A., Condit, C. D., West, R. A., Herman, B. M. & Kreidler, T. J. (1974) Martian planetwide crater distributions: Implications for geologic history and surface processes. *Icarus* **22**: 239-263.
- Staddon, L. G., Darling, J. R., Schwarz, W. H., Stephen, N. R., Schuindt, S., Dunlop, J. & Tait, K. T. (2021) Dating martian mafic crust; microstructurally constrained baddeleyite geochronology of enriched shergottites Northwest Africa (NWA) 7257, NWA 8679 and Zagami. *Geochimica et Cosmochimica Acta* **315**: 73-88.

- Storey, C. D., Jeffries, T. E. & Smith, M. (2006) Common lead-corrected laser ablation ICP–MS U–Pb systematics and geochronology of titanite. *Chemical Geology* **227**: 37-52.
- Taylor, G. J. (2013) The bulk composition of Mars. *Geochemistry* **73**: 401-420.
- Timms, N. E., Erickson, T. M., Zanetti, M. R., Pearce, M. A., Cayron, C., Cavausie, A. J., Reddy, S. M., Wittmann, A. & Carpenter, P. K. (2017) Cubic zirconia in >2370 °C impact melt records Earth's hottest crust. *Earth and Planetary Science Letters* **477**: 52-58.
- Tornabene, L. L., Moersch, J. E., McSween Jr., H. Y., McEwen, A. S., Piatek, J. L., Milam, K. A. & Christensen, P. R. (2006) Identification of large (2–10 km) rayed craters on Mars in THEMIS thermal infrared images: Implications for possible Martian meteorite source regions. *Journal of Geophysical Research: Planets* **111**.
- Treiman, A. H., Gleason, J. D. & Bogard, D. D. (2000) The SNC meteorites are from Mars. *Planetary and Space Science* **48**: 1213-1230.
- Treiman, A. H., Barrett, R. A. & Gooding, J. L. (1993) Preterrestrial aqueous alteration of the Lafayette (SNC) meteorite. *Meteoritics* **28**: 86-97.
- Udry, A., Howarth, G. H., Herd, C. D. K., Day, J. M. D., Lapen, T. J. & Filiberto, J. (2020) What Martian Meteorites Reveal About the Interior and Surface of Mars. *Journal of Geophysical Research: Planets* **125**: e2020JE006523.
- Udry, A. & Day, J. M. D. (2018) 1.34 billion-year-old magmatism on Mars evaluated from the co-genetic nakhelite and chassignite meteorites. *Geochimica et Cosmochimica Acta* **238**: 292-315.
- Vasconcelos, P. M., Farley, K. A., Malespin, C. A., Mahaffy, P., Ming, D., McLennan, S. M., Hurowitz, J. A. & Rice, M. S. (2016) Discordant K-Ar and young exposure dates for the Windjana sandstone, Kimberley, Gale Crater, Mars. *Journal of Geophysical Research: Planets* **121**: 2176-2192.
- Volkert, C. A. & Minor, A. M. (2007) Focused Ion Beam Microscopy and Micromachining. *MRS Bulletin* **32**: 389-399.
- Wadhwa, M. (2001) Redox State of Mars' Upper Mantle and Crust from Eu Anomalies in Shergottite Pyroxenes. *Science* **291**: 1527-1530.
- Walton, E. L., Kelley, S. P. & Herd, C. D. K. (2008) Isotopic and petrographic evidence for young Martian basalts. *Geochimica et Cosmochimica Acta* **72**: 5819-5837.
- White, L. F., Tait, K. T., Kamo, S. L., Moser, D. E. & Darling, J. R. (2020) Highly accurate dating of micrometre-scale baddeleyite domains through combined focused ion beam extraction and U–Pb thermal ionization mass spectrometry (FIB-TIMS). *Geochronology* **2**: 177-186.

- Wieler, R., Huber, L., Busemann, H., Seiler, S., Leya, I., Maden, C., Masarik, J., Meier, M. M. M., Nagao, K., Trappitsch, R. & Irving, A. J. (2016) Noble gases in 18 Martian meteorites and angrite Northwest Africa 7812—Exposure ages, trapped gases, and a re-evaluation of the evidence for solar cosmic ray-produced neon in shergottites and other achondrites. *Meteoritics & Planetary Science* **51**: 407-428.
- Wingate, M. T. D. & Compston, W. (2000) Crystal orientation effects during ion microprobe U–Pb analysis of baddeleyite. *Chemical Geology* **168**: 75-97.
- Wittmann, A., Kenkemann, T., Schmitt, R. T. & Stöffler, D. (2006) Shock-metamorphosed zircon in terrestrial impact craters. *Meteoritics & Planetary Science* **41**: 433-454.
- Yin, A. (2012) An episodic slab-rollback model for the origin of the Tharsis rise on Mars: Implications for initiation of local plate subduction and final unification of a kinematically linked global plate-tectonic network on Earth. *Lithosphere* **4**: 553-593.
- Zack, T. & Hogmalm, K. J. (2016) Laser ablation Rb/Sr dating by online chemical separation of Rb and Sr in an oxygen-filled reaction cell. *Chemical Geology* **437**: 120-133.
- Zhou, Q., Herd, C. D. K., Yin, Q., Li, X., Wu, F., Li, Q., Liu, Y., Tang, G. & McCoy, T. J. (2013) Geochronology of the Martian meteorite Zagami revealed by U–Pb ion probe dating of accessory minerals. *Earth and Planetary Science Letters* **374**: 156-163.
- Zipfel, J., Scherer, P., Spettel, B., Dreibus, G. & Schultz, L. (2000) Petrology and chemistry of the new shergottite Dar al Gani 476. *Meteoritics & Planetary Science* **35**: 95-106.

CHAPTER 2: PETROGRAPHIC CONTROLS ON BADDELEYITE OCCURRENCE IN A SUITE OF EIGHT BASALTIC SHERGOTTITES

2.1 Abstract

Baddeleyite (ZrO_2) is a common late-stage accessory mineral in basaltic shergottites and is a robust geochronometer for obtaining igneous crystallization ages via *in-situ* SIMS U–Pb analysis. Amiability to SIMS U–Pb dating depends in large part on the sizes and abundance of baddeleyite grains, which are generally surveyed using microbeam methods. We examine the petrography, mineralogy, geochemistry, and baddeleyite distribution in eight basaltic shergottites to identify factors that may be used to predict baddeleyite distribution. Results suggest that fractional crystallization controls baddeleyite occurrence in shergottites to the first order; samples with pyroxene major element compositions extending beyond the 1-bar stability boundary generally have higher baddeleyite abundance compared to samples with pyroxene compositions terminating at or before the stability boundary. In samples which display two pyroxene composition trends (high-Ca and low-Ca), the largest baddeleyite grains tend to be associated with Fe-Ti oxides; in samples where pyroxene composition forms a continuous trend extending beyond the 1-bar stability boundary, the largest baddeleyite grains are typically associated with polymimetic late-stage pockets. Bulk HFSE content and f_{O_2} do not appear to directly influence baddeleyite distribution. Based on our findings, we propose that pyroxene composition is a useful proxy for assessing baddeleyite abundance and distribution in shergottites and may aid in determining a sample's feasibility for U–Pb geochronology prior to conducting detailed surveys for baddeleyite characterization.

2.2 Introduction

Advances in isotopic microanalytical techniques have enabled U–Pb baddeleyite geochronology of shergottites via *in-situ* ion-beam analysis at μm -scale resolutions (Misawa and Yamaguchi, 2007; Jiang and Hsu, 2012; Moser et al., 2013; Zhou et al., 2013; Wu and Hsu, 2019). Compared to traditional chemical

chromatography methods (e.g., ID-TIMS, ICP-MS), *in-situ* analysis is much less destructive, preserves petrographic context, and overcomes the challenges of open-system chemical behaviour that may be difficult to quantify on the whole-rock scale (e.g., light REE and Sr mobility in hot desert meteorites; [Crozaz and Wadhwa, 2001](#)). The use of baddeleyite as a robust geochronometer also avoids potential contamination by common Pb reservoirs which affects whole-rock U–Pb systematics ([Bellucci et al., 2016](#)). Furthermore, high-resolution (μm - to nm-scale) microstructural and chemical mapping enables detailed assessment of shock metamorphic effects, allowing for igneous age information to be resolved even in highly shocked shergottites ([Moser et al., 2013](#); [Darling et al., 2016](#)). These advantages make *in-situ* U–Pb baddeleyite analysis an attractive option for obtaining igneous crystallization ages when sample amounts may be scarce and maximum preservation is a priority, such as in the case of rare meteorites and future samples returned from the surface of Mars ([Beatty et al., 2019](#); [Clery and Voosen, 2019](#)).

2.3 Background

Baddeleyite (monoclinic ZrO_2) is a common accessory mineral in mafic igneous rocks ([Heaman and LeCheminant, 1993](#)). The ability of baddeleyite to incorporate U (typically tens to hundreds of ppm) and exclude initial common Pb during crystallization, combined with the resistance to Pb loss under alteration up to amphibolite facies metamorphism ([Heaman and LeCheminant, 1993](#); [Millonig et al., 2013](#)), makes the mineral the principal geochronometer of interest for dating terrestrial gabbro and diabase intrusions. Advances in isotopic microanalysis since the 1990's have enabled U–Pb ages to be determined from $<50 \mu\text{m}$ baddeleyite grains with a precision better than 0.1% (2σ) using isotope dilution thermal ionization mass spectrometry (ID-TIMS; e.g., [Söderlund et al., 2005](#); [French and Heaman, 2010](#)). In addition, *in-situ* U–Pb analysis by laser ablation inductively-coupled plasma mass spectrometry (LA-ICP-MS) and secondary ion mass spectrometry (SIMS) has been achieved for baddeleyite grains as small as $\sim 10\text{--}15 \mu\text{m}$ ([Chamberlain et al., 2010](#); [Ibanez-Mejia et al., 2014](#); [Li et al., 2010](#); [Schmitt et al., 2010](#)) with a precision of $1\text{--}3\%$ (2σ) for Phanerozoic U–Pb ages (e.g., [Li et al., 2010](#); [Schmitt et al., 2010](#); [Ibanez-Mejia et al., 2014](#)).

Whereas ID-TIMS requires crushing whole rocks and separating baddeleyite grains to be dissolved for analysis, *in-situ* analysis by LA-ICP-MS and SIMS is much less destructive and thus ideal for meteoritic applications where sample volume may be small and preservation is priority.

In addition to terrestrial igneous rocks, baddeleyite occurs in lunar basalts (e.g., [Lovering and Wark, 1971](#)) and in martian meteorites. Similar to in terrestrial analogues, baddeleyite in these rocks occurs alongside late-stage phases interstitially to the major minerals, with the notable absence of hydrous accessory phases (e.g., amphiboles) which are common in terrestrial mafic rocks. [Herd et al. \(2018\)](#) provide the first comprehensive survey of baddeleyite occurrence in planetary basalts with a focus on shergottites among martian meteorites. The presence of high-pressure polymorphs, localized melting, and other shock-related features in shergottites have led to speculations that baddeleyite in these rocks crystallized as a result of shock processes (e.g., [Bouvier et al., 2008](#)); however extensive investigations into microstructures, mineral chemistry, and isotopic systematics, in addition to experimental studies of ZrO_2 phase transformations, have since established that baddeleyite in shergottites formed as a primary mineral during igneous crystallization and records the ages of shergottite magmatism on Mars ([Niihara et al., 2012; Moser et al., 2013; Zhou et al., 2013; Darling et al., 2016](#)).

In addition to early studies on SHRIMP II U–Pb baddeleyite analysis ([Misawa and Yamaguchi, 2007; Niihara, 2011](#)), SIMS U–Pb baddeleyite ages have been determined for Groves Mountains (GRV) 020090 ([Jiang and Hsu, 2012](#)), Zagami ([Zhou et al., 2013](#)), Northwest Africa (NWA) 5298 ([Moser et al., 2013; Darling et al., 2016](#)), and NWA 8653 ([Wu and Hsu, 2019](#)). In particular, a U–Pb baddeleyite age of 183 ± 7 Ma for Zagami ([Zhou et al., 2013](#)) is in agreement with Rb–Sr, Sm–Nd, and Lu–Hf ages determined from mineral separation methods, demonstrating the accuracy of *in-situ* SIMS U–Pb analysis. Furthermore, work on NWA 5298 shows that although baddeleyite in highly shocked shergottites can be subject to highly variable degrees of shock modification, these effects are localized and can be discerned through microstructural and chemical mapping of baddeleyite grains, thus allowing for igneous age information to

be resolved *via* *in-situ* U–Pb analysis (Moser et al., 2013; Darling et al., 2016). So far, U–Pb baddeleyite geochronology has been conducted only on enriched shergottites.

The recent discovery of a new, ca. 2.4 Ga shergottite age population (Herd et al., 2017; Lapen et al., 2017) highlights the significance of shergottite dating for expanding the absolute time scale of Mars, which constitute the vast majority of martian meteorites. SIMS U–Pb methods offer a less destructive alternative to traditional chemical chromatography methods, allowing for greater potential to obtain igneous ages for small-volume shergottite samples. Fundamentally, successful U–Pb baddeleyite dating relies on the number and size of baddeleyite grains that can be analyzed and U content. Baddeleyite grains in shergottites are generally smaller than 40 µm and range in abundance from 0.05 to >2 grains/mm² (Herd et al., 2018). Herd et al. (2018) report comprehensive baddeleyite petrography in nine shergottites and identify TiO₂, SiO₂ activity, Zr content, melt evolution, and variations in oxygen fugacity (f_{O_2}) as factors affecting baddeleyite crystallization in shergottite magmas. Although the most straightforward way to assess a sample’s feasibility for U–Pb baddeleyite analysis is to search for grains directly in a thin section *via* manual or automated methods (summarized in Herd et al., 2018), the petrogenetic and geochemical factors on baddeleyite crystallization presented by Herd et al. (2018) suggest that it may be possible to predict the size, abundance, and style of baddeleyite occurrence in a sample based on more readily available information such as sample petrography and mineral compositions. To this end, we aim to constrain in this study the effects of bulk chemistry, mineral chemistry, and melt evolution on baddeleyite crystallization in shergottites by examining a suite of samples with the ultimate goal to establish salient observations that may aid in assessing the feasibility of shergottite samples for SIMS U–Pb baddeleyite geochronology in future studies.

2.4 Methodology

2.4.1 Samples

Eight basaltic shergottites were selected for our study: Jiddah al Harasis (JaH) 479, Ksar Ghilane (KG) 002, NWA 10299, NWA 11057, NWA 11073, NWA 11255, NWA 12262, and NWA 12919. The survey by [Herd et al. \(2018\)](#) found that basaltic shergottites in general contain more abundant baddeleyite compared to olivine-phyric and poikilitic (formerly termed “lherzolitic”) shergottites. Hence in this study, we focus on basaltic shergottites in order to optimize the sampling size of baddeleyite grains surveyed and to allow for more direct comparison between shergottite samples. All samples are polished thin sections except for NWA 10299, which is a polished tile. Two thin sections, made from successive cuts of the same stone, were examined for JaH 479.

2.4.2 ICP-MS bulk chemistry

In order to provide compositional context for petrographic observations, samples without previously reported bulk chemical data (NWA 10299, 11057, 12262, and 12919) were analyzed for major, minor, and trace elements following protocols outlined in [Chennaoui Aoudjehane et al. \(2012\)](#). Sample powders were obtained by crushing and homogenizing contiguous (NWA 11057, 12919) or partial (NWA 10299) slices transecting the interior of the specimen, or by homogenizing dust derived from cutting the interior of the specimen (NWA 12262). Homogeneity was achieved by grinding in agate mortar and pestle under acetone by hand. The sample powder weights are: 0.25 g (NWA 10299), 0.21 g (NWA 11057), 0.15 g (NWA 12262), and 0.45 g (NWA 12919). ICP-MS analysis of sample solutions was conducted on a PerkinElmer Elan 6000 ICP-MS at the Canadian Center for Isotopic Microanalysis (CCIM), University of Alberta. Measurements were conducted at 1 ml per minute flow rate, 35 sweeps per reading, and one reading per replicate. Dwell times were 10 ms for Na, Al, K, Cu, Zn, Sr, and 20 ms for the remaining elements. Each final result is the average of three replicates.

2.4.3 EPMA petrographic characterization

Petrographic characterization was conducted on a CAMECA SX-100 electron probe microanalyzer (EPMA) at the Electron Microprobe Laboratory, University of Alberta. Wavelength-dispersive

spectrometry (WDS) X-ray maps of select elements (Si, Fe, Mg, Ca, Na, Ti, Cl, P, Zr), in addition to backscattered electron (BSE) images, were created for representative areas of each sample, with resolutions ranging between 4 and 7 $\mu\text{m}/\text{pixel}$. Beams were operated at an accelerating voltage of 20 kV and a current of 100 nA, with a spot-size of generally $<1 \mu\text{m}$. Typical analysis time is \sim 13 hours for an automated mapping session of five elements, in addition to BSE, for a map size of 2000 by 1330 pixels.

Mineral modes were estimated using the threshold histogram in ImageJ software on the combination of Si, Ti, P maps and BSE image. The estimates are more accurate for minerals which display sharp intensity peaks in the histogram (e.g., Fe-Ti oxides in Ti map, Ca-phosphates in P map) and less accurate for fine-grained minerals and minerals with broad and overlapping intensity profiles. Therefore, we associate an uncertainty of $\pm 5 \text{ vol\%}$ with modal estimates for the major silicate minerals. In samples with olivine-pyroxene-silica three-phase symplectites (JaH 479, KG 002, and NWA 12262), depending on the Si intensity contrast, fine-grained fayalitic olivine may not be fully resolved from surrounding phases; hence, modal estimates of olivine in these samples constitute only coarse-grained olivine and represent a minimum estimate of total olivine in the samples.

WDS mineral composition analysis was conducted on pyroxenes, maskelynite, and Fe-Ti oxides, under an accelerating voltage of 20 kV and a beam current of 20 nA. Pyroxenes and former igneous plagioclase (transformed into maskelynite in most cases) were analyzed with a spot size of 5–10 μm and 10 μm , respectively; defocused beams were used for pyroxenes due to the presence of μm -scale subsolidus exsolution lamellae. Analyses were arranged in traverses from cores to rims in order to fully capture the compositional range. For Fe-Ti oxides, the compositions of the spinel (titanomagnetite) and rhombohedral (ilmenite) oxide phases were averaged from 3–5 analyses each using a spot size of 1 μm or a fully focused beam corresponding to a spot size of 0 μm . Where oxyexsolution occurs in titanomagnetite (in JaH 479, KG 002, and NWA 12262), a defocused beam of 10 μm was used instead. Where olivine-pyroxene-silica symplectite occurs, olivine and pyroxene compositions were measured with a fully focused

beam; the composition of the original metastable pyroxferroite was estimated using olivine and pyroxene compositions combined with mineral modes determined from BSE images of the symplectite, following Aramovich et al. (2002).

2.4.4 Oxygen fugacity calculation

Oxygen fugacity, f_{O_2} , was calculated from Fe-Ti oxides compositional data. Averaged composition of each adjacent titanomagnetite and ilmenite grain was reduced using charge balance to calculate FeO and Fe_2O_3 from measured FeO_{total} . The reduced data were then processed using the Ghiorso and Evans (2008) Fe-Ti oxide geothermobarometer online server to calculate f_{O_2} and Fe-Ti equilibration temperature (T_{Fe-Ti}). We report f_{O_2} relative to the quartz-fayalite-magnetite (QFM) buffer of Wones and Gilbert (1969). Analyses with large deviation (>3 wt%) from 100 wt% total, excessive CaO, and/or excessive SiO₂ content were excluded from calculations.

2.4.5 Baddeleyite identification and petrographic characterization

Following element mapping sessions, Zr X-ray maps were used to visually locate and identify baddeleyite grains under the electron microprobe. As the most common Zr-bearing phase in shergottites, baddeleyite grains register as bright spots against a dark background in Zr maps. Live BSE image and energy-dispersive spectrometry (EDS) were used to further verify the identity of baddeleyite, especially when in association with Fe-sulfides which also displays high brightness in BSE. Close-up BSE images were taken of each baddeleyite occurrence to document size, morphology, and petrographic associations. We exclude from the petrographic survey grains that are less than 1 μm in length, which can be abundant in fine-grained glassy mesostasis and are not fully captured by Zr maps at a resolution of 4–7 $\mu m/pixel$. Grains situated within fractures and not in contact with other phases are likewise excluded from documentation as it cannot be definitively demonstrated that these grains were not transported to these locations as an artefact of the polishing process during sample preparation. Rare grains in direct association with shock features (e.g., shock melt pockets, shock melt veins) were documented but

excluded from statistical calculations; due to the focus of this study on igneous paragenesis of baddeleyite, secondary effects will be considered separately. Lengths and widths of baddeleyite grains were measured on close-up BSE images. Due to sharpness and resolution limits in BSE images, there is a maximum uncertainty of $\pm 0.8 \mu\text{m}$ in grain dimension measurements.

Almost the entirety of JaH 479 (two thin sections), KG 002, and NWA 10299 were surveyed for baddeleyites (areas ranging from 106 to 522 mm²). For NWA 11057, 11073, 11255, 12262, and 12919, a ~43 mm² rectangular area was selected for mapping on the rationale that if mineral modes of the selected subsection are similar to those of the whole section, then baddeleyite distribution within the subsection should be representative of the whole section as well.

2.5 Results

2.5.1 Sample petrography

Modal abundance of major phases for each meteorite is presented in Table 2.1. Results from the baddeleyite petrographic survey are presented in Table 2.2. Full mineral compositions are reported in Appendix 1. Petrographic descriptions of each sample, combined with a broad summary of mineral compositions and baddeleyite occurrences, are presented below.

2.5.1.1 JaH 479

JaH 479 is composed primarily of coarse-grained pyroxene (~45 vol%) and plagioclase (completely transformed to maskelynite; ~35 vol%) in subophitic texture (Fig. 2.1a). Subhedral cores of magnesian high-Ca pyroxene are bound by anhedral ferroan low-Ca rims, with a total range of $\text{Fs}_{22-83}\text{En}_{5-54}\text{Wo}_{12-38}$. Micron-scale exsolution lamellae are present in some pyroxene grains. Maskelynite ($\text{Ab}_{18-31}\text{An}_{66-76}\text{Or}_{3-6}$; [Lorenz et al., 2010](#)) reaches up to 2.5 mm in length. Accessory phases include titanomagnetite, ilmenite, chlorapatite, merrillite, Fe-sulfides, fayalitic olivine, silica glass, and baddeleyite. Subsolidus oxyexsolution is observed in titanomagnetite. Three-phase symplectite composed of intergrown fayalitic olivine, highly ferroan pyroxene, and silica occurs in patches on the edges of pyroxene, with a reconstructed composition

of $\text{Wo}_{19}\text{En}_8\text{Fs}_{74}$. On the distal side of symplectite patches is sometimes found a distinct mesostasis assemblage of fayalitic olivine, chlorapatite, and silica glass, occurring alongside Fe-sulfides, Fe–Ti oxides, Ca-phosphates, and/or ferroan low-Ca pyroxene. Late-stage glass pockets and silica-rich mesostasis measure up to 1 mm in size. JaH 479 is cut by a few splaying shock veins up to a few 10s of μm in thickness and showing offset and displacement of igneous minerals along vein margins. Shock melt, as thin veins and small isolated pockets ranging from 0.3 to 0.8 mm in maximum dimension (eleven across two thin sections), were identified based on their cross-cutting relationship with the igneous host rock. The matrix of shock melt pockets and shock veins have quenched to glass or quench-crystallized. Shock deformation in host rock minerals includes complete transformation of precursor igneous plagioclase to maskelynite, and mechanical twinning and mosaicism in pyroxene.

Due to the abundance of baddeleyite in JaH 479 and the large area surveyed (522 mm^2), not all baddeleyite occurrences could be imaged and documented during available instrument time. The total count of baddeleyite grains in JaH 479 was consequently estimated using the particle analysis function in ImageJ, which counts the number of high-signal spots on thresholded Zr maps. Tests were conducted on samples where baddeleyite grains are fully documented to ensure a relative level of accuracy in the counts obtained. Particle analysis yields an estimate of 580 baddeleyite grains (assumed to be $\geq 1 \mu\text{m}$) in JaH 479, corresponding to a frequency of 1.1 grains/mm^2 . It should be noted that when using the particle analysis function to estimate baddeleyite counts, the capability to resolve individual grains depends on the size of grains, the spacing between them, and the resolution of the Zr map. For example, two or more closely spaced grains may register as one spot on the Zr map and therefore be identified as one grain in the particle analysis algorithm. Also, given the mapping resolution of 5 and $7 \mu\text{m/pixel}$ for JaH 479, isolated baddeleyite grains with dimensions much below half of the magnitude of these values might not register a signal strong enough to be included in the thresholded Zr map. Hence, the baddeleyite count and frequency of JaH 479 should be considered a minimum estimate.

A total of 338 surveyed and documented baddeleyite grains yield an average length of 4.4 ± 3.3 μm (1σ) and an average aspect ratio of 2.5 (Table 2.2, Fig. 2.1a). Most of the surveyed grains are associated with pockets containing an olivine-chlorapatite-silica assemblage and with pockets of other late-stage minerals (Fe-Ti oxides, Fe-sulfides, Ca-phosphates, ferroan low-Ca pyroxene). In both cases, grains occur on or near the edge of the pocket (typically bound by maskelynite, pyroxene, or three-phase symplectite; Figs. 2.2a and b), or at phase boundaries within the pocket (Fig. 2.2c). Baddeleyite in the former setting tends to be finer-grained (mean length: 3.7 ± 2.4 μm) and more abundant per pocket compared to those in the latter setting (mean length: 5.0 ± 3.3 μm). Aside from these two prominent associations, baddeleyite is also found within or at the boundary of large grains of major phases (pyroxene, maskelynite, Ca-phosphates), with a much smaller fraction occurring within Fe-Ti oxides and fine-grained glassy mesostasis. Overall, the dimension of baddeleyite grains tends to scale proportionally with grain sizes of the hosting assemblage, being smallest in fine-grained glassy mesostasis and largest in coarse late-stage assemblages. The largest baddeleyite grain surveyed, measuring 23.3×5.3 μm , occurs with Fe-sulfides on the ferroan rim of a large grain of pyroxene (Fig. 2.2d).

Zircon has been reported in JaH 479 ([Weisberg et al., 2010](#)), however zircon was not definitively identified during EPMA sessions in this study. In some cases, submicron grains of a Zr-bearing phase adjacent to silica glass registered both Zr and Si peaks in EDS, similar to the spectrum of zircon.

2.5.1.2 KG 002

The petrography of KG 002 has been described in detail by [Llorca et al. \(2013\)](#). KG 002 is dominated by plagioclase (completely transformed to maskelynite; ~48 vol%) and pyroxene (~37 vol%), with accessory titanomagnetite, ilmenite, chlorapatite, merrillite, Fe-sulfides, fayalitic olivine, silica glass, and baddeleyite ([Llorca et al., 2013](#)). Texture ranges from ophitic to subophitic, with maskelynite displaying preferred orientation (Fig. 2.1b). KG 002 is noted for its coarse grain size relative to other basaltic shergottites ([Llorca et al., 2013](#)), with pyroxene and maskelynite reaching 4–5 mm in length.

Pyroxene is zoned, with magnesian high-Ca cores and ferroan low-Ca rims; the composition range is $\text{Fs}_{26-96}\text{En}_{3-50}\text{Wo}_{2-41}$ ([Llorca et al., 2013](#)). Maskelynite composition is $\text{Ab}_{41-49}\text{An}_{39-58}\text{Or}_{1-7}$ ([Llorca et al., 2013](#)). Three-phase symplectite consisting of intergrown fayalitic olivine, ferroan high-Ca pyroxene, and silica makes up 10–15 vol% of the sample, occurring on the edges of coarse pyroxene. The symplectite has a reconstructed bulk composition of $\text{Wo}_{18}\text{En}_6\text{Fs}_{77}$. Pockets of late-stage minerals occur between symplectite patches and maskelynite, or are enclosed within either phase; these late-stage pockets include Fe-Ti oxides, Ca-phosphates, Fe-sulfides, fayalitic olivine, and glassy mesostasis ([Llorca et al., 2013](#)). Observed among these late-stage phases is an olivine+apatite+silica±Fe-sulfides association similar to that observed in JaH 479, although Fe-sulfides are generally absent from such assemblages in JaH 479. Ca-phosphates are dominated by anhedral merrillite, with chlorapatite confined mainly to the olivine-bearing assemblage described above. Shock melt is present as small isolated pockets (up to 0.8 mm in diameter) associated with maskelynite. Up to 30- μm -wide clasts of igneous pyroxene and oxides are entrained within the former melt. One pocket has quenched to a schlieren-rich glass with flow structures, spherical vesicles, and spheres or blebs of Fe-sulfides. Three other shock melt pockets contain quench-crystallized silicate minerals. The entire sample is dissected by long, subparallel fractures. Shock melt is present within veins which connect to shock melt pockets. Pyroxene exhibits planar fractures and mosaicism.

A total of 56 baddeleyite grains were recorded across a total area of 106 mm^2 , corresponding to a frequency of 0.5 grains/ mm^2 (Table 2.2, Fig. 2.1b), with an average length of $3.2 \pm 1.9 \mu\text{m}$ and average aspect ratio of 2.5. The majority of grains occur in pockets of late-stage minerals, where they are at the edge of titanomagnetite, Fe-sulfides, or fayalitic olivine (Figs. 2.3a and b). The largest grain, measuring $11.8 \times 3.7 \mu\text{m}$, occurs near the edge of titanomagnetite (Fig. 2.3b). Very fine (<1 μm) baddeleyite grains rim inclusions of silica glass within titanomagnetite.

2.5.1.3 NWA 10299

NWA 10299 exhibits a coarse-grained subophitic texture, with elongated prismatic pyroxene (~62 vol%), reaching up to 3 mm in length, and interstitial precursor igneous plagioclase (now a quenched glass; ~29 vol%). Accessory phases include titanomagnetite, ilmenite, merrillite, apatite, Fe-sulfides, olivine, baddeleyite, and silica glass. Pockets of fine-grained, intergrown K-feldspar and glass occur on the fringes of former plagioclase and are associated with Fe-Ti oxides and Ca-phosphates. Three-phase symplectite similar to those in JaH 479 and KG 002 is absent from NWA 10299; olivine occurs only as rims around Fe-Ti oxides. Pyroxene compositions have been described in detail by [Jean et al. \(2016\)](#), with two distinct populations of high-Ca (average: Wo₃₃En₄₂Fs₂₄) and low-Ca (average: Wo₁₂En₅₄Fs₃₄) cores. Pyroxene rims measured in this study reach a ferroan composition of Wo₁₅En₁₆Fs₆₉, with even more ferroan compositions (~Fs₈₁) having been reported by [Jean et al. \(2016\)](#). The precursor igneous plagioclase has a composition range of Ab_{45–55}An_{38–54}Or_{1–13}. The studied thin section is crosscut by an anastomosing network of thin, black shock veins, and mm- to cm-size shock melt pockets. These pockets contain quench-crystallized skeletal silicate minerals and are vesiculated. Pyroxene displays planar fractures, mechanical twinning, and strong mosaicism. Former igneous plagioclase throughout the host rock has been shock-melted to form a vesiculated glass.

A total of 243 baddeleyite grains were recorded across an area of 276 mm², corresponding to a frequency of 0.9 grains/mm² (Table 2.2, Fig. 2.1c). Average grain length is 3.1±2.4 µm, with an average aspect ratio of 2.5. The most common occurrences are at phase boundaries within pockets of late-stage assemblages (Figs. 2.4a and b), and inclusions within or on the edge of Fe-Ti oxides (Fig. 2.4c). A population of finer grains occurs at the edge of K-feldspar+glass mesostasis, associated with fine-grained titanomagnetite and ferroan low-Ca pyroxene (Fig. 2.4d). Grains associated with Fe-Ti oxides tend to be singular, prismatic, and euhedral compared to those in other categories which are commonly subhedral to anhedral and can be singular, clustered, or scattered throughout the hosting assemblage. The largest

recorded grain measures $18.2 \times 3.8 \mu\text{m}$ and occurs at the edge of titanomagnetite in contact with silica glass (Fig. 2.4c).

2.5.1.4 NWA 11057

NWA 11057 is medium-grained, dominated by tabular pyroxene (~66 vol%) and coarser patches of interstitial plagioclase (completely transformed to maskelynite; ~24 vol%), with accessory titanomagnetite, ilmenite, chlorapatite, merrillite, pyrrhotite, baddeleyite, and glass. Euhedral high-Ca pyroxene ($\text{Fs}_{22-44}\text{En}_{26-43}\text{Wo}_{30-37}$) is bound by low-Ca pyroxene ($\text{Fs}_{35-60}\text{En}_{24-53}\text{Wo}_{11-19}$), both displaying increasing ferroan content from core to rim. Maskelynite composition is $\text{Ab}_{48-56}\text{An}_{41-51}\text{Or}_{1-4}$. Calcium-phosphates are dominated by coarse (up to 0.7 mm), anhedral merrillite with numerous mesostasis inclusions; apatite occurs as fine (<0.1 mm) grains within late-stage assemblages. Glassy mesostasis consists of intergrown K-feldspar and silica with fine Fe-Ti oxides and/or Fe-sulfides; this mesostasis occurs as 0.2–0.3 mm pockets or as smaller inclusions within merrillite and Fe-Ti oxides. The sample is cut by fractures filled with calcite from terrestrial weathering. NWA 11057 contains numerous localized glassy shock melt pockets, in addition to shock veins that transect the host rock. Pyroxene displays planar fractures and weak to moderate mosaicism.

A total of 34 baddeleyite grains were recorded across an area of 43 mm^2 , corresponding to a frequency of 0.8 grain/ mm^2 (Table 2.2, Fig. 2.1d). Average grain length is $3.9 \pm 3.0 \mu\text{m}$, with an average aspect ratio of 3.1. Baddeleyite mostly occurs in late-stage assemblages containing Fe-Ti oxides, Fe-sulfides, Ca-phosphates, and/or glass (Figs. 2.5a, b, and c); in half of these occurrences baddeleyite is directly associated with Fe-Ti oxides (Figs. 2.5b and c). As in NWA 10299, a lesser population of baddeleyite grains occurs on the edge of K-feldspar+glass mesostasis; these are generally smaller in size (Fig. 2.5d). The largest grain, measuring $12.5 \times 6.4 \mu\text{m}$, occurs in association with Fe-Ti oxides (Fig. 2.5b). One occurrence is within a shock melt pocket.

2.5.1.5 NWA 11073

NWA 11073 exhibits a medium-grained texture similar to NWA 11057 and is composed predominantly of pyroxene (~65 vol%) and plagioclase (completely transformed to maskelynite; ~29 vol%), with accessory titanomagnetite, ilmenite, chlorapatite, merrillite, pyrrhotite, baddeleyite, and glass. Pyroxene is zoned, with euhedral tabular high-Ca pyroxene ($\text{Fs}_{23-39}\text{En}_{29-44}\text{Wo}_{28-35}$) bounded by euhedral to subhedral low-Ca pyroxene ($\text{Fs}_{35-61}\text{En}_{25-52}\text{Wo}_{10-23}$). Maskelynite has a composition range of $\text{Ab}_{42-56}\text{An}_{41-56}\text{Or}_{1-4}$. Mesostasis pockets of K-feldspar and glass intergrowth occur adjacent to late-stage minerals, similar to NWA 11057. The sample contains numerous isolated, small shock melt pockets and thin, glassy shock veins. Shock melt pockets are zoned, with glassy centers and crystallized rims. Pyroxene grains throughout the sample show strong mosaicism and planar fractures.

A total of 33 baddeleyite grains were recorded across an area of 40 mm^2 , corresponding to a frequency of 0.8 grain/mm^2 (Table 2.2, Fig. 2.1e). Average grain length is $2.8 \pm 1.7 \mu\text{m}$, with an average aspect ratio of 3.0. Most occurrences are prismatic lathed inclusions on the edge of Fe-Ti oxides; this includes the longest grain surveyed, measuring $10.3 \times 1.0 \mu\text{m}$ (Fig. 2.6a). Where ilmenite is present, baddeleyite is adjacent to ilmenite (Fig. 2.6b). A lesser proportion of baddeleyite occurs adjacent to other phases in late-stage pockets, or as generally submicron grains in K-feldspar+glass mesostasis (Fig. 2.6d).

2.5.1.6 NWA 11255

NWA 11255 exhibits a medium-grained texture similar to NWA 11057 and NWA 11073, with predominant zoned pyroxene (~60 vol%) and plagioclase (completely transformed to maskelynite; ~32 vol%) and accessory titanomagnetite, ilmenite, pyrrhotite, merrillite, apatite, baddeleyite, and glass. Clusters of euhedral tabular high-Ca pyroxene ($\text{Fs}_{22-41}\text{En}_{27-44}\text{Wo}_{29-36}$) are bounded by euhedral to anhedral low-Ca pyroxene ($\text{Fs}_{41-59}\text{En}_{28-44}\text{Wo}_{12-18}$). Maskelynite has a composition range of $\text{Ab}_{41-55}\text{An}_{42-58}\text{Or}_{1-4}$. Ca-phosphates are dominated by anhedral merrillite, with apatite occurring as fine needles in pockets of late-stage assemblages. Mesostasis pockets containing K-feldspar and glass intergrowth are similar to those observed in NWA 11057 and NWA 11073. Small, isolated shock melt pockets are present throughout the

sample. The thin section is crosscut by a shock vein measuring ~200 µm at its widest with displacement and offset of igneous minerals along the vein margins. Pyroxene displays weak to moderate mosaicism, planar fractures, and mechanical twins.

A total of 33 baddeleyite grains were recorded across an area of 43 mm², corresponding to a frequency of 0.8 grain/mm² (Table 2.2, Fig. 2.1f). Average grain length is 3.4±2.2 µm, with an average aspect ratio of 2.4. Baddeleyite occurrences in NWA 11255 are similar to those in NWA 11057 and NWA 11073, with the majority at phase boundaries within late-stage assemblages containing Fe-sulfides, Ca-phosphates, Fe-Ti oxides, and glass (Fig. 2.7a). When occurring at the edge of Fe-Ti oxides, baddeleyite is hosted in ilmenite when the latter is present (Fig. 2.7b), similar to NWA 11073. A lesser population of baddeleyite grains are associated with K-feldspar+glass mesostasis, occurring either on the edge of the pocket, or in fine aggregates of late-stage phases contained within (Fig. 2.7c). The largest grain (10.1 × 5.3 µm) occurs with fine apatite and titanomagnetite on the low-Ca rim of pyroxene (Fig. 2.7d).

2.5.1.7 NWA 12262

NWA 12262 exhibits a medium-grained diabasic texture with subequal amounts of pyroxene (~45 vol%) and plagioclase (completely transformed to maskelynite; ~40 vol%) and accessory Fe-Ti oxides, pyrrhotite, apatite, merrillite, fayalitic olivine, baddeleyite, and glass. Subsolidus oxyexsolution is observed in Fe-Ti oxides. Zoned pyroxene ranges in composition from magnesian high-Ca pyroxene to ferroan low-Ca pyroxene ($\text{Fs}_{24-83}\text{En}_{4-51}\text{Wo}_{12-38}$). Maskelynite composition is $\text{An}_{50.9-52.1}\text{Or}_{2.1}$ ([Gattacceca et al., 2020](#)). Apatite grains, reaching up to 1 mm in length, are coarser than those observed in other samples in this study except for KG 002. Three-phase symplectite composed of a vermicular intergrowth of fayalitic olivine, hedenbergitic pyroxene, and silica occurs on the outer edges of pyroxene and has a reconstructed composition of $\text{Fs}_{72}\text{En}_6\text{Wo}_{22}$. Adjacent to symplectite are pockets of late-stage phases, including a distinct olivine-silica-pyroxene assemblage dominated by coarse-grained olivine and silica inclusions. Anhedral pyroxene in this assemblage is ferroan and low-Ca in contrast to ferroan high-Ca pyroxene in the three-

phase symplectites; the absence of fine acicular apatite from this assemblage contrasts with coarse olivine-bearing mesostasis observed in JaH 479 and KG 002. Pockets of fine, intergrown K-feldspar and glass occur between maskelynite and late-stage assemblages. Late-stage phases in NWA 12262, especially Fe-Ti oxides and Ca-phosphates, form very extensive intergrowths. The sample contains numerous isolated pockets of glassy shock melt that range from a few microns to ~3 mm in diameter. Pyroxene throughout NWA 12262 displays planar fractures and mosaicism.

A total of 71 baddeleyite grains were recorded across an area of 43 mm², corresponding to a frequency of 1.7 grain/mm² (Table 2.2, Fig. 2.1g). Average grain length is 3.7±2.6 µm, with an average aspect ratio of 2.5. Baddeleyite in NWA 12262 occurs primarily in extensive late-stage pockets, with a large proportion of grains on the edges of the olivine-silica-pyroxene assemblage mentioned above (Fig. 2.8a). Grains in this latter category are generally <5 µm, subhedral to anhedral grains scattered throughout the pocket, although a few singular grains reach up to ~14 µm in length (Fig. 2.8b, c). A lesser population of baddeleyite grains occurs as fine euhedral laths enclosed within Fe-Ti oxides or at the edge of silica inclusions within Fe-Ti oxides (Fig. 2.8d). The longest recorded baddeleyite grain, measuring 14.8 × 5.1 µm, occurs in a pocket of Fe-sulfide and glass intergrown with fine baddeleyite needles.

2.5.1.8 NWA 12919

NWA 12919 exhibits a medium-grained texture, composed of predominantly pyroxene (~56 vol%) and plagioclase (completely transformed to maskelynite; ~30 vol%), with accessory titanomagnetite, ilmenite, merrillite, chlorapatite, and Fe-sulfides, plus trace olivine and baddeleyite. Pyroxene is zoned, with euhedral cores of high-Ca pyroxene ($\text{Fs}_{19-51}\text{En}_{23-46}\text{Wo}_{25-38}$) bound by rims of low-Ca pyroxene ($\text{Fs}_{33-68}\text{En}_{15-54}\text{Wo}_{11-22}$). Maskelynite composition is $\text{Ab}_{43-57}\text{An}_{40-56}\text{Or}_{1-4}$. Pockets of K-feldspar and glass intergrowth are associated with late-stage assemblages. Trace olivine occurs on the rim of glass inclusions in Fe-Ti oxides or as intergrowths with ilmenite. Several small shock melt pockets are observed in the thin

section, as well as a network of anastomosing shock veins. Shock melt is glassy, with one highly vesiculated shock melt pocket noted. Pyroxene in the host rock exhibits planar fractures and strong mosaicism.

A total of 86 baddeleyite grains were recorded across an area of 43 mm², corresponding to a frequency of 2.0 grain/mm² (Table 2.2, Fig. 2.1h). Average grain length is 2.9±2.5 µm, with an average aspect ratio of 3.8. Baddeleyite occurs primarily on the edge of Fe-Ti oxides or enclosed within (Fig. 2.9a). Additional grains occur at phase boundaries in late-stage assemblages (Figs. 2.9b and c). A lesser proportion of grains is associated with K-feldspar+glass mesostasis; these grains are generally smaller than those in other associations (Fig. 2.9c). The largest grain recorded (14.0 × 3.1 µm) occurs on the edge of a titanomagnetite grain adjacent to K-feldspar+glass mesostasis (Fig. 2.9a).

2.5.2 Pyroxene composition trends

EPMA pyroxene composition analysis results plotted in En-Fs-Di-Hd space are presented in Fig. 2.10. NWA 11057, 11073, 11255, 10299 and 12919 exhibit two separate high-Ca and low-Ca trends, from magnesian cores to ferroan rim compositions. The most magnesian composition of the high-Ca trends overlap in a common region of $\text{Fs}_{19-23}\text{En}_{41-44}\text{Wo}_{34-38}$. Low-Ca trends begin from a magnesian composition of $\text{Fs}_{19-23}\text{En}_{41-44}\text{Wo}_{34-38}$ except for in NWA 11255, which begins at a less magnesian composition of $\text{Fs}_{41}\text{En}_{42}\text{Wo}_{17}$. In NWA 11057, 11073, and 11255, both trends terminate at or just slightly beyond the pyroxene stability boundary at 1 bar ([Lindsley, 1983](#)), with a maximum ferroan content of Fs_{59-61} . In NWA 10299 and 12919, both trends extend beyond this boundary towards the Fs-Hd join, with the low-Ca trend reaching more ferroan compositions (maximum ferroan content: Fs_{81} and Fs_{68} , respectively). The stability boundary is based on experimental compositions; pyroxene compositions to the right of the curve (“forbidden zone”) are metastable with respect to fayalitic olivine, hedenbergitic pyroxene, and silica. The formation of three-phase symplectite with reconstructed pyroxene compositions in the forbidden zone reflects the breakdown of such metastable pyroxenes (pyroxferroite; [Aramovich et al., 2002](#)).

In contrast to NWA 11057, 11073, and 11255, pyroxene compositions of JaH 479, KG 002, and NWA 12262 form a continuous range from magnesian high-Ca pyroxene to ferroan, generally low-Ca compositions extending much further beyond the pyroxene stability boundary, reaching maximum ferroan content of Fs_{83} (in JaH 479 and NWA 12262) and Fs_{96} (in KG 002). These are also samples which contain three-phase symplectites, in which pyroxene is hedenbergitic in composition.

Pyroxene directly adjacent to baddeleyite displays ferroan low-Ca compositions, which are generally among the most ferroan compositions in the sample.

2.5.3 Bulk chemical composition

ICP-MS bulk trace element analysis of NWA 10299, 11057, 12262, and 12919 results are presented in Table 2.3 alongside previously reported data for the other samples. With regards to rare earth elements (REE), all eight samples display a relatively flat chondrite-normalized profile typical of enriched shergottites (Fig. 2.11). When compared with other enriched basaltic shergottites, most of the samples display REE enrichment levels intermediate between Zagami and Shergotty, with NWA 11057 being slightly below this range and NWA 10299 slightly above. NWA 12262 displays much higher enrichment levels compared to the other samples and approaches the enrichment level of Los Angeles, which is among the most enriched shergottite compositions. The positive Ce anomaly in KG 002 has been attributed to terrestrial weathering ([Llorca et al., 2013](#)). A positive Eu anomaly is observed in NWA 11057, similar to KG 002 ([Llorca et al., 2013](#)). Available data for JaH 479 show a REE profile distinct from the rest of the samples, with a lower $(\text{La}/\text{Yb})_{\text{N}}$ value of 0.77 compared to a range of 0.88–1.06.

2.5.4 Oxygen fugacity

Oxygen fugacity calculated from Fe-Ti oxides oxythermobarometry is presented in Table 2.4. The majority of samples have f_{O_2} values between 1.0 and 1.4 log units below the quartz-fayalite-magnetite buffer (QFM–1.4 to QFM–1.0). NWA 12262 has a higher f_{O_2} value of QFM+0.1 ± 0.1, indicating more

oxidized conditions relative to the rest of the samples. The oxygen fugacity values are within the typical range of enriched shergottites (QFM–2.5 to +0.5; Herd, 2006; Walton et al., 2012; Herd, 2019).

2.5.5 Baddeleyite size distribution and petrographic associations

Baddeleyite grain-size distribution histograms are presented in Fig. 2.12. Overall, there is an exponential decrease in grain number with increasing grain size. Grains under 1 μm in length are undersampled due to the chosen length threshold for statistical considerations. In JaH 479, grains below 2 μm appear to be also undersampled; this is likely caused by larger grains being prioritized due to the time constraint involved in surveying JaH 479. In all samples, baddeleyite grains with lengths 6 μm and below account for 82–93% of the total baddeleyite count.

To test whether or not mapping a subsection of a sample still returns a representative distribution of baddeleyite sizes, the grain length distribution of each of the four maps of NWA 10299 (the number of grains per map ranges between 49 and 84) is compared to that of the four maps combined ($n=243$) (Fig. 2.13). Significant variations exist for grain lengths at or below 6 μm ; however, variations are much less at greater lengths.

Surveyed baddeleyite grains are subdivided based on petrographic associations into four categories:

1. *Late-stage pockets* – typically polymimetic containing Fe-Ti oxides, Ca-phosphates, Fe-sulfides, silica glass, highly ferroan low-Ca pyroxene, and/or fayalitic olivine, occurring on the outer edges of major silicate phases (i.e. pyroxene, maskelynite) or are enclosed within. Baddeleyite occurs on the edges of the pocket, at phase boundaries within, or are enclosed within one of the phases (except Fe-Ti oxides, see below).
2. *Olivine-bearing late-stage pockets* – These denote primarily the olivine+apatite+silica±Fe-sulfides assemblage observed in JaH 479 and KG 002, and the non-symplectite olivine+pyroxene+silica assemblage in NWA 12262. Both assemblages are characterized by

- predominant coarse anhedral olivine with blebby silica inclusions and apatite needles or feathery pyroxene. Baddeleyite occurs at phase boundaries or is enclosed within olivine.
3. *Fe-Ti oxides* – Baddeleyite is partially or entirely enclosed within a much larger grain of Fe-Ti oxide, distinct from occurrences in late-stage pockets where baddeleyite may be adjacent to Fe-Ti oxides of similar size. Baddeleyite generally occurs near or at the edge of the grain. Where ilmenite is present alongside titanomagnetite in the same grain, baddeleyite is commonly associated with ilmenite. A particular association where baddeleyite occurs in titanomagnetite around inclusions of silica glass is observed in KG 002, NWA 10299, 11073, 11255, 12262, and 12919.

4. *Glassy mesostasis* – includes pockets of predominantly silica glass and pockets of K-feldspar+glass intergrowth. Late-stage minerals, predominantly titanomagnetite and ferroan pyroxene, occur as fine grains throughout; baddeleyite is typically adjacent to one of these minerals or is right at the edge of the mesostasis pocket.

Occurrences that fall outside of the above four categories include grains enclosed in pyroxene or in maskelynite, on the edge of three-phase symplectite, and at the pyroxene-maskelynite boundary. Compared to the categories defined above, these occurrences are too low in number to be considered as individual categories for statistical analysis in our study.

Relative proportions of baddeleyite petrographic associations are summarized in Table 2.5 and Fig. 2.14. In JaH 479, KG 002, and NWA 12262, baddeleyite is predominantly associated with late-stage pockets and olivine-bearing late-stage pockets, with much smaller proportions of grains associated with Fe-Ti oxides and glassy mesostasis. In NWA 11057, 11073, 11255, and 12919, there is a greater proportion of grains associated with Fe-Ti oxides and glassy mesostasis, roughly subequal to grains associated with late-stage pockets. NWA 11073 contains the largest proportion of grains associated with Fe-Ti oxides, at ~50%. NWA 10299 is dominated by grains associated with late-stage pockets (~60%).

Mean grain length, maximum grain length, and mean aspect ratio for the four main petrographic associations are summarized in Table 2.5. Grains associated with Fe-Ti oxides have the greatest mean length in JaH 479, KG 002, NWA 10299, and NWA 11057. In NWA 11073 and NWA 11255, grains in glassy mesostasis have the greatest mean length. In NWA 12262 and NWA 12919, grains associated with late-stage pockets have the greatest mean length. In all eight samples, the longest documented grain is associated either with late-stage pockets or Fe-Ti oxides. There does not appear to be systematic variation of mean aspect ratio across the four categories, with most values between 2.0 and 3.0. Some mean values higher than 3.0 are observed for grains associated with Fe-Ti oxides and with glassy mesostasis, with NWA 12919 displaying a mean aspect ratio of 6.1 for grains associated with glassy mesostasis.

2.6 Discussion

2.6.1 Baddeleyite as a late-stage igneous mineral

Baddeleyite surveyed in the eight shergottite samples is ubiquitously associated with late-stage accessory minerals, including Fe-Ti oxides, Ca-phosphates, Fe-sulfides, K-feldspar, and SiO₂, in addition to Fe-rich silicate phases such as fayalitic olivine and ferroan pyroxene. The formation of these late-stage phases in mesostasis reflects crystallization from the last-remaining liquids enriched in incompatible elements during an igneous crystallization sequence: S in Fe-sulfides, P and REE in Ca-phosphates, Ti in Fe-Ti oxides, and Zr in baddeleyite. Furthermore, the highly ferroan compositions of pyroxene adjacent to baddeleyite reflect progressive enrichment of Fe in the remaining melts up until the last stages of crystallization. These lines of evidence indicate that baddeleyite in shergottites formed from the most chemically fractionated portions of the basaltic magma during igneous crystallization. Our observations support inference drawn by previous work that baddeleyite paragenesis in shergottites resembles that in terrestrial basalts, with two key distinctions: 1) Shergottite magmas are generally anhydrous—in contrast to terrestrial basalts which may contain hydrous minerals such as amphiboles and micas in association with baddeleyite ([Heaman and LeCheminant, 1993; Herd et al., 2018](#)). 2) Shergottite magmas are

generally more silica-undersaturated, therefore the activity of SiO_2 is insufficient to form zircon (ZrSiO_4) as a stable Zr-bearing phase under igneous late-stage conditions, in contrast to terrestrial mafic magmas which may crystallize zircon in pockets of extensively fractionated, silica-saturated pegmatitic domains (Heaman and LeCheminant, 1993). Where baddeleyite occurs alongside igneous silica in shergottites, no zircon formation is observed. However, in the NWA 5298 shergottite, shock-produced zircon forms at the boundary between baddeleyite and silica (Moser et al., 2013). This leads Herd et al. (2018) to suggest that baddeleyite and silica crystallizing from fractionated liquids are metastable and require excess energy to react to form zircon.

The association of baddeleyite with igneous silica in shergottites without the formation of zircon has been interpreted to reflect metastability in fractionated liquids without the pressure-temperature conditions necessary for zircon crystallization (Herd et al., 2018).

2.6.2 Shock pressure estimates and implications for baddeleyite paragenesis

The shock deformation and transformation effects in the studied samples are consistent with moderate to strong shock metamorphism. Shock deformation comprises planar fractures, mosaicism and mechanical twins in pyroxene, whereas transformation encompasses the formation of localized shock melt as veins and pockets and the formation of glass from plagioclase. Maskelynite is identified as a glass of plagioclase composition that is smooth and unfractured in BSE images, retains the crystal shape of the precursor igneous mineral and does not exhibit evidence of melting. The margins of maskelynite exhibit irregular fractures that radiate into neighbouring igneous minerals (e.g. pyroxene), indicating a volume change upon formation. In contrast, a “normal” plagioclase glass quenches from a liquid after pressure release, rather than a solid-state shock-transformation mechanism (e.g., maskelynite) and is distinguished by flow lines and/or vesicles. In this study, we document the complete transformation of igneous plagioclase to maskelynite in JAH 479, KG 002, NWA 11073, 11255, 12262, 11507, and 12919 and to a vesiculated glass in NWA 10299. The pressure at which plagioclase transforms depends on temperature,

chemical composition and experimental set-up (e.g., [Fritz et al., 2019](#)). Precursor igneous plagioclase in the studied shergottites is predominantly Ca-rich (An_{30-58}) with the exception of plagioclase in JaH 479 which is slightly more calcic (An_{66-76}). Given the predominantly Ca-rich compositions and the most up-to-date compilation of shock-recovery experiments ([Fritz et al., 2019](#)), the presence of maskelynite indicates shock pressures of at least $\sim 24\text{--}25$ GPa and up to ~ 45 GPa. Shock melting of plagioclase, observed in NWA 10299, requires higher shock pressures on the order of 45–55 GPa.

We find no petrographic evidence suggesting a shock-induced origin for baddeleyite in the studied samples. Although in rare instances baddeleyite is identified within shock melt pockets (five grains in total), these grains exhibit morphology and textural relationships to surrounding phases that are similar to grains not associated with shock features. We therefore consider these grains to have been entrained as unmelted clasts in localized shock features and did not form from shock processes. The presence of plagioclase melting in NWA 10299 is comparable to the highly shocked NWA 5298, for which a minimum shock pressure of 30 GPa is estimated ([Darling et al., 2016](#)). Whereas baddeleyite grains in NWA 5298 have undergone varying degrees of shock modification causing degraded crystallinity and isotopic disturbance, we do not find evidence in NWA 10299 of the granular texture exhibited by the most shock-modified baddeleyite grains in NWA 5298 ([Darling et al., 2016](#)). This suggests that conditions for baddeleyite shock modification similar to that documented in the most shocked grains in NWA 5298 were not met during the impact and launch of NWA 10299, or that such heterogeneously distributed effects were less manifested in the portion of NWA 10299 investigated in this study.

2.6.3 Controls on baddeleyite occurrence in shergottites

[Herd et al. \(2018\)](#) identify factors influencing baddeleyite occurrence in shergottite magmas. As baddeleyite is the main Zr-bearing phase in shergottites, baddeleyite crystallization should be controlled to the first order by the concentration of Zr in the melt, which in turn depends on: 1) Zr content of the parental melt, 2) enrichment of Zr through fractional crystallization, and 3) the distribution of Zr in late-

stage phases. Based on petrographic, mineralogical, and geochemical observations, we assess these factors with respect to the studied samples, namely to what extent these factors control the frequency and size of baddeleyite grains.

2.6.3.1 HFSE content of the parental melt

The Zr content of late-stage melts from which baddeleyite crystallizes is directly related to the Zr content of the parental melt under the assumption of closed-system crystallization; that is, no accumulation or melt mixing has occurred. Although the bulk compositions of some shergottites are interpreted to represent that of their starting (parental) melts (e.g., QUE 94021; [Kring et al., 2003](#)), basaltic shergottites generally contain cumulate pyroxene cores and hence do not represent parental melt compositions ([Stolper and McSween, 1979](#); [McSween and McLennan, 2014](#)). With respect to Zr and other incompatible trace elements (ITE) which do not readily partition into major igneous minerals involved in accumulation (e.g., olivine, pyroxene, plagioclase), the bulk content of these elements in cumulate portions would be lower than that of the intercumulus liquid, hence the bulk ITE content of shergottites represents a minimum estimate of that of the parental melt. Due to the complexity of modeling cumulate formation and quantifying its effect on ITE content, we will use shergottite bulk compositions as a proxy for parental melt compositions. In effect, we consider baddeleyite formation with respect to how Zr becomes concentrated in the late-stage melts.

Although Zr data are available for only two of the eight shergottite samples, high field-strength elements (HFSE) behave similarly in basaltic magmas and can be used as a proxy for relative Zr content, assuming there has not been significant fractionation of Zr-bearing phases. Bulk HFSE levels do not appear to directly correlate with baddeleyite frequency (Fig. 2.15). For grains measuring 1 μm or larger, NWA 12262 displays the highest overall HFSE enrichment levels and a high baddeleyite frequency of 1.7 grains/mm². NWA 12919 has an even higher baddeleyite frequency of 2.0 grains/mm², however its HFSE content is in the overall range defined by the rest of the samples (0.5–1.0 wt% TiO₂, 1.0–1.8 ppm Yb),

which have much lower baddeleyite frequencies of generally <1.0 grains/ mm^2 . Due to the likelihood that grains $\sim 1 \mu\text{m}$ (and up to $2 \mu\text{m}$ in JaH 479) were not fully documented, we also examine baddeleyite frequency versus HFSE content for the $\geq 4 \mu\text{m}$ grain population; NWA 12262 and NWA 12919 both have higher grain frequency (0.5 and 0.4 grain/ mm^2) relative to the other samples (<0.3 grain/ mm^2). However, for the remaining six samples the grain frequency does not appear to discriminate between those with higher and those with lower HFSE content. Therefore, bulk HFSE content does not appear to have direct control on baddeleyite abundance in the samples with respect to grains $4 \mu\text{m}$ and larger.

2.6.3.2 Fractional crystallization

Fractional crystallization in shergottites is reflected in compositional zoning in pyroxene and plagioclase. Pyroxene compositions range from magnesian cores to ferroan rims, with pyroxene adjacent to baddeleyite typically having the most ferroan composition in the sample. It follows therefore that more extensive fractional crystallization would result in a wider range and higher ferroan content in pyroxene. We therefore utilize ferrosilite content in pyroxene (Fs) as a proxy for the degree of fractional crystallization. Pyroxene compositions in NWA 11057, 11073, 11255, 10299 and 12919 separate into a high-Ca and a low-Ca series, with baddeleyite associated with pyroxenes that plot in the ferroan end of the low-Ca trend (Fig. 2.10). JaH 479, KG 002, and NWA 12262 display a relatively continuous pyroxene composition trend, with baddeleyite associated with generally ferroan low-Ca pyroxene compositions but not necessarily the most ferroan ones. A salient feature of the pyroxene composition trends is that pyroxene compositions associated with baddeleyite plot near or beyond the 1-bar stability boundary where ferroan content is too high for pyroxene to remain crystallographically stable (Lindsley, 1983).

Among samples displaying two pyroxene series, baddeleyite-associated pyroxene in NWA 11057, 11073, and 11255 plots near or at the stability boundary (Fs_{55–61}) whereas those in NWA 10299 and 12919 plot beyond the stability boundary (Fs_{57–69}). This corresponds to a lower baddeleyite frequency in the former three samples (0.8 grains/ mm^2) relative to the latter two (0.9 and 2.0 grains/ mm^2 respectively). In

JaH 479, KG 002, and NWA 12262, all baddeleyite-associated pyroxene plots beyond the stability boundary (Fs_{69-81}) and approaches the compositions of pyroxferroite as reconstructed from three-phase symplectite. This correlates with higher baddeleyite frequency in JaH 479 (>1.1 grains/ mm^2) and NWA 12262 (1.7 grains/ mm^2). The observed correlation between baddeleyite frequency and pyroxene composition suggests that higher ferroan content in pyroxene reflects higher degrees of fractional crystallization, which in turn favors baddeleyite crystallization. KG 002 appears to be an exception to this as it displays highly ferroan pyroxene compositions beyond the stability boundary yet the lowest baddeleyite frequency (0.5 grains/ mm^2) among the studied samples. However, due to the exceptionally coarse grain size of KG 002 (4–5 mm pyroxene and maskelynite grains) and the relatively small area of the surveyed thin section (14 × 10 mm), we consider it likely that the surveyed baddeleyite grains do not represent the true baddeleyite frequency in KG 002. Given that Zr content in evolved pyroxene rims may reach up to 30 ppm ([Wadhwa et al., 1998](#)), it is also possible that the very coarse pyroxene grains in KG 002 are a major sink of Zr, limiting baddeleyite crystallization in late-stage melts; Zr analysis of pyroxene in KG 002 would be required to assess this. If the surveyed grains are representative of baddeleyite occurrences in KG 002, then the contrast with JaH 479 and NWA 12262 suggests that Zr content in late-stage melts in KG 002 remained low enough that baddeleyite crystallization was suppressed.

The occurrence of three-phase symplectite in JaH 479, KG 002, and NWA 12262 as a product of pyroxferroite breakdown further indicates crystallization of metastable phases from very fractionated melts. It is worth noting that although baddeleyite may occur in mesostasis pockets adjacent to or enclosed within three-phase symplectite, it does not occur as a component within the symplectite itself. This indicates that baddeleyite crystallized from melts that remained following pyroxferroite crystallization.

The relationship between pyroxene composition and baddeleyite occurrence is observed also for shergottites surveyed by [Herd et al. \(2018\)](#); those with pyroxene compositions extending well beyond the

stability boundary (QUE 94201, NWA 1460, and Zagami “DN” lithology) have higher baddeleyite frequency (1.7–2.0 grains/mm²) compared to those with pyroxene compositions terminating near the stability boundary (NWA 3171, Zagami dark mottled lithology; <0.8 grains/mm²). Based on our observations, fractional crystallization exerts direct control on the abundance of baddeleyite occurrences in shergottites and pyroxene composition trends may be used to predict relative baddeleyite abundance in a sample.

2.6.3.3 Zr content of late-stage phases

As baddeleyite crystallization depends on the concentration of Zr in the late-stage melt, the concentration of Zr in late-stage phases also in theory affects where and how baddeleyite crystallizes. Although Zr is largely incompatible in Ca-phosphates, Fe-sulfides, and fayalitic olivine, Zr⁴⁺ substitutes for Ti⁴⁺ in Fe-Ti oxides ([Nakamura et al., 1986](#); [Nielsen et al., 1994](#)). It has been previously postulated that more oxidized conditions decrease Zr compatibility in Fe-Ti oxides, causing baddeleyite to form after Fe-Ti oxides have crystallized ([Herd et al., 2018](#)). However, only a small proportion of baddeleyite grains are associated with Fe-Ti oxides in NWA 12262 (4 out of 38; Table 2.5), which displays the most oxidized f_{O_2} value (QFM+0.1) of the studied samples. In contrast, NWA 10299, 11057, 11073, 11255, and 12919, which are less oxidized (QFM−1.4 to −1.0) contain a larger proportion of baddeleyite associated with Fe-Ti oxides. JaH 479 and KG 002, which are similarly less oxidized (QFM−1.2 and −1.0 respectively), contain a low proportion of baddeleyite associated with Fe-Ti oxides, similar to NWA 12262. We therefore conclude that f_{O_2} alone does not control the probability of baddeleyite occurring in association with Fe-Ti oxides in a given sample.

In several samples, baddeleyite occurring within Fe-Ti oxides appears to be preferentially associated with ilmenite when the latter is present. Although baddeleyite has been interpreted as forming via exsolution from ilmenite in terrestrial tholeiitic gabbros ([Naslund, 1987](#)), textural observations of baddeleyite in this study do not support such an interpretation for the surveyed shergottites.

2.6.4 Variation in baddeleyite grain size and morphology

While petrographic and geochemical observations allow for general inferences to be drawn about the abundance of baddeleyite in a shergottite sample, feasibility for U–Pb geochronology depends not only on the abundance but also on the size and morphology of the grains, particularly since baddeleyite in meteoritic samples generally approaches the lower limit of size and volume required by current analytical methods. Previous SIMS and LA-ICP-MS U–Pb baddeleyite work on shergottites and lunar basalts generally required a beam size of ~4–10 µm (e.g., [Moser et al., 2013](#); [Zhou et al., 2013](#); [Shaulis et al., 2017](#); [Wu and Hsu, 2020](#)), while [White et al. \(2020\)](#) identify a minimum volume of $15 \times 5 \times 5 \mu\text{m}^3$ for focused ion beam (FIB) baddeleyite extraction for TIMS U–Pb analysis. In addition, the variable response of baddeleyite to heterogeneously distributed shock experienced by shergottites may result in the formation of microstructural subdomains exhibiting variable U–Pb isotopic disturbance ([Moser et al., 2013](#); [Darling et al., 2016](#)). This means that an accurate analysis of U–Pb igneous crystallization age requires in theory a baddeleyite subdomain which has undergone negligible shock modification and which is at least of the dimensions mentioned above. We assess possible factors affecting baddeleyite grain size below.

In JaH 479, KG 002, NWA 10299, and 11057, baddeleyite grains associated with Fe-Ti oxides have the greatest mean length (Table 2.5), however large standard deviations associated with the mean values do not allow for baddeleyite under each petrographic association to be considered distinct populations. Maximum grain length, on the other hand, appears to correlate with grain abundance when grains are grouped by petrographic association. In samples with two pyroxene composition trends (NWA 10299, 11057, 11073, 11255, 12919), the largest baddeleyite grain generally occurs in association with Fe-Ti oxides, reaching up to 18 µm in length, whereas grains occurring in late-stage pockets and in glassy mesostasis reach lesser maximum dimensions. In NWA 10299 and 12919, which display higher degrees of fractional crystallization, the maximum length of baddeleyite grains in late-stage pockets approach those associated with Fe-Ti oxides (12–14 µm). In JaH 479 and NWA 12262, which display single, continuous pyroxene trends and much more evolved pyroxene compositions, the largest baddeleyite grains occur in

late-stage pockets and olivine-bearing late-stage pockets, reaching 23 µm in JaH 479. Baddeleyite grains in KG 002 only reach a maximum length of 7 µm, which appears to correlate with the low baddeleyite frequency in this sample. Our observations indicate a general correlation between maximum baddeleyite length and baddeleyite frequency (Table 2.5); if there is more abundant baddeleyite in a given petrographic association, then there is higher probability of crystallizing larger baddeleyite grains.

During our petrographic survey it was noted that large, singular baddeleyite grains associated with Fe-Ti oxides are more commonly euhedral compared to grains in other associations (e.g., Figs. 2.4d, 2.5b, 2.7b, and 2.9a). Ruling out an exsolution origin, this suggests that these euhedral baddeleyite grains either nucleated at the boundary of Fe-Ti oxides with an adjacent phase, or crystallized prior to being enclosed by the larger Fe-Ti oxide grains.

2.6.5 Implications for baddeleyite characterization in shergottites and other martian meteorite groups

Our petrographic and geochemical observations allow us to make general inferences on how martian meteorites are characterized with respect to baddeleyite occurrences and with respect to the amenability to *in-situ* U-Pb baddeleyite geochronology. Compared to basaltic shergottites, pyroxene compositions in olivine-phyric shergottites and poikilitic shergottites are generally magnesian and do not extend beyond the pyroxene stability boundary (e.g., [Peslier et al., 2010](#); [Rahib et al., 2019](#)). This likely reflects generally lower degrees of fractional crystallization compared to basaltic shergottites. Baddeleyite frequency in previously surveyed olivine-phyric shergottites are below 0.15 grains/mm², with a maximum dimension of 9 µm ([Herd et al., 2018](#)). [Peslier et al. \(2010\)](#) reported generally micron-sized baddeleyite grains enclosed in or adjacent to late-stage ilmenite in LAR 06319, similar to observations made in Zagami dark mottled lithology ([Herd et al., 2018](#)) and in the less fractionated, baddeleyite-poor basaltic shergottites examined in this study (NWA 11057, 11073, and 11255). This similarity, combined with the lower ferroan content in late-stage phases in LAR 06319 compared to basaltic shergottites ([Herd et al., 2018](#)), suggests a lower degree of fractional crystallization which limits baddeleyite formation.

Poikilitic (formerly termed “Iherzolitic”) shergottites are characterized by bimodal textures which represent early-stage crystallization and accumulation (poikilitic texture) followed by crystallization of more evolved assemblages in the interstices (non-poikilitic texture) (Rahib et al., 2019). Pyroxene compositions in poikilitic shergottites are generally below Fs_{50} . Baddeleyite previously reported in poikilitic shergottites occurs in areas with non-poikilitic texture (Mikouchi, 2005; Niihara, 2011; Kizovski, 2017), consistent with a late-stage crystallization origin. In addition, association of baddeleyite with ilmenite is common (Irving et al., 2008; Niihara, 2011; Ruzicka et al., 2013) suggesting a similarity in petrogenesis with the baddeleyite-poor basaltic shergottites examined in this study. Baddeleyite grains up to $\sim 10 \mu\text{m}$ in size have been reported in poikilitic shergottites (Niihara, 2011; Ruzicka et al., 2013; Kizovski, 2017) and dated via SIMS U–Pb analysis (Niihara, 2011). Therefore, although the less evolved pyroxene compositions in poikilitic and olivine-phyric shergottites suggest lower baddeleyite frequency compared to the much more evolved basaltic shergottites examined in this study (e.g., JaH 479, NWA 10299, 12262, 12919), it is still possible for poikilitic and olivine-phyric shergottites to yield baddeleyite grains of maximum dimensions ($\sim 10\text{--}12 \mu\text{m}$) similar to those found in baddeleyite-poor basaltic shergottites (e.g., NWA 11057, 11073, and 11255) and large enough for *in-situ* U–Pb analysis.

Gabbroic shergottites consist of several recent finds. Of these, NWA 6963 and 7320 are noted to display pyroxene compositions that extend beyond the stability zone (Udry et al., 2017; Filiberto et al., 2018). Although baddeleyite has not been reported in either sample, submicron zircon grains occur in evolved felsic pockets of quartz-alkali feldspar intergrowth in NWA 6963 (Filiberto et al., 2014), similar to zircon in terrestrial gabbros. The occurrence of Zr-bearing phases in gabbroic shergottites therefore appears to also be controlled by fractional crystallization as in other shergottite subclasses.

The augite-rich shergottites NWA 7635 and 8159 are distinct from other shergottite meteorites by bulk compositions, oxygen fugacity characteristics, and ca. 2.4 Ga igneous crystallization ages (Righter et al., 2014; Herd et al., 2017; Lapen et al., 2017). No Zr-bearing minerals have been reported in these two

meteorites. Although pyroxene compositions of NWA 7635 and 8159 extend beyond the stability boundary, the bulk Zr contents (9.8 and 11.1 ppm, respectively) are among the lowest of reported shergottites. In addition, both meteorites are marked by very low Ti content (0.61 and 0.65 wt% TiO_2 , respectively) and relatively oxidizing conditions (up to QFM+2 in NWA 8159) such that magnetite is the dominant oxide, with mesostasis ilmenite as the main host of Ti (Herd et al., 2017; Ruzicka et al., 2015). Given these distinctions, it is possible that Zr in NWA 7635 and 8159 is hosted mainly in the mesostasis ilmenite and does not become enriched enough in late-stage melts to crystallize baddeleyite.

Our findings in this study suggest that baddeleyite occurrence in shergottites is primarily controlled by fractional crystallization. The role of ITE enrichment in baddeleyite occurrence, as reflected in shergottite geochemical subgroup association, is a less explored factor. While the selected samples in this study were all found to be enriched shergottites, previous examination of baddeleyite in intermediate and depleted shergottites alongside enriched shergottites suggest that degree of ITE enrichment or depletion plays a minor role, if any, in baddeleyite abundance (Herd et al., 2018).

Apart from shergottites, baddeleyite has also been observed as a rare phase in Nakhla (Bridges and Grady, 1999) and in some chassignites (Chassigny, NWA 2737, and NWA 8694; Herd et al., 2018; Lorand et al., 2012; Hewins et al., 2020). In Nakhla, NWA 2737, and NWA 8694, baddeleyite occurs alongside late-stage assemblages, consistent with crystallization from fractionated interstitial melts. Herd et al. (2018) reported a single baddeleyite grain in Chassigny associated with Fe-Ti oxides within a magmatic inclusion with highly oxidized conditions, suggesting that baddeleyite stability in this case may be controlled by oxygen fugacity. Although nakhellites and chassignites are distinct from shergottites in composition and crystallization ages, the observations suggest that the baddeleyite crystallization in these mafic magmatic systems fundamentally depends on the degree of melt evolution as demonstrated by our findings in basaltic shergottites.

2.6.6 Towards a streamlined methodology for assessing shergottite samples for *in-situ* U–Pb baddeleyite analysis

Our survey of basaltic shergottites indicates that the degree of fractional crystallization, as recorded by pyroxene compositional zoning, controls baddeleyite abundance to the first order in these rocks. As pyroxene composition is among the first analyses to be obtained for newly described martian meteorites, this facilitates the preliminary assessment of whether a sample might contain abundant or scarce baddeleyite.

For locating baddeleyite grains in a sample, the most efficient method is surveying sample thin sections or polished flat surfaces under EPMA or SEM following manual or automated mapping protocols outlined in [Herd et al. \(2018\)](#). Conducting manual searches using BSE signal in live view has the advantage of saving instrument time, however at the expense of being able to locate only the larger grains. On the other hand, automated mapping such as Zr X-ray maps and combined BSE-EDS maps ([Herd et al., 2018](#)) provides more comprehensive results of baddeleyite distribution and may be done (depending on instrument configuration) as part of preliminary sample characterization. As baddeleyite occurs in association with late-stage phases, searches can be focused on mesostasis areas, guided by live-view or pre-scanned images. Essentially, the trade-off between instrument time, the size of the area surveyed, and the number and minimum size of baddeleyite grains found needs to be considered when planning how a sample should be searched. If automated mapping is conducted on smaller subsections, there may be larger variations in the distribution of smaller baddeleyite grains (<6 µm) (Fig. 2.13). Although we survey in this study baddeleyite grains down to 1 µm in length for a comprehensive investigation, current *in-situ* techniques require at the smallest a 3–4 µm spot size for ion beam U–Pb isotopic analysis (e.g., [Moser et al., 2013](#); [Zhou et al., 2013](#); [Wu and Hsu, 2020](#)). Hence if the minimum grain size of interest is known, the resolution of automated Zr mapping may be adjusted such that only grains larger than the specified threshold are identified while allowing for greater sample areas to be surveyed in a given time.

If the priority is to locate the largest baddeleyite grains, pyroxene composition trends may be used as a guideline for targeting assemblages in which they are more likely to occur. Caution is advised when examining very coarse-grained samples such as KG 002, where baddeleyite may be scarce due to unrepresentative sampling and/or uptake of Zr by large pyroxene grains during crystallization. Given the variability of U content in baddeleyite (known range in shergottites is between a few 10's of ppm and over 100 ppm), targeting large baddeleyite grains also carries the advantage of being able to increase U signal by analyzing with larger beam sizes.

2.7 Summary

We examined the petrography, mineralogy, geochemistry, and baddeleyite distribution in eight basaltic shergottites. The petrography of baddeleyite in these samples demonstrates that baddeleyite crystallized as a late-stage igneous mineral from the most chemically fractionated portions of the magma. Results from our survey of baddeleyite occurrence point to the degree of fractional crystallization, as reflected in pyroxene major element trends, as the primary control on baddeleyite abundance; samples with pyroxene compositions evolving beyond the 1-bar stability boundary generally have higher baddeleyite frequency compared to samples with pyroxene compositions terminating at or before the stability boundary. The control exerted by fractional crystallization also accounts for the overall lower abundance of baddeleyite in other shergottite petrographic subgroups.

The petrographic setting of the largest baddeleyite grains in a sample also correlates with pyroxene major element trends. In samples which display distinct high-Ca and low-Ca pyroxene series, the largest baddeleyite grains tend to be associated with Fe-Ti oxides; in samples where pyroxene composition forms a continuous trend extending beyond the stability boundary, the largest baddeleyite grains are typically associated with polymimetic late-stage pockets. Bulk HFSE content and f_{O_2} do not appear to directly influence baddeleyite distribution in these samples.

Our findings demonstrate that pyroxene composition is a useful proxy for assessing baddeleyite abundance and distribution in shergottites and may be used 1) to evaluate a sample's feasibility for *in-situ* U–Pb geochronology prior to conducting detailed imaging and 2) as a guide to search specific petrographic assemblages for baddeleyite grains sufficiently large for geochronological analysis.

Table 2.1. Modal abundance of major phases based on EPMA X-ray element maps.

	Pyroxene	Plagioclase (maskelynite or glass)	Fe-Ti oxides	Ca- phosphates	Fe-sulfides	Silica, K- feldspar, and glass	Fayalitic olivine
JaH 479	45%	35%	2%	3%	1%	4%	10% ^a
KG 002 ^b	37%	48%	2%	3%	1%	5%	4%
NWA 10299	62%	29%	2%	2%	2%	3%	–
NWA 11057	66%	24%	3%	4%	1%	3%	–
NWA 11073	65%	29%	1%	2%	1%	1%	–
NWA 11255	60%	32%	2%	2%	0.4%	3%	–
NWA 12262	45%	40%	3%	4%	1%	4%	4% ^c
NWA 12919	56%	30%	2%	3%	0.4%	4%	<1% ^d

a. Includes olivine-pyroxene-silica symplectite areas.

b. Data source: [Llorca et al. \(2013\)](#).

c. Does not include olivine-pyroxene-silica symplectite areas.

d. Visual estimate.

Table 2.2. Statistical results of the baddeleyite survey.

	Mapped area (mm ²)	# of identified grains $\geq 1 \mu\text{m}$	# of grains used for statistic calculations	Baddeleyite grain frequency (mm ⁻²)			Mean grain length (μm)	σ	Max. grain length (μm)	Mean l:w ratio
				$\geq 1 \mu\text{m}$	$\geq 4 \mu\text{m}$	$\geq 6 \mu\text{m}$				
JaH 479	522	580*	338	1.14*	0.26	0.13	4.4	3.3	23.3	2.5
KG 002	106	56	56	0.53	0.18	0.06	3.2	1.9	11.8	2.5
NWA 10299	276	243	243	0.88	0.18	0.10	3.1	2.4	18.2	2.5
NWA 11057	43	34	34	0.80	0.26	0.16	3.9	3.0	12.5	3.1
NWA 11073	40	33	33	0.83	0.13	0.03	2.8	1.7	10.3	3.0
NWA 11255	43	33	33	0.78	0.21	0.09	3.4	2.2	10.1	2.4
NWA 12262	43	71	71	1.67	0.54	0.21	3.7	2.6	14.8	2.5
NWA 12919	43	86	86	2.02	0.40	0.19	2.9	2.5	14.0	3.8

*Minimum estimates.

Table 2.3. Results of ICP-MS analysis of bulk major, minor, and trace elements.

	JaH 479 ^a	KG 002 ^b	NWA 11073 ^c	NWA 11255 ^c	NWA 12919	NWA 10299	NWA 11057	NWA 12262	NWA 12262 (duplicate)	NWA 12262 (average)	Detection Limit (DL) ^d
SiO ₂ (wt%) ^e	50.99	(60)	(61)	(60)	(56)	(63)	(52)	(52)	(52)	(52)	
TiO ₂	0.93	0.61	0.96	0.52	0.82	0.52	1.15	1.15	1.15	1.15	0.00002
Al ₂ O ₃	12.25	6.49	5.96	6.36	5.43	5.62	8.32	8.14	8.23	8.23	0.00004
Cr ₂ O ₃	0.02	0.09	0.11	0.08	0.12	0.09	0.02	0.02	0.02	0.02	0.000007
FeO	17.0	15.9	14.8	13.5	21.1	16.2	23.0	23.0	23.0	23.0	0.00048
MnO	0.43	0.43	0.46	0.36	0.37	0.31	0.36	0.36	0.36	0.36	0.000004
CaO	10.3	8.72	9.25	9.46	8.22	7.82	8.45	8.43	8.44	8.44	0.0043
MgO	4.47	6.55	6.24	6.61	5.72	4.65	3.67	3.56	3.61	3.61	0.0003
Na ₂ O	2.14	0.77	0.65	1.68	1.20	1.19	1.89	1.84	1.86	1.86	0.00007
K ₂ O	0.23	0.07	0.08	0.12	0.18	0.12	0.26	0.26	0.26	0.26	0.0007
P ₂ O ₅	0.7	0.62	0.76	0.89	0.67	0.38	1.04	1.02	1.03	1.03	0.001
Li (ppm)	7.3			3.13	3.76	3.67	4.23	4.15	4.19	4.19	0.05
Sc	37.9										
V	201	251	247	162.6	247.6	244.6	167.9	168.4	168.2	168.2	0.05
Co	30.4			30.84	32.00	29.56	29.68	29.77	29.72	29.72	0.03
Ni	32.2			35.03	34.92	43.43	34.43	35.03	34.73	34.73	0.06
Cu	22.1			9.08	31.02	10.96	1400.30 ^f	1398.34 ^f	1399.32 ^f	1399.32 ^f	0.03
Zn	89.2	68	70	71.4	74.5	60.3	90.9	91.1	91.0	91.0	0.08
Rb	7.51	4.6	3.7	5.7	5.5	1.8	10.0	10.1	10.0	10.0	0.04
Sr	108.7	51	47	65.7	73.1	70.8	75.8	76.9	76.4	76.4	0.03
Y	17	11.8	12.3	13.36	16.95	9.66	23.11	23.19	23.15	23.15	0.02
Zr	152	49	45								
Nb	3.47			5.56	4.43	2.19	6.65	6.84	6.75	6.75	0.04
Mo	0.26			0.32	0.37	0.40	0.31	0.33	0.32	0.32	0.02
Cd	0.05			<DL	<DL	<DL	<DL	<DL	<DL	<DL	0.06
Ba	112	27	98	76	211	223	46.3	45.8	46.1	46.1	0.03
La	1.40	2.11	1.66	1.75	1.96	2.45	1.32	3.55	3.53	3.54	0.03

Table 2.3. (continued) Results of ICP-MS analysis of bulk major, minor, and trace elements.

	JaH 479 ^a	KG 002 ^b	NWA 11073 ^c	NWA 11255 ^c	NWA 12919	NWA 10299	NWA 11057	NWA 12262 (duplicate)	NWA 12262 (average)	Detection Limit (DL) ^d
Ce	3.36	6.31	3.97	4.25	4.91	5.97	3.04	8.68	8.73	0.03
Pr		0.74	0.56	0.59	0.70	0.87	0.45	1.21	1.25	0.04
Nd	2.18	3.66	2.75	2.96	3.45	4.44	2.35	6.14	6.17	0.03
Sm	0.77	1.37	1.08	1.16	1.35	1.69	0.92	2.36	2.48	0.04
Eu	0.24	0.76	0.47	0.48	0.61	0.69	0.52	0.91	0.91	0.03
Gd		2.13	1.82	1.89	2.22	2.81	1.62	3.81	3.72	0.03
Tb	0.21	0.44	0.33	0.34	0.40	0.48	0.28	0.66	0.65	0.03
Dy		2.91	2.31	2.35	2.78	3.45	2.02	4.58	4.51	0.04
Ho		0.6	0.5	0.49	0.58	0.71	0.42	0.90	0.95	0.02
Er		1.77	1.37	1.37	1.64	1.83	1.10	2.51	2.49	0.04
Tm		0.25	0.2	0.19	0.24	0.27	0.17	0.37	0.36	0.06
Yb	1.27	1.68	1.28	1.28	1.53	1.78	1.03	2.34	2.33	0.05
Lu	0.25	0.24	0.18	0.17	0.22	0.24	0.15	0.33	0.32	0.04
Hf		4.57	1.6	1.4						
Pb		1.39			0.56	0.83	1.06	1.04	1.03	0.03
Th		0.54	0.4	0.3	0.46	0.43	0.20	0.67	0.68	0.01
U		0.16	0.1	0.04	0.17	0.19	<DL	0.17	0.17	0.03
(La/Yb) _N ^g	0.77	0.88	0.91	0.96	0.89	0.96	0.90		1.06	
(Sm/Nd) _N ^g	1.09	1.15	1.21	1.21	1.21	1.17	1.20		1.21	

a. From [Lorenz et al. \(2010\)](#).

b. From [Llorca et al. \(2013\)](#).

c. From [Lapen et al. \(2018\)](#).

d. Detection limits for analysis done in this study only.

e. SiO₂ is estimated by difference for all samples except KG 002 (ICP-OES; [Llorca et al., 2013](#)).

f. Contamination of Cu possible due to sample powder being made from cuttings and of small volume (<1 g).

g. Normalized to CI chondrite ([Lodders et al., 2009](#); [Palme et al., 2014](#)).

Table 2.4. Oxygen fugacity (f_{O_2}) of the studied samples.

	$\log f_{O_2}$ (ΔQFM)*	# of titanomagnetite- ilmenite pairs analyzed
JaH 479	-1.2 ± 0.4	5
KG 002	-1.0 ± 0.2	5
NWA 10299	-1.1 ± 0.7	6
NWA 11057	-1.4 ± 0.2	7
NWA 11073	-1.3 ± 0.3	7
NWA 11255	-1.1 ± 0.1	6
NWA 12262	$+0.1 \pm 0.1$	4
NWA 12919	-1.1 ± 0.2	10

* Calculated from Fe-Ti oxides oxythermobarometry ([Ghiorso and Evans, 2008](#)) and reported relative to the QFM buffer ([Wones and Gilbert, 1969](#)). Uncertainty is one standard deviation. Full Fe-Ti oxides EPMA analysis and f_{O_2} calculations are reported in Tables A1.4–A1.6 in Appendix 1.

Table 2.5. Number of documented baddeleyite grains, mean length, maximum length, and mean aspect ratio in each petrographic association category.

	JaH 479	KG 002	NWA 10299	NWA 11057	NWA 11073	NWA 11255	NWA 12262	NWA 12919
<i># of documented grains</i>								
Late-stage pockets	101	33	142	10	10	12	28	26
Ol-bearing late-stage pockets	192	13	–	–	–	–	38	–
Fe-Ti oxides	15	4	44	10	17	10	4	24
Glassy mesostasis	3	1	54	12	4	11	–	35
Other	27	5	3	2	2	–	1	1
<i>Mean length (μm)*</i>								
Late-stage pockets	5.0 ± 3.3	2.9 ± 1.8	3.0 ± 2.3	2.9 ± 1.5	2.3 ± 1.0	3.3 ± 2.7	3.8 ± 2.6	3.3 ± 2.9
Ol-bearing late-stage pockets	3.8 ± 2.4	3.7 ± 1.6	–	–	–	–	3.6 ± 2.8	–
Fe-Ti oxides	5.3 ± 3.2	3.8 ± 1.6	4.5 ± 3.4	4.7 ± 3.2	3.1 ± 2.1	3.1 ± 1.7	3.3 ± 1.1	3.2 ± 2.8
Glassy mesostasis	3.2 ± 1.0	–	2.1 ± 0.8	2.9 ± 2.0	3.3 ± 0.5	3.7 ± 1.9	–	2.3 ± 1.6
<i>Maximum length (μm)</i>								
Late-stage pockets	23.3	7.0	14.0	6.5	4.1	10.1	14.8	12.3
Ol-bearing late-stage pockets	16.8	5.8	–	–	–	–	13.6	–
Fe-Ti oxides	13.2	6.4	18.2	12.5	10.3	5.6	4.4	14.0
Glassy mesostasis	4.0	–	4.3	7.4	3.8	8.0	–	7.4
<i>Mean aspect ratio</i>								
Late-stage pockets	2.7	2.5	2.5	2.1	2.4	2.2	2.4	2.4
Ol-bearing late-stage pockets	2.3	2.5	–	–	–	–	2.5	–
Fe-Ti oxides	3.2	2.5	2.3	3.1	3.5	2.3	3.9	2.0
Glassy mesostasis	1.9	2.1	2.5	3.2	2.5	2.6	–	6.1

* Uncertainty is one standard deviation.

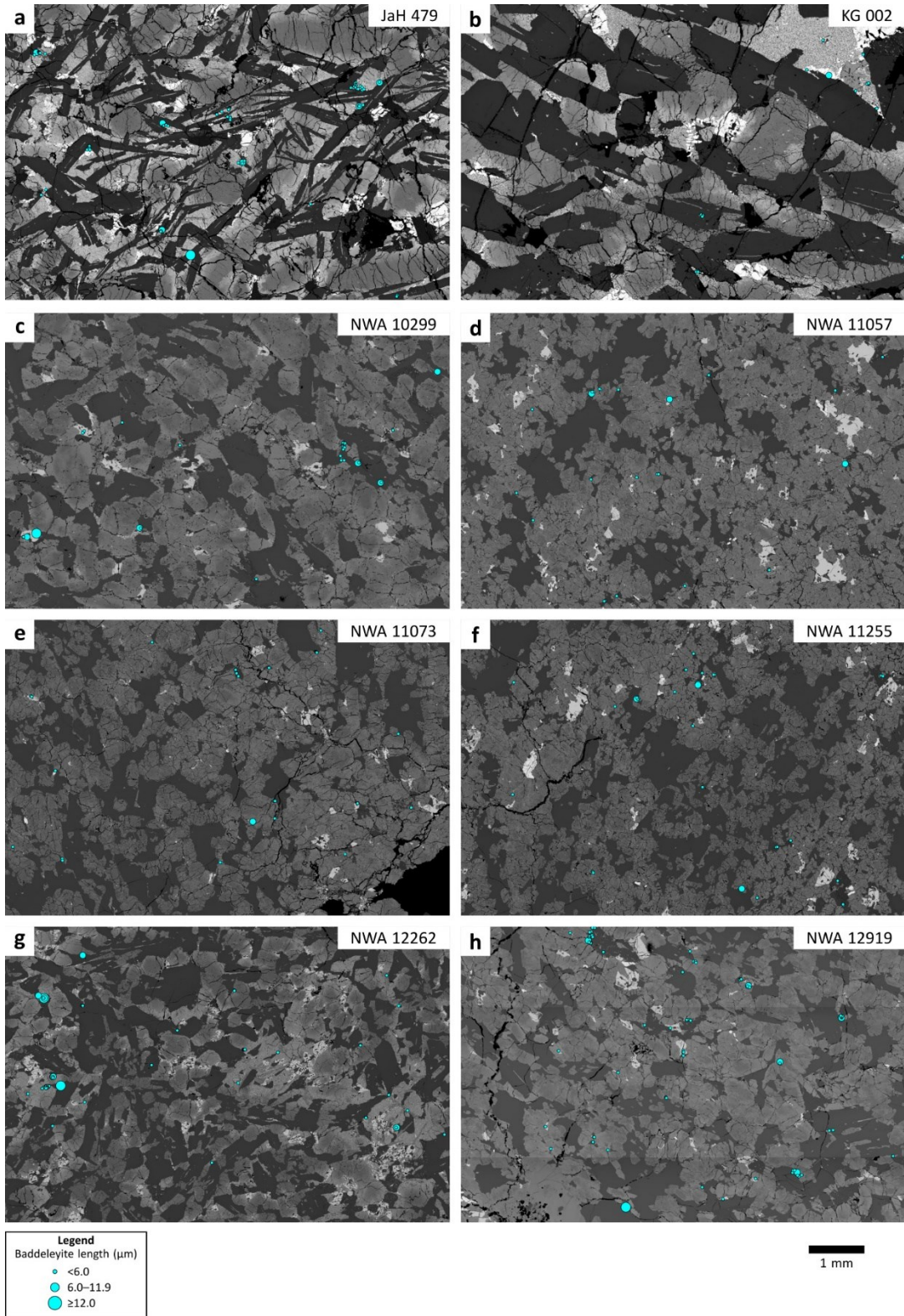


Fig. 2.1. Maps of baddeleyite occurrences in the surveyed shergottites. Scale bar applies to all parts of the figure. Maps for JaH 479, KG 002, NWA 10299 are only partially displayed to allow for direct comparison at the same scale. Full individual maps at higher resolution are included in Appendix 1.

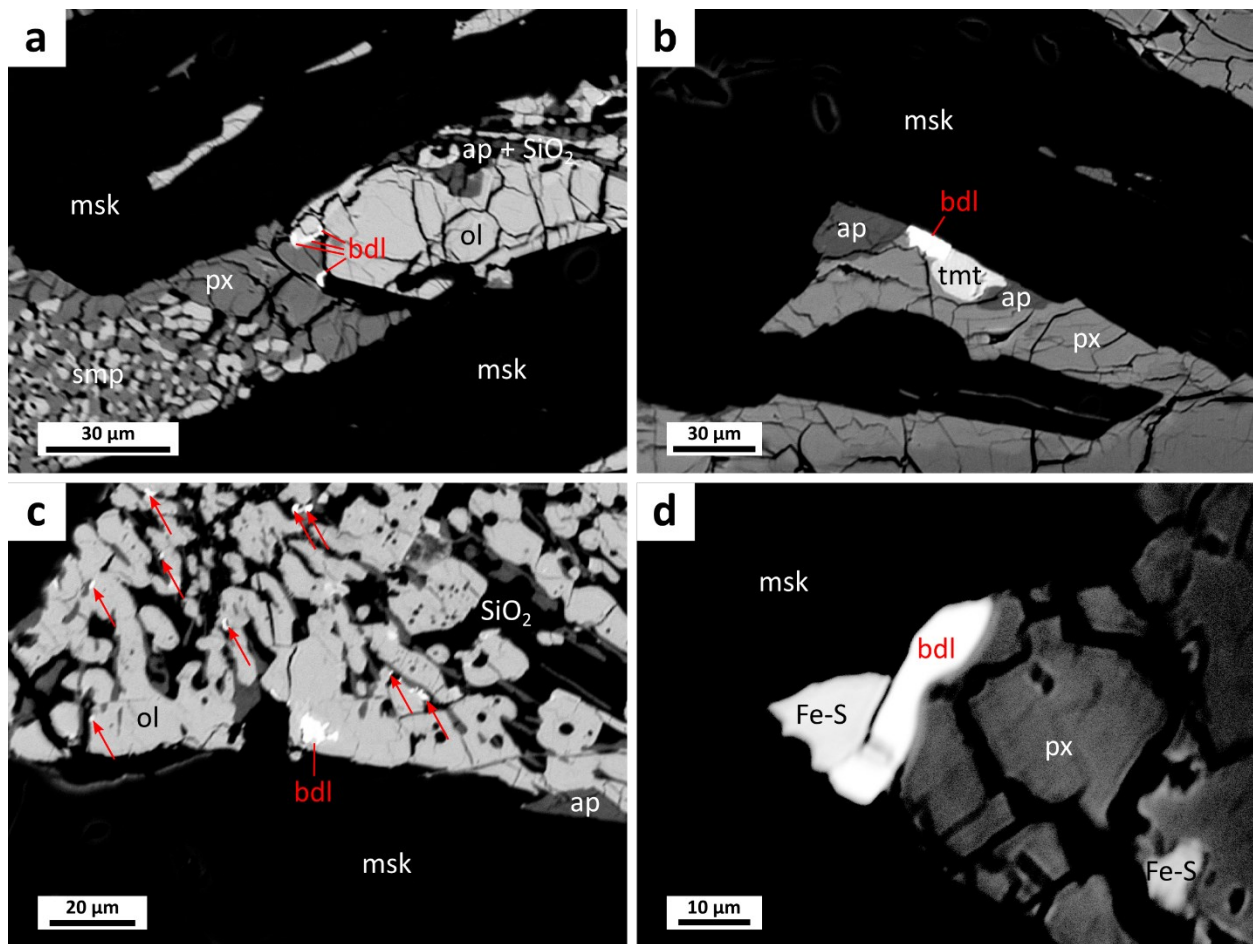


Fig. 2.2. BSE images of representative baddeleyite (bdl) occurrences in JaH 479 including a) at the edge of an olivine(ol)+apatite(ap)+silica(SiO₂) pocket adjacent to three-phase symplectite (smp), b) with apatite and titanomagnetite (tmt) at the pyroxene(px)-maskelynite(msk) boundary, c) at phase boundaries throughout an ol+ap+SiO₂ pocket (denoted by red arrows), and d) with Fe-sulfide (Fe-S) at the px-msk boundary.

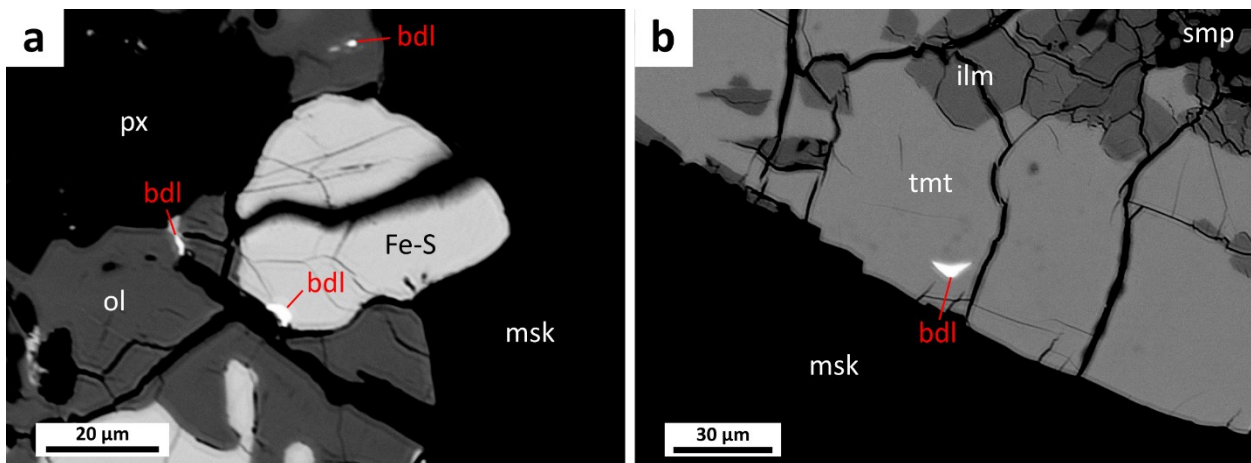


Fig. 2.3. Examples of baddeleyite (bdl) occurrences in KG 002, including a) associated with olivine (ol) and Fe-sulfide (Fe-S) in a late-stage pocket, and b) enclosed within titanomagnetite (tmt). px: pyroxene. msk: maskelynite. ilm: ilmenite. smp: three-phase symplectite.

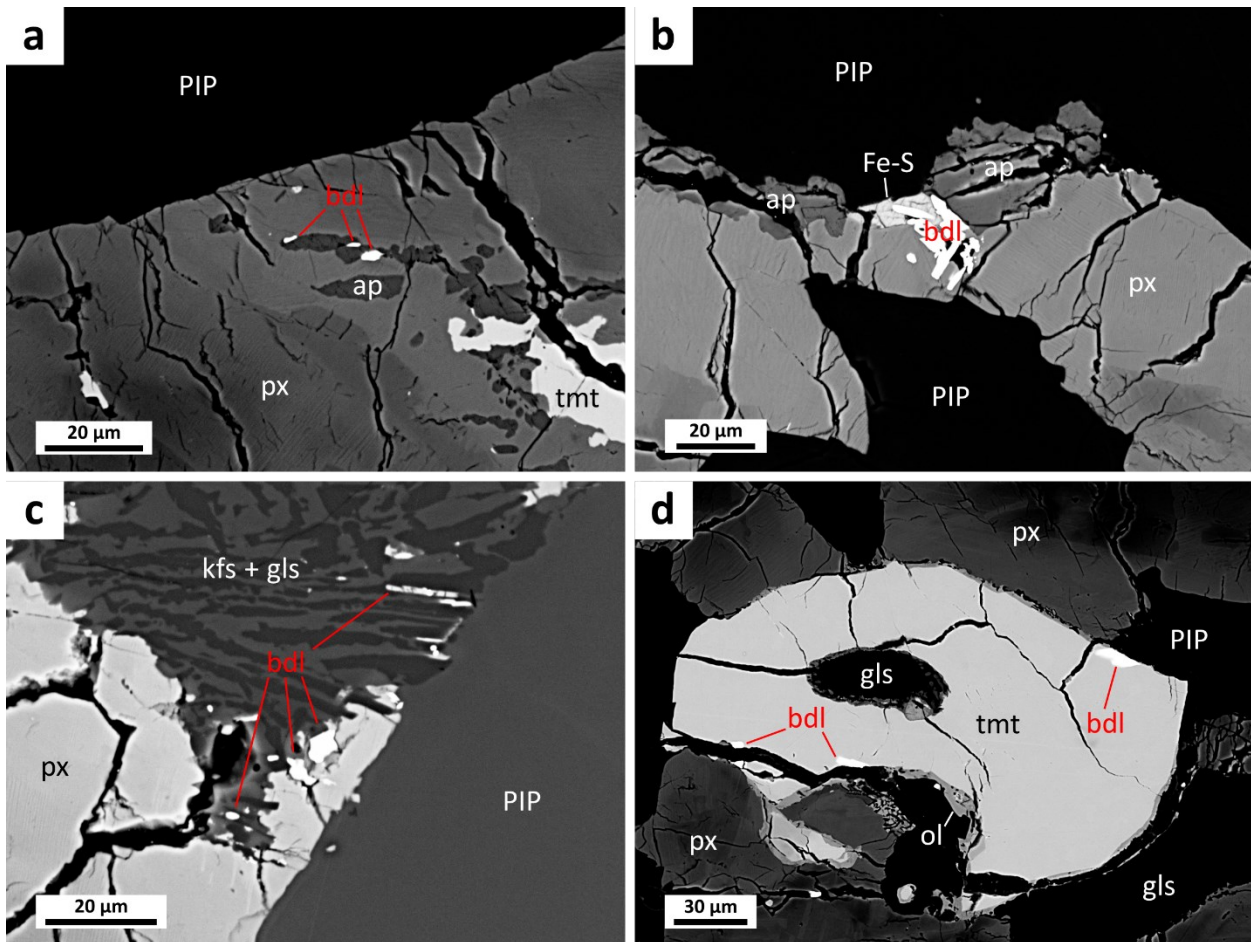


Fig. 2.4. Representative baddeleyite (bdl) occurrences in NWA 10299, including a) at the edge of an apatite(ap)+titanomagnetite(tmt) pocket in pyroxene (px), b) with apatite and Fe-sulfide (Fe-S) at the boundary between pyroxene and precursor igneous plagioclase (PIP), c) at the edge of a K-feldspar(kfs)+glass(gls) pocket, and d) at the edge of titanomagnetite. ol: olivine.

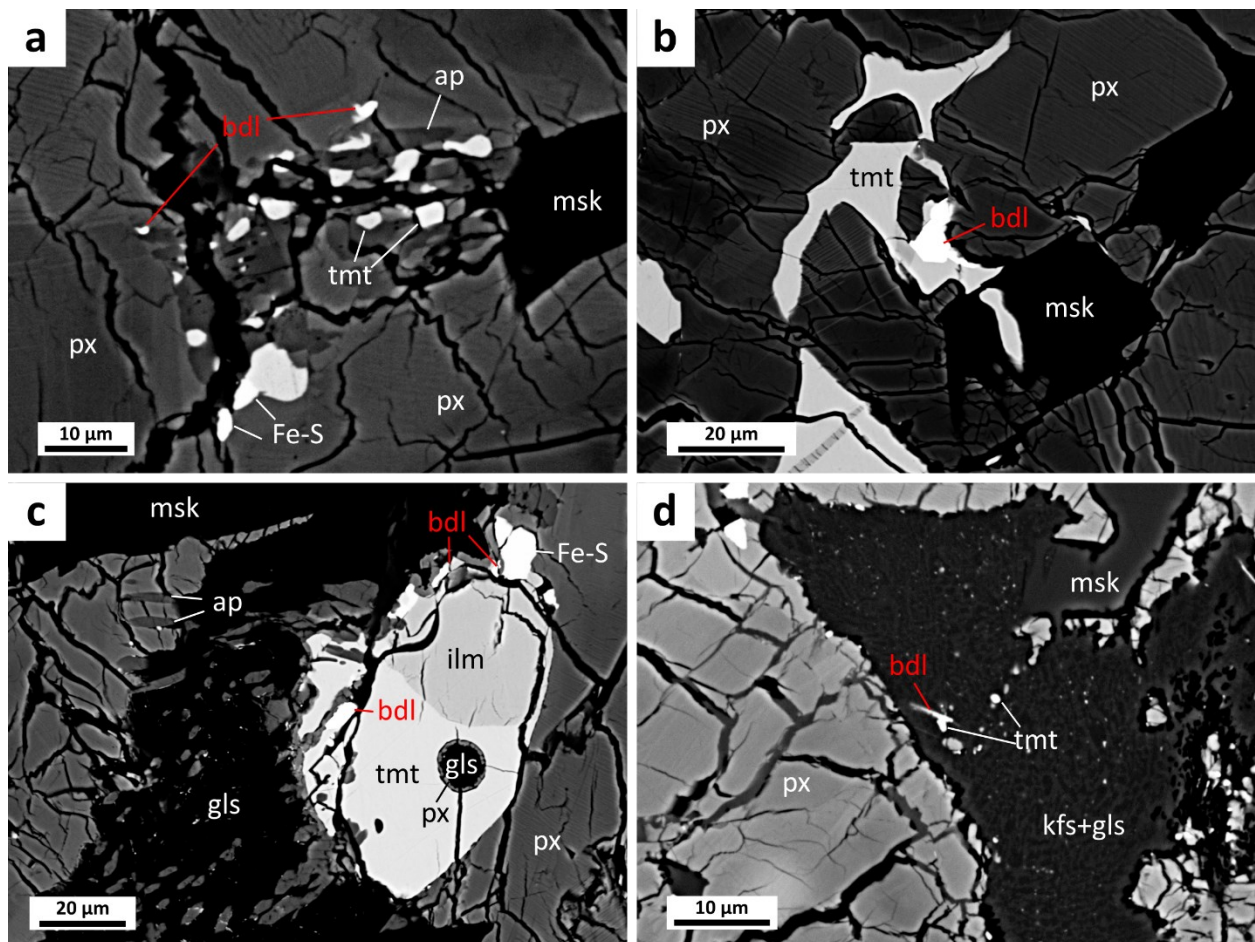


Fig. 2.5. Representative baddeleyite (bdl) occurrences in NWA 11057, including a) at the edge of an apatite(ap)+ titanomagnetite(tmt)+Fe-sulfide(Fe-S) pocket, b) at the edge of titanomagnetite, c) adjacent to titanomagnetite and ilmenite (ilm) in an Fe-Ti oxides+Fe-sulfides+apatite+glass(gls) pocket, and d) adjacent to fine titanomagnetite in K-feldspar(kfs)+glass mesostasis. px: pyroxene. msk: maskelynite.

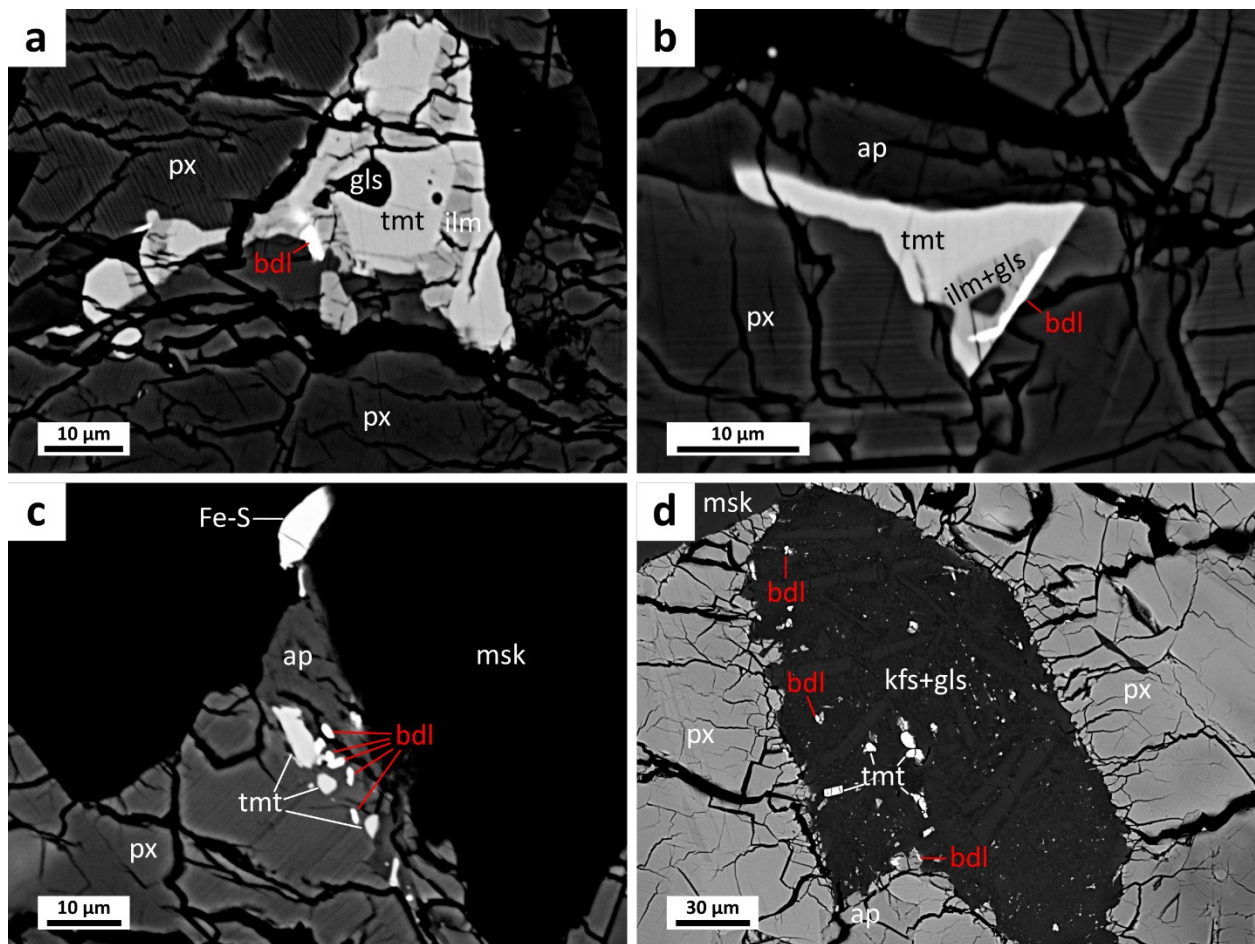


Fig. 2.6. Representative baddeleyite (bdl) occurrences in NWA 11073, including a, b) adjacent to ilmenite (ilm) at the edge of Fe-Ti oxide, c) within an apatite(ap)+ titanomagnetite(tmt)+Fe-sulfide(Fe-S) pocket at the pyroxene(px)-maskelynite(msk) boundary, and d) within and at the edge of K-feldspar(kfs)+glass(gls) mesostasis. ilm: ilmenite.

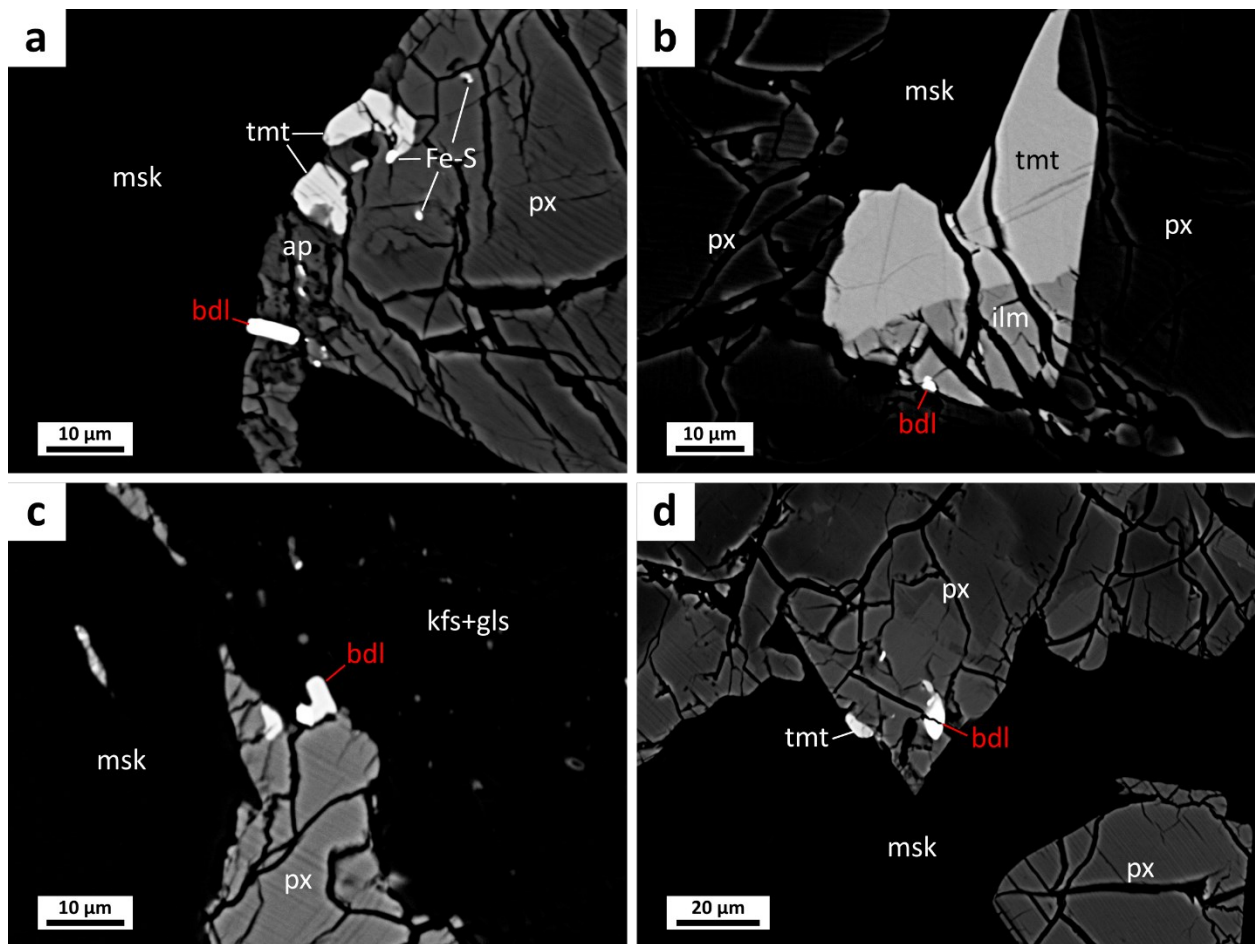


Fig. 2.7. Representative baddeleyite (bdl) occurrences in NWA 11255, including a) in an apatite(ap)+titanomagnetite(tmt)+Fe-sulfide(Fe-S) pocket at the pyroxene(px)-maskelynite(msk) boundary, b) at the edge of ilmenite(ilm), c) at the boundary between pyroxene and K-feldspar(kfs)+glass(gls) mesostasis, and d) near the edge of pyroxene.

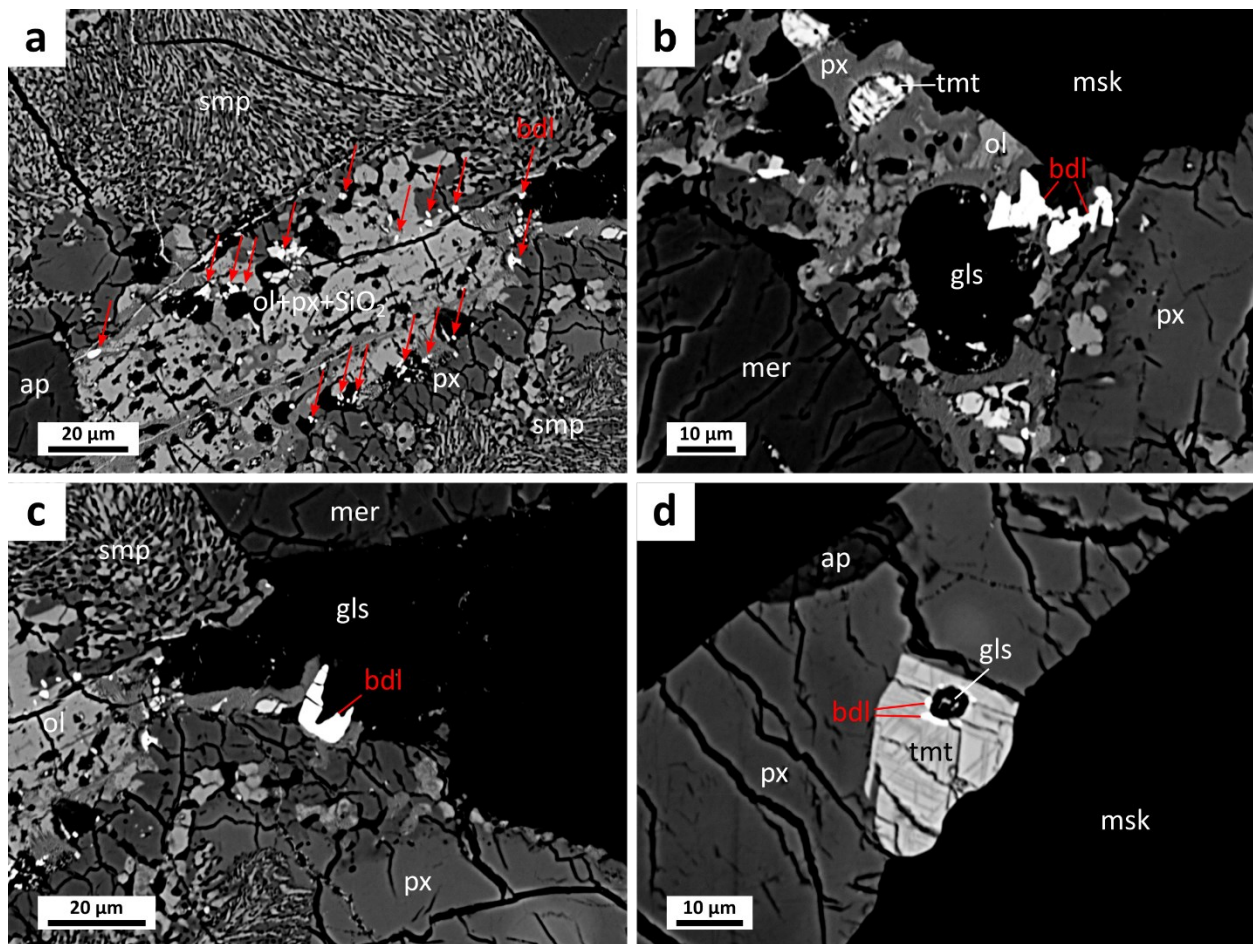


Fig. 2.8. Representative baddeleyite (bdl) occurrences in NWA 12262, including a) numerous grains (denoted by red arrows) at the edge of an olivine(ol)+pyroxene(px)+silica(SiO₂) pocket with adjacent three-phase symplectite (smp), b) at the edge of an olivine+pyroxene+glass(gls)+titanomagnetite(tmt) pocket, c) at the pyroxene-glass boundary, and d) around a glass inclusion within an exsolved titanomagnetite.

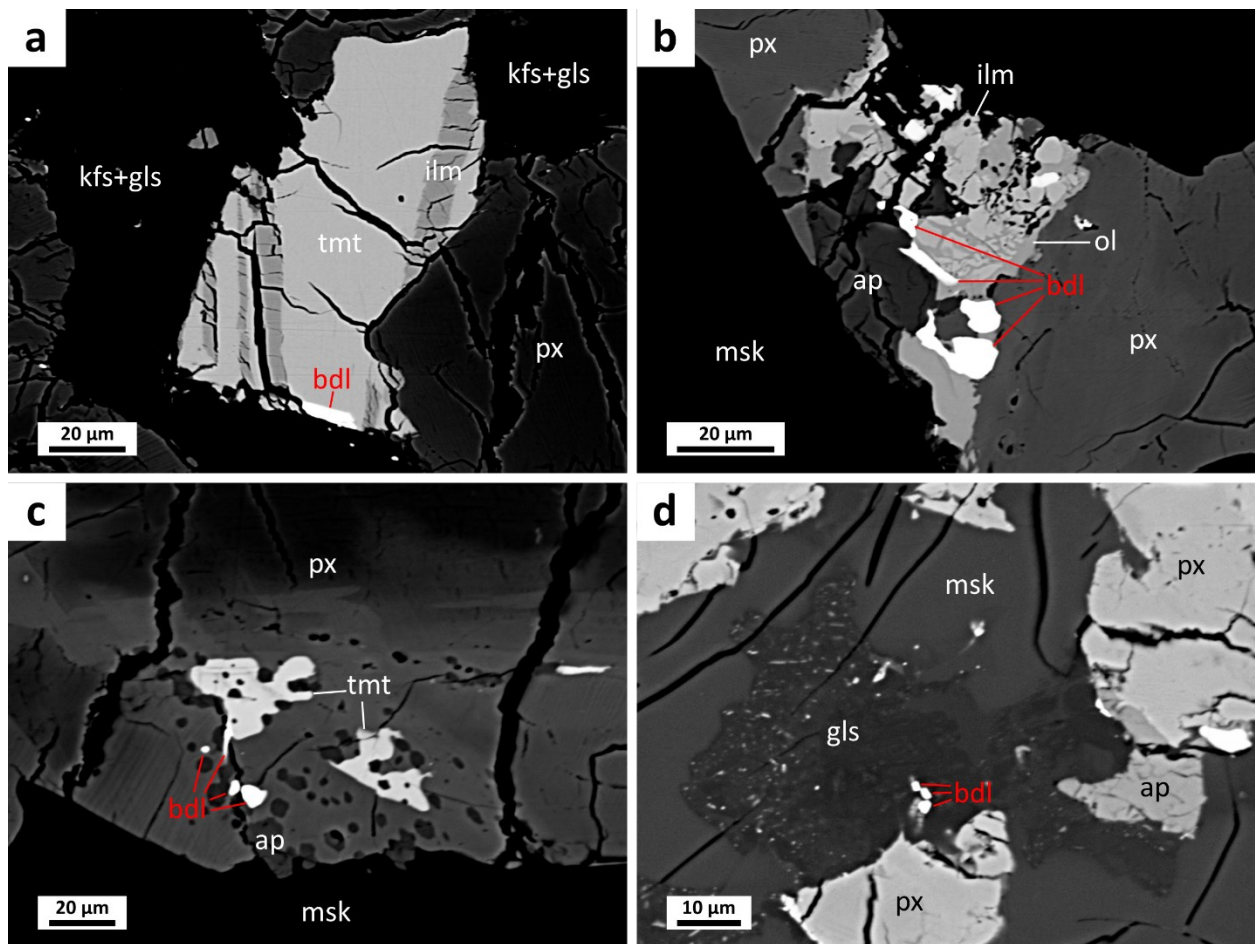


Fig. 2.9. Representative baddeleyite (bdl) occurrences in NWA 12919, including a) at the edge of titanomagnetite (tmt) adjacent to K-feldspar(kfs)+glass(gls) mesostasis, b) at phase boundaries within an apatite(ap)+olivine(ol)+ilmenite(ilm)+glass(gls) pocket, c) enclosed near the edge of pyroxene (px) with titanomagnetite and apatite, and d) within a glass+apatite pocket. msk: maskelynite.

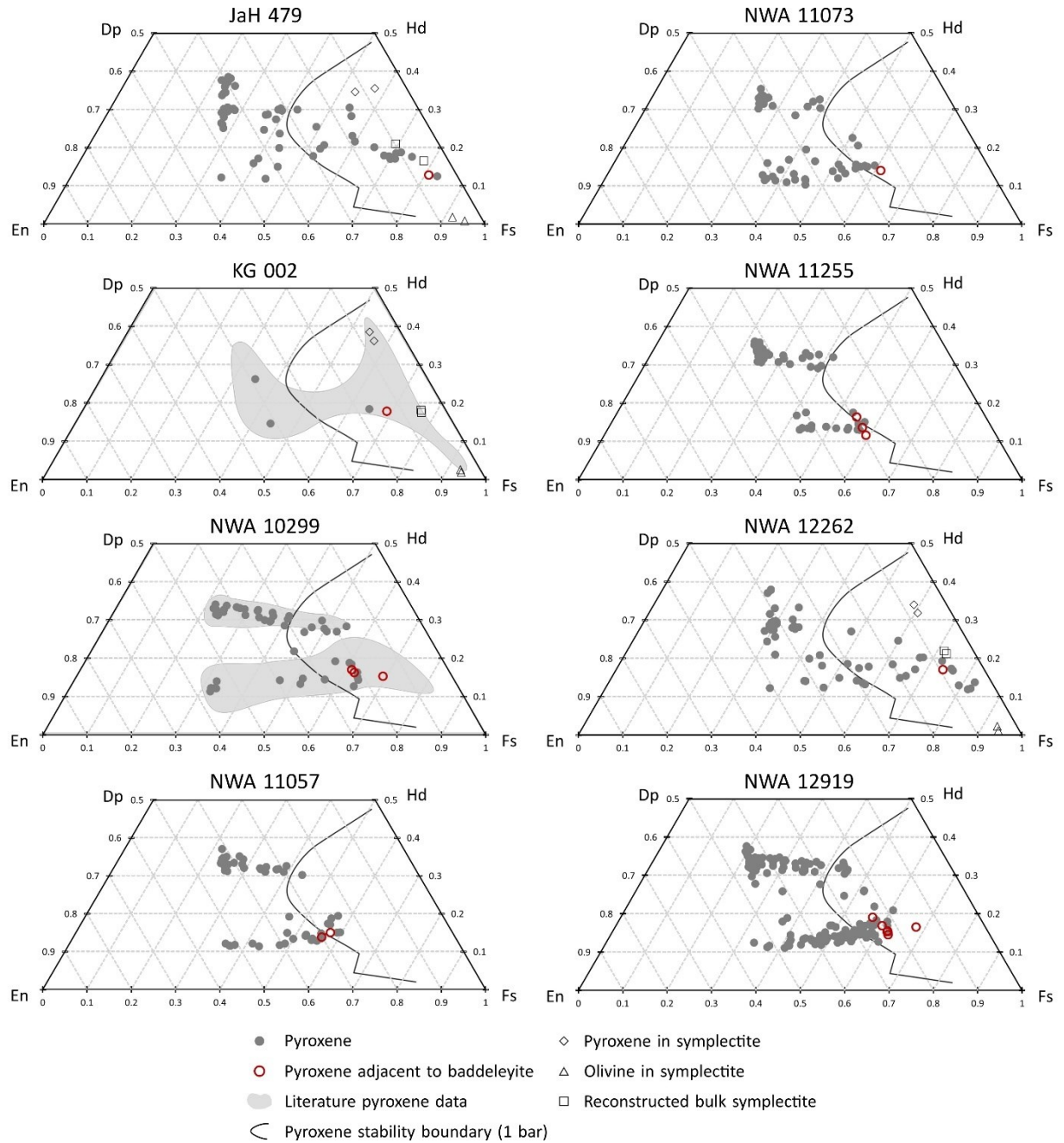


Fig. 2.10. Pyroxene compositions (grey and red circles) plotted in En-Fs-Dp-Hd quadrilateral space; red circles denote pyroxene directly adjacent to baddeleyite. Shown for reference are literature pyroxene data (grey fields) and the pyroxene stability boundary at 1 bar ([Lindsley, 1983](#)). Where three-phase symplectite is analyzed, pyroxene, olivine, and reconstructed bulk symplectite compositions are denoted by open symbols. KG 002 literature data are from [Llorca et al. \(2013\)](#). NWA 10299 literature data are from [Jean et al. \(2016\)](#). Full EPMA pyroxene and symplectite analysis is reported in tables A1.1–A1.3 in Appendix 1.

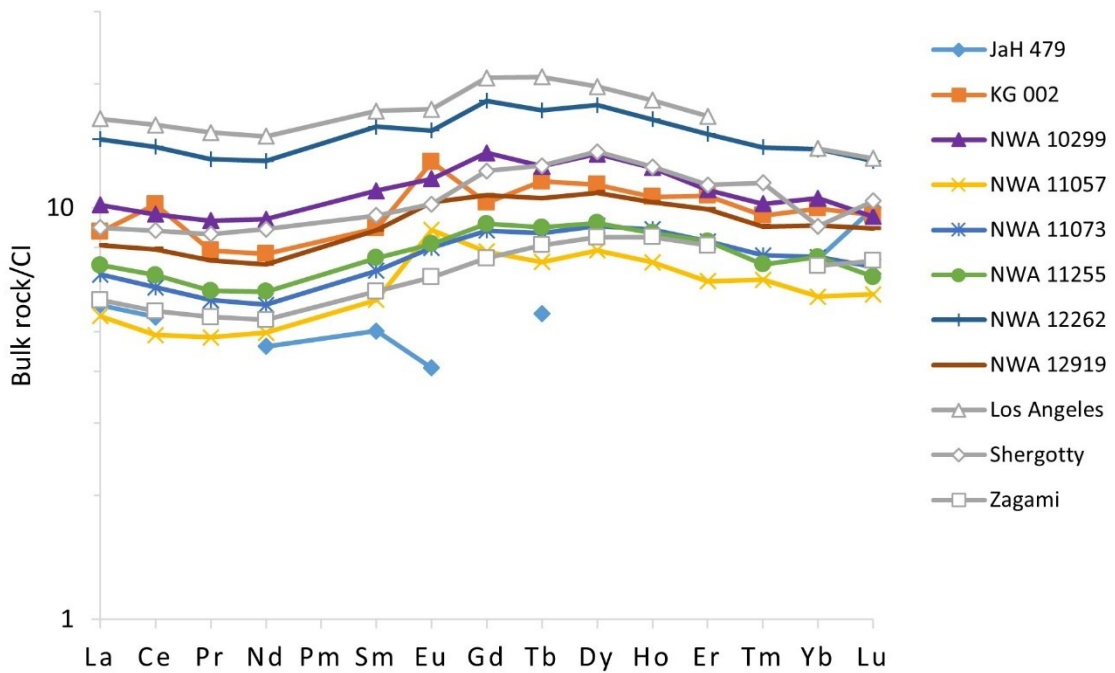


Fig. 2.11. Bulk REE normalized to CI chondrite. Shown for reference are the compositions of Los Angeles ([Jambon et al., 2002](#)), Shergotty ([Lodders, 1998](#)), and Zagami ([Barrat et al., 2001](#)). Normalized to CI chondrite ([Lodders et al., 2009; Palme et al., 2014](#)).

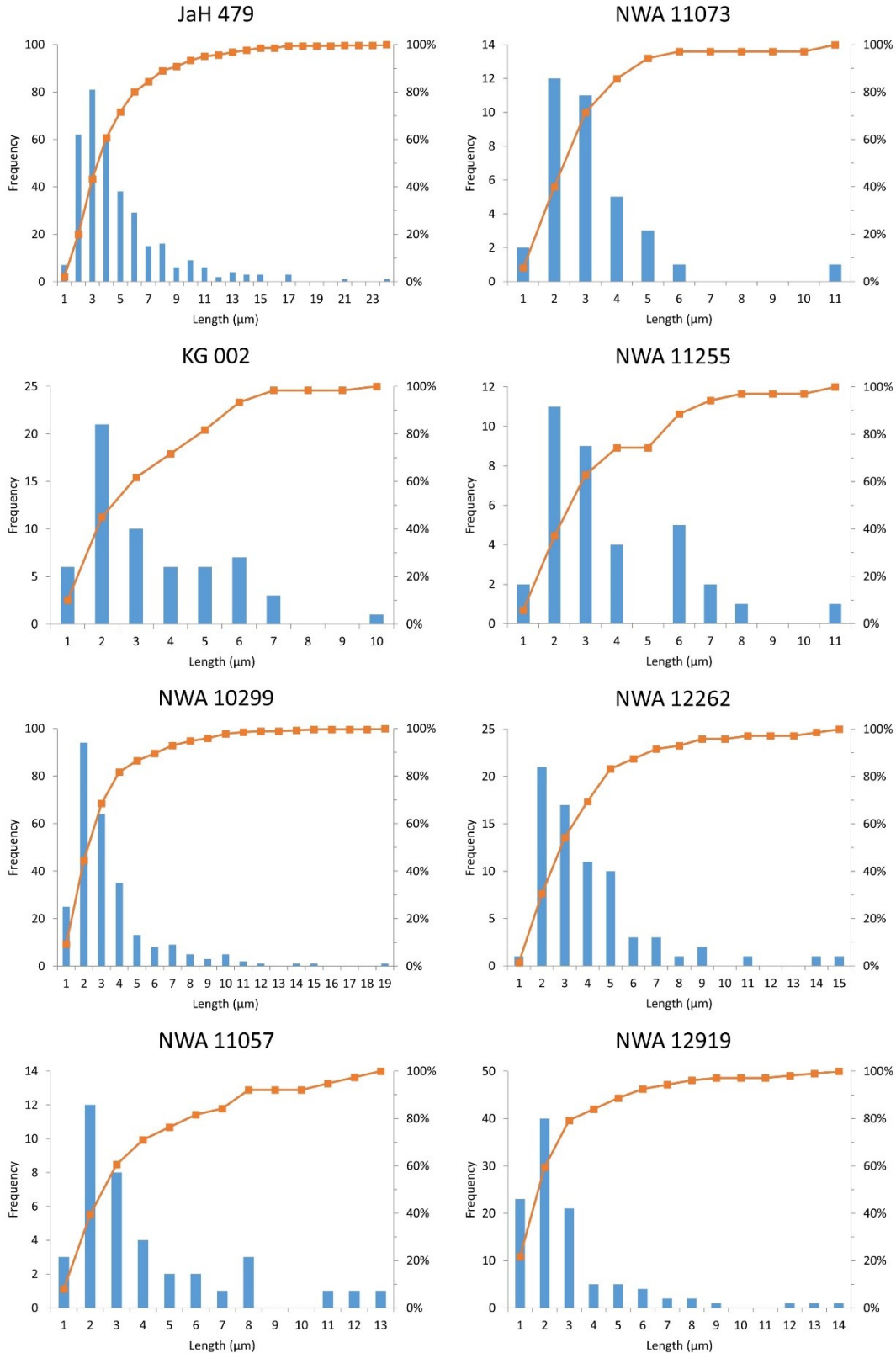


Fig. 2.12. Frequency distribution histogram and cumulative percentage of baddeleyite grain length.

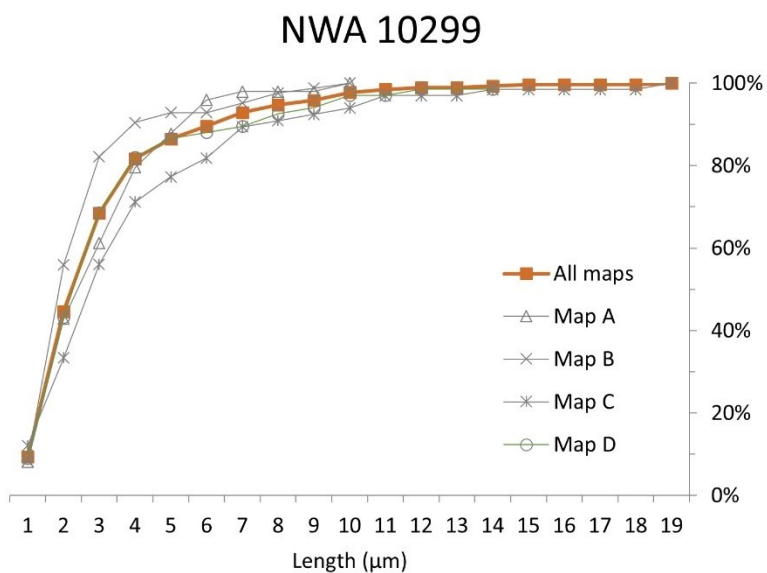


Fig. 2.13. Cumulative percentage of baddeleyite grain length in subsection maps of NWA 10299.

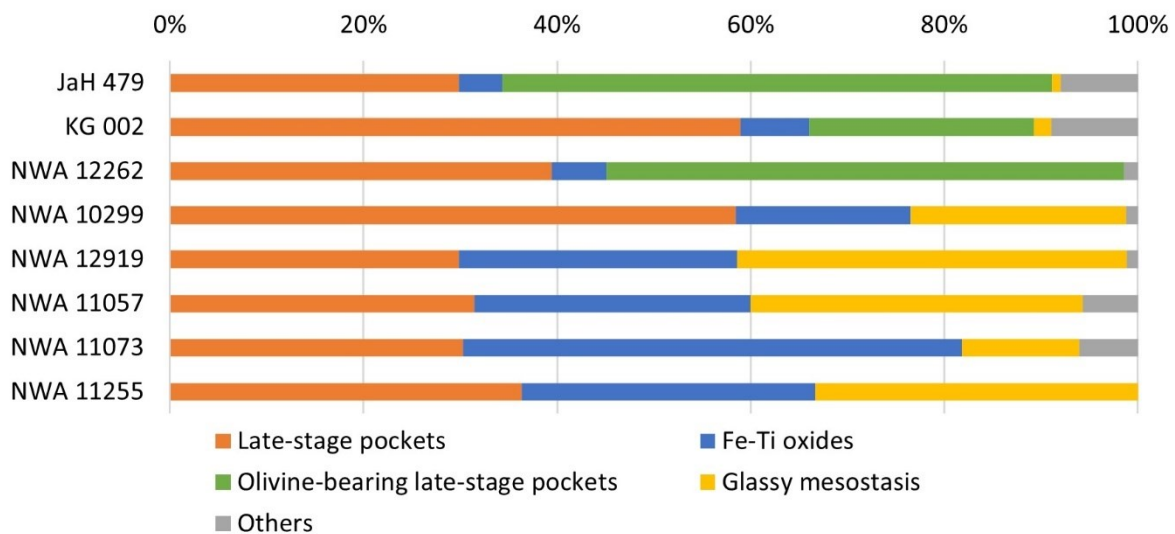


Fig. 2.14. Relative proportion of baddeleyite grains in each petrographic association.

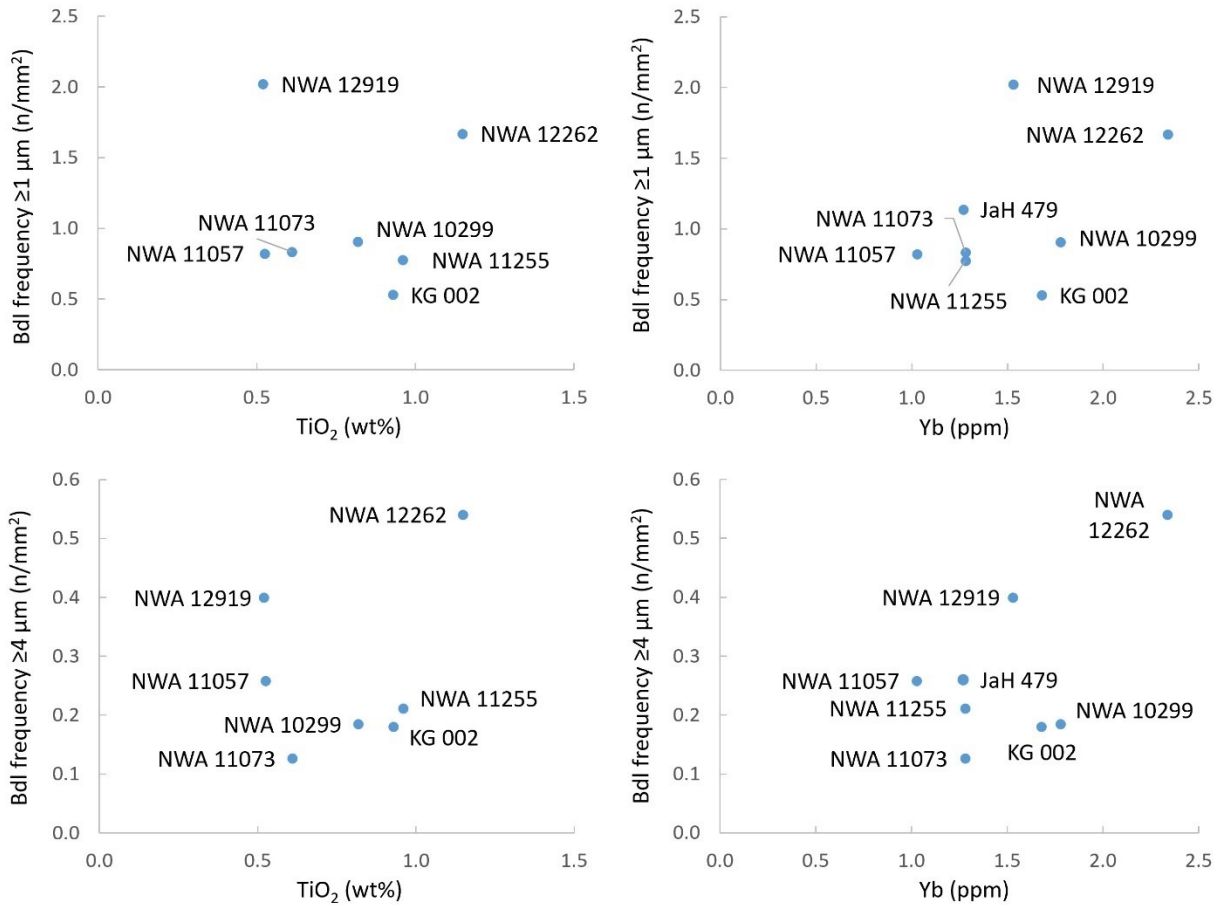


Fig. 2.15. Frequency of baddeleyite grains, at $\geq 1 \mu\text{m}$ and $\geq 4 \mu\text{m}$ populations, plotted against TiO₂ and Yb.

2.8 References

- Aoudjehane, H. C., Avicé, G., Barrat, J., Boudouma, O., Chen, G., Duke, M., Franchi, I. A., Gattacceca, J., Grady, M. M. & Greenwood, R. C. (2012) Tissint martian meteorite: A fresh look at the interior, surface, and atmosphere of Mars. *Science* **338**: 785-788.
- Aramovich, C. J., Herd, C. D. & Papike, J. J. (2002) Symplectites derived from metastable phases in martian basaltic meteorites. *American Mineralogist* **87**: 1351-1359.
- Barrat, J. A., Blichert-Toft, J., Nesbitt, R. W. & Keller, F. (2001) Bulk chemistry of Saharan shergottite Dar al Gani 476. *Meteoritics & Planetary Science* **36**: 23-29.
- Beaty, D. W., Grady, M. M., McSween, H. Y., Sefton-Nash, E., Carrier, B. L., Altieri, F., Amelin, Y., Ammannito, E., Anand, M., Benning, L. G., Bishop, J. L., Borg, L. E., Boucher, D., Brucato, J. R., Busemann, H., Campbell, K. A., Czaja, A. D., Debaille, V., Des Marais, D. J., Dixon, M., Ehlmann, B. L., Farmer, J. D., Fernandez-Remolar, D., Filiberto, J., Fogarty, J., Glavin, D. P., Goreva, Y. S., Hallis, L. J., Harrington, A. D., Hausrath, E. M., Herd, C. D. K., Horgan, B., Humayun, M., Kleine, T., Kleinhenz, J., Mackelprang, R., Mangold, N., Mayhew, L. E., McCoy, J. T., McCubbin, F. M., McLennan, S. M., Moser, D. E., Moynier, F., Mustard, J. F., Niles, P. B., Ori, G. G., Raulin, F., Rettberg, P., Rucker, M. A., Schmitz, N., Schwenzer, S. P., Sephton, M. A., Shaheen, R., Sharp, Z. D., Shuster, D. L., Siljeström, S., Smith, C. L., Spry, J. A., Steele, A., Swindle, T. D., ten Kate, I. L., Tosca, N. J., Usui, T., Van Kranendonk, M. J., Wadhwa, M., Weiss, B. P., Werner, S. C., Westall, F., Wheeler, R. M., Zipfel, J. & Zorzano, M. P. (2019) The potential science and engineering value of samples delivered to Earth by Mars sample return. *Meteoritics & Planetary Science* **54**: S3-S152.
- Bellucci, J. J., Nemchin, A. A., Whitehouse, M. J., Snape, J. F., Kielman, R. B., Bland, P. A. & Benedix, G. K. (2016) A Pb isotopic resolution to the Martian meteorite age paradox. *Earth and Planetary Science Letters* **433**: 241-248.
- Bouvier, A., Blichert-Toft, J., Vervoort, J. D., Gillet, P. & Albarède, F. (2008) The case for old basaltic shergottites. *Earth and Planetary Science Letters* **266**: 105-124.
- Chamberlain, K. R., Schmitt, A. K., Swapp, S. M., Harrison, T. M., Swoboda-Colberg, N., Bleeker, W., Peterson, T. D., Jefferson, C. W. & Khudoley, A. K. (2010) In situ U-Pb SIMS (IN-SIMS) micro-baddeleyite dating of mafic rocks: method with examples. *Precambrian Research* **183**: 379-387.
- Crozaz, G. & Wadhwa, M. (2001) The terrestrial alteration of Saharan shergottites Dar al Gani 476 and 489: A case study of weathering in a hot desert environment. *Geochimica et Cosmochimica Acta* **65**: 971-977.

- Darling, J. R., Moser, D. E., Barker, I. R., Tait, K. T., Chamberlain, K. R., Schmitt, A. K. & Hyde, B. C. (2016) Variable microstructural response of baddeleyite to shock metamorphism in young basaltic shergottite NWA 5298 and improved U–Pb dating of Solar System events. *Earth and Planetary Science Letters* **444**: 1-12.
- French, J. E. & Heaman, L. M. (2010) Precise U–Pb dating of Paleoproterozoic mafic dyke swarms of the Dharwar craton, India: implications for the existence of the Neoarchean supercraton Sclavia. *Precambrian Research* **183**: 416-441.
- Fritz, J., Greshake, A. & Stöffler, D. (2005) Micro-Raman spectroscopy of plagioclase and maskelynite in Martian meteorites: Evidence of progressive shock metamorphism. *Antarctic Meteorite Research* **18**: 96.
- Fritz J., Fernandes V. A., Greshake A., Holzwarth A., and Böttger U. (2019) On the formation of dialectic glass: Shock and thermal experiments with plagioclase of different chemical compositions. *Meteoritics and Planetary Science* **54**: 1533-1547.
- Gattacceca, J., McCubbin, F. M., Bouvier, A. & Grossman, J. (2020) The Meteoritical Bulletin, No. 107. *Meteoritics & Planetary Science* **55**: 460-462.
- Ghiorso, M. S. & Evans, B. W. (2008) Thermodynamics of rhombohedral oxide solid solutions and a revision of the Fe-Ti two-oxide geothermometer and oxygen-barometer. *American Journal of Science* **308**: 957-1039.
- Heaman, L. M. & LeCheminant, A. N. (1993) Paragenesis and U-Pb systematics of baddeleyite (ZrO_2). *Chemical Geology* **110**: 95-126.
- Herd, C. D. (2006) Insights into the redox history of the NWA 1068/1110 martian basalt from mineral equilibria and vanadium oxybarometry. *American Mineralogist* **91**: 1616-1627.
- Herd, C. (2019) Reconciling redox: making spatial and temporal sense of oxygen fugacity variations in martian igneous rocks. *LPI*: 2746.
- Herd, C. D., Moser, D. E., Tait, K., Darling, J. R., Shaulis, B. J. & McCoy, T. J. (2018) Crystallization of Baddeleyite in Basaltic Rocks from Mars, and Comparisons with the Earth, Moon, and Vesta. *Microstructural Geochronology: Planetary Records Down to Atom Scale*: 137-166.
- Herd, C. D., Walton, E. L., Agee, C. B., Muttik, N., Ziegler, K., Shearer, C. K., Bell, A. S., Santos, A. R., Burger, P. V. & Simon, J. I. (2017) The Northwest Africa 8159 martian meteorite: Expanding the martian sample suite to the early Amazonian. *Geochimica et Cosmochimica Acta* **218**: 1-26.

- Ibanez-Mejia, M., Gehrels, G. E., Ruiz, J., Vervoort, J. D., Eddy, M. P. & Li, C. (2014) Small-volume baddeleyite (ZrO_2) U–Pb geochronology and Lu–Hf isotope geochemistry by LA-ICP-MS. Techniques and applications. *Chemical Geology* **384**: 149-167.
- Jambon, A., Barrat, J. A., Sautter, V., Gillet, P., Göpel, C., Javoy, M., Joron, J. L. & Lesourd, M. (2002) The basaltic shergottite Northwest Africa 856: Petrology and chemistry. *Meteoritics & Planetary Science* **37**: 1147-1164.
- Jean, M. M., Howarth, G. H., Bodnar, B., Klyukin, Y. & Taylor, L. A. (2016) Petrogenesis of the New Basaltic Shergottite Northwest Africa 10299: fO_2 Consistent with an Intermediate to Depleted Geochemical Source. *LPI*: 2698.
- Jiang, Y. & Hsu, W. (2012) Petrogenesis of Grove Mountains 020090: An enriched “Iherzolitic” shergottite. *Meteoritics & Planetary Science* **47**: 1419-1435.
- Kring, D. A., Gleason, J. D., Swindle, T. D., Nishiizumi, K., Caffee, M. W., Hill, D. H., Jull, A. T. & Boynton, W. V. (2003) Composition of the first bulk melt sample from a volcanic region of Mars: Queen Alexandra Range 94201. *Meteoritics & Planetary Science* **38**: 1833-1848.
- Lapen, T. J., Righter, M., Andreasen, R., Irving, A. J., Satkoski, A. M., Beard, B. L., Nishiizumi, K., Jull, A. T. & Caffee, M. W. (2017) Two billion years of magmatism recorded from a single Mars meteorite ejection site. *Science Advances* **3**: e1600922.
- Lapen, T. J., Righter, M., Gao, Y. & Irving, A. J. (2018) Representative Bulk Elemental Compositions for a Suite of Shergottites. *LPI*: 2773.
- Li, Q., Li, X., Liu, Y., Tang, G., Yang, J. & Zhu, W. (2010) Precise U–Pb and Pb–Pb dating of Phanerozoic baddeleyite by SIMS with oxygen flooding technique. *Journal of Analytical Atomic Spectrometry* **25**: 1107-1113.
- Lindsley, D. H. (1983) Pyroxene thermometry. *American Mineralogist* **68**: 477-493.
- Llorca, J., Roszjar, J., Cartwright, J. A., Bischoff, A., Ott, U., Pack, A., Merchel, S., Rugel, G., Fimiani, L. & Ludwig, P. (2013) The Ksar Ghilane 002 shergottite—the 100th registered Martian meteorite fragment. *Meteoritics & Planetary Science* **48**: 493-513.
- Lodders, K. (1998) A survey of shergottite, nakhlite and chassigny meteorites whole-rock compositions. *Meteoritics & Planetary Science* **33**: A183-A190.
- Lodders K., Palme H., and Gail H. 2009. 4.4 Abundances of the elements in the Solar System. In: *Solar system*, edited by Anonymous : Springer. pp. 712-770.
- Lorenz, C. A., Ivanova, M. A., Teplyakova, S. N., Korochantsev, A. V., Franchi, I. A. & Ott, U. (2010) Basaltic Shergottite, Jiddat Al Harasis 479. *Meteoritics & Planetary Science* **73**: 5228.

- Lovering J. F., and Wark D. A. 1971. Uranium-enriched phases in Apollo 11 and Apollo 12 basaltic rocks. *Lunar and Planetary Science Conference Proceedings*. pp. 151.
- Millonig, L. J., Gerdes, A. & Groat, L. A. (2013) The effect of amphibolite facies metamorphism on the U–Th–Pb geochronology of accessory minerals from meta-carbonatites and associated meta-alkaline rocks. *Chemical Geology* **353**: 199-209.
- Misawa, K. & Yamaguchi, A. (2007) U-Pb ages of NWA 856 baddeleyite. *M&PSA* **42**: 5228.
- Moser, D. E., Chamberlain, K. R., Tait, K. T., Schmitt, A. K., Darling, J. R., Barker, I. R. & Hyde, B. C. (2013) Solving the Martian meteorite age conundrum using micro-baddeleyite and launch-generated zircon. *Nature* **499**: 454.
- Niihara, T. (2011) Uranium-lead age of baddeleyite in shergottite Roberts Massif 04261: Implications for magmatic activity on Mars. *Journal of Geophysical Research: Planets* **116**.
- Niihara, T., Kaiden, H., Misawa, K., Sekine, T. & Mikouchi, T. (2012) U–Pb isotopic systematics of shock-loaded and annealed baddeleyite: implications for crystallization ages of Martian meteorite shergottites. *Earth and Planetary Science Letters* **341**: 195-210.
- Palme, H., Lodders, K. & Jones, A. (2014) Solar system abundances of the elements. *Planets, Asteroids, Comets and The Solar System, Volume 2 of Treatise on Geochemistry (Second Edition)*. Edited by Andrew M. Davis. Elsevier, 2014., p.15-36 2.
- Righter, M., Andreasen, R., Lapen, T. J. & Irving, A. J. (2014) The age and source composition for depleted shergottite Northwest Africa 7635: A 2.3 Ga magmatic rock from early Amazonian Mars. *LPI*: 2550.
- Shaulis, B. J., Righter, M., Lapen, T. J., Jolliff, B. J. & Irving, A.J. (2017) 3.1 Ga crystallization age for magnesian and ferroan gabbro lithologies in the Northwest Africa 773 clan of lunar meteorites. *Geochimica et Cosmochimica Acta* **213**: 435-456.
- Schmitt, A. K., Chamberlain, K. R., Swapp, S. M. & Harrison, T. M. (2010) In situ U–Pb dating of micro-baddeleyite by secondary ion mass spectrometry. *Chemical Geology* **269**: 386-395.
- Söderlund, U., Isachsen, C. E., Bylund, G., Heaman, L. M., Patchett, P. J., Vervoort, J. D. & Andersson, U. B. (2005) U–Pb baddeleyite ages and Hf, Nd isotope chemistry constraining repeated mafic magmatism in the Fennoscandian Shield from 1.6 to 0.9 Ga. *Contributions to Mineralogy and Petrology* **150**: 174.
- Stolper, E. & McSween Jr, H. Y. (1979) Petrology and origin of the shergottite meteorites. *Geochimica et Cosmochimica Acta* **43**: 1475-1498.

- Wadhwa, M., Crozaz, G., Taylor, L. A. & McSween Jr, H. Y. (1998) Martian basalt (shergottite) Queen Alexandra Range 94201 and lunar basalt 15555: A tale of two pyroxenes. *Meteoritics & Planetary Science* **33**: 321-328
- Walton, E. L., Irving, A. J., Bunch, T. E. & Herd, C. (2012) Northwest Africa 4797: A strongly shocked ultramafic poikilitic shergottite related to compositionally intermediate Martian meteorites. *Meteoritics & Planetary Science* **47**: 1449-1474.
- Weisberg, M. K., Smith, C., Herd, C., Haack, H., Yamaguchi, A., Chennaoui Aoudjehane, H., Welzenbach, L. & Grossman, J. N. (2010) The Meteoritical Bulletin, No. 98, September 2010. *Meteoritics & Planetary Science* **45**: 1530-1551.
- Wones, D. R. & Gilbert, M. C. (1969) The fayalite-magnetite-quartz assemblage between 600 and 800 °C. *American Journal of Science* **267**: 480-488.
- Wu, Y. & Hsu, W. (2019) Trace Element Geochemistry and U-Pb Chronology of the Basaltic Shergottite Northwest Africa 8653. *LPICo* **82**: 6282.
- Zhou, Q., Herd, C. D., Yin, Q., Li, X., Wu, F., Li, Q., Liu, Y., Tang, G. & McCoy, T. J. (2013) Geochronology of the Martian meteorite Zagami revealed by U-Pb ion probe dating of accessory minerals. *Earth and Planetary Science Letters* **374**: 156-163.

CHAPTER 3: Baddeleyite microstructural response to shock metamorphism in enriched shergottites:

SIMS U–Pb baddeleyite geochronology of Jiddat al Harasis (JaH) 479, Northwest Africa (NWA) 10299,

and NWA 12919

3.1 Abstract

Baddeleyite (monoclinic zirconia; $m\text{-ZrO}_2$) occurs as a late-stage accessory mineral in shergottites and has seen increasing application as a geochronometer for determining igneous crystallization ages *via* *in-situ* secondary ion mass spectrometry (SIMS) U–Pb analyses. During shergottite ejection from the surface of Mars, baddeleyite develops a range of microstructures in response to shock metamorphism. Although igneous U–Pb isotopic compositions are preserved in these shocked baddeleyite grains, Pb-loss has also been observed and there remains a general paucity of constraints on the limits of shock conditions under which baddeleyite retains closed-system U–Pb isotopic behavior. To investigate this, we have examined baddeleyite in the enriched shergottites Jiddat al Harasis (JaH) 479, Northwest Africa (NWA) 10299, and NWA 12919 using coupled electron backscatter diffraction (EBSD) microstructural analyses and SIMS U–Pb geochronology. EBSD analysis reveals widespread phase transformation to high-pressure orthogonal polymorphs ($o\text{-ZrO}_2$) followed by reversion. JaH 479 contains more grains with preserved magmatic orientations than the other two shergottites, suggesting that it experienced lower bulk shock pressures. Suppressed nucleation of reverted $m\text{-ZrO}_2$ in NWA 10299 and NWA 12919 further points to insufficient post-shock temperature gradients, in contrast to JaH 479 where greater variation in local temperature conditions enabled the development of $\mu\text{-scale}$ domains of reverted $m\text{-ZrO}_2$. Individual grains that are separated into two distinct microstructural domains may reflect controls on shock propagation due to shock impedance contrast among the surrounding phases. SIMS U–Pb baddeleyite analysis yields igneous crystallization ages of 210 ± 9 Ma (JaH 479), 196 ± 11 Ma (NWA 10299), and 188 ± 11 Ma (NWA 12919). We find no evidence for resolvable Pb loss in the surveyed baddeleyite grains, suggesting that temperature conditions associated with partial phase transformation (Group 2

microstructure) and complete phase transformation with suppressed nucleation during reversion (Group 3 microstructure) were insufficient to cause significant Pb diffusion. Given the robust baddeleyite U–Pb isotope systematics in the majority of shergottites dated by SIMS methods thus far, we argue that shock conditions experienced by the bulk of shergottites were insufficient to introduce U–Pb isotopic mobility, in contrast to what is observed in the heavily shocked NWA 5298 shergottite. Our findings place additional constraints on baddeleyite microstructural response to shock conditions of shergottite ejection and demonstrate that baddeleyite in shergottites is robust for U–Pb igneous geochronology when combined with microstructural observations.

3.2 Introduction

Constraining the absolute time scale of Mars is critical to understanding the planet’s evolution and processes responsible for shaping the planet’s surface and interior (e.g., [Borg and Drake, 2005](#); [Foley et al., 2005](#); [Debaille et al., 2008](#); [Ehlmann and Edwards, 2014](#); [Lapen et al., 2017](#); [Cassata et al., 2018](#); [Udry et al., 2020](#)). In the absence of returned samples, martian meteorites remain the only specimens of Mars available for radiometric dating in terrestrial laboratory settings. The majority of martian meteorites represent mafic to ultramafic hypabyssal and extrusive igneous rocks, with crystallization ages currently defined in five distinct populations: 1) 4.5–4.3 Ga igneous clasts and individual minerals in the polymict regolith breccia Northwest Africa (NWA) 7034 and its pairs (e.g., [Goodwin et al., 2022](#)), 2) the 4.09 ± 0.03 Ga Allan Hill (ALH) 84001 orthopyroxenite ([Lapen et al., 2010](#)), 3) the ~ 2.4 Ga augite-rich shergottites ([Herd et al., 2017](#); [Lapen et al., 2017](#)), 4) the ~ 1.5 to 1.3 Ga nakhlites and chassignites (e.g., [Borg and Drake, 2005](#); [Park et al., 2014](#); [Cohen et al., 2017](#)), 5) < 1.5 Ga detrital zircons in NWA 7533 (paired with NWA 7034; [Costa et al., 2020](#)) and 6) the 716–157 Ma shergottites (e.g., [Nyquist et al., 2001](#); [Borg and Drake, 2005](#); [Park et al., 2014](#); [Righter et al., 2018](#); [Udry et al., 2020](#); [Váci and Agee, 2020](#)). The known spectrum of absolute ages is dominated by shergottites (49 out of 64 dated; [Udry et al., 2020](#) and references therein; [Váci and Agee, 2020](#) and references therein; [Ferdous and Brandon, 2020](#); [Staddon et al., 2021b](#); [Wu et al., 2021](#)).

2021; Lindner et al., 2022; O’Neal et al., 2022), the most abundant group of martian meteorites (>80% by number; Udry et al., 2020). The prevalence of late Amazonian igneous ages defined by Rb–Sr, Sm–Nd, and Lu–Hf isotope systematics in the vast majority of shergottites contrasts with crater chronology indicating that most of Mars is covered by ancient (>3.5 Ga) crust (e.g., Hartmann and Neukum, 2001). This apparent paradox is attributed to mechanical thresholds required for near-surface lithologies to survive ejection and launch during impact events (Melosh, 1984; Head et al., 2002). The resulting prevalence of young volcanic rocks in the martian meteorite record yields insights into persistent igneous activity at select volcanic centres (e.g., Tharsis and Elysium regions) long after the decline of the mantle dynamo (e.g., Lapan et al., 2017; Lagain et al., 2021).

The majority of shergottite dating has been conducted using isotope dilution thermal ionization mass spectrometry (ID-TIMS) Rb–Sr, Sm–Nd, or Lu–Hf analysis. However, this approached can be limited by available sample volume or terrestrial alteration (e.g., Ferdous et al., 2017). These limitations may be overcome by *in-situ* U–Pb baddeleyite analysis via secondary ion mass spectrometry (SIMS), which not only has greater potential for preserving the overall sample, but also allows for isotopic data to be evaluated in combination with other *in-situ* information (e.g., Moser et al., 2013; Darling et al., 2016; Staddon et al., 2021b). The SIMS method utilizes the advantages of baddeleyite (monoclinic zirconia, $m\text{-ZrO}_2$) as a common accessory phase in some shergottites (Herd et al., 2018a; Sheen et al., 2021) and as a robust U–Pb geochronometer, which incorporates U and excludes Pb during crystallization and resists open-system behavior in a range of terrestrial metamorphic conditions (Heaman and LeCheminant, 1994). At the time of this study, six shergottites have been dated by *in-situ* U–Pb baddeleyite analysis (Misawa and Yamaguchi, 2007; Niihara, 2011; Jiang and Hsu, 2012; Moser et al., 2013; Zhou et al., 2013; Darling et al., 2016; Staddon et al., 2021b; Wu et al., 2021).

Gaps remain in understanding how U–Pb isotope systematics in baddeleyite behaves under the range of shock conditions experienced by shergottites during ejection from Mars. Electron backscatter

diffraction (EBSD) analysis of baddeleyite yields microstructural evidence for widespread phase transformation to, and subsequent reversion from, high-pressure polymorphs of zirconia ([Darling et al., 2016](#); [Staddon et al., 2021b](#)). Variably recrystallized baddeleyite in the highly shocked shergottite NWA 5298 (estimated bulk shock pressure ≥ 42 Gpa) exhibits up to 80% Pb loss ([Darling et al., 2016](#)), whereas a suite of three less shocked shergottites (NWA 7257, NWA 8679, Zagami) show no resolvable link between baddeleyite microstructural response and U–Pb isotope systematics ([Staddon et al., 2021b](#)). [Staddon et al. \(2021b\)](#) suggested NWA 7257, NWA 8679 and Zagami experienced insufficient post-shock heating to cause resolvable Pb mobility across baddeleyite grain boundaries. Open-system behavior in baddeleyite such as that exhibited by a small population of grains in NWA 5298 has yet to be observed in other shergottites and it remains to be constrained at which point significant disturbance of the U–Pb system begins to be exhibited in shocked baddeleyite in shergottites.

In addition, it is unclear to what extent petrography exerts influence on baddeleyite microstructural response to shock metamorphism. In NWA 5298, preserved magmatic crystallographic orientations are observed in association with phases of relatively high shock impedance (i.e., resistance to shock wave propagation; [Darling et al., 2016](#)), however this phenomenon is not observed in NWA 7257, NWA 8679, and Zagami ([Staddon et al., 2021b](#)). Shergottite geochronology fundamentally relies on resolving primary igneous isotopic compositions, which in turn depend on a combination of petrographic, microstructural, and geochemical factors. Therefore, constraining any link between sample petrography and baddeleyite microstructures may potentially allow a preliminary assessment of feasibility for U–Pb dating based on petrographic information, which is more readily obtainable than EBSD data (cf. [Sheen et al., 2021](#)).

In this study, we examine baddeleyite occurrence, microstructures, and U–Pb isotope systematics in three previously undated shergottites, with the aims to 1) evaluate any link between baddeleyite microstructure and U–Pb isotope systematics in shergottites with bulk shock pressures outside those

covered in previous studies and 2) assess the role of petrography in baddeleyite's response to impact shock with respect to microstructures and U–Pb isotope systematics.

3.3 Baddeleyite petrography and microstructural response to shock

Baddeleyite in shergottites occurs as a late-stage accessory phase and is commonly associated with Fe–Ti oxides, ferroan clinopyroxene, fayalitic olivine, Ca phosphates, Fe sulfides, and/or silica glass (Herd et al., 2018a; Sheen et al., 2021). Of the major shergottite petrographic subgroups, basaltic shergottites contain more abundant baddeleyite compared to olivine-phyric and poikilitic shergottites (Herd et al., 2018a). Abundance in basaltic shergottites further scales with the degree of fractional crystallization. This reflects primary control on baddeleyite crystallization by progressive Zr enrichment in the melt driven by magma evolution and fractional crystallization (Herd et al., 2018a; Sheen et al., 2021). Dependence on Zr content also suggests baddeleyite to be in theory more abundant in shergottites sourced from more incompatible trace element (ITE) enriched mantle compositions (i.e., enriched shergottites over intermediate and depleted shergottites). Previous work report baddeleyite frequencies of up to 2 grains/mm² in basaltic shergottites (Herd et al., 2018a; Sheen et al., 2021). Grains range from euhedral prismatic (tabular or elongated) to anhedral, reaching up to ~40 µm in length but are commonly under 10 µm.

Zirconia exists in various metastable polymorphs depending on pressure-temperature conditions. Baddeleyite, with a monoclinic structure (*m*-ZrO₂), is stable below 3.3 GPa and 1170°C and commonly displays simple or polysynthetic twins (Smith and Newkirk, 1965; Wingate and Compston, 2000; Ohtaka et al., 2001; Takagi et al., 2020). At pressures of ≥3.3 GPa, *m*-ZrO₂ undergoes phase transformation into a series of orthorhombic structures (*o*-ZrO₂; Bouvier et al., 2000; Ohtaka et al., 2001; Takagi et al., 2020). With increasing temperature, *m*-ZrO₂ transforms into tetragonal (*t*-ZrO₂) and cubic (*c*-ZrO₂) structures at >1170°C and >2370°C, respectively (Nielsen, 2013; Belov et al., 2018). These high-pressure or high-temperature polymorphs revert to *m*-ZrO₂ at ambient conditions, with the reverted monoclinic domains

linked by systematic orientation relationships (ORs) due to correspondence of nucleating reverted m -ZrO₂ with the crystal symmetry of the parental polymorph ([Kelly and Rose, 2002](#); [Cayron et al., 2010](#); [Timms et al., 2017](#); [White et al., 2018](#)). Hence although direct observation of meta-stable polymorphs is challenging ([Niihara et al., 2012](#); [Zhou et al., 2013](#); [Takagi et al., 2020](#)), baddeleyite microstructures preserve evidence for phase transformations that may have occurred.

Historically, a paucity of baddeleyite microstructural measurements in planetary materials has led to speculation that baddeleyite in shergottites has undergone melting and complete U–Pb age resetting, or represents the breakdown product of zircon ([Bouvier et al., 2008](#); [El Goresy et al., 2013](#)). EBSD evidence for preserved magmatic twinning in NWA 5298, NWA 7257, NWA 8679, and Zagami confirms baddeleyite in shergottites to be a primary mineral ([Darling et al., 2016](#); [Staddon et al., 2021b](#)). Although Pb loss is observed in heavily shocked baddeleyite grains in NWA 5298, robust U–Pb isotopic composition is retained in grains showing EBSD and cathodoluminescence (CL) evidence for limited shock modification ([Darling et al., 2016](#)). In NWA 7257, NWA 8679, and Zagami, baddeleyite displays orthogonally related m -ZrO₂ domains, suggesting widespread phase transformation to o -ZrO₂ ([Staddon et al., 2021b](#)); low post-shock temperature estimates (<220°C) associated with Zagami ([Stöffler et al., 1986](#); [Nyquist et al., 2001](#); [Fritz et al., 2005](#)) indicates that high-temperature transformation to t -ZrO₂ was not possible ([Staddon et al., 2021b](#)). The observation of poorly diffracting grains in all four shergottites (termed “quasi-amorphous” by [Darling et al., 2016](#)) has been interpreted to represent nanoscale crystallographic ordering of reverted m -ZrO₂ that reflect suppressed nucleation caused by limited post-shock heating ([Staddon et al., 2021b](#)). Robust U–Pb igneous crystallization ages in NWA 7257, NWA 8679, and Zagami led [Staddon et al. \(2021b\)](#) to conclude that conditions of shock metamorphism were insufficient to cause significant disturbance in baddeleyite U–Pb isotope systematics. Microstructural analysis is therefore a powerful tool for evaluating baddeleyite U–Pb data in relation to the shock history of shergottite samples.

3.4 Samples

Specimens of three basaltic shergottites, Jiddat al Harasis (JaH) 479, NWA 10299, and NWA 12919 were selected for this study from the University of Alberta Meteorite Collection (accession numbers MET11619/TEP1, MET11774/2, and MET11776/4). These shergottites are all derived from incompatible element (ITE) enriched mantle sources ($\text{La}/\text{Yb}_{\text{CI}} > 0.8$; [Sheen et al., 2021](#)). The petrology and baddeleyite occurrences of these samples were previously reported by [Lorenz et al. \(2010\)](#), [Jean et al. \(2016\)](#), and [Sheen et al. \(2021\)](#).

3.4.1 JaH 479

JaH 479 is composed of coarse-grained (mm-scale) clinopyroxene ($\text{Fs}_{23-83}\text{En}_{5-54}\text{Wo}_{12-38}$) and plagioclase ($\text{Ab}_{18-31}\text{An}_{66-76}\text{Or}_{3-6}$) in subophitic texture, with accessory titanomagnetite (showing subsolidus exsolution lamellae), ilmenite, chlorapatite, merrillite, Fe sulfides, fayalitic olivine, and silica glass. Clinopyroxene is compositionally zoned, with high-Ca magnesian cores and progressively low-Ca ferroan rims. Three-phase symplectite composed of intergrown fayalitic olivine, ferroan clinopyroxene, and silica reflect breakdown of metastable pyroxferroite ([Aramovich et al., 2002](#)). Surveyed baddeleyite grains have an average length of $4.4 \pm 3.3 \mu\text{m}$ (1σ , $n=338$), reaching a maximum size of $23.3 \times 5.3 \mu\text{m}$. Most grains occur in coarse-grained mesostasis, with particular affinity for an olivine±apatite±silica assemblage. A smaller population of grains is associated with fine, glassy mesostasis.

3.4.2 NWA 10299

NWA 10299 exhibits coarse-grained subophitic texture, with elongate prismatic clinopyroxene and interstitial plagioclase ($\text{Ab}_{45-55}\text{An}_{38-54}\text{Or}_{1-13}$). Clinopyroxene compositions are separated into high-Ca ($\text{Fs}_{22-54}\text{En}_{17-45}\text{Wo}_{22-34}$) and low-Ca ($\text{Fs}_{32-69}\text{En}_{16-57}\text{Wo}_{11-19}$) trends, both with increasing ferroan content from core to rim. Accessory phases are similar to those in JaH 479, with the exception of the absence of three-phase symplectite; exsolution in titanomagnetite is also lacking. Baddeleyite grains measure $3.1 \pm 2.4 \mu\text{m}$ in length on average ($n=243$), with the largest grain measuring $12.5 \times 11.4 \mu\text{m}$. Grains occur in late-stage pockets, glassy mesostasis, or are enclosed in Fe-Ti oxides.

3.4.3 NWA 12919

NWA 12919 is medium-grained (grains up to 1 mm in length). Clinopyroxene generally consists of high-Ca cores ($\text{Fs}_{19-51}\text{En}_{23-46}\text{Wo}_{25-38}$) bounded by low-Ca rims ($\text{Fs}_{33-68}\text{En}_{15-54}\text{Wo}_{11-22}$). Plagioclase has a composition of $\text{Ab}_{43-57}\text{An}_{40-56}\text{Or}_{1-4}$. Accessory phases include titanomagnetite, ilmenite, merrillite, chlorapatite, Fe sulfides, with trace olivine. Baddeleyite has an average length of $2.9 \pm 2.5 \mu\text{m}$ ($n=86$), with occurrences in petrographic settings similar to those in NWA 10299. A larger proportion of grains are enclosed in Fe-Ti oxides compared to JaH 479 and NWA 10299.

3.4.4 Shock features and bulk shock pressure estimates

Shock deformation and transformation effects in the three chosen shergottites are consistent with moderate to strong bulk shock metamorphism. Deformation comprises planar fractures, mosaicism, and mechanical twins in clinopyroxene, whereas transformation includes the formation of localized shock melt as veins and pockets, as well as the transformation of precursor igneous plagioclase. Plagioclase in JaH 479 and NWA 12919 has been transformed to maskelynite, suggesting bulk shock pressures or at least ~ 24 GPa and up to ~ 45 GPa, with minor grains in JaH 479 showing weak anisotropy ([Lorenz et al., 2010](#); [Sheen et al., 2021](#)). In NWA 10299, plagioclase has been shock-melted into a liquid which then quenched into a vesiculated glass following pressure release, indicating higher shock pressures, in the range of 45–55 GPa ([Sheen et al., 2021](#)). Shock features in JaH 479 and NWA 12919 are similar those documented in NWA 7257, NWA 8679, and Zagami previously investigated for baddeleyite microstructures and U–Pb geochronology by [Staddon et al. \(2021b\)](#). The estimated shock pressure conditions for JaH 479 and NWA 12919 are also therefore similar to that constrained for Zagami (~ 30 GPa; [Stöffler et al., 1986](#); [Fritz et al., 2005](#)). Compared to these five shergottites, NWA 10299 and NWA 5298 are more extensively shocked; both have higher bulk shock pressure estimates (≥ 42 GPa for NWA 5298) and display the transformation of plagioclase into vesiculated glass ([Darling et al., 2016](#)). However, plagioclase melting is more pervasive in NWA 5298 than in NWA 10299. Furthermore, baddeleyite grains in NWA 10299 (as well as in JaH 479

and NWA 12919) do not exhibit zircon rims or a granular texture, both of which are associated with shock melt pockets and clinopyroxene recrystallization in NWA 5298 ([Darling et al., 2016](#)). We therefore consider the degree of shock metamorphism experienced by NWA 10299 to be lower than that of NWA 5298. Hence NWA 10299 is considered an intermediate member between the shock conditions represented by NWA 5298 and those of the shergottites examined by [Staddon et al. \(2021b\)](#).

3.5 Methodology

3.5.1 EBSD baddeleyite microstructure analysis

Shergottite samples, consisting one polished thin section (JaH 479) and two polished thick sections (NWA 10299, NWA 12919) (Fig. 3.1), were cut and mounted in epoxy. To ensure high-quality polish for EBSD analysis, the mounts underwent 0.5 µm mechanical polishing followed by 20–40 minutes of vibratory polishing with 50 nm alumina suspension. The polished mounts were imaged using a TESCAN MIRA3 field emission gun scanning electron microscope (FEG-SEM) at the Electron Microscopy and Microanalysis Unit, University of Portsmouth. Mapping of NWA 10299 was previously conducted on CAMECA SX-100 electron probe microanalyzer (EPMA) at the Electron Microprobe Laboratory, University of Alberta ([Sheen et al., 2021](#)). Mounts were mapped in backscatter electron (BSE) and energy dispersive X-ray spectroscopy (EDS) imaging. Baddeleyite grains in JaH 479 and NWA 12919 were identified using the Oxford Instruments INCA Feature software; those in NWA 10299 were previously identified using methods described in [Sheen et al. \(2021\)](#).

EBSD analyses were performed on a Zeiss EVO MA10 LaB₆ SEM with an Oxford Instruments Symmetry S2 detector following methods outlined in [Staddon et al. \(2021b\)](#). Samples were run uncoated under variable pressure; full EBSD conditions are detailed in Table 3.1. Data were processed offline in Oxford Instruments AZtecCrystal and AZtecHKL Channel 5. A wild spike correction was applied to replace isolated indexed pixels with zero solutions (i.e., not indexed), followed by noise reduction (level 8) which infills zero solutions pixels that are surrounded by eight indexed pixels. Where present, an additional

correction step was applied to remove systematic mis-indexing ($180^\circ/\langle 101 \rangle$), caused by mirror symmetry of the b-axis in monoclinic systems; this is described in detail in [Staddon et al. \(2021b\)](#). Interpretation of microstructural data was mainly based on band contrast (BC), inverse pole figure (IPF) maps, and stereographic projections. BC represents the intensity of Kikuchi bands relative to the overall electron backscatter pattern (EBSP) and reflects the degree of diffraction and therefore crystallinity in baddeleyite and surrounding phases. IPF-colored maps display the absolute orientation relative to the sample normal. The IPF-colored data is further plotted in a series of pole figures, each of which shows the lower hemisphere stereographic projection of a specified crystallographic direction or set of crystallographic directions related by symmetry. As IPF coloring does not distinguish between crystal directions related by crystallographic symmetry, pixels with the same color may not represent the same crystal orientation. The use of multiple stereographic projections helps to distinguish between these orientations and allows crystallographic ORs to be evaluated.

3.5.2 SIMS U–Pb analysis

SIMS U–Pb baddeleyite analysis of the three shergottites was conducted using a CAMECA IMS 1280-HR ion microprobe at the Heidelberg Ion Probe (HIP) facility at the Institute of Earth Sciences, Heidelberg University. Target grains were selected based on a combination of size, morphology, petrography, and microstructural data. The sample sections were cut from the epoxy mounts following EBSD analysis and re-mounted at the HIP with the Phalaborwa and FC4b baddeleyite standards ([Heaman and LeCheminant, 1993](#); [Heaman, 2009](#); [Chamberlain et al., 2010](#)) and coated with gold. SIMS analysis followed protocols outlined in [Staddon et al. \(2021b\)](#), with a 0.5–1 nA primary O[−] beam. Secondary ions were extracted at 10 kV. Although a ~5 um spot size was intended for analysis, SEM images taken after SIMS sessions showed actual spot sizes of ~8–12 um in the long axis. Mass resolution ($M/\Delta M$; 10% peak height) was tuned to ~4650 to resolve interferences from rare earth elements (REEs) and Hf oxides. Oxygen flooding was employed by bleeding 1×10^{-5} mbar O₂ into the sample chamber to suppress crystal-

orientation-dependent U/Pb fractionation (orientation effect; [Wingate and Compston, 2000](#)) and to enhance Pb⁺ ionization ([Chamberlain et al., 2010](#); [Li et al., 2010](#); [Schmitt et al., 2010](#)). Each analysis included 40 seconds of pre-sputtering to remove any surface Pb contamination, followed by up to 20 collection cycles. Each cycle measured the ions $^{90}\text{Zr}_2\text{O}^+$, $^{204}\text{Pb}^+$, $^{206}\text{Pb}^+$, $^{207}\text{Pb}^+$, $^{208}\text{Pb}^+$, $^{232}\text{Th}^+$, $^{238}\text{U}^+$, $^{238}\text{UO}^+$, and $^{238}\text{UO}_2^+$ using an on-axis ion counter in single collection mode. Counting times are listed in Appendix 2. Each full 20-cycle analysis ran for ~45 min, however some analyses of smaller baddeleyite grains were ended before 20 cycles due to the grain being sputtered through. Cycles associated with this process showed sharp decrease in $^{90}\text{Zr}_2\text{O}^+$, $^{238}\text{U}^+$, $^{238}\text{UO}^+$, and $^{238}\text{UO}_2^+$ signals and were excluded during data reduction. Baddeleyite standards were analyzed at the beginning and end of each day of analytical session.

Reduction of isotopic data followed protocols outlined in [Chamberlain et al. \(2010\)](#) and [Schmitt et al. \(2010\)](#). U/Pb elemental fractionation was calibrated using the power law relationship between $^{206}\text{Pb}/^{238}\text{U}$ and UO_2^+/U^+ of the Phalaborwa baddeleyite reference material. The FC4b baddeleyite was analyzed as a secondary reference material. Common Pb corrected weighted mean ^{207}Pb - ^{206}Pb and ^{206}Pb - ^{238}U ages of FC4b were 1102.0 ± 4.4 Ma (mean square of weighted deviates, MSWD 2.1; 95% confidence interval) and 1104.2 ± 7.8 Ma (MSWD 0.55; 95% confidence interval) respectively, in good agreement with published values ([Chamberlain et al., 2010](#); Appendix 2).

For calculating igneous crystallization ages, Tera-Wasserburg concordia diagrams of $^{238}\text{U}/^{206}\text{Pb}$ and $^{207}\text{Pb}/^{206}\text{Pb}$ isotopic ratios uncorrected for common Pb were used (e.g. [Schoene, 2014](#)). Baddeleyite analyses typically yielded low $^{206}\text{Pb}/^{204}\text{Pb}$ ratios (<200) such that applying common Pb correction using measured ^{204}Pb would result in large uncertainties. This is due to common Pb contribution from matrix phases overlapped by the primary beam, as well as the young, <500 Ma crystallization age of most shergottites, which results in low in-growth of ^{206}Pb and low total counts of ^{204}Pb . If the analyzed baddeleyite grains are cogenetic and have not experienced U-Pb isotopic disturbance, $^{238}\text{U}/^{206}\text{Pb}$ and $^{207}\text{Pb}/^{206}\text{Pb}$ ratios uncorrected for common Pb should yield an array in Tera-Wasserburg concordia

diagram, reflecting mixing between common Pb and radiogenic Pb endmembers. The y-axis intercept of the regressed discordia represents the initial $^{207}\text{Pb}/^{206}\text{Pb}$ ratio of the common Pb component, whereas the lower intercept (with concordia) represents the crystallization age.

3.6 Results

3.6.1 EBSD baddeleyite microstructures

EBSD analysis was conducted for a total of 69 baddeleyite occurrences: 24 in JaH 479, 19 in NWA 10299, and 26 in NWA 12919 (Table 3.2). The observed microstructures are grouped based on the classification of [Staddon et al. \(2021b\)](#), which describes increasing complexity in baddeleyite microstructural response to generally increasing shock metamorphic processes:

Group 1: Group 1 represents grains that show the least microstructural modification by shock metamorphism. Indexing is mostly continuous, showing a single orientation or orientations typical of baddeleyite magmatic twinning ($180/\langle 001 \rangle$ or $180/\langle 100 \rangle$) (Fig. 3.2a). Group 1 grains show evidence of shock-induced crystal-plastic deformation (CPD) which manifests as cumulative misorientation (rotation of the crystal structure from a specified point) typically of $<15^\circ$. Whereas Group 1 grains previously reported in NWA 7257, NWA 8679, and Zagami ([Staddon et al., 2021b](#)) show strong BC indicative of good diffraction, those observed in this study generally show moderate to weak BC; this is attributed to the grains being adjacent to strongly diffracting phases which dominate the BC signals (Fig. 3.2a).

Group 2: Group 2 grains exhibit a dominant orientation, with or without magmatic twinning, with up to 20° of cumulative misorientation. Accompanying this main domain are smaller domains related by orthogonal (i.e., separated by 90°) ORs, appearing as a set of three clusters in $\langle 100 \rangle$, $\langle 010 \rangle$, and $\langle 001 \rangle$ pole diagrams (Fig. 3.2b). Group 2 grains appear to have experienced more extensive CPD compared to Group 1 grains.

Group 3: Group 3 grains are distinguished by very weak but variable BC across most of the grain, resulting in limited, isolated indexing (Fig. 3.2c) or a complete lack thereof (Fig. 3.2d). Although weak

diffraction can be a result of poor sample polishing, this is not supported by strong BC in surrounding phases such as titanomagnetite and clinopyroxene. This result strongly indicates degraded crystallinity to be the cause of the low BC in baddeleyite grains. Any areas of sufficient BC to allow indexing form isolated domains separated by areas of lowered crystallinity (zero solutions; Fig. 3.2d). Indexing domains may show simple or orthogonal ORs, in addition to mis-indexed orientations likely caused by poor diffraction.

Group 4: [Staddon et al. \(2021b\)](#) described a fourth microstructural group in the NWA 8679 shergottite characterized by interlocking, orthogonally related domains that dominate the grain area, with complex internal microstructures and overall stronger diffraction than Group 3. In this study, we found no baddeleyite grain that can be definitively classified as Group 4. Orthogonally related domains are observed in some Group 3 grains, however most of the grain area remains dominated by poor crystallinity (i.e., lack of indexing). Grains that show a mixture of microstructural groups are classified based on the most dominant group with respect to proportion of grain area, following the method of [Staddon et al. \(2021b\)](#). The exception to this is a small number of grains ($n=4$) where strong BC and indexing concentrate in one side of the grain while the other side is marked by weak to very weak BC (Fig. 3.2e). As strong diffraction of the surrounding phases rules out poor polishing, the contrast in BC indicates a difference in crystallinity in the two portions of the grain, resulting in the grain displaying Group 3 alongside another microstructural group (Group 1, 2, or 4). These four grains are given a separate “mixed group” designation in this study to reflect heterogeneous microstructural response in different portions of the same grain.

Microstructural group 3 dominates the examined baddeleyite grains in NWA 10299 (17 out of 19) and NWA 12919 (25 out of 27) (Table 3.3). In contrast, JaH 479 contains more diverse microstructures, with Group 3 constituting only a little over half of the grains ($n=13$), followed by Group 2 ($n=7$) and Group 1 ($n=2$). NWA 10299 and NWA 12919 each feature one Group 1 grain and one of mixed groups: Group 3 and 4 in NWA 10299 and Group 1 and 3 in NWA 12919. Mixed group grains in JaH 479 ($n=2$) likewise display some diversity, with Group 3 mixed with Group 2 or 4.

In mixed group grains, the degree of crystallinity is unevenly distributed with one portion of the grain showing stronger BC and hence more extensive indexing than the remaining poorly diffracting area (Fig. 3.2e). In addition, a subset of Group 3 grains shows indexing only in sections of the rim. In all the above instances, baddeleyite is bound by more than one phase. Where in contact with titanomagnetite, maskelynite, and clinopyroxene, baddeleyite displays stronger crystallinity. Apart from mixed group and Group 3 grains, uneven distribution of microstructural response is also observed in a Group 2 grain in JaH 479 (F418-R; Fig. 3.2b), where reverted orthogonal domains occur only on the side of the grain that is bound by mesostasis (fayalitic) olivine whereas the remainder of the grain, bound by maskelynite, exhibits preserved magmatic orientation.

As baddeleyite in NWA 10299 and NWA 12919 are dominated by Group 3 microstructures, no link with petrographic setting can be evaluated (Table 3.2). Although the only Group 1 grains in NWA 10299 and NWA 12919 are enclosed in Fe-Ti oxide, Group 3 grains are also present in this petrographic setting. Two grains associated with shock melt pockets in NWA 12919 also display Group 3 microstructure. In JaH 479, which hosts baddeleyite with more diverse microstructures, the petrographic setting does not appear to correlate between grains which preserve magmatic orientations (Groups 1 and 2) and those that do not (Group 3; Table 3.2). We further note that in the same late-stage pockets, grains separated by <20 µm display different microstructure groups (e.g., F418-L and F418-R, F629A-L and F629A-R; Table 3.2).

3.6.2 SIMS U–Pb isotopic analysis

Results of SIMS baddeleyite U–Pb isotopic analysis in JaH 479 (n=15), NWA 10299 (n=14), and NWA 12919 (n=9) are summarized in Table 3.4. The $^{238}\text{U}/^{206}\text{Pb}$ ratio of the analyses has a range of 4.471–34.968 and $^{207}\text{Pb}/^{206}\text{Pb}$ ratio has a range of 0.0528–0.7704. The calculated proportion of radiogenic ^{206}Pb (out of total measured ^{206}Pb) is between 14% and 100%. Only the analyses 54A-1 and 54A-2 in NWA 10299 (conducted on the same grain) yielded $^{206}\text{Pb}/^{204}\text{Pb}$ ratios of >500.

Baddeleyite $^{207}\text{Pb}/^{206}\text{Pb}$ and $^{238}\text{U}/^{206}\text{Pb}$ ratios in JaH 479 yield discordia in Tera-Wasserburg space

with a lower intercept age of 209.7 ± 9.1 Ma (95% confidence) and an upper intercept $^{207}\text{Pb}/^{206}\text{Pb}$ ratio of 0.942 ± 0.054 (95% confidence), with a mean square weighted deviation (MSWD) of 1.6 (Fig. 3.3a). Applying ^{207}Pb correction using the upper intercept $^{207}\text{Pb}/^{206}\text{Pb}$ ratio yields a weighted mean age of 207.2 ± 8.0 Ma (95% confidence; MSWD=1.14), within uncertainty of the discordia lower intercept age. Grain F212, which plots outside the uncertainty envelope of the discordia regression formed by the rest of the analyses, was rejected from age calculations. We attribute the measured U–Pb composition of F212 to the small exposed area of the baddeleyite target and overlapping by the beam with the adjacent merrillite and Fe-sulfide grains, as verified by post-SIMS images of the analysis pit (Figs. 3.4a, b). This caused the U/Pb fractionation to deviate from that of pure baddeleyite against which the unknowns are calibrated. Although Pb loss can also cause U–Pb isotopic composition to shift towards higher $^{238}\text{U}/^{206}\text{Pb}$ ratios, we find no evidence for recrystallization or alteration in the adjacent merrillite or Fe-sulfide to support this hypothesis.

Baddeleyite analyses in NWA 10299 yield a discordia lower intercept age of 196 ± 11 Ma (95% confidence), with an upper intercept $^{207}\text{Pb}/^{206}\text{Pb}$ of 0.95 ± 0.31 (95% confidence) and a MSWD of 5.5 (Fig. 3.3b). The uncertainty in the upper intercept is greater compared to JaH 479 and NWA 12919 as analyses in NWA 10299 yielded generally more radiogenic $^{207}\text{Pb}/^{206}\text{Pb}$ compositions (<0.44), with the lowest proportion of radiogenic ^{206}Pb being 56%. Analysis 75-2 yielded the most radiogenic Pb composition measured in this study, with a $^{207}\text{Pb}/^{206}\text{Pb}$ ratio of 0.1012 ± 0.0185 and $^{206}\text{Pb}/^{204}\text{Pb}$ ratio of -65758. This analysis is concordant with a $^{206}\text{Pb}–^{238}\text{U}$ age of 182.9 ± 16 (2σ) and hence controls the lower intercept of the NWA 10299 discordia. The weighted mean of $^{206}\text{Pb}–^{238}\text{U}$ dates, corrected using the upper intercept $^{207}\text{Pb}/^{206}\text{Pb}$ of 0.95, yields an age of 192.8 ± 8.7 Ma (95% confidence, MSWD=4.5), within uncertainty of the lower intercept age.

Nine baddeleyite analyses in NWA 12919 yield a discordia lower intercept age of 188 ± 11 Ma (95% confidence) and an upper intercept $^{207}\text{Pb}/^{206}\text{Pb}$ of 0.844 ± 0.027 (95% confidence; MSWD=1.5; Fig. 3.3c). Using the upper intercept $^{207}\text{Pb}/^{206}\text{Pb}$ ratio, the ^{207}Pb -corrected dates yield a weighted mean age of 187 ± 11 Ma (MSWD=1.2).

With the exception of NWA 10299_23, all U–Pb analyses in NWA 10299 and NWA 12919 are Group 3 grains, attributable to the prevalence of the microstructural group in these two samples. Although larger grains were preferentially selected over smaller grains for SIMS analysis so to reduce beam overlap with non-baddeleyite phases, we observe no link between grain size and microstructural grouping. In JaH 479, Group 1 ($n=2$) and Group 2 ($n=3$) are represented in U–Pb analyses alongside Group 3 ($n=9$), in addition to one mixed group grain.

Of the three examined shergottites, analyses in NWA 10299 span a narrower range of $^{207}\text{Pb}/^{206}\text{Pb}$ compositions (0.0528–0.4436) compared to JaH 479 (0.1001–0.7704) and NWA 12919 (0.1607–0.7319). This is attributed to the generally larger size of target grains in NWA 10299 which resulted in lower contribution of common Pb from surrounding phases. The contribution of non-radiogenic Pb by surrounding phases is confirmed by measurement of smaller grains ($<5\text{ }\mu\text{m}$), which typically yield less radiogenic uncorrected $^{207}\text{Pb}/^{206}\text{Pb}$ ratios than larger grains. The large size of the analysis spots relative to most of the baddeleyite targets also introduced analytical scatter in measured $^{238}\text{U}/^{206}\text{Pb}$ ratios through overlapping with surrounding non-baddeleyite phases, causing Pb/U ratio to shift from that of pure baddeleyite against which the unknowns are calibrated. Additional analytical scatter is attributed to the orientation effect, a well-known phenomenon in baddeleyite ([Wingate and Compston, 2000](#)). Similar to results reported in [Staddon et al. \(2021b\)](#), some of the baddeleyite standard analyses in this study yielded slightly reverse discordant U–Pb compositions (Appendix 2). As irregular topography and non-baddeleyite phases are ruled out in the standard analyses, we attribute this observation to analytical scatter caused by localized orientation effects which were suppressed by the oxygen flooding technique but not entirely

eliminated. Matrix mismatch between the crystalline standards and the poorly crystalline unknowns may be an additional source of analytical scatter; however, Staddon et al. (2021b) argued that it is less significant than localized orientation effects supported by results of repeated analyses of Zagami (Zhou et al., 2013). Significant scatter is observed in a cluster of analyses in NWA 10299 that have radiogenic $^{207}\text{Pb}/^{206}\text{Pb}$ compositions (<0.2), with paired analyses not within uncertainties of each other despite being measured on the same grain (54A-1 and 54A-2, 75-1 and 75-2, 79-1 and 79-2; Fig. 3.3b). In addition to the sources of analytical scatter described above, we attribute the scatter in these analyses to topography effects caused by the larger-than-intended spot sizes when performing two closely adjacent analyses. Instead of two separate pits, post-SIMS images showed one large pit indicating that the second analysis in the sequence largely overlapped the pit left by the first analysis, causing shifts in Pb/U relative sensitivity and resulting in scatter in measured $^{238}\text{U}/^{206}\text{Pb}$ ratios. As all three pairs of analyses were performed in a right-to-left sequence (relative to the optical field of view of the SIMS instrument), consistently higher $^{238}\text{U}/^{206}\text{Pb}$ in the second analyses relative to the first further supports topography effect as the main cause of the systematic scatter in these analyses in Tera-Wasserburg space. We note that this also results in the second analyses having younger ^{207}Pb -corrected ages than the first. The topographic effect is also observed in analysis 74, where the analysis spot overlapped a large fracture adjacent to the baddeleyite grain, causing the measured U–Pb isotopic composition to plot to the left of discordia and out of uncertainty with the rest of the analyses.

3.7 Discussion

3.7.1 Baddeleyite microstructure and shock history

The baddeleyite microstructures observed in this study reflect the response to varying dynamics in shock processes. The relatively good crystallinity and preserved magmatic orientations in Group 1 grains (Fig. 3.5b) indicate minimal shock modification and limited shock pressures of <3.3 GPa (Takagi et al., 2020). With increasing shock pressure, the occurrence of orthogonally related domains in Group 2 grains

indicates localized phase transformation to high-pressure polymorphs and subsequent reversion to *m*-ZrO₂ (Fig. 3.5e). More complete transformation to high-pressure polymorphs is shown by widespread degraded crystallinity in Group 3 grains (Fig. 3.5d). Although there is a greater extent of transformation, nucleation of reverted *m*-ZrO₂ domains was limited by low post-shock temperature gradients, resulting in nm-scale crystallographic ordering that diffracts below the length scales of EBSD measurements employed in this study (30–80 nm; Table 3.1). If the post-shock heating is sufficient, reverted *m*-ZrO₂ nucleates into μ m-scale domains large enough to be detected in EBSD, with well-defined orthogonal ORs in pole diagrams (Group 4; Fig. 3.5f). The four-group classification therefore represents a continuum of at least two varying conditions. Group 2 and Group 4 grains share similar post-shock temperature gradients for the formation of μ m-scale reverted *m*-ZrO₂ domains, but the former undergoes only partial phase transformation. Both Group 3 and Group 4 grains have undergone whole-grain phase transformation and reversion but differ in post-shock temperature history. Therefore, baddeleyite microstructure is determined by the combination of 1) the degree of homogeneity of shock distribution throughout the grain and 2) the post-shock temperature gradient (Fig. 3.5).

The distribution of baddeleyite microstructures in JaH 479, NWA 10299, and NWA 12919 likely reflects different shock conditions during ejection from Mars. The prevalence of Group 3 microstructures in NWA 10299 and NWA 12919 indicates widespread high-pressure phase transformations, with peak shock pressures of at least 3.3 GPa ([Takagi et al., 2020](#)). This is consistent with bulk shock pressure estimates for NWA 10299 (45–55 GPa) and NWA 12919 (24–45 GPa) based on transformations of plagioclase ([Sheen et al., 2021](#)). However, nucleation of reverted *m*-ZrO₂ was suppressed by the short duration and/or insufficient magnitude of post-shock heating and cooling, resulting in crystallographic ordering mostly on the nanometer scale— below the EBSD length scales employed in this study (30–80 nm).

In contrast to NWA 10299 and NWA 12919, JaH 479 exhibits larger proportions of Group 1 and Group 2 microstructures. Preserved magmatic orientations and twinning in Group 1 and Group 2 grains point to local peak shock pressures of <3.3 GPa. Micron-scale domains with orthogonal ORs in Group 2 grains reflect more protracted post-shock heating and cooling which favored greater nucleation of reverted m -ZrO₂. Nevertheless, Group 3 microstructure still constitutes 13 out of 24 of the examined grains in JaH 479, suggesting a larger variation in local shock pressures and temperatures compared to NWA 10299 and NWA 12919. This heterogeneity is also evidenced in closely neighboring grains in JaH 479 that exhibit different microstructure groups.

Group 4 microstructure is observed only in parts of two mixed group grains, indicating that post-shock heating was limited. [Staddon et al. \(2021b\)](#) reported two Group 4 grains out of 31 grains analyzed in three shergottites; both grains were observed in NWA 8679. The relative rarity of Group 4 microstructure in shergottites examined in this study and in [Staddon et al. \(2021b\)](#) therefore suggests that the temperature history of these moderately shocked shergottites generally does not favor extensive nucleation of reverted m -ZrO₂.

Our observations further illustrate that the microstructural groups do not represent a simple linear scale of increasing degree of shock metamorphism, but reflect local changes in pressure and temperature over time (Fig. 3.5; [Staddon et al., 2021b](#)). JaH 479 and NWA 12919 both have estimated bulk shock pressure of 24–45 GPa constrained by the transformation of plagioclase to maskelynite. However, a greater preservation of magmatic domains in JaH 479 suggests a lower bulk shock pressure relative to NWA 12919. A larger number of grains showing reverted m -ZrO₂ domains in JaH 479 (Group 2 and mixed group grains) also indicate greater heterogeneity in local temperatures compared to the Group 3-dominated NWA 12919. Reviewing shock metamorphism in chondrites and mafic meteorites, [Hu and Sharp \(2022\)](#) suggest that low temperature and moderate shock pressure, as opposed to high shock pressure, are required to create large temperature heterogeneities in the bulk rock. This is in agreement

with the preservation of weak anisotropy in some plagioclase grains in JaH 479 ([Lorenz et al., 2010](#)), suggesting that JaH 479 is less shocked than NWA 12919.

The difference between plagioclase transformation to maskelynite in NWA 12919 and melting into a vesiculated glass in NWA 10299 does not appear to influence the prevalence of Group 3 microstructure in both shergottites, suggesting a more uniform, shorter thermal history at higher bulk shock pressures relative to JaH 479. We note that the formation of zircon rims on baddeleyite, observed in NWA 5298 ([Darling et al., 2016](#)), is absent from the three shergottites examined in this study and from those in [Staddon et al. \(2021b\)](#). As excess thermal energy is required to drive the reaction between baddeleyite and adjacent siliceous phases to produce zircon, the absence of zircon rims suggests that post-shock heating experienced by these shergottites was less intense than that of NWA 5298.

Crystal-plastic deformation provides additional insight into the timing and dynamics of shock conditions. Magmatic domains in Group 2 grains generally exhibit greater CPD (up to 25°) than that in Group 1 grains (<20°). In Group 2 grains, CPD of the magmatic domains is also greater than in the reverted domains, consistent with observations by [Staddon et al. \(2021b\)](#). Complex deformation is evidenced in a few Group 2 grains where the magmatic domain exhibits CPD along two distinct orientations. These observations suggest that CPD in magmatic domains scales with local peak shock conditions. The less extensive CPD in the reverted domains suggests that deformation processes had decreased in magnitude at the time of the nucleation of *m*-ZrO₂.

3.7.2 Baddeleyite petrography and shock response

Previous work found some degree of petrographic control on baddeleyite microstructures in the highly shocked NWA 5298, where the preservation of magmatic orientations in Group 1 grains is linked to phases of relatively high shock impedance (clinopyroxene, three-phase symplectite, titanomagnetite, and mesostasis, relative to plagioclase and Ca-phosphates; [Darling et al., 2016](#)). However, this link was not definitively observed in the shergottites examined by [Staddon et al. \(2021b\)](#). In this study, we likewise

found only limited evidence for such a relationship. Group 1 grain F458 in JaH 479 is enclosed in the center a large (~1 mm) clinopyroxene grain, which may account for the preservation of magmatic orientations. Although some other Group 1 grains are also associated with phases of relatively high shock impedance, this association is not exclusive and other microstructural groups also occur in similar settings elsewhere in the samples (Table 3.2). As petrographic characterization was carried out using sample sections, there is also uncertainty in additional phases with which a grain may be associated in the third dimension (i.e., above or below the plane of the sample surface). We again emphasize that of the three shergottites examined in this study, only JaH 479 contains enough baddeleyite microstructural diversity for petrographic links to be assessed.

Heterogeneous shock response is observed in mixed group grains and a few Group 2 grains, all of which are bound by phases with contrasting shock impedance. The mixed group grain F1/454 in NWA 12919, which is bound by clinopyroxene and apatite, shows a sharp contact between the magmatic domain (Group 1) and the reverted domain (Group 3). In grain F418 in JaH 479 (Group 2), reverted domains occur on the olivine-bound side of the grain whereas magmatic twinning is preserved on the maskelynite-bound side (Fig. 3.2b). Although shock propagation in martian meteorites is inherently highly complex ([Sharp and DeCarli, 2006](#)), we argue that baddeleyite grains with heterogeneous shock response reflect some control by contrasts in the bulk properties of surrounding phases. This is consistent with the conclusion drawn by [Darling et al. \(2016\)](#) that shock impedance of major minerals influences baddeleyite microstructural response.

3.7.3 Baddeleyite microstructures and U–Pb isotope systematics

The three new SIMS U–Pb baddeleyite discordia ages determined in this study (JaH 479: 210 ± 9 Ma, NWA 10299: 196 ± 11 Ma; NWA 12919: 188 ± 11 Ma) are in agreement with the known age range of enriched shergottites (223–157 Ma; [Udry et al., 2020](#)) determined using U–Pb and other radiogenic isotopic systems. We find no evidence of resolvable Pb loss in the baddeleyite grains analyzed this study.

The individual common Pb corrected ^{207}Pb dates are within uncertainty of the sample discordia age and the 95% confidence interval of the weighted mean common Pb corrected age. We therefore consider the U–Pb results to be robust and any Pb loss is negligible with respect to analytical uncertainties of the SIMS methods. The observed scatter in U–Pb data is attributed to analytical effects including variable Pb/U fractionation due to irregular topography, baddeleyite orientation effects, and mixed analysis due to overlap with surrounding phases, which may also contribute to variable $^{207}\text{Pb}/^{206}\text{Pb}$. As larger grains typically yield more radiogenic $^{207}\text{Pb}/^{206}\text{Pb}$ ratios, the availability of large baddeleyite grains can be crucial for constraining U–Pb igneous ages by fixing the lower intercept of the discordia regression.

Due to varying amounts of common Pb contribution from non-baddeleyite phases and, to a lesser extent, from baddeleyite itself, the U–Pb analyses define an array in Tera-Wasserburg space that represents mixing between radiogenic and non-radiogenic reservoirs. The common Pb $^{207}\text{Pb}/^{206}\text{Pb}$ ratios determined *via* discordia upper intercepts of JaH 479 (0.942 ± 0.054), NWA 10299 (0.95 ± 0.31), and NWA 12919 (0.844 ± 0.027) reflect mixed common Pb input from both martian (>0.95 for enriched shergottites; [Bellucci et al., 2015](#)) and modern terrestrial (0.836; [Stacey and Kramers, 1975](#)) reservoirs. This is in agreement with discordia upper intercept $^{207}\text{Pb}/^{206}\text{Pb}$ ratios reported for Zagami, NWA 7257, NWA 8679, and NWA 8653 ([Zhou et al., 2013](#); [Staddon et al., 2021b](#); [Wu et al., 2021](#)) and with Pb isotopic compositions of major igneous minerals in enriched shergottites ([Moser et al., 2013](#); [Bellucci et al., 2015](#); [Staddon et al., 2021b](#)). The upper intercept $^{207}\text{Pb}/^{206}\text{Pb}$ ratio of NWA 12919 is lower than that of JaH 479 and is within uncertainty of the modern terrestrial common Pb composition of 0.836, suggesting greater input from terrestrial weathering and alteration. Shock features such as fractures, shock melt veins, and shock melt pockets act as pathways for terrestrial weathering and alteration in hot desert environments ([Crozaz and Wadhwa, 2001](#); [Crozaz et al., 2003](#)). However, NWA 12919 and JaH 479 do not significantly differ in the distribution of such shock features or in the proportion of SIMS analyses that overlapped shock fractures (shock melt having been explicitly avoided during selection of baddeleyite targets). We

attribute the difference in upper intercept $^{207}\text{Pb}/^{206}\text{Pb}$ ratio between the two shergottites to possible differences in terrestrial history and/or uneven distribution of terrestrial components within the bulk specimens. This may be supported by the large difference in mass—and thus surface area to volume ratio—between JaH 479 (553 g) and NWA 12919 (7.5 g) ([Meteoritical Bulletin Database](#)). Although the common Pb $^{207}\text{Pb}/^{206}\text{Pb}$ ratio of NWA 10299 is consistent with the other two shergottites, large uncertainty precludes comparison of terrestrial vs martian common Pb input.

Our examination of JaH 479, NWA 10299, and NWA 12919 suggests no link between baddeleyite microstructures and U–Pb isotope systematics. The absence of resolvable open-system U–Pb behavior in baddeleyite provides relative constraint on the thermal history of the three shergottites. Uranium-lead age-resetting observed in NWA 5298 reflects more intensive and/or protracted post-shock heating compared to conditions inferred for the shergottites examined in this study. Microstructural measurements have been performed on a handful of shergottites ([Moser et al., 2013; Darling et al., 2016; Cox et al., 2018; Kizovski et al., 2020; Staddon et al., 2020, 2021a, 2021b](#)), however the formation of zircon rims is thus far unique to NWA 5298 and indicates extra thermal energy input required to drive the reaction between baddeleyite and silica-bearing melt or fluid ([Darling et al., 2016; Herd et al., 2018a](#)). The importance of the duration of post-shock heating is further demonstrated by defect-controlled age-resetting in protolith baddeleyite in the Sudbury impact structure, which reflects protracted heating from the impact melt sheet and from subsequent tectonic metamorphism ([White et al., 2017, 2018](#)), on timescales (kyr to Myr) significantly greater than those experienced by shergottites during ejection (ms to s; e.g., [Baziotis et al., 2013; Greshake et al., 2013; Min et al., 2017](#)). The lack of resolvable U–Pb disturbance in baddeleyite in JaH 479, NWA 10299, and NWA 12919 is therefore consistent with the prevalence of Group 3 microstructure, indicating lower temperatures and/or shorter durations of post-shock heating (relative to NWA 5298) that was insufficient to introduce significant Pb volume diffusion. The observation of Group 3 microstructure in grains associated with shock melt pockets in NWA 12919

(Table 3.2) likewise demonstrates that the formation of these shock melt pockets involved less energy than those associated with granular baddeleyite in NWA 5298. As no Group 4 grains were observed in this study, it remains to be tested whether or not U–Pb isotope systematics remain robust under locally prolonged heating that enables development of μm -scale domains of reverted $m\text{-ZrO}_2$.

The lack of resolvable U–Pb isotopic disturbance in JaH 479, NWA 10299, and NWA 12919 is similar to findings in NWA 7257, NWA 8679, and Zagami ([Staddon et al., 2021b](#)). In addition, a 188 ± 8 Ma U–Pb baddeleyite age has been reported for the enriched shergottite NWA 8653, in which granular or zircon-rimmed baddeleyite are also not reported based on only BSE imaging ([Wu et al., 2021](#)). The prevalence of robust baddeleyite U–Pb isotope systematics in shergottites that have been dated by SIMS methods suggests that baddeleyite Pb loss induced by shock metamorphism may be restricted to shergottites such as NWA 5298 where prolonged post-shock heating resulted in the formation of granular and zircon-rimmed baddeleyite. Results from our study further affirm the use of baddeleyite as a robust U–Pb chronometer in shergottites for determining igneous crystallization ages.

Difference in the timescale associated with shock metamorphism also accounts for the discrepancy between baddeleyite experimental constraints and shergottite studies. [Niihara et al. \(2012\)](#) found baddeleyite to be resistant to large-scale disturbance in U–Pb isotope systematics at shock loading pressures up to 57 GPa followed by annealing at temperatures up to 1300°C . However the duration of high shock condition (>1 GPa; dwell time) in experiments is typically under microseconds, orders of magnitude less than the millisecond-scale dwell times estimated for shergottite ejection events (e.g., [Beck et al., 2005](#); [Sharp et al., 2019](#); [Bowling et al., 2020](#); cf. [Deutsch and Schärer, 1990](#)). Therefore, evaluating baddeleyite microstructures based on quantitative estimates of shock conditions should ideally consider the factor of time in conjunction with pressure and temperature (i.e., P-T-t paths).

3.7.4 Implications for shergottite magmatism and ejection

The three new shergottite igneous crystallization ages determined in this study— 210 ± 9 Ma (JaH 479), 196 ± 11 Ma (NWA 10299), and 188 ± 11 Ma (NWA 12919)—fall in the 223–157 Ma age range of enriched shergottites. The 210 ± 9 Ma age of JaH 479 places it on the older end of the enriched shergottite age range alongside NWA 8679 (220 ± 23 Ma; [Staddon et al., 2021b](#)) and NWA 7755 (223 ± 46 Ma; [O’Neal et al., 2022](#)), which are both within uncertainty of the JaH 479 age. When compared to the igneous age range of intermediate (716–170 Ma; [Shih et al., 2011](#); [Righter et al., 2018](#)) and depleted shergottites (582–234 Ma; [Schulz et al., 2020](#); [Debaille et al., 2022](#)), enriched shergottites are more tightly clustered towards the younger end of the overall shergottite age spectrum. As the geochemical grouping of shergottites reflects the incompatible trace element (ITE) and isotopic compositions of the mantle sources from which shergottite magmas were derived, the differences in age range suggest distinct periods of magmatism associated with each mantle reservoir as sampled by the shergottite record (e.g., [Lapen et al., 2017](#)).

There remains a general paucity of constraints on the spatial relationship among shergottites prior to ejection. There is broad consensus that nakhlites and chassignites were ejected in a single impact event based on similarities in igneous age, ejection age, and chemical and isotopic compositions (e.g., [Nyquist et al., 2001](#); [Treiman, 2005](#); [Cohen et al., 2017](#); [Udry and Day, 2018](#)). In contrast, shergottites exhibit much greater diversity in these attributes that cannot be adequately reconciled in a single-event interpretation (cf., [Werner et al., 2014](#)). Cosmic-ray exposure (CRE) ages have been used to identify possible launch events for multiple shergottites, with estimates ranging from two to twenty ejection events depending on the inclusion of additional criteria ([Nyquist et al., 2001](#); [Herzog and Caffee, 2014](#); [Irving et al., 2017](#); [Lapen et al., 2017](#); [Krietsch, 2020](#); [Udry et al., 2020](#)). Of the three shergottites examined in this study, only JaH 479 has been previously analyzed for noble gases, yielding a mean CRE age of 2.1 ± 0.4 Ma (2σ ; [Cartwright et al., 2010](#)). Enriched shergottites that share a similar CRE age with JaH 479 include Dho 378 (2.1 ± 1.0 Ma; Sm–Nd age 157 ± 24 Ma; [Nyquist et al., 2006](#); [Park et al., 2008](#)), NWA 856 (2.1 ± 0.8 Ma; weighted mean of Rb–Sr, Sm–Nd, and U–Pb baddeleyite ages 182 ± 10 Ma; [Mathew et al., 2003](#); [Brandon et al., 2004](#); [Misawa](#)

and Yamaguchi, 2007; Bereznov et al., 2010; Ferdous et al., 2017), NWA 1068 (2.0 ± 0.7 Ma; Sm–Nd age 182 ± 11 Ma; Mathew et al., 2003; Shih et al., 2003; Nishiizumi et al., 2004), and NWA 7257 (2.8 ± 0.6 Ma; U–Pb baddeleyite age 195 ± 15 Ma; Wieler et al., 2016; Staddon et al., 2021b). We note that the 210 ± 9 Ma age of JaH 479 is within uncertainty of NWA 7257, but older than the other three shergottites. If only igneous and CRE ages are considered, a single event launching these five shergottites would suggest magmatism at the same location spanning at least ~ 53 Myr. Due to large uncertainties typically associated with CRE ages and possible complexities in pre-ejection geological relationships (e.g., Combs et al., 2019; Rahib et al., 2019; Krietsch, 2020), this interpretation remains speculative and further consideration should examine ITE and isotopic compositions in combination with age data to evaluate any possible petrogenetic links (e.g., Lapen et al., 2017; Rahib et al., 2019). Constraining the number of martian meteorite ejection events remains an active field of study and there is ongoing research aiming to link numerical modeling of impact cratering, crater counting surface ages, and surface spectroscopic signatures with martian meteorite ages, compositions, and petrological constraints on impact shock conditions to arrive at identifying the source craters of martian meteorites (e.g., Tornabene et al., 2006; Herd et al., 2018b; Hamilton et al., 2020; Lagain et al., 2021; 2022).

3.7.5 Implications for Mars sample return missions

Together with previous *in-situ* geochronology studies of shergottites (e.g., Misawa and Yamaguchi, 2007; Niihara, 2011; Jiang and Hsu, 2012; Moser et al., 2013; Zhou et al., 2013; Darling et al., 2021; Staddon et al., 2021; Wu et al., 2021; Lindner et al., 2022; McFarlane and Spray, 2022), results from our study provide guidelines for future research investigating the ages of martian samples. Compared to mineral separation methods, *in-situ* U–Pb measurements favor sample preservation and may therefore be more suitable for geochronology of low-volume specimens provided that suitable targets (e.g., baddeleyite, zircon; see also Lindner et al., 2022) are present. As igneous crystallization ages have been determined for only 40% of shergottites to date (49 out of 145; as of May 2022 and excluding paired

stones; compilation by A. J. Irving, URL: <https://imca.cc/mars/martian-meteorites-list.htm>), an increased number of analyses would refine the resolution of the age record and provide additional constraints on the ages of shergottites.

The advantages of *in-situ* dating have further application in developing analytical methods for future returned samples from Mars, which require more stringent preservation protocols than meteorite specimens (MEPAG E2E-iSAG, 2011). Given the long residence time of surficial lithologies on Mars, baddeleyite is more resistant than major igneous minerals to weathering and alteration at the martian surface which can introduce contamination and cause open-system isotopic behavior on the whole-rock scale (e.g., Borg et al., 1997, 2005; Bellucci et al., 2016). Furthermore, as surficial lithologies on Mars record protracted cratering histories due to the absence of crustal recycling (e.g., Park et al., 2008; Walton et al., 2008; McCubbin et al., 2016), the combination of SIMS U–Pb geochronology with EBSD microstructural analysis would enable the evaluation of near-surface shock metamorphism and the associated impact events. The presence of baddeleyite and zircon in ~4.5–4.3 Ga igneous clasts in the martian regolith breccia (NWA 7034 and pairs) suggests that they may be common in ancient crustal materials that cover most of Mars (McCubbin et al., 2016; Goodwin et al., 2022). Radiometric geochronology of returned Mars samples, guided by microstructural shock constraints, will allow an absolute time scale to be established for the martian surface independent of cratering chronology and against which cratering chronology may be calibrated. A field-based geologic time scale of Mars will not only aid in constraining the evolution of the planet’s surface and interior, but also determining the source locations of martian meteorites (e.g., Returned Sample Science Board, 2017; Beatty et al., 2019; Udry et al., 2020).

3.8 Conclusions

Our study investigated the baddeleyite microstructures and U–Pb geochronology of the enriched shergottites JaH 479, NWA 10299, and NWA 12919. EBSD analyses reveal widespread microstructural

evidence for phase transformation to high-pressure zirconia polymorphs, followed by reversion to $m\text{-ZrO}_2$ under varying post-shock temperature conditions. Such microstructures are particularly prevalent in NWA 10299 and NWA 12919 (Group 3), whereas JaH 479 contains a higher proportion of grains that preserve magmatic orientations and twinning (Groups 1 and 2), potentially suggesting a lower bulk shock pressure than the former two samples. Inhibited nucleation of reverted $m\text{-ZrO}_2$ in NWA 10299 and NWA 12919 contrasts with numerous μm -scale reverted $m\text{-ZrO}_2$ domains in JaH 479 grains (Groups 2), pointing to larger heterogeneity in post-shock temperatures in JaH 479. This would be consistent with a more moderate bulk shock pressure, lower than that experienced by NWA 10299 and NWA 12919. There is no systematic control by the petrographic setting of baddeleyite on the grain-to-grain variation in microstructural response, however micron-scale heterogeneous shock response within individual baddeleyite grains appears to be controlled by shock impedance contrast among the adjacent phases.

SIMS U–Pb baddeleyite analysis yields igneous crystallization ages of 210 ± 9 Ma (JaH 479), 196 ± 11 Ma (NWA 10299), and 188 ± 11 Ma (NWA 12919), all within the range defined by known enriched shergottite ages (223–157 Ma). We found no evidence for resolvable Pb loss in the analyzed baddeleyite grains, consistent with observations in NWA 7257, NWA 8679, and Zagami ([Staddon et al., 2021b](#)) but in contrast with NWA 5298 ([Darling et al., 2016](#)). The observed scatter in U–Pb data is attributed to crystal orientation effects, topographic effects, and overlap with neighbouring phases. Despite this, a concordant analysis was measured in a large grain in NWA 10299, highlighting the importance of baddeleyite grain size for statistically robust (i.e. resistant to errors arising from non-ideal conditions) SIMS U–Pb geochronology. Our results yield no definitive link between baddeleyite shock response and U–Pb isotope systematics in microstructural groups 1–3, indicating that post-shock heating was insufficient in magnitude and/or duration to introduce significant volume diffusion of Pb, unlike that observed in highly shocked grains in NWA 5298. Although the relationship between Group 4 microstructure and U–Pb isotope systematics remains to be tested, the results from our study agree with previous findings in NWA

7257, NWA 8679, and Zagami by [Staddon et al. \(2021b\)](#). The collective suite of six shergottites in these two studies exhibits typical bulk shock features of most shergottites (e.g., fracturing of silicates, phosphates, and oxides, mosaicism of pyroxene, plagioclase transformation to maskelynite, shock melt veins and pockets) and does not contain granular or zircon-rimmed baddeleyite that are distinct in NWA 5298. As such, we argue that shock conditions required for causing resolvable U–Pb mobility in baddeleyite were not attained by the majority of shergottites. Results from our study place additional constraints on baddeleyite microstructural response under shock conditions experienced by shergottites and further demonstrate that baddeleyite U–Pb isotope systematics are a robust tool for constraining shergottite igneous crystallization ages. This technique therefore has an important potential application for chronological investigation of future returned samples from Mars.

Table 3.1. Instrument parameters for EBSD baddeleyite microstructure analysis.

<i>Instrumentation</i>	
SEM Model	Zeiss EVO MA10 LaB ₆
EBSD detector	Oxford Instruments Symmetry S2 EBSD detector
EBSD software	Oxford Instruments AZtecCrystal, AZtecHKL Channel 5
<i>SEM set up</i>	
Coating	None
Accelerating voltage	20 kV
Beam current	1.5-2 nA
Tilt	70°
Working distance	~14 mm
<i>EBSD data collection and reduction</i>	
Step size	30-80 nm
Hough resolution	60-70
Collection time per frame	<120 ms
Background	100 frames
EBSP exposure (frame time)	<2 ms
EBSP frame averaging	8-10×
Kikuchi band detection min/mas	8
Baddeleyite match unit	Kudoh et al. (1986)
Raw data noise correction	Wild spike, noise-reduction (level 8), mis-indexing

Table 3.2. Baddeleyite microstructures determined by EBSD analysis, with petrographic associations.

Grain ID	Microstructure Group	Petrographic Group*	Adjacent Phases**	% $m\text{-ZrO}_2$ Indexed	Maximum CPD (°)
JaH 479					
F3	3	A	cpx, tmt	10	20
F38	2	A	cpx, gls	70	20
F85	3	B	mes, px	0	n/a
F92	2	C	tmt, ksp+sil	90	<30
F93	2	B	ol, gls, msk	90	20
F117	1	other	msk	70	15-18
F129	mixed (3+2)	A	msk, tmt	20	<25
F166	mixed (3+4)	B	ol, gls	25	<10
F212	3	A	FeS, mer, cpx, tmt	20	<40
F298	2	other	sym, msk	40	<20
F303	2	B	ol, cpx	50	15-20
F333	3	C	tmt, cpx	10	10
F348	3	B	cpx, ol	2	n/a
F355	3	B	ol, apt	0	n/a
F418-L	3	B	ol, msk	5	n/a
F418-R	2	B	msk, ol	70	<20
F458	1	other	cpx	70	<20
F600A	3	B	sym, msk	5	20
F600B	3	B	ol, msk	0	n/a
F629A-L	2	B	ol, ksp+sil	50	<25
F629A-R	3	B	mer, ol, ksp+sil	0	n/a
F682	3	C	tmt, gls	10	n/a
Grain A	3	C	tmt, gls	10	12
Grain B	3	B	ol, gls	0	n/a
NWA 10299					
Bdy001	3	C	tmt, gls	0	n/a
Bdy017	3	A	cpx, plg	5	12
Bdy018	1	C	tmt, cpx	60	12
Bdy021	3	C	tmt, cpx	5	n/a
Bdy023	mixed (3+4)	other	cpx, plg	30	<20
Bdy033	3	A	tmt, plg	5	<10
Bdy041	3	A	cpx, mes	2	<10
Bdy052a	3	C	cpx, plg	2	5
Bdy052b	3	C	cpx, plg	0	n/a
Bdy053	3	C	tmt, cpx	20	22
Bdy054A	3	C	tmt, ksp+sil	0	n/a
Bdy054B	3	C	tmt	0	n/a
Bdy055	3	C	tmt	2	<5
Bdy062	3	C	tmt, plg	40	<18

Table 3.2.(continued) Baddeleyite microstructures determined by EBSD analysis, with petrographic associations.

Grain ID	Microstructure Group	Petrographic Group*	Adjacent Phases**	% <i>m</i> -ZrO ₂ Indexed	Maximum CPD (°)
Bdy063	3	A	tmt, gls	0	n/a
Bdy071	3	C	tmt, gls, cpx	2	10
Bdy074	3	other	cpx, plg	20	<10
Bdy075	3	C	tmt, cpx	25	<15
Bdy079	3	A	cpx	10	<22
NWA 12919					
F1/105	3	A	cpx, tmt, apt	0	n/a
F1/117	3	A	tmt, apt, cpx, ksp+sil	0	n/a
F1/163	3	A	cpx, tmt	0	n/a
F1/170	3	C	ilm	0	n/a
F1/182	1	C	tmt, FeS, msk	70	12
F1/192	3	other	melt	0	n/a
F1/205	3	C	ksp+sil, tmt	0	n/a
F1/251	3	other	msk, cpx	5	<10
F1/325	3	D	mes	0	n/a
F1/326	3	D	mes	0	n/a
F1/375	3	D	melt	2	n/a
F1/435	3	A	cpx, mer	0	n/a
F1/454	mixed (3+1)	A	apt, cpx	40	10
F1/482A	3	C	tmt, ksp+sil	0	n/a
F1/484	3	A	cpx, ilm, FeS	5	<20
F1/525	3	C	tmt, ilm, ksp+sil	5	<14
F1/526	3	C	tmt, ksp+sil	20	<10
F2/13	3	C	FeS, tmt	2	<5
F2/19	3	other	cpx, ksp+sil	0	n/a
F2/45-L	3	C	ilm, cpx	0	n/a
F2/45-R	3	C	ilm, cpx	0	n/a
F2/77	3	C	tmt, gls, cpx	1	n/a
F2/97	3	C	tmt, cpx	0	n/a
F2/112	3	C	tmt, cpx	0	n/a
F2/143	3	A	ol, apt	1	<10
F2/158	3	C	tmt, ksp+sil	0	n/a
F2/166	3	D	mes	1	n/a

* Petrographic groups follow those reported in [Sheen et al. \(2021\)](#); A: polymineralic late-stage pockets, B: olivine-bearing coarse mesostasis, C: Fe-Ti oxides, D: glassy mesostasis.

** Cpx: clinopyroxene. Tmt: titanomagnetite. Gl: glass. Mes: glassy mesostasis. Ksp+sil: K-feldspar+silica intergrowth. Ol: olivine. Msk: maskelynite. FeS: Fe-sulfide. Mer: merrillite. Sym: three-phase symplectite. Apt: apatite. Plg: plagioclase glass (NWA 10299 only). Ilm: ilmenite.

Table 3.3. Distribution of baddeleyite microstructural groups in the studied samples.

Sample	n	Group 1	Group 2	Group 3	Mixed
JaH 479	24	2	7	13	2
NWA 10299	19	1	0	17	1
NWA 12919	27	1	0	25	1

Table 3.4. SIMS U–Pb isotopic analysis of baddeleyite in JaH 479, NWA 10299, and NWA 12919.

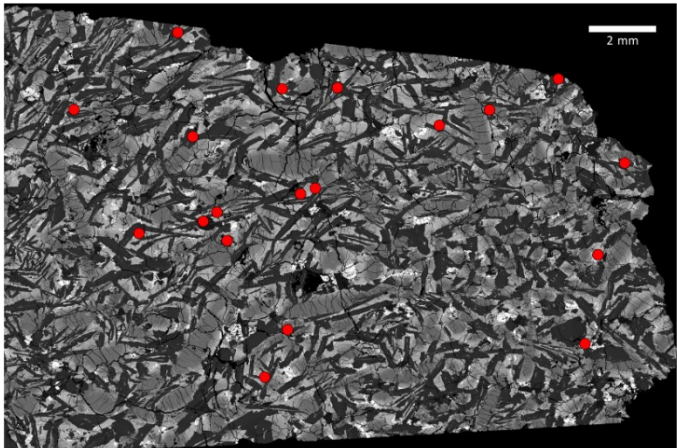
Sample	Analysis	Microstructure	$^{238}\text{U}/^{206}\text{Pb}$	2σ	$^{207}\text{Pb}/^{206}\text{Pb}$	2σ	$^{204}\text{Pb}/^{206}\text{Pb}$	2σ	^{207}Pb -corrected Age (Ma)*	2σ	$^{206}\text{Pb}_{\text{r}}\%$	UO_2/U
JaH 479	F600B	3	22.744	3.451	0.2852	0.0173	0.0279	0.0070	205	32	74	13.23
JaH 479	F600A	3	20.853	3.820	0.3612	0.0300	0.0253	0.0049	198	38	65	10.78
JaH 479	F682	3	19.992	4.511	0.3285	0.0514	0.0254	0.0054	218	52	69	9.562
JaH 479	F418-L	3	26.957	3.637	0.1445	0.0237	0.0075	0.0027	210	29	89	13.27
JaH 479	F355	3	4.471	0.823	0.7704	0.0632	0.0547	0.0119	272	130	19	13.29
JaH 479	F298	2	30.261	4.624	0.1001	0.0052	0.0043	0.0010	198	30	94	12.11
JaH 479	F303	2	11.217	2.092	0.6119	0.0385	0.0489	0.0083	209	50	37	12.52
JaH 479	F85	3	11.774	4.894	0.4377	0.0824	0.0444	0.0121	303	134	57	6.385
JaH 479	F3	3	25.438	3.126	0.1962	0.0095	0.0124	0.0022	209	26	84	14.61
JaH 479	F629A-L	2	17.748	3.932	0.3023	0.0556	0.0202	0.0051	256	60	72	7.684
JaH 479	F629A-R	3	22.960	2.345	0.2296	0.0471	0.0161	0.0046	221	27	80	10.65
JaH 479	F458	1	29.375	2.123	0.1293	0.0063	0.0068	0.0014	197	14	91	13.03
JaH 479	F212	3	17.602	1.616	0.6302	0.0403	0.0458	0.0086	127	24	35	12.79
JaH 479	F166	mixed (3 and 4)	10.581	1.319	0.6792	0.0368	0.0570	0.0110	177	42	29	10.48
JaH 479	F117	1	25.537	2.872	0.1159	0.0051	0.0053	0.0008	230	26	93	9.204
NWA 10299	1	3	32.388	1.783	0.1336	0.0189	0.0067	0.0028	178	12	91	12.81
NWA 10299	41	3	20.162	2.073	0.3554	0.0214	0.0209	0.0072	208	43	66	12.4
NWA 10299	52A	3	29.713	2.201	0.1300	0.0120	0.0062	0.0025	195	16	91	13.2
NWA 10299	53	3	32.717	4.407	0.1587	0.0120	0.0060	0.0047	171	24	88	15.42
NWA 10299	54A-1	3	33.254	1.720	0.0605	0.0039	0.0015	0.0009	189	10	99	13.56
NWA 10299	54A-2	3	34.968	1.854	0.0528	0.0032	0.0004	0.0005	181	10	100	15.84
NWA 10299	62	3	19.857	2.724	0.3976	0.0252	0.0352	0.0117	196	51	61	14.13
NWA 10299	74	3	29.059	1.169	0.0745	0.0039	0.0017	0.0007	212	9	97	12.02
NWA 10299	75-1	3	29.467	1.515	0.0944	0.0134	0.0046	0.0032	205	11	95	13.11
NWA 10299	75-2	3	34.756	3.064	0.1012	0.0185	0.0000	0.0000	173	16	94	13.19
NWA 10299	79-1	3	27.716	1.723	0.1167	0.0111	0.0029	0.0028	212	15	93	10.79
NWA 10299	79-2	3	32.446	2.558	0.1337	0.0187	0.0065	0.0048	178	16	91	11.59
NWA 10299	23	mixed (3 and 4)	23.964	2.308	0.3231	0.0714	0.0155	0.0099	185	39	70	9.239
NWA 10299	21	3	18.986	2.067	0.4436	0.0866	0.0185	0.0173	188	63	56	11.38

Table 3.4.(continued) SIMS U–Pb isotopic analysis of baddeleyite in JaH 479, NWA 10299, and NWA 12919.

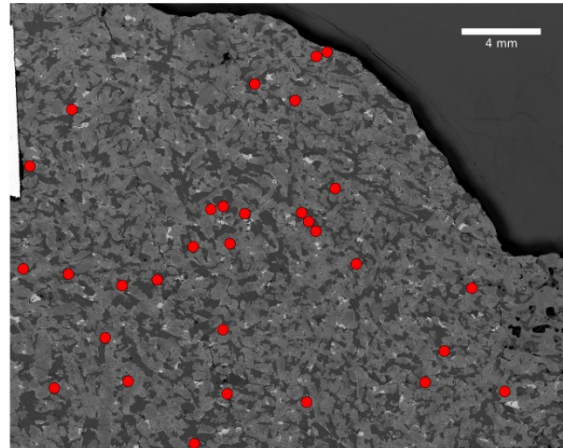
Sample	Analysis	Microstructure	$^{238}\text{U}/^{206}\text{Pb}$	2σ	$^{207}\text{Pb}/^{206}\text{Pb}$	2σ	$^{204}\text{Pb}/^{206}\text{Pb}$	2σ	^{207}Pb -corrected Age (Ma)*	2σ	$^{206}\text{Pb}_r\%$	UO_2/U
NWA 12919	F2/166	3	17.400	1.438	0.4849	0.0248	0.0301	0.0041	165	19	45	7.047
NWA 12919	F1/525	3	4.542	0.521	0.7319	0.0218	0.0473	0.0050	197	60	14	13.89
NWA 12919	F1/482A	3	8.418	1.301	0.6286	0.0310	0.0417	0.0086	205	47	27	13.39
NWA 12919	F1/484	3	16.827	1.776	0.4391	0.0502	0.0268	0.0038	192	32	51	13.5
NWA 12919	F1/251	3	20.014	2.462	0.3299	0.0682	0.0234	0.0054	205	37	65	6.255
NWA 12919	F1/205	3	23.538	3.467	0.2093	0.0487	0.0115	0.0037	215	35	80	4.21
NWA 12919	F2/45-R	3	10.307	1.176	0.6104	0.0348	0.0350	0.0051	181	37	29	13.73
NWA 12919	F2/19	3	28.950	1.989	0.1607	0.0155	0.0086	0.0022	189	14	86	8.712
NWA 12919	F1/105	3	11.005	3.883	0.5908	0.0602	0.0372	0.0070	184	79	32	10.34

* ^{207}Pb -corrected age is determined using common Pb $^{207}\text{Pb}/^{206}\text{Pb}$ ratios determined by discordia regression in Tera-Wasserburg plots (Fig. 3.3): 0.942 ± 0.054 (JaH 479), 0.95 ± 0.31 (NWA 10299), and 0.844 ± 0.027 (NWA 12919).

Jah 479



NWA 10299



NWA 12919

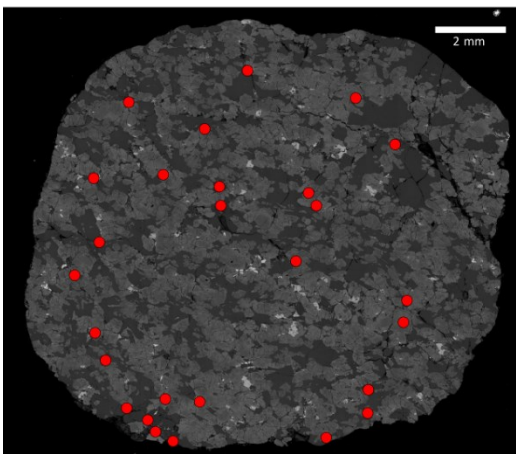


Fig. 3.1. BSE images of sample sections examined in this study, with baddeleyite targets for EBSD and SIMS analyses labeled.

a) Group 1: NWA 10299_18

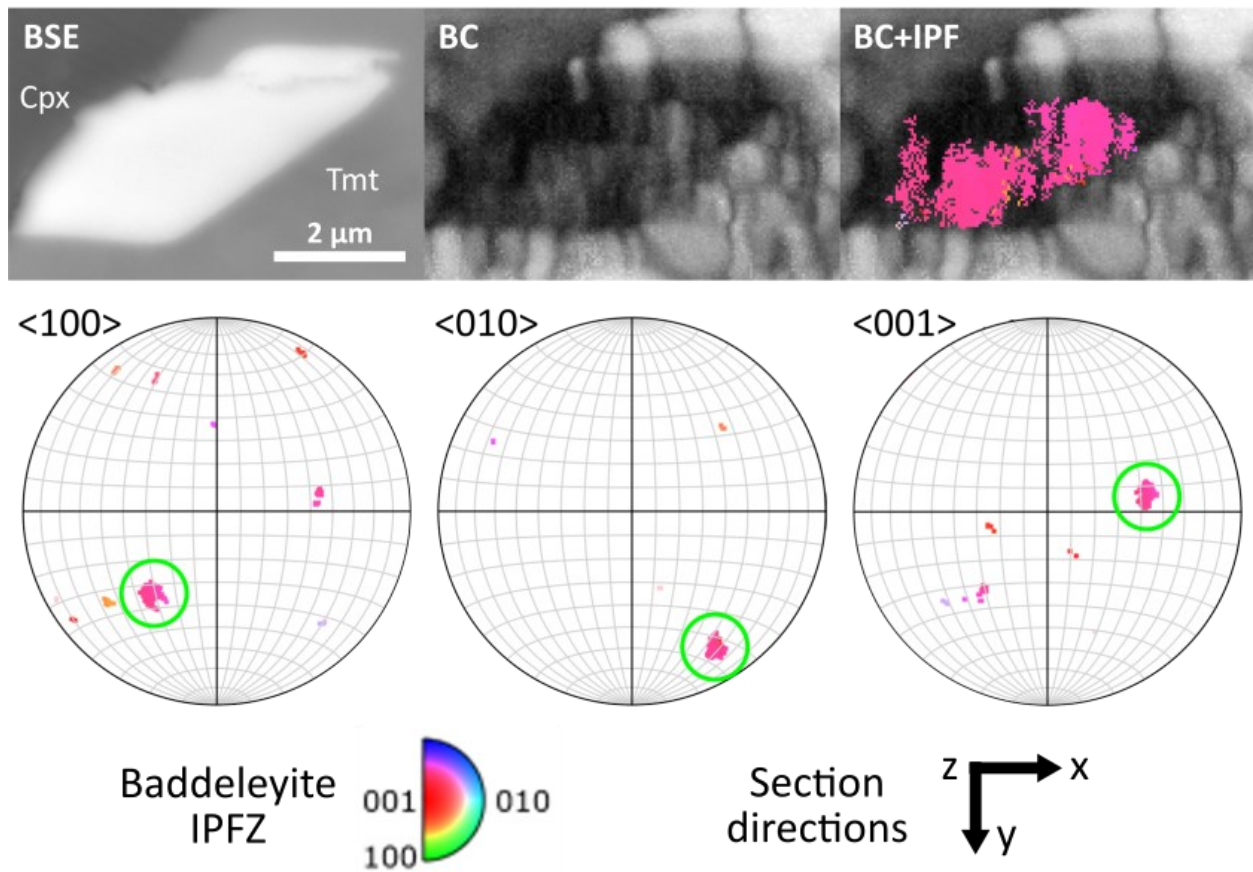


Fig. 3.2. Electron backscatter diffraction (EBSD) maps and pole figures of Group 1, 2, 3, and mixed group baddeleyite microstructures. a) Group 1 NWA 10299 grain 18, yielding degraded crystallinity and simple magmatic orientation (green circles) with crystal-plastic deformation (CPD).

b) Group 2: JaH 479_F418

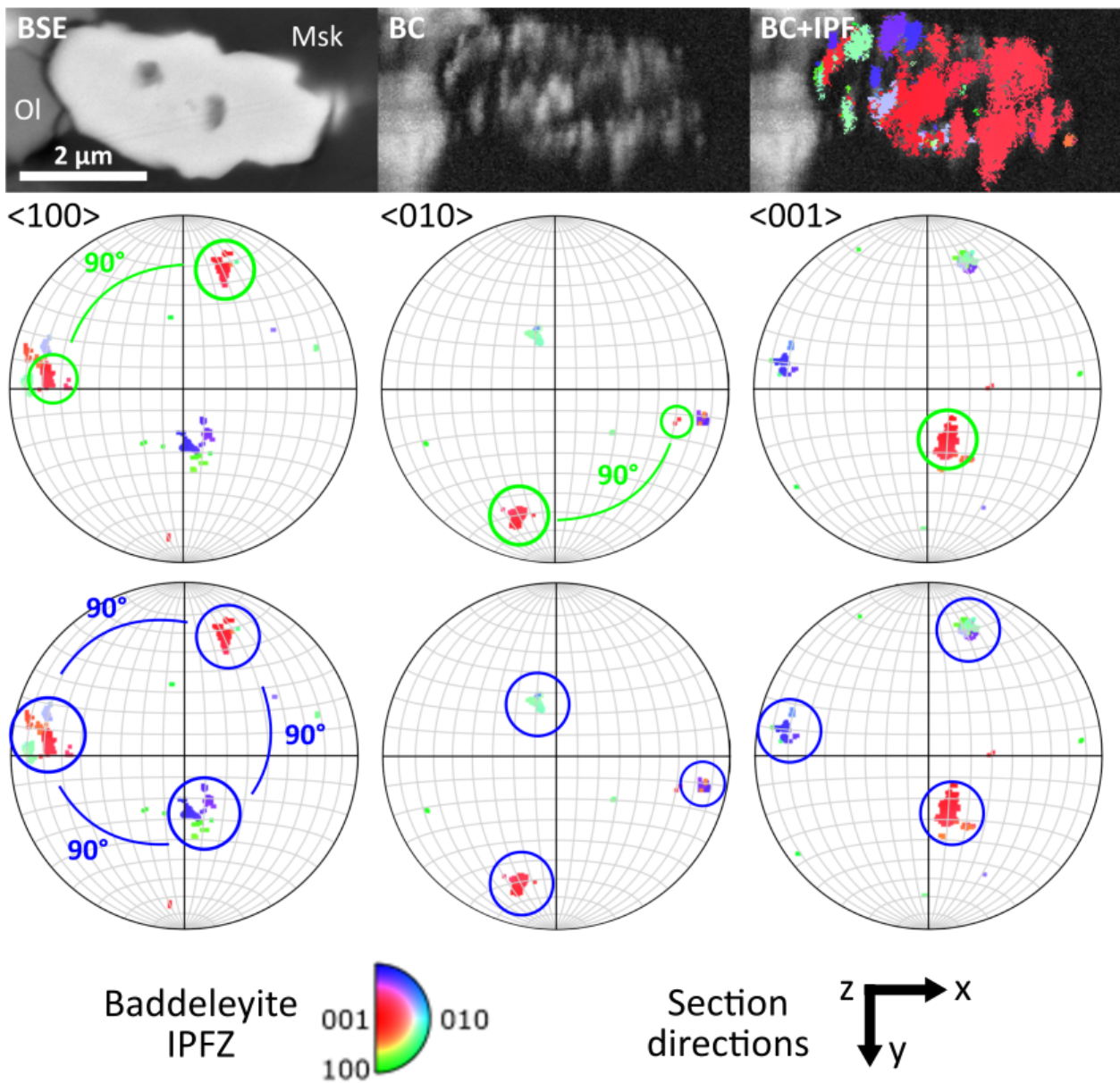
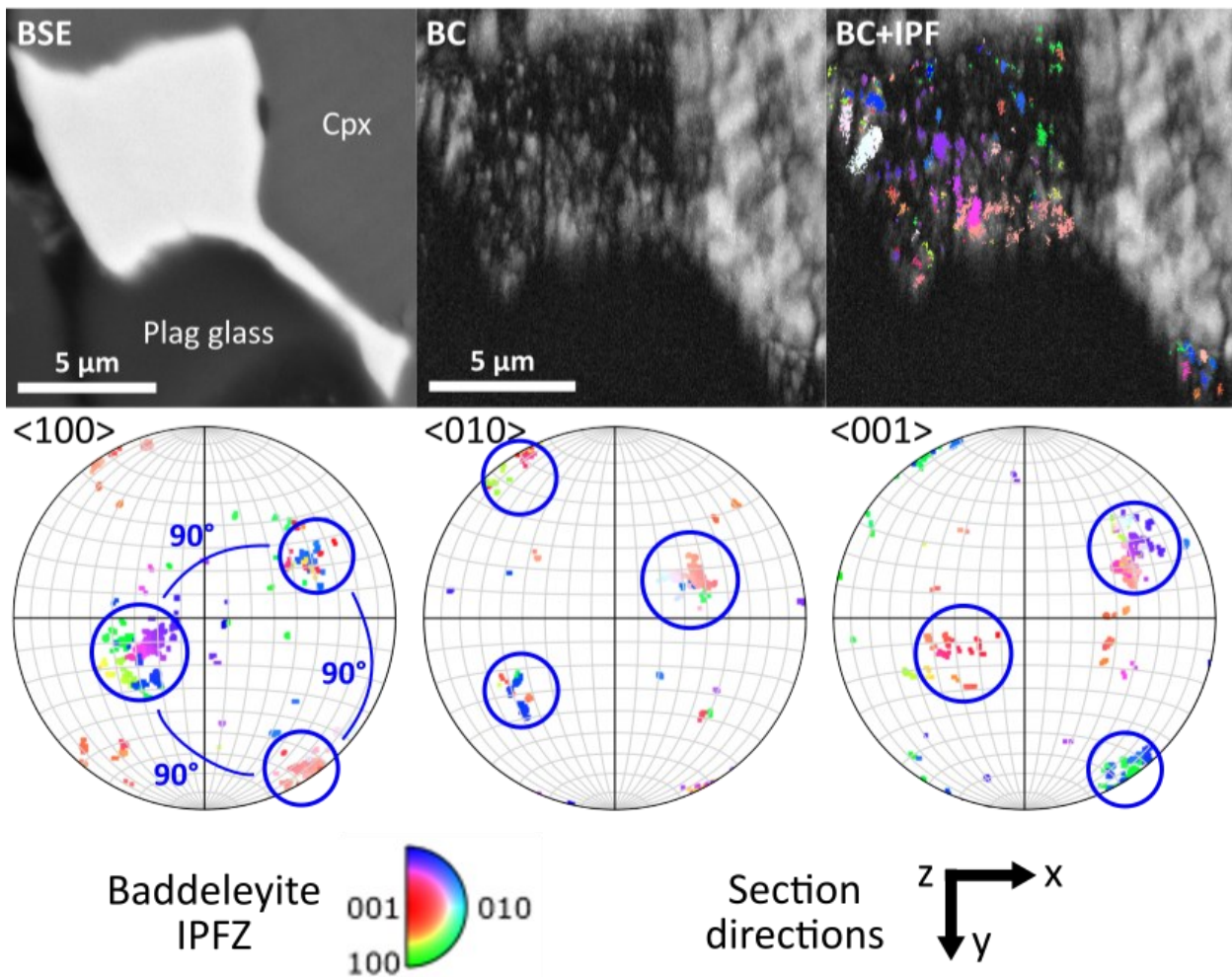


Fig. 3.2.(continued) Electron backscatter diffraction (EBSD) maps and pole figures of Group 1, 2, 3, and mixed group baddeleyite microstructures. b) Group 2 JaH 479 grain F418, showing a dominant magmatic twin domains with a common <001> and 90° rotations in <100> and <010> (180° / $<001>$ twinning; green circles). Reverted subdomains form a set of three clusters with orthogonal ORs (blue circles), indicative of reversion from $\alpha\text{-ZrO}_2$. Charging during EBSD analysis has resulted in slight in-run shift. BSE: backscatter electron image. IPF: inverse pole figure coloring, based on the orientation of the crystallographic z-axis. OI: olivine. Msk: maskelynite.

c) Group 3: NWA 10299_74



d) Group 3: NWA 10299_54A



Fig. 3.2.(continued) Electron backscatter diffraction (EBSD) maps and pole figures of Group 1, 2, 3, and mixed group baddeleyite microstructures. c-d) Group 3 NWA 10299 grains 74 and 54A, showing degraded crystallinity in band contrast (BC) map despite strong BC in adjacent minerals, suggesting quasi-amorphous microstructures that diffract at length-scales below EBSD measurements. Some localized preserved baddeleyite domains with orthogonal ORs are observed in c) but diffraction is completely absent in d). Charging during EBSD analysis has resulted in slight in-run shift. BSE: backscatter electron image. IPF: inverse pole figure coloring, based on the orientation of the crystallographic z-axis. Cpx: clinopyroxene. Tmt: titanomagnetite. Gls: glass.

e) Mixed groups (1+3): NWA 12919_F1/454

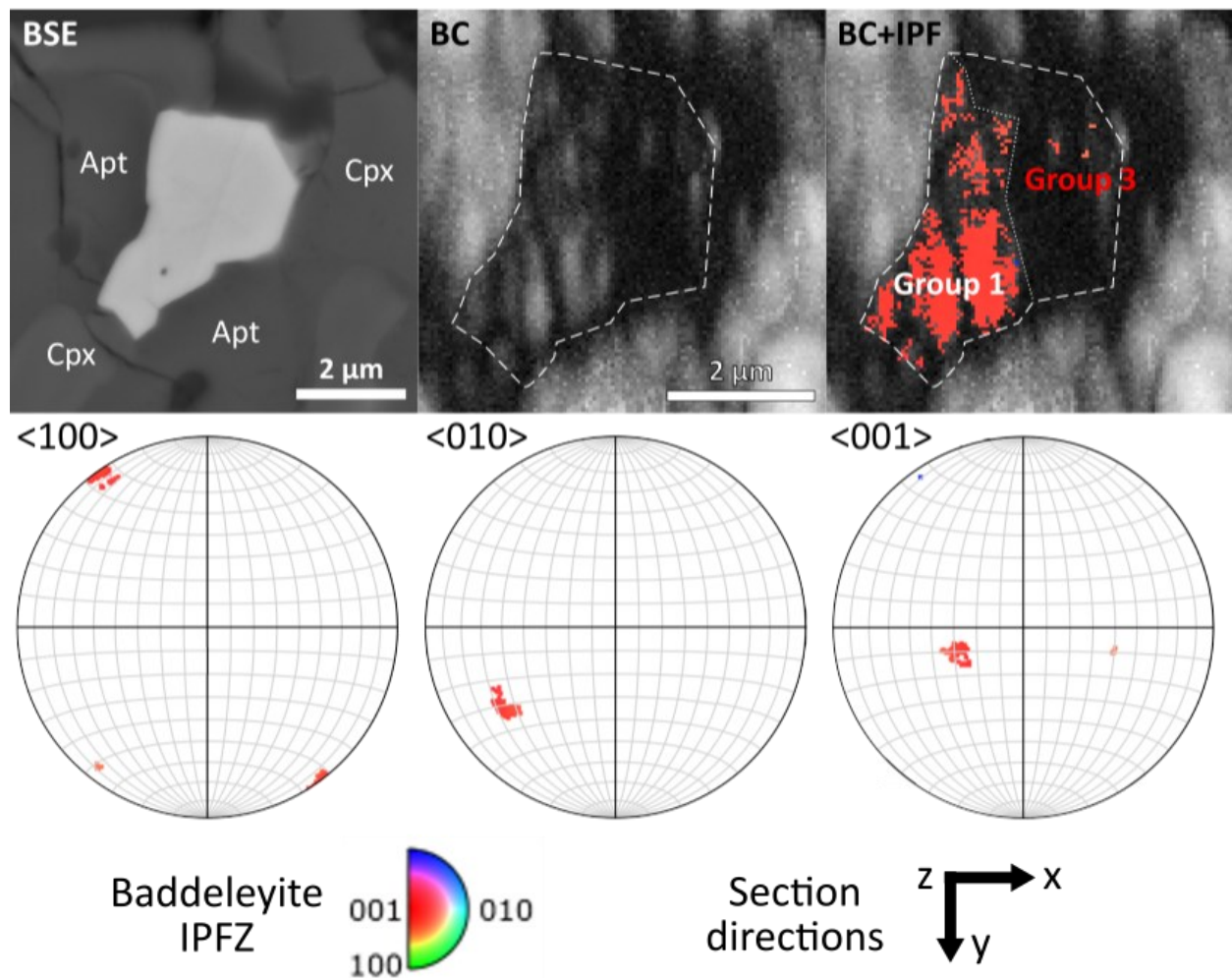
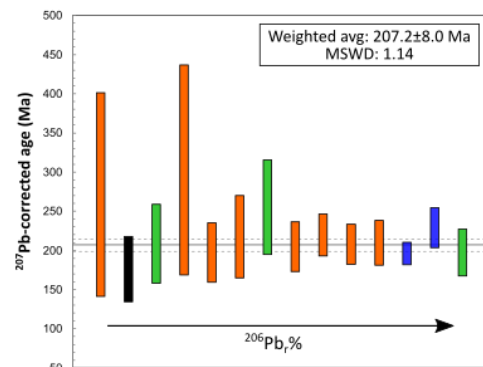
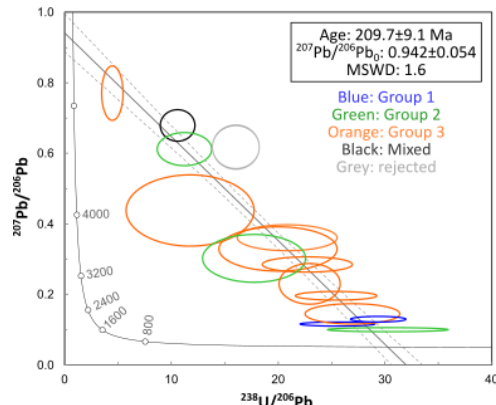
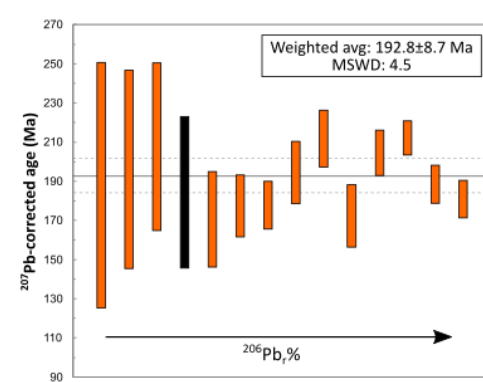
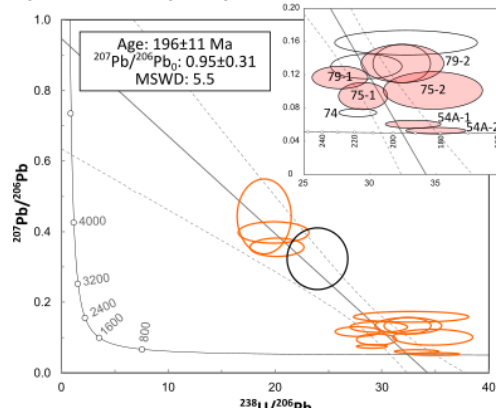


Fig. 3.2.(continued) Electron backscatter diffraction (EBSD) maps and pole figures of Group 1, 2, 3, and mixed group baddeleyite microstructures. e) Mixed group grain F1/454 in NWA 12919, showing Group 1 microstructure in one portion and Group 3 microstructure in the other. Charging during EBSD analysis has resulted in slight in-run shift. BSE: backscatter electron image. IPF: inverse pole figure coloring, based on the orientation of the crystallographic z-axis. Cpx: clinopyroxene. Tmt: titanomagnetite. Ol: olivine. Msk: maskelynite. Apt: apatite. Gls: glass.

a) JaH 479 (n=16)



b) NWA 10299 (n=14)



c) NWA 12919 (n=9)

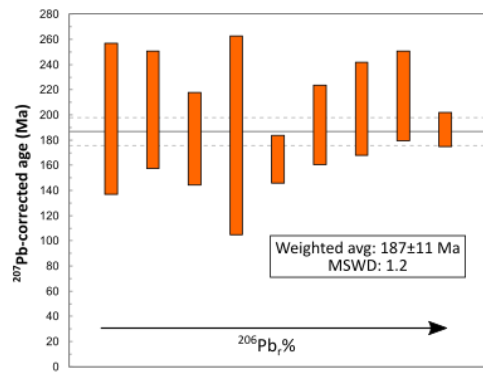
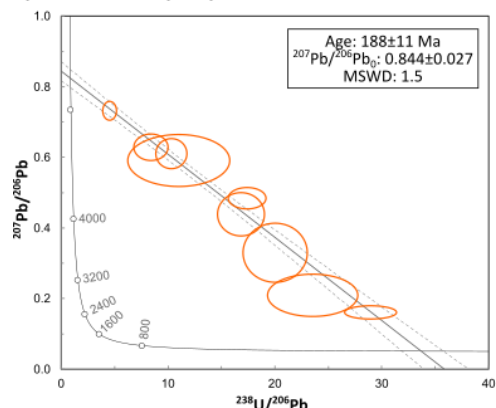


Fig. 3.3. Tera-Wasserburg plots of U-Pb isotopic analysis of baddeleyite (uncorrected for common Pb) in a) JaH 479, b) NWA 10299, and c) NWA 12919, with the weighted mean of ^{207}Pb -corrected ages. Inset in b) shows zoomed-in view of analyses with radiogenic $^{207}\text{Pb}/^{206}\text{Pb} < 0.2$ compositions, with paired analyses (measured on the same baddeleyite grain) highlighted by the red shaded ellipses. Analyses are colored according to microstructural grouping (Table 3.3). Ellipses denote 2σ . Intercept uncertainties and weighted mean age uncertainties are reported at 95% confidence intervals. Error envelope (dashed grey curves) of the discordia regression (solid grey curve) denote 2σ uncertainties. Data bars in weighted average plot are arranged in increasing percentage of radiogenic ^{206}Pb ($^{206}\text{Pb}_r$). Dashed grey lines in weighted average plots denote 2σ uncertainties of ^{207}Pb -corrected weighted mean age. All plots generated in Isoplot (Ludwig, 2003).

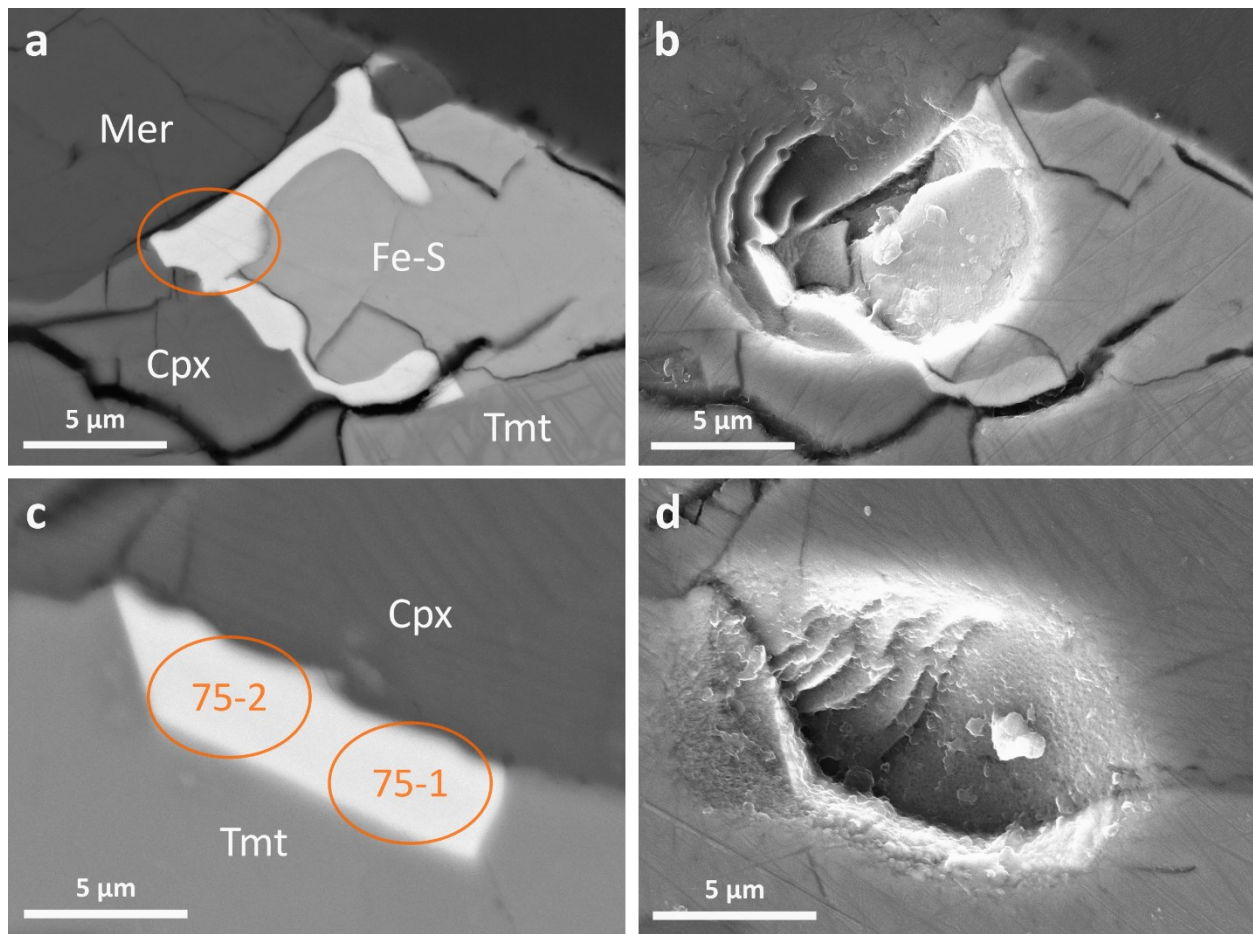


Fig. 3.4. Comparison of SEM images taken before and after SIMS analyses. a) and b): Grain F212 in JaH 479. c) and d): Grain 75 in NWA 10299. In a) and c), the approximate locations of the ion beam are marked in orange ellipses, with a long axis of 5 μm which was approximately the expected size during these sessions. Post-SIMS images show that the analysis spots were larger than intended, with significant portions overlapping into surrounding non-baddeleyite phases. In the case of NWA 10299, analysis 75-2 largely overlapped the spot left by analysis 75-1. Cpx: clinopyroxene. Fe-S: iron sulfide. Mer: merrillite. Tmt: titanomagnetite.

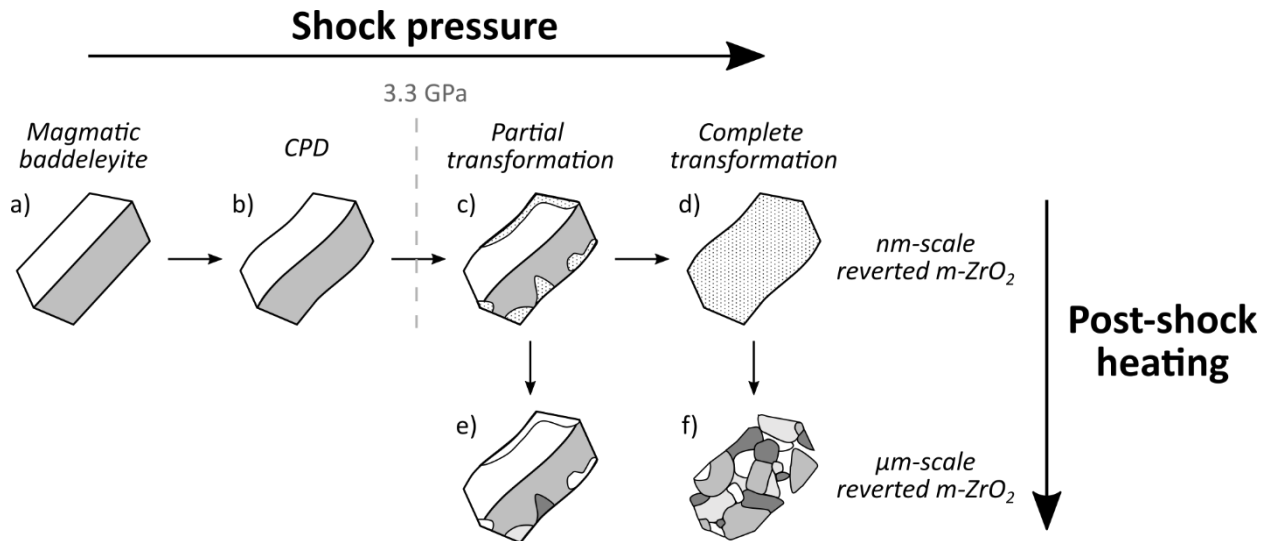


Fig. 3.5. Schematic diagram illustrating baddeleyite microstructural response to varying shock conditions, modified after [Staddon et al. \(2021\)](#). During impact shock metamorphism, magmatic baddeleyite (a) undergoes crystal-plastic deformation (CPD; b: Group 1). At pressures ≥ 3.3 GPa, transformation to $o\text{-ZrO}_2$ takes place which overprints parts of the grain (c) or its entirety (d: Group 3) depending on the homogeneity of peak shock distribution. Under low post-shock temperatures, nucleation of reverted $m\text{-ZrO}_2$ is suppressed results in quasi-amorphous ($<30\text{--}80$ nm reverted $m\text{-ZrO}_2$) microstructures. With increasing magnitude and/or duration of post-shock heating, reverted $m\text{-ZrO}_2$ form μm -scale domains that possess orthogonal ORs (e: Group 2; f: Group 4). In this study and in [Staddon et al. \(2021\)](#), no group designation is given to the microstructure depicted in c), which is considered Group 1 or Group 3 based on the relative proportion of magmatic vs. quasi-amorphous domains.

3.9 References

- Aramovich, C. J., Herd, C. D. K. & Papike, J. J. (2002) Symplectites derived from metastable phases in martian basaltic meteorites. *American Mineralogist* **87**: 1351-1359.
- Baziotis I., Liu Y., and Taylor L. 2013. Detailed Raman Spectroscopic Study of the Tissint Meteorite: Extraordinary Occurrence of High Pressure Polymorphs in a Single Fresh Piece of Martian Shergottite. pp. EGU2013-5463.
- Beaty, D. W., Grady, M. M., McSween, H. Y., Sefton-Nash, E., Carrier, B. L., Altieri, F., Amelin, Y., Ammannito, E., Anand, M., Benning, L. G., Bishop, J. L., Borg, L. E., Boucher, D., Brucato, J. R., Busemann, H., Campbell, K. A., Czaja, A. D., Debaille, V., Des Marais, D. J., Dixon, M., Ehlmann, B. L., Farmer, J. D., Fernandez-Remolar, D., Filiberto, J., Fogarty, J., Glavin, D. P., Goreva, Y. S., Hallis, L. J., Harrington, A. D., Hausrath, E. M., Herd, C. D. K., Horgan, B., Humayun, M., Kleine, T., Kleinhenz, J., Mackelprang, R., Mangold, N., Mayhew, L. E., McCoy, J. T., McCubbin, F. M., McLennan, S. M., Moser, D. E., Moynier, F., Mustard, J. F., Niles, P. B., Ori, G. G., Raulin, F., Rettberg, P., Rucker, M. A., Schmitz, N., Schwenzer, S. P., Sephton, M. A., Shaheen, R., Sharp, Z. D., Shuster, D. L., Siljeström, S., Smith, C. L., Spry, J. A., Steele, A., Swindle, T. D., ten Kate, I. L., Tosca, N. J., Usui, T., Van Kranendonk, M. J., Wadhwa, M., Weiss, B. P., Werner, S. C., Westall, F., Wheeler, R. M., Zipfel, J. & Zorzano, M. P. (2019) The potential science and engineering value of samples delivered to Earth by Mars sample return. *Meteoritics & Planetary Science* **54**: S3-S152.
- Beck, P., Gillet, P., El Goresy, A. & Mostefaoui, S. (2005) Timescales of shock processes in chondritic and martian meteorites. *Nature* **435**: 1071-1074.
- Bellucci, J. J., Nemchin, A. A., Whitehouse, M. J., Humayun, M., Hewins, R. & Zanda, B. (2015) Pb-isotopic evidence for an early, enriched crust on Mars. *Earth and Planetary Science Letters* **410**: 34-41.
- Bellucci, J. J., Nemchin, A. A., Whitehouse, M. J., Snape, J. F., Kielman, R. B., Bland, P. A. & Benedix, G. K. (2016) A Pb isotopic resolution to the Martian meteorite age paradox. *Earth and Planetary Science Letters* **433**: 241-248.
- Belov, G. V., Dyachkov, S. A., Levashov, P. R., Lomonosov, I. V., Minakov, D. V., Morozov, I. V., Sineva, M. A. & Smirnov, V. N. (2018) The IVTANTHERMO-Online database for thermodynamic properties of individual substances with web interface. *Journal of Physics: Conference Series* **946**: 012120.
- Berezhnoy, A. A., Bunch, T. E., Ma, P., Herzog, G. F., Knie, K., Rugel, G., Faestermann, T. & Korschinek, G. (2010) Al-26, Be-10, and Mn-53 in Martian Meteorites. *Meteoritics and Planetary Science Supplement* **73**: 5306.

- Borg, L. & Drake, M. J. (2005) A review of meteorite evidence for the timing of magmatism and of surface or near-surface liquid water on Mars. *Journal of Geophysical Research: Planets* **110**.
- Borg, L. E., Edmunson, J. E. & Asmerom, Y. (2005) Constraints on the U-Pb isotopic systematics of Mars inferred from a combined U-Pb, Rb-Sr, and Sm-Nd isotopic study of the Martian meteorite Zagami. *Geochimica et Cosmochimica Acta* **69**: 5819-5830.
- Borg, L. E., Nyquist, L. E., Taylor, L. A., Wiesmann, H. & Shih, C. (1997) Constraints on Martian differentiation processes from Rb-Sr and Sm-Nd isotopic analyses of the basaltic shergottite QUE 94201. *Geochimica et Cosmochimica Acta* **61**: 4915-4931.
- Bouvier, P., Djurado, E., Lucaleau, G. & Le Bihan, T. (2000) High-pressure structural evolution of undoped tetragonal nanocrystalline zirconia. *Physical Review B* **62**: 8731.
- Bouvier, A., Blichert-Toft, J., Vervoort, J. D., Gillet, P. & Albarède, F. (2008) The case for old basaltic shergottites. *Earth and Planetary Science Letters* **266**: 105-124.
- Bowling, T. J., Johnson, B. C., Wiggins, S. E., Walton, E. L., Melosh, H. J. & Sharp, T. G. (2020) Dwell time at high pressure of meteorites during impact ejection from Mars. *Icarus* **343**: 113689.
- Brandon A. D., Nyquist L. E., Shih C. -, and Wiesmann H. 2004. Rb-Sr and Sm-Nd Isotope Systematics of Shergottite NWA 856: Crystallization Age and Implications for Alteration of Hot Desert SNC Meteorites. pp. 1931.
- Cartwright, J. A., Herrmann, S., Ivanova, M. A., Korochantseva, E. V., Lorenz, C. A. & Ott, U. (2010) Noble Gas and CRE Age Measurement of New Basaltic Shergottite JaH 479. *Meteoritics and Planetary Science Supplement* **73**: 5049.
- Cassata, W. S., Cohen, B. E., Mark, D. F., Trappitsch, R., Crow, C. A., Wimpenny, J., Lee, M. R. & Smith, C. L. (2018) Chronology of martian breccia NWA 7034 and the formation of the martian crustal dichotomy. *Science Advances* **4**: eaap8306.
- Cayron, C., Douillard, T., Sibil, A., Fantozzi, G. & Sao-Jao, S. (2010) Reconstruction of the Cubic and Tetragonal Parent Grains from Electron Backscatter Diffraction Maps of Monoclinic Zirconia. *Journal of the American Ceramic Society* **93**: 2541-2544.
- Chamberlain, K. R., Schmitt, A. K., Swapp, S. M., Harrison, T. M., Swoboda-Colberg, N., Bleeker, W., Peterson, T. D., Jefferson, C. W. & Khudoley, A. K. (2010) In situ U-Pb SIMS (IN-SIMS) micro-baddeleyite dating of mafic rocks: Method with examples. *Precambrian Research* **183**: 379-387.
- Cohen, B. E., Mark, D. F., Cassata, W. S., Lee, M. R., Tomkinson, T. & Smith, C. L. (2017) Taking the pulse of Mars via dating of a plume-fed volcano. *Nature Communications* **8**: 640.

- Combs, L. M., Udry, A., Howarth, G. H., Righter, M., Lapen, T. J., Gross, J., Ross, D. K., Rahib, R. R. & Day, J. M. D. (2019) Petrology of the enriched poikilitic shergottite Northwest Africa 10169: Insight into the martian interior. *Geochimica et Cosmochimica Acta* **266**: 435-462.
- Costa, M. M., Jensen, N. K., Bouvier, L. C., Connelly, J. N., Mikouchi, T., Horstwood, M. S. A., Suuronen, J., Moynier, F., Deng, Z., Agranier, A., Martin, L. A. J., Johnson, T. E., Nemchin, A. A. & Bizzarro, M. (2020) The internal structure and geodynamics of Mars inferred from a 4.2-Gyr zircon record. *Proceedings of the National Academy of Sciences* **117**: 30973-30979.
- Cox M. A., Daly L., Cavosie A. J., Bland P. A., Lee M. R., Cohen B. E., Cairney J. M., Eder K., and Yang L. 2018. Complex Twinning in Baddeleyite from the Martian Meteorite North West Africa (NWA) 11522; Preliminary Results. pp. 6257.
- Crozaz, G. & Wadhwa, M. (2001) The terrestrial alteration of saharan shergottites dar al gani 476 and 489: a case study of weathering in a hot desert environment. *Geochimica et Cosmochimica Acta* **65**: 971-977.
- Crozaz, G., Floss, C. & Wadhwa, M. (2003) Chemical alteration and REE mobilization in meteorites from hot and cold deserts. *Geochimica et Cosmochimica Acta* **67**: 4727-4741.
- Darling, J. R., Moser, D. E., Barker, I. R., Tait, K. T., Chamberlain, K. R., Schmitt, A. K. & Hyde, B. C. (2016) Variable microstructural response of baddeleyite to shock metamorphism in young basaltic shergottite NWA 5298 and improved U-Pb dating of Solar System events. *Earth and Planetary Science Letters* **444**: 1-12.
- Debaille, V., Yin, Q. -, Brandon, A. D. & Jacobsen, B. (2008) Martian mantle mineralogy investigated by the ^{176}Lu - ^{176}Hf and ^{147}Sm - ^{143}Nd systematics of shergottites. *Earth and Planetary Science Letters* **269**: 186-199.
- Debaille V., Roland J., Goderis S., Hublet G., and Pourkhorsandi H. 2022. Asuka 12325: Expanding the Chemical Variety of the Martian Mantle Sampled by Shergottites. pp. 2433.
- Deutsch, A. & Schärer, U. (1990) Isotope systematics and shock-wave metamorphism: I. U-Pb in zircon, titanite and monazite, shocked experimentally up to 59 GPa. *Geochimica et Cosmochimica Acta* **54**: 3427-3434.
- Ehlmann, B. L. & Edwards, C. S. (2014) Mineralogy of the Martian Surface. *Annual Review of Earth and Planetary Sciences* **42**: 291-315.
- El Goresy, A., Gillet, P., Miyahara, M., Ohtani, E., Ozawa, S., Beck, P. & Montagnac, G. (2013) Shock-induced deformation of Shergottites: Shock-pressure and perturbations of magmatic ages on Mars. *Geochimica et Cosmochimica Acta* **101**: 233-262.

- Ferdous J., and Brandon A. D. (2020). Crystallization Age of Enriched Poikilitic Shergottite Northwest Africa 7397 Determined from Sm-Nd Isotope Systematics. pp. 1064.
- Ferdous, J., Brandon, A. D., Peslier, A. H. & Pirotte, Z. (2017) Evaluating crustal contributions to enriched shergottites from the petrology, trace elements, and Rb-Sr and Sm-Nd isotope systematics of Northwest Africa 856. *Geochimica et Cosmochimica Acta* **211**: 280-306.
- Foley, C. N., Wadhwa, M., Borg, L. E., Janney, P. E., Hines, R. & Grove, T. L. (2005) The early differentiation history of Mars from 182W-142Nd isotope systematics in the SNC meteorites. *Geochimica et Cosmochimica Acta* **69**: 4557-4571.
- Fritz, J., Greshake, A. & Stöffler, D. (2005) Micro-Raman spectroscopy of plagioclase and maskelynite in Martian meteorites: Evidence of progressive shock metamorphism. *Antarctic Meteorite Research* **18**: 96.
- Goodwin, A., Garwood, R. J. & Tartèse, R. (2022) A Review of the “Black Beauty” Martian Regolith Breccia and Its Martian Habitability Record. *Astrobiology* **22**: 755-767.
- Greshake, A., Fritz, J., Böttger, U. & Goran, D. (2013) Shear-induced ringwoodite formation in the Martian shergottite Dar al Gani 670. *Earth and Planetary Science Letters* **375**: 383-394.
- Hamilton J. S., Herd C. D. K., Walton E. L., and Tornabene L. L. 2020. Prioritizing Candidate Source Craters for Martian Meteorites. pp. 2607.
- Heaman, L. M. (2009) The application of U-Pb geochronology to mafic, ultramafic and alkaline rocks: An evaluation of three mineral standards. *Chemical Geology* **261**: 43-52.
- Heaman, L. M. & LeCheminant, A. N. (1993) Paragenesis and U-Pb systematics of baddeleyite (ZrO_2). *Chemical Geology; Geochemistry of Accessory Minerals* **110**: 95-126.
- Herd, C. D. K., Walton, E. L., Agee, C. B., Muttik, N., Ziegler, K., Shearer, C. K., Bell, A. S., Santos, A. R., Burger, P. V., Simon, J. I., Tappa, M. J., McCubbin, F. M., Gattaccea, J., Lagroix, F., Sanborn, M. E., Yin, Q., Cassata, W. S., Borg, L. E., Lindvall, R. E., Kruijer, T. S., Brennecka, G. A., Kleine, T., Nishiizumi, K. & Caffee, M. W. (2017) The Northwest Africa 8159 martian meteorite: Expanding the martian sample suite to the early Amazonian. *Geochimica et Cosmochimica Acta* **218**: 1-26.
- Herd, C. D. K., Moser, D. E., Tait, K., Darling, J. R., Shaulis, B. J. & McCoy, T. J. (2018a) Crystallization of Baddeleyite in Basaltic Rocks from Mars, and Comparisons with the Earth, Moon, and Vesta. *Microstructural Geochronology*: 137-166.
- Herd C. D. K., Tornabene L. L., Bowling T. J., Walton E. L., Sharp T. G., Melosh H. J., Hamilton J. S., Viviano C. E., and Ehlmann B. L. (2018b). Constraining the Source Craters of the Martian Meteorites: Implications for Prioritization of Returned Samples from Mars. pp. 6097.

- Herzog G. F., and Caffee M. W. 2014. Cosmic-Ray Exposure Ages of Meteorites. In: , edited by Davis A. M. pp. 419-454.
- Hu, J. & Sharp, T. G. (2022) Formation, preservation and extinction of high-pressure minerals in meteorites: temperature effects in shock metamorphism and shock classification. *Progress in Earth and Planetary Science* **9**: 6.
- Irving A. J., Kuehner S. M., Lapen T. J., Righter M., Busemann H., Wieler R., and Nishiizumi K. 2017. Keeping Up with the Martian Meteorites and Constraining the Number of Separate Launch Sites on Mars. pp. 2068.
- Ivanov, B. A., Jay Melosh, H. & Head, J. N. (2002) Martian Meteorite Launch: High-Speed Ejecta from Small Craters. *Science* **298**: 1752-1756.
- Jean M. M., Howarth G. H., Bodnar B., Klyukin Y., and Taylor L. A. 2016. Petrogenesis of the New Basaltic Shergottite Northwest Africa 10299: fO₂ Consistent with an Intermediate to Depleted Geochemical Source. pp. 2698.
- Jiang, Y. & Hsu, W. (2012) Petrogenesis of Grove Mountains 020090: An enriched “Iherzolitic” shergottite. *Meteoritics & Planetary Science* **47**: 1419-1435.
- Kelly, P. M. & Francis Rose, L. R. (2002) The martensitic transformation in ceramics — its role in transformation toughening. *Progress in Materials Science* **47**: 463-557.
- Kizovski, T. V., Izawa, M. R. M., Tait, K. T., Moser, D. E., Day, J. M. D., Hyde, B. C., White, L. F., Kovarik, L., Taylor, S. D., Pereira, D. E., Barker, I. R. & Joy, B. R. (2020) Petrogenesis, alteration, and shock history of intermediate shergottite Northwest Africa 7042: Evidence for hydrous magmatism on Mars? *Geochimica et Cosmochimica Acta* **283**: 103-123.
- Krietsch, D. (2020) Alteration on asteroids, diversity of primordial volatiles and their carriers in carbonaceous chondrites, and martian shergottite sampling sites - studied by meteoritic noble gases. *Ph.D. Thesis*.
- Lagain, A., Benedix, G. K., Servis, K., Baratoux, D., Doucet, L. S., Rajšić, A., Devillepoix, H. A. R., Bland, P. A., Towner, M. C., Sansom, E. K. & Miljković, K. (2021) The Tharsis mantle source of depleted shergottites revealed by 90 million impact craters. *Nature Communications* **12**: 6352.
- Lagain, A., Bouley, S., Zanda, B., Miljković, K., Rajšić, A., Baratoux, D., Payré, V., Doucet, L. S., Timms, N. E., Hewins, R., Benedix, G. K., Malarewic, V., Servis, K. & Bland, P. A. (2022) Early crustal processes revealed by the ejection site of the oldest martian meteorite. *Nature Communications* **13**: 3782.

- Lapen, T. J., Righter, M., Brandon, A. D., Debaille, V., Beard, B. L., Shafer, J. T. & Peslier, A. H. (2010) A Younger Age for ALH84001 and Its Geochemical Link to Shergottite Sources in Mars. *Science* **328**: 347-351.
- Lapen, T. J., Righter, M., Andreasen, R., Irving, A. J., Satkoski, A. M., Beard, B. L., Nishiizumi, K., Timothy Jull, A. J. & Caffee, M. W. (2017) Two billion years of magmatism recorded from a single Mars meteorite ejection site. *Science Advances* **3**: e1600922.
- Li, Q., Li, X., Liu, Y., Tang, G., Yang, J. & Zhu, W. (2010) Precise U-Pb and Pb-Pb dating of Phanerozoic baddeleyite by SIMS with oxygen flooding technique. *Journal of Analytical Atomic Spectrometry* **25**: 1107-1113.
- Lindner M., Hezel D. C., Gerdes A., Marschall H. R., and Brenker F. E. 2022. Age of enriched gabbroic shergottite Northwest Africa 6963 and its Si-rich mesostasis (abstract). *88th Annual Meeting of the Meteoritical Society 2022*:Abstract #6137 (LPI Contrib. No. 2695).
- Lorenz, C. A., Ivanova, M. A., Teplyakova, S. N., Korochantsev, A. V., Franchi, I. A. & Ott, U. (2010) Basaltic Shergottite, Jiddat Al Harasis 479. *Meteoritics and Planetary Science Supplement* **73**: 5228.
- Ludwig, K. R. (2003) User's manual for isoplot 3.00, a geochronological toolkit for microsoft excel. *Berkeley Geochronl.Cent.Spec.Publ.* **4**: 25-32.
- Mathew, K. J., Marty, B., Marti, K. & Zimmermann, L. (2003) Volatiles (nitrogen, noble gases) in recently discovered SNC meteorites, extinct radioactivities and evolution. *Earth and Planetary Science Letters* **214**: 27-42.
- McCubbin, F. M., Boyce, J. W., Novák-Szabó, T., Santos, A. R., Tartèse, R., Muttik, N., Domokos, G., Vazquez, J., Keller, L. P., Moser, D. E., Jerolmack, D. J., Shearer, C. K., Steele, A., Elardo, S. M., Rahman, Z., Anand, M., Delhaye, T. & Agee, C. B. (2016) Geologic history of Martian regolith breccia Northwest Africa 7034: Evidence for hydrothermal activity and lithologic diversity in the Martian crust. *Journal of Geophysical Research: Planets* **121**: 2120-2149.
- McFarlane, C. R. M. & Spray, J. G. (2022) The Los Angeles martian diabase: Phosphate U-Th-Pb geochronology and mantle source constraints. *Geochimica et Cosmochimica Acta* **326**: 166-179.
- Meteoritical Bulletin Database. URL: <https://www.lpi.usra.edu/meteor/about.php>. Last updated on August 19, 2022. Accessed on August 23, 2022.
- Melosh, H. J. (1984) Impact ejection, spallation, and the origin of meteorites. *Icarus* **59**: 234-260.
- MEPAG E2E-iSAG (2012) Planning for Mars Returned Sample Science: Final Report of the MSR End-to-End International Science Analysis Group (E2E-iSAG). *Astrobiology* **12**: 175-230.

- Min, K., Farah, A. E., Lee, S. R. & Lee, J. I. (2017) (U-Th)/He ages of phosphates from Zagami and ALHA77005 Martian meteorites: Implications to shock temperatures. *Geochimica et Cosmochimica Acta* **196**: 160-178.
- Misawa, K. & Yamaguchi, A. (2007) U-Pb Ages of NWA 856 Baddeleyite. *Meteoritics and Planetary Science Supplement* **42**: 5228.
- Moser, D. E., Chamberlain, K. R., Tait, K. T., Schmitt, A. K., Darling, J. R., Barker, I. R. & Hyde, B. C. (2013) Solving the Martian meteorite age conundrum using micro-baddeleyite and launch-generated zircon. *Nature* **499**: 454-457.
- Nielsen, R.H., Schleiwitz, J.H., Nielsen, H. & Updated, b. S. (2013) Zirconium and Zirconium Compounds. *Kirk-Othmer Encyclopedia of Chemical Technology*: 1-46.
- Niihara, T. (2011) Uranium-lead age of baddeleyite in shergottite Roberts Massif 04261: Implications for magmatic activity on Mars. *Journal of Geophysical Research: Planets* **116**.
- Niihara, T., Kaiden, H., Misawa, K., Sekine, T. & Mikouchi, T. (2012) U-Pb isotopic systematics of shock-loaded and annealed baddeleyite: Implications for crystallization ages of Martian meteorite shergottites. *Earth and Planetary Science Letters* **341-344**: 195-210.
- Nishiizumi K., Hillegonds D. J., McHargue L. R., and Jull A. J. T. (2004). Exposure and Terrestrial Histories of New Lunar and Martian Meteorites. pp. 1130.
- Nyquist L. E., Ikeda Y., Shih C., Reese Y. D., Nakamura N., and Takeda H. (2006). Sm-Nd age and Nd-and Sr-isotopic evidence for the petrogenesis of Dhofar 378. 30th Symposium on antarctic Meteorites.
- Nyquist L. E., Bogard D. D., Shih C. -, Greshake A., Stöffler D., and Eugster O. (2001). Ages and Geologic Histories of Martian Meteorites. Chronology and Evolution of. pp. 105-164.
- Ohtaka, O., Fukui, H., Kunisada, T., Fujisawa, T., Funakoshi, K., Utsumi, W., Irifune, T., Kuroda, K. & Kikegawa, T. (2001) Phase relations and equations of state of ZrO₂ under high temperature and high pressure. *Physical Review B* **63**: 174108.
- O'Neal E. W., Ostwald A. M., Udry A., Gross J., Righter M., McQuaig D. R., Lapen T. J., Howarth G. H., and Johnsen R. 2022. Melt Inclusion, Trace Element, and Isotopic Analyses of a Poikilitic Shergottite Suite: Implications for Martian Magmatism. pp. 2449.
- Park, J., Bogard, D. D., Mikouchi, T. & McKay, G. A. (2008) Dhofar 378 Martian shergottite: Evidence of early shock melting. *Journal of Geophysical Research: Planets* **113**.
- Park, J., Bogard D. D., Nyquist L. E. & Herzog, G. F. (2014) Issues in dating young rocks from another planet: Martian shergottites. *Geological Society, London, Special Publications* **378**: 297-316.

- Returned Sample Science Board, Carrier B. L., Beaty D. W., McSween H. Y., Czaja A. D., Goreva Y. S., Hausrath E. M., Herd C. D. K., Humayun M., McCubbin F. M., McLennan S. M., Pratt L. M., Sephton M. A., Steele A., and Weiss B. P. (2017). Strategies for Investigation Early Mars Using Returned Samples. pp. 3051.
- Righter M., Lapen T. J., and Irving A. J. (2018). Extending the Range in Ages and Source Compositions of Shergottites: Lu-Hf and Sm-Nd Age and Isotope Systematics of Northwest Africa 4480. pp. 2609.
- Schmitt, A. K., Chamberlain, K. R., Swapp, S. M. & Harrison, T. M. (2010) In situ U-Pb dating of micro-baddeleyite by secondary ion mass spectrometry. *Chemical Geology* **269**: 386-395.
- Schoene B. (2014). 4.10 - U-Th-Pb Geochronology. In: *Treatise on Geochemistry (Second Edition)*, edited by Holland H. D. and Turekian K. K. Oxford: Elsevier. pp. 341-378.
- Schulz, T., Povinec, P. P., Ferrière, L., Jull, A. J. T., Kováčik, A., Sýkora, I., Tusch, J., Münker, C., Topa, D. & Koeberl, C. (2020) The history of the Tissint meteorite, from its crystallization on Mars to its exposure in space: New geochemical, isotopic, and cosmogenic nuclide data. *Meteoritics & Planetary Science* **55**: 294-311.
- Sharp T. G., and de Carli P. S. (2006). Shock Effects in Meteorites. In: , edited by Lauretta D. S. and McSween H. Y. pp. 653.
- Sharp, T. G., Walton, E. L., Hu, J. & Agee, C. (2019) Shock conditions recorded in NWA 8159 martian augite basalt with implications for the impact cratering history on Mars. *Geochimica et Cosmochimica Acta* **246**: 197-212.
- Sheen, A. I., Herd, C. D. K., Hamilton, J. & Walton, E. L. (2021) Petrographic controls on baddeleyite occurrence in a suite of eight basaltic shergottites. *Meteoritics & Planetary Science* **56**: 1502-1530.
- Shih C. -, Nyquist L. E., Wiesmann H., and Barrat J. A. (2003). Age and Petrogenesis of Picritic Shergottite NWA1068: Sm-Nd and Rb-Sr Isotopic Studies. pp. 1439.
- Shih, C. -, Nyquist, L. E., Reese, Y. & Misawa, K. (2011) Sm-Nd and Rb-Sr studies of Iherzolitic shergottite Yamato 984028. *Polar Science* **4**: 515-529.
- Smith, D. K. & Newkirk, W. (1965) The crystal structure of baddeleyite (monoclinic ZrO₂) and its relation to the polymorphism of ZrO₂. *Acta Crystallographica* **18**: 983-991.
- Stacey, J. S. & Kramers, J. D. (1975) Approximation of terrestrial lead isotope evolution by a two-stage model. *Earth and Planetary Science Letters* **26**: 207-221.
- Staddon L. G., Darling J. R., Stephen N. R., Dunlop J., and Tait K. T. (2020). Baddeleyite Microstructures in Variably Shocked Martian Meteorites: An Opportunity to Link Shock Barometry and Robust Geochronology. 51st Annual Lunar and Planetary Science Conference, pp. 2302.

- Staddon L., Darling J., Schwarz W., Stephen N., Schuindt S., Dunlop J., and Tait K. (2021a). Combined microstructural analysis and in-situ U-Pb chronology of baddeleyite within shergottites. *Goldschmidt* 2021. doi: 10.7185/gold2021.7956
- Staddon, L. G., Darling, J. R., Schwarz, W. H., Stephen, N. R., Schuindt, S., Dunlop, J. & Tait, K. T. (2021b) Dating martian mafic crust; microstructurally constrained baddeleyite geochronology of enriched shergottites Northwest Africa (NWA) 7257, NWA 8679 and Zagami. *Geochimica et Cosmochimica Acta* **315**: 73-88.
- Stöffler, D., Ostertag, R., Jammes, C., Pfannschmidt, G., Gupta, P. R. S., Simon, S. B., Papike, J. J. & Beauchamp, R. H. (1986) Shock metamorphism and petrography of the Shergotty achondrite. *Geochimica et Cosmochimica Acta* **50**: 889-903.
- Takagi, S., Kyono, A., Nozawa, S., Kawai, N., Inukai, K., Fukaya, R., Funamori, N., Adachi, S. & Ichiyangagi, K. (2020) In Situ Observation of the Phase Transition Behavior of Shocked Baddeleyite. *Geophysical Research Letters* **47**: e2020GL089592.
- Timms, N. E., Erickson, T. M., Pearce, M. A., Cavosie, A. J., Schmieder, M., Tohver, E., Reddy, S. M., Zanetti, M. R., Nemchin, A. A. & Wittmann, A. (2017) A pressure-temperature phase diagram for zircon at extreme conditions. *Earth-Science Reviews* **165**: 185-202.
- Tornabene, L. L., Moersch, J. E., McSween Jr., H. Y., McEwen, A. S., Piatek, J. L., Milam, K. A. & Christensen, P. R. (2006) Identification of large (2–10 km) rayed craters on Mars in THEMIS thermal infrared images: Implications for possible Martian meteorite source regions. *Journal of Geophysical Research: Planets* **111**.
- Treiman, A. H. (2005) The nakhlite meteorites: Augite-rich igneous rocks from Mars. *Geochemistry* **65**: 203-270.
- Udry, A., Howarth, G. H., Herd, C. D. K., Day, J. M. D., Lapen, T. J. & Filiberto, J. (2020) What Martian Meteorites Reveal About the Interior and Surface of Mars. *Journal of Geophysical Research: Planets* **125**: e2020JE006523.
- Váci, Z. & Agee, C. (2020) Constraints on Martian Chronology from Meteorites. *Geosciences* **10**.
- Walton, E. L., Kelley, S. P. & Herd, C. D. K. (2008) Isotopic and petrographic evidence for young Martian basalts. *Geochimica et Cosmochimica Acta* **72**: 5819-5837.
- Werner, S. C., Ody, A. & François Poulet (2014) The Source Crater of Martian Shergottite Meteorites. *Science* **343**: 1343-1346.

- White, L. F., Darling, J. R., Moser, D. E., Reinhard, D. A., Prosa, T. J., Bullen, D., Olson, D., Larson, D. J., Lawrence, D. & Martin, I. (2017) Atomic-scale age resolution of planetary events. *Nature Communications* **8**: 15597.
- White, L. F., Darling, J. R., Moser, D. E., Cayron, C., Barker, I., Dunlop, J. & Tait, K. T. (2018) Baddeleyite as a widespread and sensitive indicator of meteorite bombardment in planetary crusts. *Geology* **46**: 719-722.
- Wieler, R., Huber, L., Busemann, H., Seiler, S., Leya, I., Maden, C., Masarik, J., Meier, M. M. M., Nagao, K., Trappitsch, R. & Irving, A. J. (2016) Noble gases in 18 Martian meteorites and angrite Northwest Africa 7812—Exposure ages, trapped gases, and a re-evaluation of the evidence for solar cosmic ray-produced neon in shergottites and other achondrites. *Meteoritics & Planetary Science* **51**: 407-428.
- Wingate, M. T. D. & Compston, W. (2000) Crystal orientation effects during ion microprobe U–Pb analysis of baddeleyite. *Chemical Geology* **168**: 75-97.
- Wu, Y., 徐伟彪, Li, Q., Che, X. & Liao, S. (2021) Heterogeneous martian mantle: Evidence from petrology, mineral chemistry, and in situ U-Pb chronology of the basaltic shergottite Northwest Africa 8653. *Geochimica et Cosmochimica Acta* **309**: 352-365.
- Zhou, Q., Herd, C. D. K., Yin, Q., Li, X., Wu, F., Li, Q., Liu, Y., Tang, G. & McCoy, T. J. (2013) Geochronology of the Martian meteorite Zagami revealed by U–Pb ion probe dating of accessory minerals. *Earth and Planetary Science Letters* **374**: 156-163.

CHAPTER 4: A feasibility assessment of micromill sampling for Rb–Sr and Sm–Nd geochronology of shergottites

4.1 Abstract

Accurate dating of martian meteorites is crucial for understanding key events in the planet's evolution. However, not all martian meteorites are amenable to geochronologic techniques currently in use for these rocks. The priority of sample preservation precludes use of low-volume specimens from mineral separation methods, whereas the less destructive *in-situ* SIMS U–Pb method depends on the availability of U-bearing accessory minerals. Micromilling allows for spatially-guided sampling of targets down to the sub-mm scale, therefore enabling chromatography-based analysis while preserving the overall specimen. This study presents an evaluation of micromill sampling for extracting individual mineral fractions *in-situ* from shergottites, the most common group of martian meteorites, for Rb–Sr and Sm–Nd geochronology. Based on trace element content in major minerals in shergottites (pyroxene, plagioclase, olivine, and merrillite) and assuming a minimum of 0.25 ng Sr and 1 ng Nd is required to achieve a baseline isotopic precision, the minimum required sample volume ranges in the orders of 10^5 – $10^7 \mu\text{m}^3$ for one Sr isotopic analysis and 10^5 – $10^9 \mu\text{m}^3$ for one Nd isotopic analysis. Considering the need for sample purity, significant limitations exist in the maximum sampling resolution of the micromill instrument ($\sim 40 \mu\text{m}$ for the conical carbide drill bit chosen for this study) with respect to shergottite petrography. Insufficient grain size, irregular morphology, and the presence of small inclusions may reduce the area that can be drilled per grain. Shock-induced fractures, which sometimes act as pathways for terrestrial alteration, are pervasive in shergottites and create additional challenges for effective high-purity sampling. In addition, variation in trace element content in the target minerals may result in the realistic required drilling volumes being orders of magnitude greater than the minimum estimates. Lastly, estimated drilling time per fraction may reach over five hours for pyroxene (Sr, Nd), plagioclase (Nd), and olivine (Sr, Nd), increasing the susceptibility to a larger procedural blank as well as requiring constant, labor-intensive

monitoring for long durations. Based on these technical and physical constraints we do not consider micromill sampling to be currently compatible with Sr isotopic analysis of olivine and Nd isotopic analysis of pyroxene, plagioclase, and olivine in shergottites. Feasibility of geochronology applications may be improved with future advances in analytical development, such as increasing the micromill sampling resolution and reducing the mass of analytes required for isotopic analysis.

4.2 Introduction

Sample availability is a key consideration in the methods by which martian meteorites are studied. Numbering 331 individual stones (as of May 2022), the martian meteorite inventory represents only ~0.2% of the total number of meteorites recovered worldwide ([Meteoritical Bulletin](#)). The priority of sample preservation makes martian meteorites inherently incompatible with many sampling protocols commonly used in studies of terrestrial geology. For example, analyzing martian meteorites for bulk major and trace elements normally take a total of <2 g of crushed sample (e.g., [Udry and Day, 2018](#)); by comparison, the same method applied to terrestrial basalts requires the sample powder to be split from a larger volume which has been crushed and homogenized in order to reduce the effect of modal heterogeneity. Approximately 31% of martian meteorites weigh under 50 g and 17% are under 20 g ([Meteoritical Bulletin](#)). Therefore, preserving the specimen and maximizing scientific information are crucial considerations when analyzing martian meteorites.

The study of radiogenic isotopes (e.g., Rb–Sr, Sm–Nd, Lu–Hf, U–Pb) in martian meteorites have yielded insights into not only the timing of major events in Mars geologic history, but also the nature and evolution of its mantle reservoirs (e.g., [McSween, 1994](#); [Borg et al., 1997, 2002](#); [Debaille et al., 2008](#); [Herd et al., 2017](#); [Lapen et al., 2017](#); [Bellucci et al., 2020](#); [Udry et al., 2020](#); [Nicklas et al., 2021](#)). Conventionally, radiogenic isotope dating of martian meteorites is conducted by chemical chromatography analyses (e.g., ID-TIMS, ICP-MS) of mineral fractions separated from crushed bulk samples (e.g., [Borg et al., 1997, 2003](#); [Lapen et al., 2017](#); [Combs et al., 2019](#)). Obtaining statistically robust multi-mineral isochrons depends on

the number of fractions available, the purity of the fractions, the precision and accuracy of each analysis, and the range of parent-to-daughter element ratios defined by the fractions for maximizing precision of the isochron regression. In particular, careful handpicking and cleaning are required to ensure that a primary igneous isotopic signature free of disturbance from secondary processes (e.g., alteration, impact shock) is measured ([Edmunson et al., 2005](#)).

In contrast to bulk sampling, *in-situ* analysis (e.g., LA-ICPMS, SIMS) is performed on specified targets at μm -scale resolutions while preserving the petrographic context; this enables isotopic data to be assessed using spatial information such as chemical mapping and/or microstructural analysis (e.g., [Moser et al., 2013](#); [Darling et al., 2016](#); [Staddon et al., 2021](#)). Secondary ion mass spectrometry (SIMS) data for shergottites, the most common group of martian meteorites, has demonstrated that baddeleyite U–Pb ages agree with igneous crystallization ages obtained using chemical chromatography methods (Rb–Sr, Sm–Nd, etc.), as well as elucidated the effects of impact shock on U–Pb isotope systematics (e.g., [Zhou et al., 2013](#); [Moser et al., 2013](#); [Darling et al., 2016](#); [Staddon et al., 2021](#)). Laser ablation inductively coupled plasma mass spectrometry (LA-ICP-MS) U–Pb baddeleyite analysis has been developed for terrestrial basalts ([Ibanez-Mejia et al., 2014](#)), however application to martian meteorites has not been as widespread as SIMS ([Hays et al., 2011](#)) due to the capability of SIMS to sample at smaller spot sizes (minimum 3–4 μm , compared to >8 μm for LA-ICP-MS). Compared to chemical chromatography methods, the main challenges to *in-situ* isotopic analysis are matrix matching, minimizing isobaric interferences, and optimizing signal detection by choosing targets with sufficient analyte concentrations and by adjusting operating parameters such as spot size and pulse rate (e.g., [Ibanez-Mejia et al., 2014](#)). For these reasons, *in-situ* analysis has been successfully applied to only some of the radiogenic isotopic systems that are analyzed by bulk sampling methods.

An additional category of sampling methods, microsampling, has found increasing geological applications in recent years. By mechanically separating mm- to μm -scale volumes from a target,

microsampling combines the advantages of conducting chemical chromatography analysis and preserving the overall petrographic context. In the field of meteoritics, μ m- to sub- μ m-sized sampling has been achieved for U-Pb accessory mineral geochronology by focused ion beam extraction combined with isotope dilution thermal ionized mass spectrometry (FIB-TIMS; e.g., [White et al., 2020](#)). Micromilling (or microdrilling), which operates on scale of 10's of μ ms and greater, has been commonly applied to textured geological materials such as zoned minerals and carbonates ([Charlier et al., 2006](#); [Hoffmann et al., 2009](#); [Pollington and Baxter, 2011](#)). The development of wet-based micromill sampling has further enabled applications in micro-volume trace element and radiogenic isotope analysis (e.g., [Charlier et al., 2006](#); [Harlou et al., 2009](#)). In meteoritic studies, micromill sampling has been applied to trace element, stable isotope, and radiogenic isotope analyses of chondrites and irons (e.g., [Cook et al., 2007](#); [Sikdar and Rai, 2020](#); [Nakanishi et al., 2022](#)).

With respect to sample preservation, SIMS and FIB U-Pb baddeleyite analyses have the greatest potential for obtaining geochronological data with minimum sample usage. However, U-Pb baddeleyite geochronology relies in large part on the presence of the target mineral in sufficient quantity and of sufficient size for analysis; these conditions in turn depend on magma composition, melt evolution, and conditions of crystallization (e.g., [Herd et al., 2018](#); [Sheen et al., 2021](#)). For samples that do not meet these criteria, bulk crushing and mineral separation is currently the only available way to investigate geochronology, however amenability to bulk sampling may be limited if the specimen volume is scarce. The compatibility of microsampling with chemical chromatography offers a potential solution by bypassing sample crushing, allowing individual minerals to be analyzed while preserving the overall meteorite specimen. Based on these factors, it is in theory possible to conduct multi-mineral geochronology of martian meteorites by combining microsampling with ID-TIMS or ICP-MS isotopic analysis. In contrast to the μ m-scale resolution at which FIB operates, micromilling is capable of sampling at the mm- and sub-mm-scale and hence more compatible with extracting larger sample volumes. The

aim of this study is to assess the feasibility of such an application to Rb–Sr and Sm–Nd geochronology of shergottites, the largest and most chemically and petrographically diverse group of martian meteorites. Essentially, we ask the question: is micromill sampling compatible with extracting major igneous minerals in shergottites for Rb–Sr and Sm–Nd geochronology? And we seek to determine any limitations of such an application.

4.3 Methodology

We conduct the feasibility assessment by examining the following factors (Fig. 4.1):

1. Technical constraints: mass of analyte required for isotopic analysis, sampling resolution of the micromill, procedural blank contribution
2. Physical constraints: shergottite petrography and mineralogy, with respect to extracting the require mass of analytes
3. Amount of drilling required based on 1) and 2)
4. The inferred resulting footprint on a specimen

Micromilling for this study was conducted on a Merchantek/New Wave Research MicroMill in the Arctic Resources Geochemistry Laboratory (ARGL), University of Alberta. The micromill is housed in a laminar flow hood under ultra-clean protocols to ensure minimal contamination during preparation and analysis of microvolume samples.

4.3.1 The micromill sample method (wet-based)

In principle, the micromill instrument combines optical microscopy with precision drilling (Fig. 4.2). Sample characterization and the plotting of drilling patterns are carried out under an optical microscope ("scope view") before the sample is moved by the motorized stage to the drilling assembly ("drill view") to be excavated. During drilling, lateral movement (X- and Y-directions) is provided by the motorized stage and vertical movement (Z-direction) is supported by the drilling assembly overhead. Position reproducibility is $\pm 1 \mu\text{m}$.

The wet-based collection method developed by [Charlier et al. \(2006\)](#) was adapted for this study as it enables collection of microvolume samples while minimizing contamination. The polished epoxy mount sample was cleaned in an ultrasonic bath of MilliQ water for 15–20 minutes. The drill bit was cleaned in an ultrasonic bath of ethanol for the same duration of time. To attach the sample to the micromill stage, 3M double-sided carbon tape was used for quick mounting and demounting while ensuring sample stability during drilling, as well as minimizing potential contamination onto the sample surface and the stage assembly. Calibration was carried out at the start of every drilling session to ensure that patterns defined under scope view were accurately executed in drill view. Drilling patterns in the micromill can be customized with the desired parameters including drilling depth, drill speed, number of passes, depth increment per pass, etc. For wet-based collection, a small piece of parafilm (<1 cm in length and width) was attached to the sample surface with a $<5 \times 5$ mm hole cut in the center to expose the drilling target. A droplet of MilliQ water was then placed on top of the drilling target using pre-cleaned micropipette; the droplet was held in place by surface tension against the cut-out hole. During drilling, excavated powder was captured in the water droplet. In this study, we found that the water droplet is prone to evaporating during drilling and that water had to be added to the droplet at five minute intervals to prevent it from drying out.

After drilling was complete, the slurry containing the sample powder was transferred away from the sample surface using a pre-cleaned micropipette. As prescribed by [Charlier et al. \(2006\)](#), a slow pumping motion was applied to mobilize any trapped fragments from the sample surface into the slurry to maximize sample recovery. The sample slurry was transferred into pre-cleaned, custom-made PTFE weighing boats, dried overnight at 70°C and weighed on a microbalance. After the weight of the boat with the dried down sample was recorded, the sample was removed from the boat using small amounts of MilliQ water from a new micropipette tip with a slow pumping motion to mobilize the dried sample into suspension. The sample slurry was transferred into a pre-cleaned Teflon beaker for dissolution procedures.

The emptied weighing boat was then dried down again at 80 °C before its weight without the sample was recorded. The difference between the two weights was recorded as the sample weight.

The amount of sampling that can be done in each micromill session is limited to the area of the sample surface that can be exposed under the parafilm cut-out. Based on experimenting with different cut-out hole sizes in this study, we found that the hole becomes less efficient at retaining the water droplet by surface tension at a size greater than 5 × 5 mm, causing the droplet to spill and spread over the parafilm. This is not only more prone to drying out during drilling but also becomes more difficult to be pipetted, reducing sample recovery.

4.3.2 Determining the micromill sampling resolution and drilling geometry

The micromill instrument is compatible with a wide assortment of drill bits, with carbide bits and diamond coated bits being the most prevalent in geological applications. To determine the highest sampling resolution that can be achieved by the micromill, a conical carbide bit (2500-0033S 0.008 carbide by Elemental Scientific Lasers) was chosen for this study. Scanning electron microscopy (SEM) images were taken of two bits to document tip geometry and wear. The first bit, 001C, was used to drill very shallow (~5 µm depth) patterns in a synthetic basaltic glass to determine the maximum drilling resolution. The second bit, 001B, was used in fifteen sessions of sampling the same glass with a maximum drilling depth of 30 µm per pass (outlined in the next section). Total drilling time was under 2 minutes for bit 001C and 625 minutes for bit 001B. After drilling by bit 001C, the basaltic glass sample was cleaned and imaged under SEM to characterize the geometry of the drilled patterns. Imaging was conducted at the Scanning Electron Microscope Laboratory at the University of Alberta using a Zeiss Sigma 300 VP-FESEM with an accelerating voltage of 10–25 kV.

4.3.3 Evaluating trace element composition of total procedural blank

To investigate trace element input from the micromilling procedure, 2.780 mg of sample powder was micromilled using bit 001B from two pieces of a synthetic basaltic glass, SGY. The glass was created

from a mixture of reagent grade (certified $\leq 0.01\%$ impurities) major and minor element oxides plus carbonate. The mixture was melted and quenched with no contact with PGE filament ([Blinova and Herd, 2009](#)). Therefore, contamination from the micromilling procedure is expected to reflect in the trace element levels of the milled powder. The glass pieces were mounted in epoxy (Epotek 301) and were milled by series of overlapping holes instead of rastering as we believe the latter would result in greater wear to the drill bit. Drilling was conducted with the drill speed set at 20%; we found that higher speeds would cause the water droplet to splatter, resulting in sample loss.

Following micromill sampling, the remaining glass material was extracted for trace element analysis in order to compare with the micromilled powder. This was done by first polishing down the epoxy mount such that all micromill-sampled surfaces were removed. The epoxy was then dissolved using the Epoxy Remover manufactured by Allied High Tech Products Inc.; the active ingredient is dimethyl sulfoxide. The extracted glass pieces were cleaned in four steps of ultrasonic bath: isopropyl alcohol (a few seconds), distilled water (5 minutes), acetone (15 minutes), then two cycles of MilliQ water (10 minutes each). The glass pieces showed no evidence of surface impurities after cleaning in ultrasonic baths.

Following methods outlined in [Charlier et al. \(2006\)](#), two procedural blanks were prepared for bit 001B. This was done by letting the drill bit spin with the tip suspended in a water droplet seated on a top of a clean parafilm surface for the average duration of a typical drill session (~45 min). To compare potential trace element contribution from a new, unused tip to that from a used one, the blanks were prepared before the first use of the bit, then again after the final drilling session. Two additional blanks were prepared during the dissolution steps.

Trace element compositions were analyzed on a Thermo Scientific Element XR high-resolution magnetic sector inductively-coupled plasma mass spectrometer (HR-ICP-MS) at the Arctic Resources Geochemistry Laboratory (ARGL), University of Alberta, using a method modified from [Ottley et al. \(2003\)](#). Samples were dissolved in 2.5 mL concentrated HNO_3 and 4 mL concentrated HF at 150°C for 48 hours.

Insoluble fluorides were removed by the addition of 1 mL concentrate HNO₃ and evaporation to near dryness twice. The dried samples were diluted to 10 mL with a stock solution of 3% HNO₃ with trace HF, doped with 10 ppb In as an internal standard. Samples were then heated at 80 °C overnight to ensure dissolution. After cooling the samples were diluted to give a final dissolution factor of × 5000. At each dilution step the same stock diluent with In internal standard was used to ensure consistency of the internal standard; this was later used to correct for fluctuations in instrumental conditions during analysis. Analyses were completed using an ESI Teflon nebulizer with an uptake rate of ~50 µL/min. Gas flow rates were 0.8 L/min for the auxiliary gas and 1.0 L/min for the sample gas. The ESI Omega Desolvator was tuned relative to the gas flow parameters to yield signal sensitivity equivalent to 1.2 Mcps on ¹¹⁵In (1 ppb) and oxide formation rate of around 3% (UO/U); flow rates were 4.1 L/min for Ar and 1.40 mL/min for N₂. Each measurement cycle lasted approx. 3 minutes and involved 6 runs and 4 passes, 50 samples per peak with 0.01 sec sampling times. The BHVO-2 basalt was analyzed alongside the samples as a secondary standard. The accuracy of the standard material relative to their accepted values is generally within 10% or better for most elements. Data were processed using an in-house data reduction spreadsheet which propagates uncertainties from the calibration lines for each element, corrections for isobaric interferences (including uncertainties in oxide production), blank correction and internal standard normalisation into the final uncertainty estimates.

4.3.4 Trace element LA-ICPMS of NWA 10299

The volume of sample needed for chromatography-based isotopic analysis is determined by the mass of analyte required for analysis and the concentration of the analyte in the sampling target. We constrain the distribution of Sr and Nd in pyroxene, former igneous plagioclase (referred to as plagioclase for the rest of this study for simplicity), olivine, and merrillite by compiling literature trace element data including *in-situ* LA-ICPMS analysis as well as ICPMS and SIMS analyses of mineral fractions used in geochronology studies.

In addition to literature compilation, we conducted trace element LA-ICPMS analysis on a polished thick section of Northwest Africa (NWA) 10299, a basaltic shergottite, as part of an assessment of the specimen's feasibility for micromill extraction. Trace element analysis of pyroxene and plagioclase was conducted on a New Wave UP-231 Nd YAG laser coupled to a Thermo ICAP-Q quadrupole inductively coupled plasma mass spectrometer at the Canadian Centre for Isotopic Microanalysis (CCIM), University of Alberta. Trace elements were analyzed with 30 µm spot size, 5 Hz pulse rate, and 3–4 J/cm² laser fluence, with ~0.5 L/min He and 2 mL/min N₂ flow rate through the ablation cell. ICP gas flow rates were 14 L/min (cool gas), 0.8 L/min (auxiliary gas), and 0.725 L/min (nebulizer gas). For each analysis, dwell time was 1 ms per mass, with 45 s ablation and 25 s background measurement. All trace element data were corrected for laser and ICP-MS elemental fractionation with internal element Ca calibrated by EPMA ([Sheen et al., 2021](#)) and the external standard BCR-2G. Reference materials NIST 610 and NIST 612 were analyzed as secondary standards to monitor reproducibility and instrument drift. As NWA 10299 is a basaltic shergottite, no olivine is available for analysis. Although merrillite occurs in NWA 10299, no EPMA data were available for internal calibration.

4.4 Results

4.4.1 Geometry of micromill drill bits

SEM images of micromill drill bits used in this study are presented in Fig. 4.3. The drilling surface is conical, measuring ~1.48 mm in length and ~0.64 mm in diameter, with a point angle of 23.5°. The very tip of the bit measures ~30 µm in diameter. Bit 001B exhibited slight defects in the tip prior to first use (Fig. 4.3c). Comparison of pre-use and after-use images suggests that ~33 µm of the tip length was worn away by drilling (Fig. 4.3d). Direct wear to the bit during drilling is supported by images of test patterns drilled by bit 001C, which show sub-micron sized flecks of a high-BSE signal material inside the excavated cavities (Fig. 4.4); EDS analysis yielded W and Co peaks in the flecks, similar to the EDS spectra exhibited

by the bit. The absence of such peaks from the spectra of the basaltic glass suggests the fleck material to be carbide lost from the drill bit.

4.4.2 Trace element composition of total procedural blanks

Results of HR-ICPMS trace element analysis of the synthetic basaltic glass SGY and procedural blanks are summarized in Table 4.1. Trace element levels in the two micromilling and dissolution blanks are generally on the order of 0.1 to 1's of ppt with the exception of Sc, V, Cr, Mn, Nb, and Mo, which reach up to 100's of ppt. Titanium in the pre-use blank measures 1.7 ppb, whereas Ca measures 46 ppb. Copper, Rb, Sr, Ba, and Hf are below detection limit in both blanks. Magnesium, Zn, and Ga are below detection limit only in the pre-use blank and Ca, Cu, Gd, Lu, and Pb are below detection limit only in the used-bit blank. With the exceptions of Cr and Mn, trace element levels in the pre-use blank are higher than those in the after-use blank by an average factor of ~5. Cobalt measures ~70 ppb in the pre-use blank and ~130 ppb in the after-use blank. In contrast, the dissolution-only blank contains 20 ppt Co. Most trace elements in the dissolution-only blank were not quantified, with Ti measuring 276 ppt and Sc, Rb, Sr, Ba, Gd, Hf, and Ta measuring up to 10's of ppt.

Large ion lithophile element (LILE; Rb, Cs, Sr, Ba, Pb) content in micromilled SGY powder generally ranges from under 1 ppm to a few ppm's, with Sr having the highest concentration at ~20 ppm. High field strength element (HFSE; Y, Nb, REE, Hf, Ta, Th, U) content ranges from a few ppb to hundreds of ppb. Combined average of the two SGY whole pieces displays overall higher trace element levels than the micromilled powder, by factors of up to ~3 with the exception of Pb (a factor of ~5). Average cobalt content in the whole pieces is 0.44 ppm, two orders of magnitude lower than in the micromilled powder (58.56 ppm).

4.4.3 Trace elements LA-ICPMS of NWA 10299 major minerals

Results of LA-ICPMS trace element analysis of pyroxene and plagioclase in NWA 10299 are summarized in Table 4.2. Rubidium is below detection limit in most analyses, measuring 0.2–0.3 ppm in

plagioclase glass. Strontium concentration is 0.24–1.83 ppm in clinopyroxene and 24.0–25.2 ppm in plagioclase. Neodymium is below detection limit in most silicate analyses, measuring ~0.10 ppm in only two clinopyroxene analyses. Samarium is below detection limit in all silicate analyses. The Sr content of plagioclase (24–25 ppm) in NWA 10299 is below the lowest value previously reported in literature (43 ppm, [Shafer et al., 2010](#)).

4.4.4 Minimum required micromilling volumes for Sr, Nd isotopic analyses

To estimate how much micromilling is required to yield enough sample for Sr and Nd isotopic analyses, we assume a starting point of 0.250 ng Sr and 1 ng Nd minimum required for TIMS and MC-ICP-MS analysis ([Chu et al., 2009](#); [Harlou et al., 2009](#); [Huang et al., 2012](#)). This is divided by the Sr and Nd concentrations in the target mineral to arrive at a minimum required mass, which is in turn divided by the mineral density to yield the minimum required volume. Based on phases most commonly used in shergottite Rb–Sr and Sm–Nd geochronology, we estimate minimum required volumes for pyroxene, plagioclase, olivine, and merrillite based on Sr and Nd concentrations reported in shergottite literature and in this study (Table 4.3). Using the upper limit of Sr concentration range in literature, the minimum required sample volumes are on the order of $10^5 \mu\text{m}^3$ for plagioclase and merrillite, $10^6 \mu\text{m}^3$ for pyroxene, and $10^7 \mu\text{m}^3$ olivine. The same calculation applied to TIMS Nd isotopic analysis yields minimum required sample volumes on the order of $10^5 \mu\text{m}^3$ for merrillite, $10^7 \mu\text{m}^3$ for pyroxene and plagioclase, and $10^9 \mu\text{m}^3$ for olivine.

4.5 Discussion

4.5.1 Micromill blank contribution

With respect to Sr isotopic analysis, previous studies by [Charlier et al. \(2006\)](#) and [Harlou et al. \(2009\)](#) demonstrated that it is possible to achieve low long-term total procedural blanks (<0.5% of total Sr) for micromilled samples containing as little as 3 ng Sr. Although multiple blank measurements were not possible in this study for determining a long-term average procedural blank value, blanks collected

before and after the use of drill bit 001B yielded Rb and Sr levels below detection limits. Images of excavated patterns and drill bits after use show evidence of carbide material being lost by the drill bit during drilling by coming into contact with the sample surface. This is supported by the much higher Co content in the micromilled glass powder (~59 ppm) compared to the bulk glass (0.44 ppm), as Co is used as a binding agent in carbides. Furthermore, both micromilling+dissolution blanks contain ppb levels of Co compared to 20 ppt in the dissolution blank, indicating that carbide material is lost by the drill bit to the water droplet even when no contact is made with the solid sample surface.

The consistently higher trace element levels in the bulk glass analyses compared to the micromilled powder suggests contamination in the former. The glass pieces were extracted by dissolving the epoxy mount. Given the multiple cycles of ultrasonic baths, it is unlikely that the dimethyl sulfoxide solvent remained on the glass surface prior to dissolution. Although dimethyl sulfoxide is known to interact with smectite (e.g., [Stanjek et al., 2018](#)), the synthetic glass sample did not contain clay minerals, hence alteration of the sample by dimethyl sulfoxide is also unlikely. We attribute the contamination in the bulk glass analyses to epoxy that may have remained trapped in surface irregularities and/or cracks in the glass and could not be observed under microscope. The presence of contamination precludes an accurate assessment of the composition of the pure bulk glass. The measured trace element content of the micromilled powder, therefore, constitutes the maximum estimate of contamination that is introduced by the combined micromilling and dissolution procedures.

Investigation by [Charlier et al. \(2006\)](#) and [Harlou et al. \(2009\)](#) of various components involved in Rb–Sr isotopic analysis of micromilled samples showed that the total procedural blank is dominated by the Sr spec resin used during column chemistry; average Sr blank introduced during column steps was 4.0 pg versus a long-term average total procedural blank of 5.4 pg ([Harlou et al., 2009](#)). However, in these studies the drill bit contribution was assessed by water rinses. Assuming that the drill bit is homogeneous in composition, trace element contribution by the bit to the micromilling procedural blank should be

proportional to the wear introduced by drilling. Therefore, with other factors held constant, the micromilling procedural blank may ideally be minimized by reducing the total drilling time and/or the area of contact between the bit and the sample solid (e.g., drilling depth per pass). A more precise evaluation of blank contribution may be conducted by directly analyzing the composition of the drill bit, as has been previously reported for diamond-coated bits ([Pollington and Baxter, 2011](#)).

We further note that the concentration of most trace elements in the pre-use micromill procedural blank is higher than in the after-use one. If all other factors are held constant and additional sources of contamination are assumed to be negligible, the discrepancy in trace element levels may represent different amounts of carbide shedding. As any measured carbide loss occurs only at the interface between the drill bit and the water droplet, the rate at which the water droplet was replenished during the ~45 min sampling sessions may cause variations in the total surface area of the drill bit that was in contact with water during this time. The defect observed in bit 001B before first use may also result in a different total area in contact with water as compared to the after-use geometry. However, this difference should be negligible as the water droplet covered up to a few mm's of the bit length during the preparation of both blanks.

Concentrations of Nd and Sm in the procedural blanks collected in this study are in the range of a few ppt, with Sr and Rb below detection limits; this contrasts with water rinses of drill bits in [Harlou et al. \(2009\)](#), which reports higher Sr and Rb levels (up to a few pg) compared to Nd and Sm (below detection limits). This may be attributed to compositional differences in the drill bits as this study used bits from a manufacturer different from those in [Harlou et al. \(2009\)](#). The discrepancy may also be caused by differences in blank contribution from additional components during the collection procedure (e.g., parafilm, micropipette tip). An evaluation of Nd and Sm blank contribution from diamond-coated drill bits was reported by [Pollington and Baxter \(2011\)](#), achieved by directly dissolving the drill bit. The sampling protocol developed in their study, for the analysis of garnet annuli, bypasses drill bit contamination by

collecting only solid material isolated between trenches cut by the micromill. Although this method enables cleaning and removes practically all blank contribution from the micromilling procedure, it has only been applied to mm-scale targets with a large sampling footprint (i.e. volume lost to drilling is greater than the volume of the extracted sample).

As our assessment focuses on contamination arising from the drilling process, the two procedural blanks collected in this study bypassed the Teflon weighing boats. For a comprehensive assessment of blank contribution in each micromilled fraction for isotopic analysis, the weighing boats should also be examined.

4.5.2 Required drilling volume

We examine shergottite petrography, with NWA 10299 as a case example, for the feasibility of extracting the estimated minimum required volumes of each target phase using the micromill (Table 4.3).

For ideal sampling:

1. The mineral should be of large enough grain size to support the required sample volume either by extracting a single grain or several grains, without needing to mill deep into the grains so as to minimize sampling non-target phases in the z-direction.
2. The petrography and mineral morphology should accommodate the micromill sampling resolution (which varies with the drill bit geometry and drilling depth used), such that sampling of non-target phases in the lateral direction is minimized.
3. The drilling time and number of sessions for extracting each fraction should be minimized, in order to minimize procedural contamination.

To evaluate factors 1 and 2, we convert volumes estimated in Table 4.3 into equivalent drilling area. To minimize the likelihood of encountering non-target phases in the subsurface, we assume a standard petrographic thin section with 30 μm thickness and a maximum allowed drilling depth of 20 μm . Although a thicker section allows for greater drilling depth, a standard thin section is more compatible

with transmitted light microscopy which can aid in avoiding non-target phases in the sample subsurface when drilling.

The equivalent minimum drilling area required for the four target minerals for Sr and Nd isotopic analysis is listed in Table 4.4. Equivalent minimum areas for plagioclase, merrillite, and pyroxene for creating one Sr fraction are on the order of $10^4 \mu\text{m}^2$. When compared to typical plagioclase grains in NWA 10299, the drilling area can be accommodated within a single grain (Fig. 4.5a). Because merrillite is generally finer-grained than plagioclase, the required drilling area is supported by sampling several grains in one session (Fig. 4.5b). However, the subhedral morphology of merrillite in NWA 10299 may reduce the sampleable area per grain as the micromill drill hole at this drilling depth has a diameter of $\sim 40 \mu\text{m}$. Typical pyroxene grains in NWA 10299 are under 1 mm in length and width, which when compared with the estimated minimum required drilling area also necessitates multiple grains to be sampled for creating one fraction (Fig. 4.5c). The minimum required drilling area for olivine is on the order of $10^5 \mu\text{m}^2$, an order of magnitude greater than those required for the other three minerals. Although NWA 10299 is a basaltic shergottite and does not contain olivine, olivine is ubiquitous to olivine-phyric and poikilitic shergottites, commonly occurring as prismatic megacrysts ranging from a few hundreds of μm to greater than 1 mm in size (e.g., [Zipfel et al., 2000](#); [Usui et al., 2009](#); [Gross et al., 2011](#)). Similar to merrillite and pyroxene, the minimum required drilling area determined for olivine can be fulfilled by combining several grains into one fraction. For Nd isotopic analysis, the minimum required drilling areas are up to three orders of magnitude greater than those for Sr isotopic analysis with the exception of merrillite, which is only ~ 3 times greater than that for Sr (Table 4.4). This requires significantly larger number of grains to be sampled in order to create one fraction for Nd isotopic analysis.

The above estimates assume an ideal and simplified scenario where each target mineral is compositionally homogeneous, has the highest Sr or Nd concentration in the range reported in literature,

and can be milled in the entirety of its exposed surface area on the sample section. However, many additional aspects inherent to shergottites create technical complications for micromill sampling.

4.5.2.1 Compositional variation

Estimates in Tables 4.4 and 4.5 assume the highest Sr and Nd concentrations out of the reported range for the target minerals. Realistically, variation of trace element content within a grain, between grains, and between shergottites would cause the actual required drilling volume to be greater than the minimum estimates. Within-grain variation is most prominently exhibited by pyroxene, which is commonly zoned in shergottites as a result of evolving melt compositions during crystal growth (e.g., [Wadhwa et al., 1994](#)). Fractional crystallization, for example, causes incompatible elements to be more enriched in pyroxene rims compared to cores. The Sr and Nd values used for pyroxene estimates in tables 4.4 and 4.5 represent such evolved rim compositions. Therefore, if entire grains of pyroxene were sampled, the overall trace element concentration would be diluted by the less enriched zones; this requires a larger volume to be drilled to achieve the required analyte mass. Furthermore, trace element content varies from shergottite to shergottite as a function of mantle source composition(s) and magmatic history. We note that surveyed pyroxene in NWA 10299 contains 0.24–1.83 ppm Sr, up to two orders of magnitude lower than the maximum concentration of 49.7 ppm used in calculations. Hence, sampling pyroxene in NWA 10299 for Sr isotopic analysis may require a drilling volume up to 200 times greater than the minimum estimate.

The within-grain variation of incompatible trace elements in plagioclase, olivine, and merrillite in shergottites has been less studied. Variations in the surveyed plagioclase and merrillite in NWA 10299 are more likely controlled by between-grain compositional differences. We note that the reported ranges of Sr in plagioclase and merrillite and of Nd in merrillite span one order of magnitude. Therefore the realistic required drilling volume for these minerals would vary over a range less than those where the reported range is much larger, such as the three orders of magnitude range of Sr in olivine (Table 4.3).

4.5.2.2 Grain morphology vs. drilling resolution

At a drilling depth of 20 µm, the micromill drill bit chosen for this study has a sampling resolution of ~40 µm (Fig. 4.5). We deem this to be the finest tip size of currently commercially available drill bits. Although pyroxene, plagioclase, and olivine in shergottites commonly occur in grain sizes of hundreds of µm to a few mm, grain boundaries are rarely perfectly linear, such that any shape irregularities on a scale finer than 40 µm preclude sampling the very edges of the grain. While merrillite observed in NWA 10299 is largely subhedral, euhedral and anhedral occurrences are also common in shergottites ([Shearer et al., 2015](#)). Large, euhedral grains are preferred in order to maximize the proportion of area that can be sampled without drilling into neighbouring phases.

The presence of inclusions poses further challenges to sampling pure mineral fractions. Late-stage phases in shergottites commonly occur in the interstices of major mineral grains, sometimes enveloped within the rim of the latter. In NWA 10299, pyroxene rims host assemblages of Ca-phosphates, Fe-Ti oxides, fayalitic olivine, Fe sulfides, glass, and/or baddeleyite ([Sheen et al., 2021](#)), often at grain sizes under 10's of µm. Olivine in shergottites is also observed to contain inclusions of spinel and trapped melt (e.g., [Goodrich et al., 2003](#); [Usui et al., 2012](#)), which occur at sizes ranging from 10's of µm to under 10 µm and can be pervasive. Merrillite, as a late-stage accessory phase, may contain inclusions of glass and/or apatite (e.g., [McCubbin et al., 2014](#)). The presence of inclusions at a scale finer than the ~40 µm sampling resolution would require avoiding portions of a target grain in order to obtain a pure mineral fraction; this reduces the total sampleable area per grain and a greater number of grains needs to be sampled to create one fraction for isotopic analysis. An additional complication in the case of pyroxene is that pyroxene rims are often the most enriched in incompatible elements out of the whole grain; reduced sampling of these rims also increases the volume of pyroxene needed to reach the required analyte mass. Compared to pyroxene, olivine, and merrillite, inclusions are less pervasive in plagioclase in shergottites; intergrowths

of K-feldspar and silica, despite being commonly associated with plagioclase, form distinct patches on the edge of plagioclase grains and can be more easily avoided during sampling compared to inclusions.

4.5.2.3 Shock features and alteration

Shergottites, like other meteorites sourced from differentiated bodies, underwent shock metamorphism during ejection from the parent body, resulting in a wide range of secondary features that crosscut the igneous texture ([Fritz et al., 2017](#)). These include (but are not limited to) planar deformation, fractures, mosaicism, transformation of igneous plagioclase to maskelynite or vesiculated glass, and the formation of shock melt pockets and/or veins (e.g., [Walton et al., 2012](#)). Fractures in shergottites are extensive, irregular, and occur on multiple scales (e.g., Fig. 4.5). These may act as pathways for terrestrial alteration, as evidenced in the infilling of fractures by secondary minerals (carbonates, sulfates, etc.), the remobilization of Ce in silicates in cold desert meteorites, and LREE contamination with a terrestrial crustal signature in hot desert meteorites ([Croaz et al., 2003](#)). Because micromilled powder cannot be cleaned, these secondary phases must be avoided when drilling in order for the igneous isotopic signature to be accurately measured. Previous studies on hot desert shergottites have found significant terrestrial contamination in Rb–Sr and Sm–Nd isotope systematics that cannot be eliminated by leaching, resulting in increased age uncertainties (e.g., [Borg et al., 2001](#); [Nyquist et al., 2001](#); [Ferdous et al., 2017](#)). This is likely attributed to alteration phases trapped within extensive fractures that can be on scales smaller than the separated mineral grains. Assuming that contamination from terrestrial alteration is limited to the fracture cavities and do not significantly extend into the lattice structure of adjacent igneous minerals, such contamination can in theory be avoided during micromilling by avoiding fractures. However, the high density of fractures in shergottites may limit the area available for sampling per mineral grain with respect to the ~40 µm maximum drilling resolution. Like inclusions, this can significantly reduce the area that can be drilled per grain such that a greater number of grains needs to be sampled to create a single fraction. Alteration in shergottites can be a highly heterogeneous process, with some grains of the same mineral

more affected by others ([Crozaz et al., 2003](#)). Because not all fractures in a sample may be equally subjected to weathering and alteration, chemical mapping may be used to characterize the distribution of secondary phases in fractures across a sample. If a fractured grain contains negligible alteration phases, then it might be possible to sample the entire grain for isotopic analysis.

Shock melt pockets and veins in shergottites represent a mix of melted whole-rock components with fractionated parent/daughter nuclides and higher susceptibility to terrestrial weathering compared to the host rock ([Jagoutz, 1989](#); [Zipfel et al., 2000](#); [Wadhwa et al., 2001](#)). These features are generally less pervasive and more locally confined than fractures and can be more easily avoided during drilling. We further note that, although plagioclase is generally less prone to fracturing compared to other major igneous minerals in shergottites, there is evidence in some shergottites for local assimilation of Ca-phosphates during shock melting of plagioclase, which modifies the trace element ratios and results in non-isochronous isotopic compositions (e.g., [Shafer et al., 2010](#); [Ferdous et al., 2017](#)). As these plagioclase compositions are characterized by higher-than-normal P content, chemical mapping may aid in identifying these domains.

4.5.3 Effects of encountering non-target phases

Due to complexities in grain size, morphology, and texture, not all target phases in shergottites may support micromill sampling in an idealized fashion of obtaining the required volume in one continuous block of excavation without encountering non-target phases. If only igneous phases are present and all phases are assumed to be cogenetic, incursion into an adjacent mineral during drilling would result in a mixed isotopic composition that is a function of the proportion of the minerals present, the concentration of the elements of concern in each mineral, and the respective isotopic composition of each mineral. The resulting isotopic ratios would, in theory, be intermediate between the isotopic ratios of the involved minerals. A combination of pure and mixed mineral fractions may therefore increase the

precision of an isochron regression, whereas having only mixed fractions may reduce it due to decreased data spread.

With respect to Rb–Sr systematics, plagioclase and merrillite are the main carriers of Sr in shergottites and typically define the low end of Rb/Sr ratios whereas pyroxene and olivine define the high end. As Sr and Rb contents in plagioclase and merrillite are generally 1–2 orders of magnitude greater than in pyroxene and olivine (Table 4.3), mixing would be dominated by the Rb–Sr isotopic composition of the former two minerals. It is therefore more crucial for isochron purposes to sample pure fractions of pyroxene and olivine than for plagioclase and merrillite. Merrillite is also the main carrier of Nd and Sm, with concentrations of 2–3 orders of magnitude greater than silicates (Table 4.3). Obtaining pure silicate fractions is therefore important for achieving sufficient data spread in Sm–Nd space.

The sensitivity of low-Sr and low-Nd minerals to mixed sampling with high-Sr and high-Nd minerals further illustrates the need to avoid non-target phases when drilling. For example, melt inclusions in olivine have been found to contain Sr and Nd concentrations up to four orders of magnitude greater than the olivine host ([Shafer et al., 2010](#)). Apatite, the other major Ca-phosphate mineral in shergottites subordinate to merrillite, also contains high Sr and Nd and may occur as fine inclusions. While apatite inclusions in a pyroxene rim can significantly modify the trace element composition of a micromilled pyroxene fraction, apatite inclusions in merrillite (e.g., [McCubbin et al., 2014](#)) would have less effect as both the inclusion and the host are major Sr and Nd carriers. If a low-Sr or low-Nd phase is encountered when sampling a high-Sr or high-Nd target, the resulting effect on the final mixed isotopic composition would also be less drastic than the other way around.

4.5.4 Realistic required mass and sampling time

In addition to petrographical and geochemical constraints on micromill sampling, we evaluate analytical constraints associated with the minimum required analyte mass. For the purpose of arriving at a minimum estimate, we have chosen in this study a target mass of 0.250 ng Sr and 1 ng Nd based on

studies on small-sample Sr and Nd isotopic analyses (Chu et al., 2009; Harlou et al., 2009; Harvey and Baxter, 2009). Although Sm–Nd isotopic analysis has been achieved for samples containing as little as 0.100 ng Nd with external reproducibility of 37 ppm (2 relative standard deviations; e.g., Li et al., 2007; Wakaki and Ishikawa, 2018; Reinhard et al., 2019), we note that in Sm–Nd shergottite geochronology studies the total recovered Nd in a fraction is typically a few ng, with larger analytical uncertainties at samples sizes of <0.5 ng Nd (e.g., Symes et al., 2008; Shih et al., 2011). The mass of recovered Sr per fraction in shergottite geochronology is typically much greater than the chosen 0.250 ng limit as Rb and Sr are usually purified from the same mineral fractions used for Sm–Nd geochronology.

To estimate the drilling time needed for obtaining one mineral fraction, we assume a drilling rate of $2.3 \times 10^5 \mu\text{m}^3/\text{min}$ estimated from micromill sessions during this study. For a fraction of 0.250 ng Sr, sampling times for plagioclase and merrillite are under 10 minutes for the entire range of Sr concentrations reported in shergottites (Fig. 4.6a, b). Pyroxene sampling may be done in less than an hour if Sr concentration is greater than ~5 ppm, whereas olivine sampling would take at least an hour. Sampling time may take over five hours if the target mineral contains less than ~1 ppm Sr as can be the case for pyroxene and olivine (Fig. 4.6a, b). For a fraction of 1 ng Nd, only merrillite can be sampled in under an hour; sampling time for pyroxene, plagioclase, and olivine exceeds five hours (Fig. 4.6c, d). Although the micromill instrument is capable of running long sessions (with the longest achieved during this study being 97 minutes), the wet-based sampling method is not suitable for operating at a scale of several hours. This is chiefly due the water droplet, in which drilling takes place, is prone to evaporating as a combined result of low humidity in the fume hood environment and increased water temperature from friction-induced heating of the drill bit and the sample surface. During drilling sessions in this study, we found that the water droplet had to be replenished approximately every five minutes to prevent it from drying out. This makes the sampling procedure a labor-intensive process especially if running for long durations. Realistically, a fraction that requires several hours of drilling time (e.g. olivine for Nd) may be split into

multiple sessions considering that only a maximum 5 x 5 mm sample area can be exposed for drilling each session. Sampling in multiple sessions may increase the procedural blank which can affect the final analytical precision given the low Sr or Nd content in these minerals (<1 ppm). Based on these factors we do not consider the five hours or greater drilling time required for a 1 ng Nd fraction to be feasible for silicates in shergottite.

4.5.5 Current limits on micromill sampling for mineral Sr, Nd isotopic analysis

With shergottite petrography and geochemistry as unalterable constraints on micromill sampling, we assess other technical constraints identified in this study that may be advanced upon in future for increased feasibility of sampling shergottites for multi-mineral Rb–Sr and/or Sm–Nd geochronology.

- *Drilling resolution* – Finer conical drill bits with a smaller tip diameter, preferably down to ~10 µm or under, would enable more flexible sampling that bypasses non-target phases. This should be combined with upgraded optical microscopy of the micromill instrument so that heterogeneities on the scale of a few microns to 10's of microns can be more easily identified during drilling.
- *Required analyte mass* – A smaller required mass of Sr and or Nd for isotopic analysis is the only alterable factor for effectively reducing the drilling volume needed. This depends on advances in TIMS capabilities (e.g., signal resolution) for increased precision of microvolume analysis as well as achieving lower procedural blanks for the micromilling and column chemistry procedures.

Based on current constraints identified in this study, we consider micromill sampling of shergottites to be feasible for extracting only select minerals for Sr (plagioclase, merrillite, and pyroxene) and Nd (merrillite) isotopic analyses, whereas sampling other minerals is limited by long drilling time required. Sampling feasibility of these minerals is further limited by the availability of grains with sufficient dimensions and favorable morphologies (e.g., with few or no inclusions) compatible with the maximum drilling resolution of ~40 µm. Being able to sample merrillite alone precludes the feasibility of Sm–Nd geochronology. Although combining plagioclase, merrillite, and pyroxene analyses may achieve some data

spread in Rb–Sr space, it remains to be tested how this data spread compares to mineral fractions obtained from bulk separation protocols. We note that the inability of the micromill method to discriminate sampling by specific gravity and/or magnetic susceptibility may result in limited ability to sample end-member compositions of a specific mineral for maximizing the overall Rb/Sr spread. Further studies, preferably directly testing shergottite samples for micromilling, are required to assess the feasibility of constructing Rb–Sr isochrons.

4.5.6 Alternative applications

This study demonstrates the theoretical feasibility of micromill extraction of select minerals in shergottites for Sr and Nd isotopic analysis. If the crystallization age of a shergottite is known, mineral Sr and Nd isotopic compositions can be used to calculate initial $^{87}\text{Sr}/^{86}\text{Sr}$ and $^{143}\text{Nd}/^{144}\text{Nd}$ ratios of the rock, which provide constraints on the composition of the mantle source(s) from which the parent magma was derived. Mantle source isotopic compositions have been used not only to establish geochemical groupings of shergottites, but also constrain potential petrogenetic links among shergottites as well as elucidating the evolution of the martian mantle (e.g., [Borg et al., 2002](#); [Debaille et al., 2008](#); [Combs et al., 2019](#)). As initial $^{87}\text{Sr}/^{86}\text{Sr}$ and $^{143}\text{Nd}/^{144}\text{Nd}$ ratios are typically constrained from whole-rock powder analysis or as part of Rb–Sr and Sm–Nd geochronology, micromill sampling may provide a less destructive alternative for determining initial Sr and Nd isotopic compositions if the crystallization age is already known. For this application, merrillite would be the most suitable target for sampling as it contains both Sr and Nd in sufficient amounts such that maximum scientific information can be obtained with minimum drilling required.

4.6 Conclusions

Our assessment identifies limitations associated with micromill operation and with shergottite petrography and mineral chemistry that make micromill sampling unsuitable for multi-mineral Rb–Sr and Sm–Nd geochronology of shergottites. Due to the variability of Sr and Nd concentrations in the target

minerals, extracting enough mineral volume for one fraction for isotopic analysis may take from under an hour (plagioclase, merrillite, and pyroxene for Sr; merrillite for Nd) to over five hours (olivine for Sr; pyroxene, plagioclase, and olivine for Nd), with long micromill sessions being more labor-intensive and prone to greater procedural blanks. In addition, the presence of complex mineral morphologies, fine-grained inclusions, fracture-induced terrestrial alteration, and/or shock melt features may reduce the amount of sampleable area per grain with respect to the maximum sampling resolution of the micromill (~40 µm at a drilling depth of 20 µm for the drill bit selected for this study), leading to inefficient sampling for obtaining pure mineral fractions. Based on these factors we consider micromill sampling for Sr and Nd isotopic analysis to be suitable for only select minerals in shergottites, specifically those that contain sufficient concentrations of the target elements to keep the required sample volume low (plagioclase, merrillite, and pyroxene for Sr; merrillite for Nd). Application for Sm–Nd geochronology is therefore not feasible under current technical constraints. Feasibility for constructing Rb–Sr isochrons, namely the capability to achieve sufficient Rb/Sr data spread for statistically robust regression, remains to be tested. Potential advances in increasing drilling resolution and decreasing required analyte mass may enhance the application of micromill sampling for shergottite geochronology.

Table 4.1. HR-ICPMS trace element analysis of bulk synthetic basaltic glass SGY, micromilled powder, and procedural blanks.

Sample	SGY - micromilled powder	SGY - whole piece 1	SGY - whole piece 2	SGY - whole pieces avg	Proc. Blk1 - unused bit + dissolution	Proc. Blk2 - used bit + dissolution	Proc. Blk3 - dissolution only
Mass (mg)	2.780	14.8	17.8				
	(ppm)				(ppt)		
Mg	163060	147211	145482	146347	b.d.	881	27799
Ca	30448	53419	53994	53707	46106	b.d.	21911
Sc	0.06	0.07	0.07	0.07	29.6	4.3	3.3
Ti	2441	3677	3575	3626	1709	421	276
V	3.70	10.15	9.75	9.95	559	106	18
Cr	4732	3291	2940	3115	77	763	851
Mn	4682	4817	4686	4752	35	81	101
Co	58.56	0.43	0.44	0.44	70316	130420	20
Cu	7.49	2.32	3.04	2.68	b.d.	b.d.	44
Zn	5.33	2.24	1.74	1.99	b.d.	1337	1358
Ga	0.20	0.15	0.15	0.15	b.d.	2.1	b.d.
Rb	0.30	0.36	0.36	0.36	b.d.	b.d.	3.5
Sr	19.76	25.27	25.18	25.22	b.d.	b.d.	80.7
Y	0.38	0.68	0.68	0.68	2.2	1.9	0
Nb	0.52	0.98	0.93	0.96	78.4	50.4	0
Mo	1.20	0.48	0.54	0.51	307.2	20.1	30.6
Cs	0.01	0.03	0.03	0.03	2.5	0.2	0
Ba	5.81	7.46	12.55	10.00	b.d.	b.d.	57.4
La	0.56	0.99	1.00	1.00	2.9	1.4	0
Ce	1.51	2.22	2.24	2.23	3.4	2.8	0
Pr	0.12	0.20	0.20	0.20	0.8	0.5	0
Nd	0.37	0.64	0.65	0.64	6.2	1.0	0
Sm	0.07	0.12	0.12	0.12	3.2	0.2	0
Eu	0.01	0.02	0.03	0.03	0.5	0.1	0
Gd	0.07	0.10	0.10	0.10	3.7	b.d.	11.4
Tb	0.01	0.02	0.02	0.02	0.3	0.1	0
Dy	0.06	0.09	0.10	0.10	1.5	0.3	0
Ho	0.01	0.02	0.02	0.02	0.4	0.1	0
Er	0.04	0.06	0.06	0.06	1.0	0.2	0
Yb	0.05	0.09	0.09	0.09	1.4	0.2	0
Lu	0.01	0.01	0.01	0.01	0.3	b.d.	0
Hf	0.66	0.84	0.83	0.83	b.d.	b.d.	4.4
Ta	0.07	0.13	0.13	0.13	3.7	1.2	14.3
Pb	1.02	4.60	6.40	5.50	2.3	b.d.	0
Th	0.09	0.18	0.18	0.18	1.7	0.3	0
U	0.12	0.24	0.27	0.25	1.1	0.2	0

b.d. = below detection limit

Table 4.2. Results of LA-ICPMS trace element analysis of pyroxene and plagioclase glass in NWA 10299. All concentrations are reported in ppm.

Pyroxene												Plagioclase														
	px_1	px_2	px_3	px_4	px_5	px_6	px_7	px_8	plg_1	plg_2	plg_3	n=3	Gao et al. (2002)	n=3	Gao et al. (2002)	n=3	Gao et al. (2002)									
	High-Ca	Low-Ca	High-Ca	Low-Ca	High-Ca		High-Ca	High-Ca		Plag core	2σ	Plag core	2σ	Plag rim	2σ	2σ	2σ									
	core	2σ	rim	2σ	core	2σ	rim	2σ	core	2σ	core	2σ	core	2σ	core	2σ	2σ	2σ								
Rb	b.d.	b.d.	b.d.	b.d.	b.d.	b.d.	b.d.	b.d.	0.212	0.098	b.d.	0.261	0.082	406	12	431	31	2.1	32							
Sr	0.36	0.04	0.36	0.05	1.27	0.07	0.24	0.05	1.03	0.15	1.83	0.20	0.39	0.04	0.46	0.05	24.0	1.6	25.2	2.0	543	15	497	78	5.3	75
Y	0.91	0.05	0.87	0.05	0.61	0.05	1.19	0.06	0.49	0.03	0.76	0.03	1.05	0.05	0.90	0.04	0.136	0.043	b.d.	b.d.	492	15	450	38	2.3	38
Zr	0.59	0.09	1.80	0.34	b.d.	b.d.	2.24	0.28	0.28	0.09	0.60	0.10	1.11	0.15	1.49	0.24	0.77	0.25	b.d.	b.d.	497	20	439	38	3.8	37
Nb	b.d.	b.d.	b.d.	b.d.	b.d.	b.d.	b.d.	b.d.	b.d.	b.d.	b.d.	b.d.	b.d.	b.d.	b.d.	b.d.	486	15	420	40	2.8	36				
Cs	b.d.	b.d.	b.d.	b.d.	b.d.	b.d.	b.d.	b.d.	b.d.	b.d.	b.d.	b.d.	b.d.	b.d.	b.d.	b.d.	328	10	360	42	2.5	41				
Ba	b.d.	b.d.	3.09	0.39	b.d.	b.d.	0.77	0.16	4.49	0.3	0.58	0.15	b.d.	13.57	0.83	2.51	0.3	4.87	0.71	637	24	425	40	5.4	37	
La	0.025	0.008	b.d.	b.d.	b.d.	b.d.	0.025	0.008	b.d.	0.025	0.008	b.d.	b.d.	b.d.	b.d.	453	12	457	36	2.1	37					
Ce	0.061	0.011	b.d.	b.d.	b.d.	b.d.	0.021	0.007	0.072	0.014	0.033	0.009	0.073	0.014	0.037	0.012	b.d.	b.d.	436	14	448	39	2.8	38		
Pr	0.019	0.006	b.d.	b.d.	b.d.	b.d.	0.018	0.006	b.d.	0.016	0.005	b.d.	b.d.	b.d.	b.d.	433	13	430	37	2.6	37					
Nd	0.105	0.034	b.d.	b.d.	b.d.	b.d.	b.d.	b.d.	b.d.	0.104	0.033	b.d.	b.d.	b.d.	b.d.	455	14	430	36	3.0	35					
Sm	b.d.	b.d.	b.d.	b.d.	b.d.	b.d.	b.d.	b.d.	b.d.	b.d.	b.d.	b.d.	b.d.	b.d.	b.d.	477	17	449	38	3.0	37					
Eu	0.031	0.010	b.d.	b.d.	b.d.	b.d.	b.d.	b.d.	b.d.	b.d.	b.d.	0.077	0	b.d.	428	13	460	35	2.4	35						
Gd	0.117	0.037	b.d.	b.d.	b.d.	b.d.	0.109	0.034	0.124	0.039	0.114	0.036	b.d.	b.d.	b.d.	460	15	420	37	2.8	36					
Tb	0.020	0.007	b.d.	b.d.	b.d.	b.d.	0.017	0.005	0.020	0.006	0.017	0.005	b.d.	b.d.	b.d.	435	12	442	36	2.1	36					
Dy	0.156	0.026	0.161	0.051	b.d.	0.160	0.051	0.076	0.024	0.124	0.018	0.195	0.030	0.107	0.024	b.d.	b.d.	464	16	426	36	2.7	36			
Ho	0.041	0.005	0.038	0.012	0.027	0.009	0.039	0.012	0.017	0.005	0.026	0.006	0.041	0.006	0.035	0.006	b.d.	b.d.	471	15	448	38	2.3	38		
Er	0.11	0.02	0.117	0.037	0.079	0.025	0.120	0.038	0.046	0.015	0.059	0.014	0.111	0.021	0.099	0.015	b.d.	b.d.	464	13	426	38	2.2	37		
Tm	0.019	0.007	b.d.	b.d.	b.d.	0.035	0.011	b.d.	b.d.	0.019	0.006	0.016	0.005	b.d.	b.d.	b.d.	487	14	420	38	2.0	37				
Yb	0.083	0.026	0.187	0.059	b.d.	0.179	0.056	0.069	0.022	0.073	0.023	0.094	0.030	0.079	0.025	b.d.	b.d.	474	16	460	39	3.0	40			
Lu	0.019	0.006	b.d.	b.d.	b.d.	0.030	0.010	b.d.	0.015	0.005	0.020	0.006	0.016	0.005	b.d.	b.d.	472	14	435	37	2.0	37				
Hf	b.d.	b.d.	b.d.	b.d.	0.146	0.046	b.d.	b.d.	b.d.	b.d.	b.d.	b.d.	b.d.	b.d.	b.d.	418	12	418	35	2.6	35					
Ta	b.d.	b.d.	b.d.	b.d.	b.d.	b.d.	b.d.	b.d.	b.d.	b.d.	b.d.	b.d.	b.d.	b.d.	b.d.	484	13	376	40	2.2	36					
Th	b.d.	b.d.	b.d.	b.d.	b.d.	b.d.	b.d.	b.d.	b.d.	b.d.	b.d.	b.d.	b.d.	b.d.	b.d.	484	14	451	38	2.2	27					
U	b.d.	b.d.	b.d.	b.d.	b.d.	b.d.	b.d.	b.d.	b.d.	b.d.	b.d.	b.d.	b.d.	b.d.	b.d.	440	15	457	37	2.2	27					

b.d. = below detection limit

Table 4.3. The range of Sr and Nd concentrations in major minerals in shergottite literature, with minimum volume required for analysis based on 0.250 ng Sr and 1 ng Nd for isotopic analysis.

	Pyroxene	Plagioclase	Olivine	Merrillite
Density (g/cm ³)	3.3	2.7	3.6	3.1
Sr (ppm)	0.25-49.7	24-346	0.006-6.9	85-334
Minimum mass (μg)	5.0	0.72	36.2	0.75
Minimum volume (μm ³)	1.5×10^6	2.7×10^5	1.0×10^7	2.4×10^5
Nd (ppm)	0.012-4.59	0.049-6.02	0.008-0.13	14.5-459
Minimum mass (μg)	218	166	7.7×10^3	2.2
Minimum volume (μm ³)	6.6×10^7	6.2×10^7	2.1×10^9	7.0×10^5

Sr, Nd data: Balta et al. (2013), Basu Sarbadhikari et al. (2009), Combs et al. (2019), Ferdous et al. (2019), Harvey et al. (1993), Howarth and Udry (2017), Hui et al. (2011), Liu et al. (2011), Misawa et al. (2006), Misawa et al. (2008), Morikawa et al. (2001), Shafer et al. (2010), Shearer et al. (2015), Shih et al. (2005), Shih et al. (2011), Symes et al. (2008), Usui et al. (2008), Usui et al. (2010), Walton et al. (2012), this study.

Table 4.4. Minimum required sampling area, in μm², for Sr and Nd isotopic analyses assuming a drilling depth of 20 μm. Based on required sampling volumes determined in Table 4.3.

	Pyroxene	Plagioclase	Olivine	Merrillite
Sr	7.6×10^4	1.3×10^4	5.0×10^5	1.2×10^4
Nd	3.3×10^6	3.1×10^6	1.1×10^8	3.5×10^4

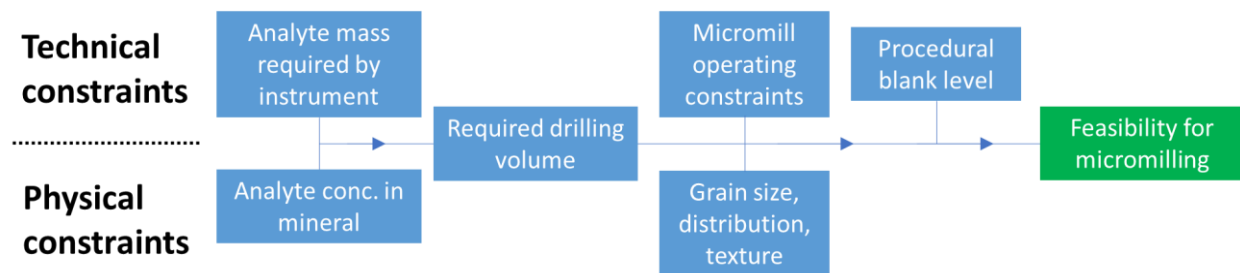


Fig. 4.1. Breakdown of the feasibility assessment for applying micromill sampling to mineral Sr, Nd isotopic analyses in shergottites.

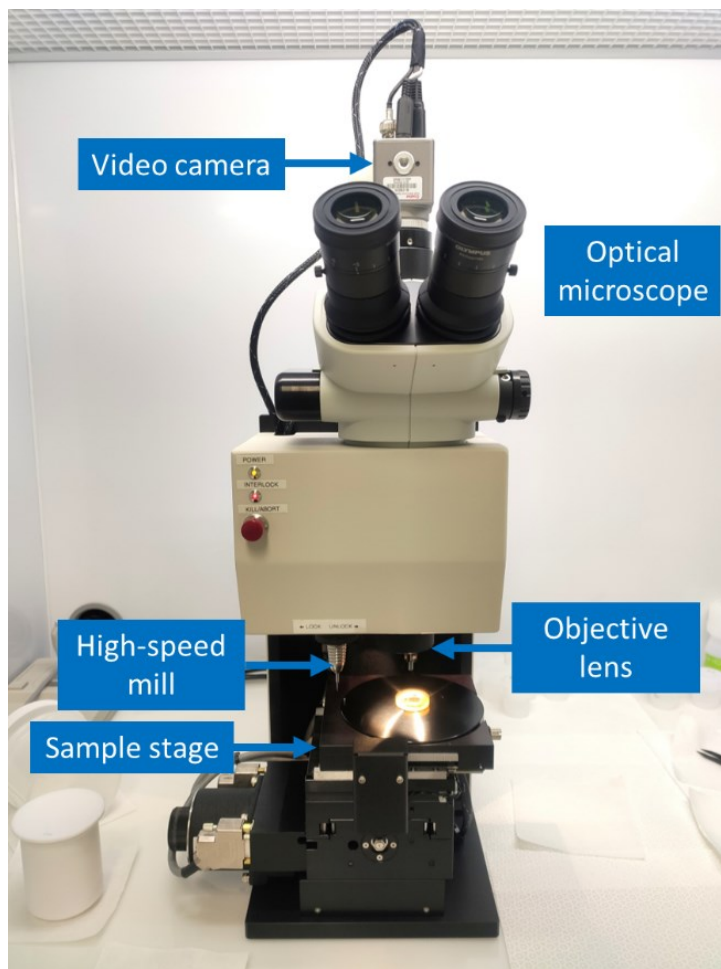


Fig. 4.2. Photograph of the Merchantek/New Wave Research MicroMill instrument used in this study, with key components labeled. Samples are characterized and drilling patterns are defined under an optical microscope on the right before the sample stage moves to the drilling assembly on the left for sampling.

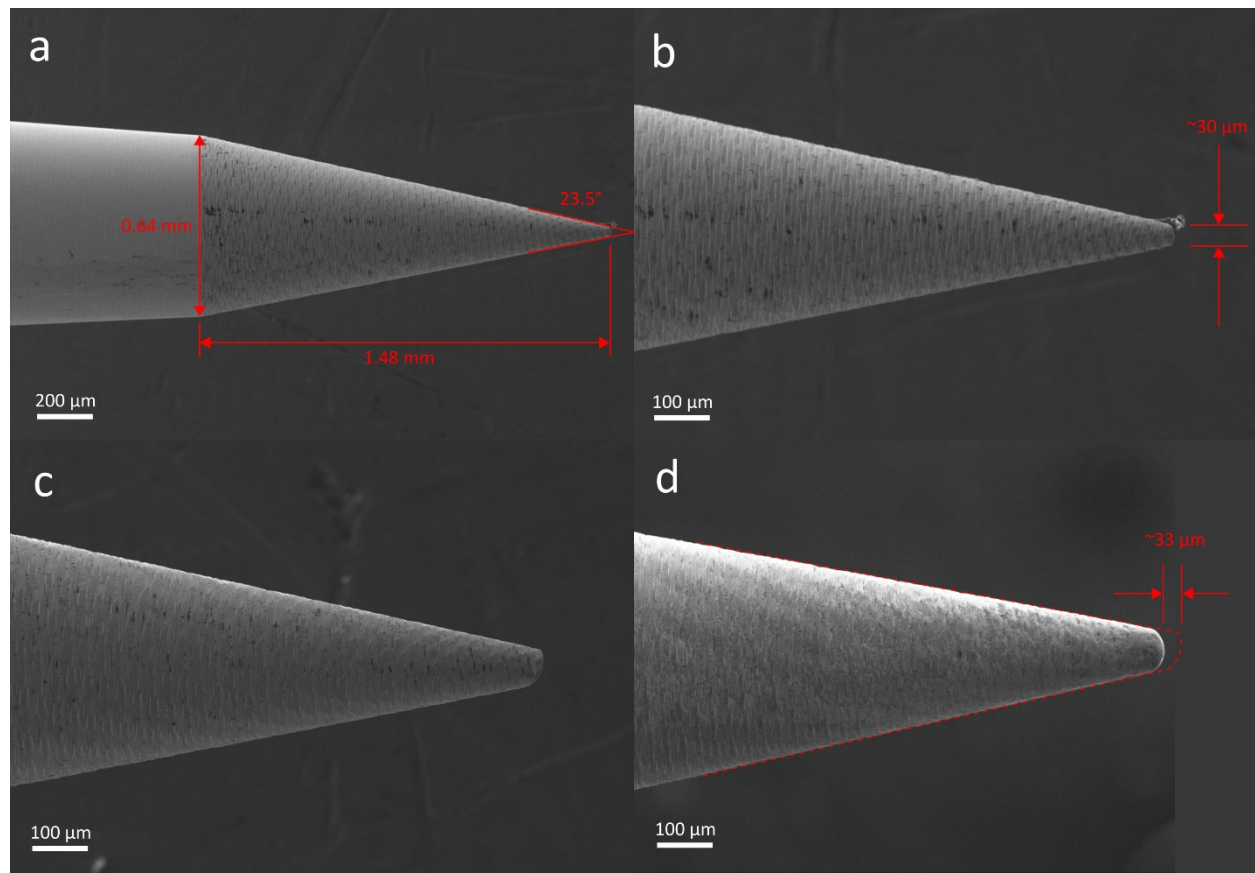


Fig. 4.3. Secondary electron SEM images of carbide drill bits used in this study: a, b) 001C before use, c) 001B before use, and d) 001B after last use, with outline of pre-use tip profile marked in red dashed curve.

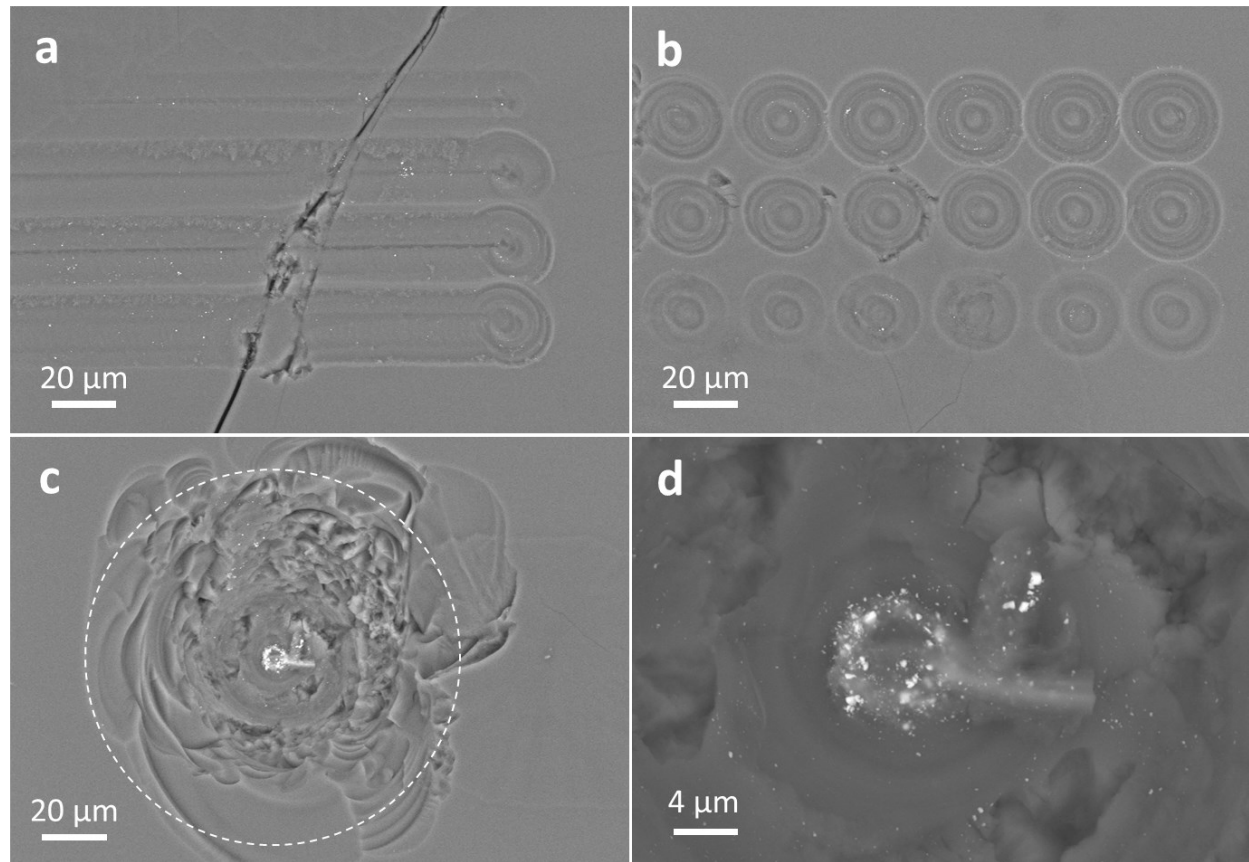


Fig. 4.4. BSE images of test patterns performed by bit 001B on synthetic basaltic glass SGY, showing flecks of high BSE-signal material determined to be carbide shed by the drill bit: a) four parallel linear rasters at 5 μm depth, b) rectangular array of single holes at 5 μm depth, with 30 μm spacing, c) single hole at 200 μm depth, drilled in 8 passes of 25 μm depth increments, and d) close-up of carbide flecks at the bottom of the hole shown in c).

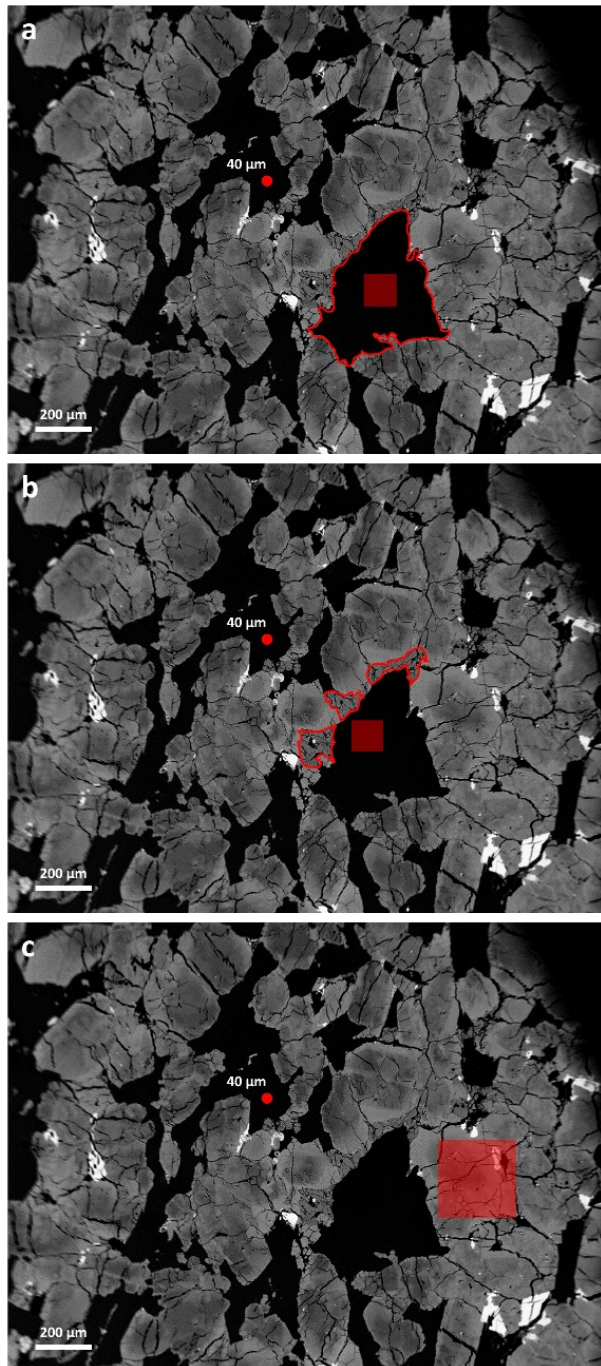


Fig. 4.5. BSE image of a representative area of NWA 10299 annotated with equivalent schematic sampling area sizes for obtaining the minimum required volume for Sr isotopic analysis for A) plagioclase, B) merrillite, and C) pyroxene. Sampling area is denoted by red squares, calculated assuming a drilling depth of 20 μm (Table 4.4). For plagioclase and merrillite, the target grains are outlined in red. For reference of drilling resolution, the size of a 20 μm deep drill hole (\sim 40 μm diameter) is represented by the red dot.

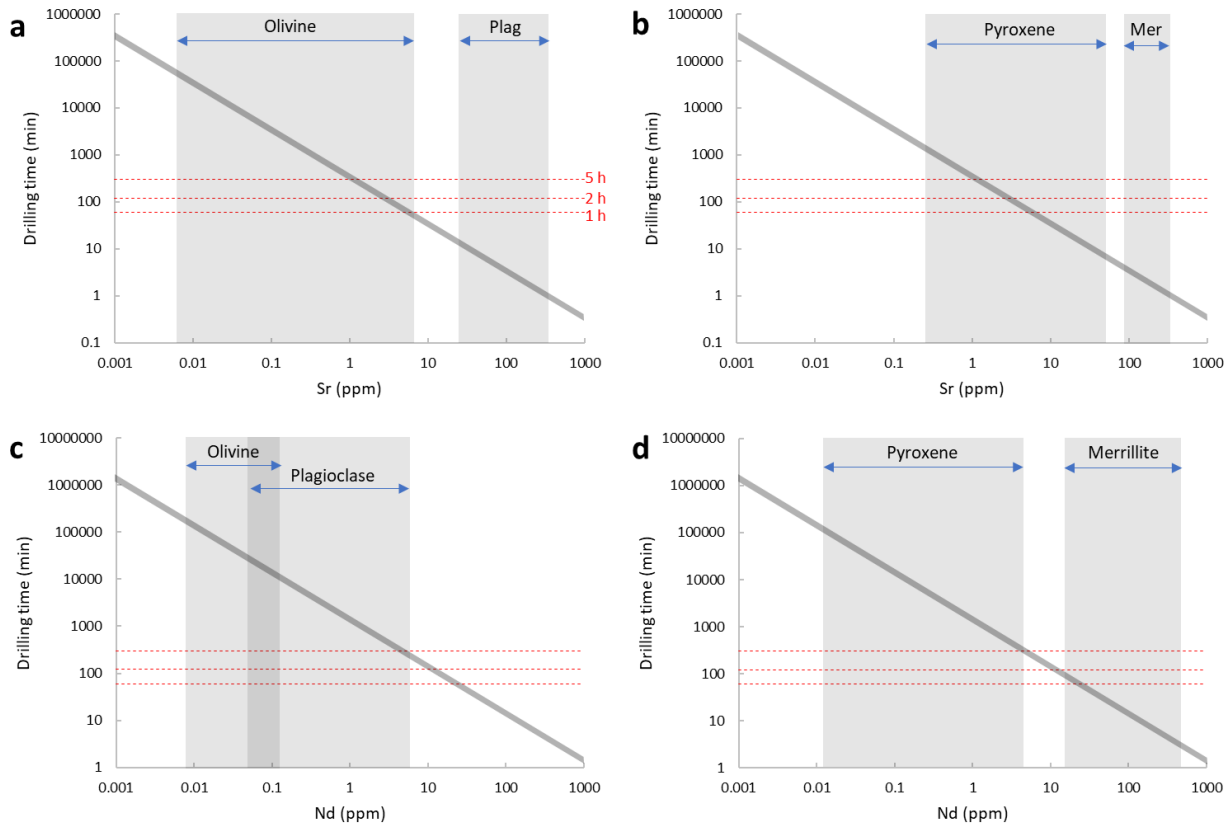


Fig. 4.6. Estimated drilling time for obtaining the minimum required Sr and Nd mass (0.250 ng and 1 ng, respectively) in a target of known Sr or Nd concentration. Dark grey curve denotes a bulk drilling rate of $2.3 \times 10^5 \mu\text{m}^3/\text{min}$ for the range of mineral densities considered in this study (2.7–3.6 g/cm³). Light grey bars indicate the range of Sr and Nd contents in pyroxene, plagioclase (Plag), olivine, and merrillite (Mer) in shergottites (Table 4.3). Red dashed lines denote the 1-hour, 2-hour, and 5-hour marks on the y-axis.

4.7 References

- Balta, J. B., Sanborn, M., McSween Jr., H. Y. & Wadhwa, M. (2013) Magmatic history and parental melt composition of olivine-phyric shergottite LAR 06319: Importance of magmatic degassing and olivine antecrysts in Martian magmatism. *Meteoritics & Planetary Science* **48**: 1359-1382.
- Basu Sarbadhikari, A., Day, J. M. D., Liu, Y., Rumble, D. & Taylor, L. A. (2009) Petrogenesis of olivine-phyric shergottite Larkman Nunatak 06319: Implications for enriched components in martian basalts. *Geochimica et Cosmochimica Acta* **73**: 2190-2214.
- Bellucci, J. J., Herd, C. D. K., Whitehouse, M. J., Nemchin, A. A., Kenny, G. G. & Merle, R. E. (2020) Insights into the chemical diversity of the martian mantle from the Pb isotope systematics of shergottite Northwest Africa 8159. *Chemical Geology* **545**: 119638.
- Blinova, A. & Herd, C. D. K. (2009) Experimental study of polybaric REE partitioning between olivine, pyroxene and melt of the Yamato 980459 composition: Insights into the petrogenesis of depleted shergottites. *Geochimica et Cosmochimica Acta* **73**: 3471-3492.
- Borg, L. E., Nyquist, L. E., Taylor, L. A., Wiesmann, H. & Shih, C. (1997) Constraints on Martian differentiation processes from Rb-Sr and Sm-Nd isotopic analyses of the basaltic shergottite QUE 94201. *Geochimica et Cosmochimica Acta* **61**: 4915-4931.
- Borg, L. E., Nyquist, L. E., Reese, Y., Wiesmann, H. & Shih, C. Y. (2001) The age of Dhofar 019 and its relationship to the other Martian meteorites. *Lunar and Planetary Science XXXII*, abstract #1144.
- Borg, L. E., Nyquist, L. E., Wiesmann, H. & Reese, Y. (2002) Constraints on the petrogenesis of Martian meteorites from the Rb-Sr and Sm-Nd isotopic systematics of the Iherzolitic shergottites ALH77005 and LEW88516. *Geochimica et Cosmochimica Acta* **66**: 2037-2053.
- Borg, L. E., Nyquist, L. E., Wiesmann, H., Shih, C. & Reese, Y. (2003) The age of Dar al Gani 476 and the differentiation history of the martian meteorites inferred from their radiogenic isotopic systematics. *Geochimica et Cosmochimica Acta* **67**: 3519-3536.

- Britvin, S. N., Krivovichev, S. V. & Armbruster, T. (2016) Ferromerrillite, Ca₉NaFe₂₊(PO₄)₇, a new mineral from the Martian meteorites, and some insights into merrillite–tuite transformation in shergottites. *European Journal of Mineralogy* **28**: 125-136.
- Charlier, B. L. A., Ginibre, C., Morgan, D., Nowell, G. M., Pearson, D. G., Davidson, J. P. & Ottley, C. J. (2006) Methods for the microsampling and high-precision analysis of strontium and rubidium isotopes at single crystal scale for petrological and geochronological applications. *Chemical Geology* **232**: 114-133.
- Chu, Z., Chen, F., Yang, Y. & Guo, J. (2009) Precise determination of Sm, Nd concentrations and Nd isotopic compositions at the nanogram level in geological samples by thermal ionization mass spectrometry. *Journal of Analytical Atomic Spectrometry* **24**: 1534-1544.
- Combs, L. M., Udry, A., Howarth, G. H., Righter, M., Lapen, T. J., Gross, J., Ross, D. K., Rahib, R. R. & Day, J. M. D. (2019) Petrology of the enriched poikilitic shergottite Northwest Africa 10169: Insight into the martian interior. *Geochimica et Cosmochimica Acta* **266**: 435-462.
- Cook, D. L., Wadhwa, M., Clayton, R. N., Dauphas, N., Janney, P. E. & Davis, A. M. (2007) Mass-dependent fractionation of nickel isotopes in meteoritic metal. *Meteoritics & Planetary Science* **42**: 2067-2077.
- Crozaz, G., Floss, C. & Wadhwa, M. (2003) Chemical alteration and REE mobilization in meteorites from hot and cold deserts. *Geochimica et Cosmochimica Acta* **67**: 4727-4741.
- Darling, J. R., Moser, D. E., Barker, I. R., Tait, K. T., Chamberlain, K. R., Schmitt, A. K. & Hyde, B. C. (2016) Variable microstructural response of baddeleyite to shock metamorphism in young basaltic shergottite NWA 5298 and improved U–Pb dating of Solar System events. *Earth and Planetary Science Letters* **444**: 1-12.
- Debaille, V., Yin, Q. -, Brandon, A. D. & Jacobsen, B. (2008) Martian mantle mineralogy investigated by the ¹⁷⁶Lu–¹⁷⁶Hf and ¹⁴⁷Sm–¹⁴³Nd systematics of shergottites. *Earth and Planetary Science Letters* **269**: 186-199.

- Edmunson, J., Borg, L. E., Shearer, C. K. & Papike, J. J. (2005) Defining the mechanisms that disturb the Sm-Nd isotopic systematics of the Martian meteorites: Examples from Dar al Gani 476 and Allan Hills 77005. *Meteoritics & Planetary Science* **40**: 1159-1174.
- Ferdous, J., Brandon, A. D., Peslier, A. H. & Pirotte, Z. (2017) Evaluating crustal contributions to enriched shergottites from the petrology, trace elements, and Rb-Sr and Sm-Nd isotope systematics of Northwest Africa 856. *Geochimica et Cosmochimica Acta* **211**: 280-306.
- Fritz, J., Greshake, A. & Fernandes, V. A. (2017) Revising the shock classification of meteorites. *Meteoritics & Planetary Science* **52**: 1216-1232.
- Gao, S., Liu, X., Yuan, H., Hattendorf, B., Günther, D., Chen, L. & Hu, S. (2002) Determination of Forty Two Major and Trace Elements in USGS and NIST SRM Glasses by Laser Ablation-Inductively Coupled Plasma-Mass Spectrometry. *Geostandards Newsletter* **26**: 181-196.
- Goodrich, C. A., Herd, C. D. K. & Taylor, L. A. (2003) Spinels and oxygen fugacity in olivine-phyric and Iherzolitic shergottites. *Meteoritics & Planetary Science* **38**: 1773-1792.
- Gross, J., Treiman, A. H., Filiberto, J. & Herd, C. D. K. (2011) Primitive olivine-phyric shergottite NWA 5789: Petrography, mineral chemistry, and cooling history imply a magma similar to Yamato-980459. *Meteoritics & Planetary Science* **46**: 116-133.
- Harlou, R., Pearson, D. G., Nowell, G. M., Ottley, C. J. & Davidson, J. P. (2009) Combined Sr isotope and trace element analysis of melt inclusions at sub-ng levels using micro-milling, TIMS and ICPMS. *Chemical Geology* **260**: 254-268.
- Harvey, J. & Baxter, E. F. (2009) An improved method for TIMS high precision neodymium isotope analysis of very small aliquots (1–10 ng). *Chemical Geology* **258**: 251-257.
- Harvey, R. P., Wadhwa, M., McSween, H. Y. & Crozaz, G. (1993) Petrography, mineral chemistry, and petrogenesis of Antarctic Shergottite LEW88516. *Geochimica et Cosmochimica Acta* **57**: 4769-4783.

- Hays, N. R., Drake M. J., and Gehrels G. G. 2011. U-Th-Pb Analysis of Baddeleyites in Shergottite Meteorites. 42nd Annual Lunar and Planetary Science Conference. pp. 1243.
- Herd, C. D. K., Walton, E. L., Agee, C. B., Muttik, N., Ziegler, K., Shearer, C. K., Bell, A. S., Santos, A. R., Burger, P. V., Simon, J. I., Tappa, M. J., McCubbin, F. M., Gattaccea, J., Lagroix, F., Sanborn, M. E., Yin, Q., Cassata, W. S., Borg, L. E., Lindvall, R. E., Kruijer, T. S., Brennecke, G. A., Kleine, T., Nishiizumi, K. & Caffee, M. W. (2017) The Northwest Africa 8159 martian meteorite: Expanding the martian sample suite to the early Amazonian. *Geochimica et Cosmochimica Acta* **218**: 1-26.
- Herd, C. D. K., Moser, D. E., Tait, K., Darling, J. R., Shaulis, B. J. & McCoy, T. J. (2018) Crystallization of Baddeleyite in Basaltic Rocks from Mars, and Comparisons with the Earth, Moon, and Vesta. *Microstructural Geochronology*: 137-166.
- Hoffmann, D. L., Spötl, C. & Mangini, A. (2009) Micromill and in situ laser ablation sampling techniques for high spatial resolution MC-ICPMS U-Th dating of carbonates. *Chemical Geology* **259**: 253-261.
- Howarth, G. H. & Udry, A. (2017) Trace elements in olivine and the petrogenesis of the intermediate, olivine-phyric shergottite NWA 10170. *Meteoritics & Planetary Science* **52**: 391-409.
- Huang, K., Blusztajn, J., Oppo, D. W., Curry, W. B. & Peucker-Ehrenbrink, B. (2012) High-precision and accurate determinations of neodymium isotopic compositions at nanogram levels in natural materials by MC-ICP-MS. *Journal of Analytical Atomic Spectrometry* **27**: 1560-1567.
- Hui, H., Peslier, A. H., Lapen, T. J., Shafer, J. T., Brandon, A. D. & Irving, A. J. (2011) Petrogenesis of basaltic shergottite Northwest Africa 5298: Closed-system crystallization of an oxidized mafic melt. *Meteoritics & Planetary Science* **46**: 1313-1328.
- Ibanez-Mejia, M., Gehrels, G. E., Ruiz, J., Vervoort, J. D., Eddy, M. P. & Li, C. (2014) Small-volume baddeleyite (ZrO_2) U-Pb geochronology and Lu-Hf isotope geochemistry by LA-ICP-MS. Techniques and applications. *Chemical Geology* **384**: 149-167.

- Jagoutz, E. (1989) Sr and Nd isotopic systematics in ALHA 77005: Age of shock metamorphism in shergottites and magmatic differentiation on Mars. *Geochimica et Cosmochimica Acta* **53**: 2429-2441.
- Lapen, T. J., Righter, M., Andreasen, R., Irving, A. J., Satkoski, A. M., Beard, B. L., Nishiizumi, K., Timothy Jull, A. J. & Caffee, M. W. (2017) Two billion years of magmatism recorded from a single Mars meteorite ejection site. *Science Advances* **3**: e1600922.
- Li, C., Chen, F. & Li, X. (2007) Precise isotopic measurements of sub-nanogram Nd of standard reference material by thermal ionization mass spectrometry using the NdO⁺ technique. *International Journal of Mass Spectrometry* **266**: 34-41.
- Liu, T., Li, C. & Lin, Y. (2011) Rb-Sr and Sm-Nd isotopic systematics of the Iherzolitic shergottite GRV 99027. *Meteoritics & Planetary Science* **46**: 681-689.
- McCubbin, F. M., Shearer, C. K., Burger, P. V., Hauri, E. H., Wang, J., Elardo, S. M. & Papike, J. J. (2014) Volatile abundances of coexisting merrillite and apatite in the martian meteorite Shergotty: Implications for merrillite in hydrous magmas. *American Mineralogist* **99**: 1347-1354.
- McSween Jr., H. Y. (1994) What we have learned about Mars from SNC meteorites. *Meteoritics* **29**: 757-779.
- Misawa, K., Yamada, K., Nakamura, N., Morikawa, N., Yamashita, K. & Premo, W. R. (2006) Sm-Nd isotopic systematics of Iherzolitic shergottite Yamato-793605. *Antarctic Meteorite Research*: 45-57.
- Misawa, K., Park, J., Shih, C. -, Reese, Y., Bogard, D. D. & Nyquist, L. E. (2008) Rb-Sr, Sm-Nd, and Ar-Ar isotopic systematics of Iherzolitic shergottite Yamato 000097. *Polar Science* **2**: 163-174.
- Morikawa, N., Misawa, K., Kondorosi, G., Premo, W. R., Tatsumoto, M. & Nakamura, N. (2001) Rb-Sr isotopic systematics of Iherzolitic shergottite Yamato-793605. *Antarctic Meteorite Research* **14**: 47-60.

Moser, D. E., Chamberlain, K. R., Tait, K. T., Schmitt, A. K., Darling, J. R., Barker, I. R. & Hyde, B. C. (2013) Solving the Martian meteorite age conundrum using micro-baddeleyite and launch-generated zircon. *Nature* **499**: 454-457.

Nakanishi, N., Yokoyama, T., Okabayashi, S., Iwamori, H. & Hirata, T. (2022) Geochemical constraints on the formation of chondrules: Implication from Os and Fe isotopes and HSE abundances in metals from CR chondrites. *Geochimica et Cosmochimica Acta* **319**: 254-270.

Nicklas, R. W., Day, J. M. D., Vaci, Z., Udry, A., Liu, Y. & Tait, K. T. (2021) Uniform oxygen fugacity of shergottite mantle sources and an oxidized martian lithosphere. *Earth and Planetary Science Letters* **564**: 116876.

Nomenclature Committee of the Meteoritical Society. The Meteoritical Bulletin Database.
<http://www.lpi.usra.edu/meteor/> (accessed 25 May, 2022)

Nyquist L. E., Reese Y., Wiesmann H., and Shih C. (2001). Age of EET79001B and implications for shergottite origins. Lunar and Planetary Science Conference. pp. 1407.

Ottley C. J., Pearson D. G., and Irvine G. J. 2003. A routine method for the dissolution of geological samples for the analysis of REE and trace elements via ICP-MS. In: *Plasma Source Mass Spectrometry: Applications and Emerging Technologies*, edited by Holland G. and Tanner S. D.: The Royal Society of Chemistry. pp. 221-230.

Pollington, A. D. & Baxter, E. F. (2011) High precision microsampling and preparation of zoned garnet porphyroblasts for Sm–Nd geochronology. *Chemical Geology* **281**: 270-282.

Reinhard A., Inglis J. D., Steiner R., LaMont S., and Jackson M. G. 2019. Isotopic Analysis of Sub-Nanogram Nd Samples Using New ATONA Amplifiers. AGU Fall Meeting Abstracts. pp. V11D-0111.

Shafer, J. T., Brandon, A. D., Lapen, T. J., Righter, M., Peslier, A. H. & Beard, B. L. (2010) Trace element systematics and ^{147}Sm – ^{143}Nd and ^{176}Lu – ^{176}Hf ages of Larkman Nunatak 06319: Closed-system

fractional crystallization of an enriched shergottite magma. *Geochimica et Cosmochimica Acta* **74**: 7307-7328.

Shearer, C. K., Burger, P. V., Papike, J. J., McCubbin, F. M. & Bell, A. S. (2015) Crystal chemistry of merrillite from Martian meteorites: Mineralogical recorders of magmatic processes and planetary differentiation. *Meteoritics & Planetary Science* **50**: 649-673.

Sheen, A. I., Herd, C. D. K., Hamilton, J. & Walton, E. L. (2021) Petrographic controls on baddeleyite occurrence in a suite of eight basaltic shergottites. *Meteoritics & Planetary Science* **56**: 1502-1530.

Shih, C., Nyquist, L. E., Wiesmann, H., Reese, Y. & Misawa, K. (2005) Rb-Sr and Sm-Nd dating of olivine-phyric shergottite Yamato 980459: Petrogenesis of depleted shergottites. *Antarctic meteorite research* **18**: 46-65.

Shih, C. -, Nyquist, L. E., Reese, Y. & Misawa, K. (2011) Sm-Nd and Rb-Sr studies of lherzolitic shergottite Yamato 984028. *Polar Science* **4**: 515-529.

Sikdar, J. & Rai, V. K. (2020) Si-Mg isotopes in enstatite chondrites and accretion of reduced planetary bodies. *Scientific Reports* **10**: 1273.

Staddon, L. G., Darling, J. R., Schwarz, W. H., Stephen, N. R., Schuindt, S., Dunlop, J. & Tait, K. T. (2021) Dating martian mafic crust; microstructurally constrained baddeleyite geochronology of enriched shergottites Northwest Africa (NWA) 7257, NWA 8679 and Zagami. *Geochimica et Cosmochimica Acta* **315**: 73-88.

Stanjek, H., Glasemann, R. & Hellmann, A. (2013) Smectite contents of road aggregates derived from crushed volcanic rocks and their impact on the durability of road pavements. *Clay Minerals* **48**: 463-471.

Symes, S. J. K., Borg, L. E., Shearer, C. K. & Irving, A. J. (2008) The age of the martian meteorite Northwest Africa 1195 and the differentiation history of the shergottites. *Geochimica et Cosmochimica Acta* **72**: 1696-1710.

- Udry, A. & Day, J. M. D. (2018) 1.34 billion-year-old magmatism on Mars evaluated from the co-genetic nakhlite and chassignite meteorites. *Geochimica et Cosmochimica Acta* **238**: 292-315.
- Udry, A., Howarth, G. H., Herd, C. D. K., Day, J. M. D., Lapen, T. J. & Filiberto, J. (2020) What Martian Meteorites Reveal About the Interior and Surface of Mars. *Journal of Geophysical Research: Planets* **125**: e2020JE006523.
- Usui, T., McSween, H. Y. & Floss, C. (2008) Petrogenesis of olivine-phyric shergottite Yamato 980459, revisited. *Geochimica et Cosmochimica Acta* **72**: 1711-1730.
- Usui, T., Sanborn, M., Wadhwa, M. & McSween, H. Y. (2010) Petrology and trace element geochemistry of Robert Massif 04261 and 04262 meteorites, the first examples of geochemically enriched Iherzolitic shergottites. *Geochimica et Cosmochimica Acta* **74**: 7283-7306.
- Usui, T., Alexander, C. M. O., Wang, J., Simon, J. I. & Jones, J. H. (2012) Origin of water and mantle–crust interactions on Mars inferred from hydrogen isotopes and volatile element abundances of olivine-hosted melt inclusions of primitive shergottites. *Earth and Planetary Science Letters* **357-358**: 119-129.
- Wadhwa, M. (2001) Redox State of Mars' Upper Mantle and Crust from Eu Anomalies in Shergottite Pyroxenes. *Science* **291**: 1527-1530.
- Wadhwa, M., McSween, H. Y. & Crozaz, G. (1994) Petrogenesis of shergottite meteorites inferred from minor and trace element microdistributions. *Geochimica et Cosmochimica Acta* **58**: 4213-4229.
- Wakaki, S. & Ishikawa, T. (2018) Isotope analysis of nanogram to sub-nanogram sized Nd samples by total evaporation normalization thermal ionization mass spectrometry. *International Journal of Mass Spectrometry* **424**: 40-48.
- Walton, E. L., Irving, A. J., Bunch, T. E. & Herd, C. D. K. (2012) Northwest Africa 4797: A strongly shocked ultramafic poikilitic shergottite related to compositionally intermediate Martian meteorites. *Meteoritics & Planetary Science* **47**: 1449-1474.

White, L. F., Tait, K. T., Kamo, S. L., Moser, D. E. & Darling, J. R. (2020) Highly accurate dating of micrometre-scale baddeleyite domains through combined focused ion beam extraction and U–Pb thermal ionization mass spectrometry (FIB-TIMS). *Geochronology* **2**: 177–186.

Zhou, Q., Herd, C. D. K., Yin, Q., Li, X., Wu, F., Li, Q., Liu, Y., Tang, G. & McCoy, T. J. (2013) Geochronology of the Martian meteorite Zagami revealed by U–Pb ion probe dating of accessory minerals. *Earth and Planetary Science Letters* **374**: 156–163.

Zipfel, J., Scherer, P., Spettel, B., Dreibus, G. & Schultz, L. (2000) Petrology and chemistry of the new shergottite Dar al Gani 476. *Meteoritics & Planetary Science* **35**: 95–106.

CHAPTER 5: CONCLUSIONS

Findings from the research presented in this dissertation affirm the importance of *in-situ* geochronology techniques for determining the absolute time scale of Mars. This is demonstrated by the application of mineral chemistry for assessing baddeleyite distribution in shergottites and by microstructural constraints on baddeleyite U–Pb isotope systematics under shock metamorphism. Physical characteristics of shergottites limit the application of micromill extraction for conducting Rb–Sr and Sm–Nd geochronology, whereas *in-situ* SIMS U–Pb baddeleyite analysis remains an established and robust technique and builds on successive analytical advancements and shergottite studies include those presented in this dissertation.

A petrographic survey of a suite of eight shergottites confirms that baddeleyite crystallized as an igneous accessory mineral. The link between baddeleyite abundance and pyroxene major element trends demonstrates that baddeleyite crystallization in shergottite magmas is controlled to the first order by fractional crystallization; samples with pyroxene compositions evolving beyond the 1-bar stability boundary contain more abundant baddeleyite than samples with pyroxene compositions contained within the stability boundary. The petrographic setting in which the largest baddeleyite grains are more likely to occur also discriminates between samples with different pyroxene composition trends. In samples showing separate high-Ca and low-Ca pyroxene series, the largest baddeleyite grains tend to be associated with Fe-Ti oxides, whereas in samples showing one continuous pyroxene trend extending past the stability boundary, they are more typically found in polymimetic late-stage pockets. Bulk HFSE content and f_{O_2} do not appear to directly influence baddeleyite distribution. These findings demonstrate that pyroxene composition is a useful proxy for assessing baddeleyite distribution in unknown shergottite samples. As pyroxene composition is among the first data reported for new shergottites, a preliminary evaluation of a sample's feasibility for U–Pb baddeleyite analysis can therefore be made before conducting any detailed baddeleyite search.

EBSDD microstructural analysis of baddeleyite in JaH 479, NWA 10299, and NWA 12919 reveals widespread phase transformation to high-pressure polymorphs (≥ 3.3 GPa) caused by shock metamorphism. Complexities in microstructure result from the combined factors of local peak shock pressure and post-shock thermal gradient. The greater preservation of magmatic orientations (Group 1 and Group 2 microstructures) in JaH 479 relative to NWA 10299 and NWA 12919 indicates that the former experienced a lower bulk shock pressure. However, whereas prevalence of Group 3 microstructure in NWA 10299 and NWA 12919 suggests insufficient post-shock heating which suppressed nucleation of reverted $m\text{-ZrO}_2$, the occurrence of μm -scale reverted $m\text{-ZrO}_2$ subdomains (Group 2 and Group 4) in JaH 479 reflects more protracted local waste heat dissipation. Greater pressure-temperature heterogeneity in JaH 479 is consistent with the absence of high bulk shock pressure.

SIMS U–Pb baddeleyite analysis yields three new shergottite igneous ages: 210 ± 9 Ma (JaH 479), 196 ± 11 Ma (NWA 10299), and 188 ± 11 Ma (NWA 12919). Observed scatter in measured $^{206}\text{Pb}/^{238}\text{U}$ ratios is attributed to analytical effects, some of which were amplified by the analytical spots being larger than intended. The lack of resolvable Pb loss in the analyzed baddeleyite indicates negligible Pb diffusion during the formation of Group 1, 2, and 3 microstructures. All three shergottites lack the granular or zircon-rimmed baddeleyite previously observed in NWA 5298, suggesting that baddeleyite Pb loss may be specifically tied to the excess heating involved in forming these morphologies, which is absent from the bulk of shergottites. The three U–Pb crystallization ages are within the range of known age of enriched shergottites (223–157 Ma). These findings demonstrate baddeleyite to be a robust U–Pb geochronometer for determining shergottite crystallization ages, with microstructural constraints on U–Pb isotope systematics.

The feasibility assessment of micromill sampling identifies both technical and physical factors that limit the application for extracting major minerals in shergottites for chromatography-based Rb–Sr and Sm–Nd geochronology. SEM images and ICP-MS analysis of micromilled synthetic glass show appreciable

Co contribution from the carbide drill bit. However, trace element contribution from the micromill cannot be accurately quantified as the bulk glass analysis contains contamination by a non-micromill source, most likely remnant epoxy on and/or within the glass. Based on shergottite literature data and LA-ICPMS trace element analysis of NWA 10299, the minimum volume required for creating one fraction of Sr (0.25 ng) and Nd (1 ng) isotopic analysis ranges between 10^5 and $10^9 \mu\text{m}^3$ for olivine, pyroxene, plagioclase, and merrillite. However, shergottite petrography poses physical limitations with respect to the maximum drilling resolution of $\sim 40 \mu\text{m}$; grain size, morphology, compositional zoning, and inclusions may significantly reduce the proportion of each mineral grain that can be sampled. Shock features such as fractures and shock melt, which can act as pathways for terrestrial contamination, further limit effective sampling of pure mineral fractions. Furthermore, drilling at maximum resolution corresponds to over three hours of instrument time for extracting certain minerals (e.g., olivine for Nd), increasing the susceptibility to larger blanks. These factors preclude effective micromill sampling for Rb–Sr and Sm–Nd geochronology of shergottites; such an application may become more feasible with future advances in increasing drill resolution and/or reducing analyte mass required for ID-TIMS and/or ICP-MS isotopic analysis.

Determining the timing of mafic magmatism on Mars remains a frontier in Mars research. The results presented in this dissertation confirm previous findings that baddeleyite U–Pb isotope systematics in shergottites is robust for igneous geochronology, while demonstrating that the method is more robust and widely applicable than previously envisioned. Petrochemical proxies exist to assess a shergottite's feasibility for baddeleyite analysis without necessitating a detailed baddeleyite search. Furthermore, the combined protocol of EBSD microstructural analysis and SIMS U–Pb geochronology provides pressure–temperature constraints on shock metamorphism, with potential application for determining pre-ejection geological relationships among shergottite populations (e.g., source craters). In light of ongoing preparation for the return of samples from the surface of Mars, findings presented in this dissertation also

provides potential guidelines for designing *in-situ* geochronology protocols for the returned samples. The development of an absolute time scale based on the combined geochronology of martian meteorites and returned surface samples will not only create a unified geological framework for Mars research, but also help to determine the source locations and field context from which martian meteorites originated.

BIBLIOGRAPHY

- Acuña, M. H., Connerney, J. E. P., Wasilewski, P., Lin, R. P., Anderson, K. A., Carlson, C. W., McFadden, J., Curtis, D. W., Mitchell, D., Reme, H., Mazelle, C., Sauvaud, J. A., d'Uston, C., Cros, A., Medale, J. L., Bauer, S. J., Cloutier, P., Mayhew, M., Winterhalter, D. & Ness, N. F. (1998) Magnetic Field and Plasma Observations at Mars: Initial Results of the Mars Global Surveyor Mission. *Science* **279**: 1676-1680.
- Aoudjehane, H. C., Aviße, G., Barrat, J., Boudouma, O., Chen, G., Duke, M., Franchi, I. A., Gattacceca, J., Grady, M. M. & Greenwood, R. C. (2012) Tissint martian meteorite: A fresh look at the interior, surface, and atmosphere of Mars. *Science* **338**: 785-788.
- Aramovich, C. J., Herd, C. D. & Papike, J. J. (2002) Symplectites derived from metastable phases in martian basaltic meteorites. *American Mineralogist* **87**: 1351-1359.
- Baker, V. R. (2001) Water and the martian landscape. *Nature* **412**: 228-236.
- Balta, J. B., Sanborn, M., McSween Jr., H. Y. & Wadhwa, M. (2013) Magmatic history and parental melt composition of olivine-phyric shergottite LAR 06319: Importance of magmatic degassing and olivine antecrysts in Martian magmatism. *Meteoritics & Planetary Science* **48**: 1359-1382.
- Barrat, J. A., Blichert-Toft, J., Nesbitt, R. W. & Keller, F. (2001) Bulk chemistry of Saharan shergottite Dar al Gani 476. *Meteoritics & Planetary Science* **36**: 23-29.
- Basu Sarbadhikari, A., Day, J. M. D., Liu, Y., Rumble, D. & Taylor, L. A. (2009) Petrogenesis of olivine-phyric shergottite Larkman Nunatak 06319: Implications for enriched components in martian basalts. *Geochimica et Cosmochimica Acta* **73**: 2190-2214.
- Baziotis, I. P., Liu, Y., DeCarli, P. S., Jay Melosh, H., McSween, H. Y., Bodnar, R. J. & Taylor, L. A. (2013) The Tissint Martian meteorite as evidence for the largest impact excavation. *Nature Communications* **4**: 1404.
- Beaty, D. W., Grady, M. M., McSween, H. Y., Sefton-Nash, E., Carrier, B. L., Altieri, F., Amelin, Y., Ammannito, E., Anand, M., Benning, L. G., Bishop, J. L., Borg, L. E., Boucher, D., Brucato, J. R., Busemann, H., Campbell, K. A., Czaja, A. D., Debaille, V., Des Marais, D. J., Dixon, M., Ehlmann, B. L., Farmer, J. D., Fernandez-Remolar, D., Filiberto, J., Fogarty, J., Glavin, D. P., Goreva, Y. S., Hallis, L. J., Harrington, A. D., Hausrath, E. M., Herd, C. D. K., Horgan, B., Humayun, M., Kleine, T., Kleinhenz, J., Mackelprang, R., Mangold, N., Mayhew, L. E., McCoy, J. T., McCubbin, F. M., McLennan, S. M., Moser, D. E., Moynier, F., Mustard, J. F., Niles, P. B., Ori, G. G., Raulin, F., Rettberg, P., Rucker, M. A., Schmitz, N., Schwenzer, S. P., Sephton, M. A., Shaheen, R., Sharp, Z. D., Shuster, D. L., Siljeström, S., Smith, C. L., Spry, J. A., Steele, A., Swindle, T. D., ten Kate, I. L., Tosca, N. J.,

- Usui, T., Van Kranendonk, M. J., Wadhwa, M., Weiss, B. P., Werner, S. C., Westall, F., Wheeler, R. M., Zipfel, J. & Zorzano, M. P. (2019) The potential science and engineering value of samples delivered to Earth by Mars sample return. *Meteoritics & Planetary Science* **54**: S3-S152.
- Beck, P., Gillet, P., El Goresy, A. & Mostefaoui, S. (2005) Timescales of shock processes in chondritic and martian meteorites. *Nature* **435**: 1071-1074.
- Bellucci, J. J., Nemchin, A. A., Whitehouse, M. J., Humayun, M., Hewins, R. & Zanda, B. (2015) Pb-isotopic evidence for an early, enriched crust on Mars. *Earth and Planetary Science Letters* **410**: 34-41.
- Bellucci, J. J., Nemchin, A. A., Whitehouse, M. J., Snape, J. F., Kielman, R. B., Bland, P. A. & Benedix, G. K. (2016) A Pb isotopic resolution to the Martian meteorite age paradox. *Earth and Planetary Science Letters* **433**: 241-248.
- Bellucci, J. J., Herd, C. D. K., Whitehouse, M. J., Nemchin, A. A., Kenny, G. G. & Merle, R. E. (2020) Insights into the chemical diversity of the martian mantle from the Pb isotope systematics of shergottite Northwest Africa 8159. *Chemical Geology* **545**: 119638.
- Belov, G. V., Dyachkov, S. A., Levashov, P. R., Lomonosov, I. V., Minakov, D. V., Morozov, I. V., Sineva, M. A. & Smirnov, V. N. (2018) The IVTANTHERMO-Online database for thermodynamic properties of individual substances with web interface. *Journal of Physics: Conference Series* **946**: 012120.
- Berezhnoy, A. A., Bunch, T. E., Ma, P., Herzog, G. F., Knie, K., Rugel, G., Faestermann, T. & Korschinek, G. (2010) Al-26, Be-10, and Mn-53 in Martian Meteorites. *Meteoritics and Planetary Science Supplement* **73**: 5306.
- Bibring, J.-P., Langevin, Y., Mustard, J. F., François Poulet, Arvidson, R., Gendrin, A., Gondet, B., Mangold, N., Pinet, P., Forget, F., Michel Berthé, Jean-Pierre Bibring, Gendrin, A., Cécile Gomez, Gondet, B., Jouplet, D., François Poulet, Soufflot, A., Vincendon, M., Combes, M., Drossart, P., Thérèse Encrenaz, Fouchet, T., Merchiorri, R., Belluci, G., Altieri, F., Formisano, V., Capaccioni, F., Cerroni, P., Coradini, A., Fonti, S., Koralev, O., Kottsov, V., Ignatiev, N., Moroz, V., Titov, D., Zasova, L., Loiseau, D., Mangold, N., Pinet, P., Sylvain Douté, Schmitt, B., Sotin, C., Hauber, E., Hoffmann, H., Jaumann, R., Keller, U., Arvidson, R., Mustard, J. F., Duxbury, T., François Forget & Neukum, G. (2006) Global Mineralogical and Aqueous Mars History Derived from OMEGA/Mars Express Data. *Science* **312**: 400-404.
- Blinova, A. & Herd, C. D. K. (2009) Experimental study of polybaric REE partitioning between olivine, pyroxene and melt of the Yamato 980459 composition: Insights into the petrogenesis of depleted shergottites. *Geochimica et Cosmochimica Acta* **73**: 3471-3492.
- Bogard, D. D. & Johnson, P. (1983) Martian Gases in an Antarctic Meteorite? *Science* **221**: 651-654.

- Borg, L. & Drake, M. J. (2005) A review of meteorite evidence for the timing of magmatism and of surface or near-surface liquid water on Mars. *Journal of Geophysical Research: Planets* **110**.
- Bogard, D. D. & Park, J. (2008) 39Ar-40Ar dating of the Zagami Martian shergottite and implications for magma origin of excess 40Ar. *Meteoritics & Planetary Science* **43**: 1113-1126.
- Borg, L. E., Nyquist, L. E., Taylor, L. A., Wiesmann, H. & Shih, C. (1997) Constraints on Martian differentiation processes from Rb-Sr and Sm-Nd isotopic analyses of the basaltic shergottite QUE 94201. *Geochimica et Cosmochimica Acta* **61**: 4915-4931.
- Borg, L. E., Nyquist, L. E., Reese, Y., Wiesmann, H. & Shih, C. Y. (2001) The age of Dhofar 019 and its relationship to the other Martian meteorites. *Lunar and Planetary Science XXXII*, abstract #1144.
- Borg, L. E., Nyquist, L. E., Wiesmann, H. & Reese, Y. (2002) Constraints on the petrogenesis of Martian meteorites from the Rb-Sr and Sm-Nd isotopic systematics of the Iherzolitic shergottites ALH77005 and LEW88516. *Geochimica et Cosmochimica Acta* **66**: 2037-2053.
- Borg, L. E., Nyquist, L. E., Wiesmann, H., Shih, C. & Reese, Y. (2003) The age of Dar al Gani 476 and the differentiation history of the martian meteorites inferred from their radiogenic isotopic systematics. *Geochimica et Cosmochimica Acta* **67**: 3519-3536.
- Borg, L. E., Edmunson, J. E. & Asmerom, Y. (2005) Constraints on the U-Pb isotopic systematics of Mars inferred from a combined U-Pb, Rb-Sr, and Sm-Nd isotopic study of the Martian meteorite Zagami. *Geochimica et Cosmochimica Acta* **69**: 5819-5830.
- Bouvier, P., Djurado, E., Lucaleau, G. & Le Bihan, T. (2000) High-pressure structural evolution of undoped tetragonal nanocrystalline zirconia. *Physical Review B* **62**: 8731.
- Bouvier, A., Blichert-Toft, J., Vervoort, J. D. & Albarède, F. (2007) The Conundrum of the Age of Shergottites. *38th Annual Lunar and Planetary Science Conference*: 1683.
- Bouvier, A., Blichert-Toft, J. & Albarède, F. (2009) Martian meteorite chronology and the evolution of the interior of Mars. *Earth and Planetary Science Letters* **280**: 285-295.
- Bouvier, A., Blichert-Toft, J., Vervoort, J. D. & Albarède, F. (2005) The age of SNC meteorites and the antiquity of the Martian surface. *Earth and Planetary Science Letters* **240**: 221-233.
- Bouvier, A., Blichert-Toft, J., Vervoort, J. D., Gillet, P. & Albarède, F. (2008) The case for old basaltic shergottites. *Earth and Planetary Science Letters* **266**: 105-124.
- Bowling, T. J., Johnson, B. C., Wiggins, S. E., Walton, E. L., Melosh, H. J. & Sharp, T. G. (2020) Dwell time at high pressure of meteorites during impact ejection from Mars. *Icarus* **343**: 113689.

- Brandon A. D., Nyquist L. E., Shih C. -, and Wiesmann H. 2004. Rb-Sr and Sm-Nd Isotope Systematics of Shergottite NWA 856: Crystallization Age and Implications for Alteration of Hot Desert SNC Meteorites. pp. 1931.
- Brasser, R., Werner, S. C. & Mojzsis, S. J. (2020) Impact bombardment chronology of the terrestrial planets from 4.5 Ga to 3.5 Ga. *Icarus* **338**: 113514.
- Britvin, S. N., Krivovichev, S. V. & Armbruster, T. (2016) Ferromerrillite, Ca₉NaFe₂₊(PO₄)₇, a new mineral from the Martian meteorites, and some insights into merrillite–tuite transformation in shergottites. *European Journal of Mineralogy* **28**: 125-136.
- Cartwright, J. A., Herrmann, S., Ivanova, M. A., Korochantseva, E. V., Lorenz, C. A. & Ott, U. (2010) Noble Gas and CRE Age Measurement of New Basaltic Shergottite JaH 479. *Meteoritics and Planetary Science Supplement* **73**: 5049.
- Cassata, W. S., Cohen, B. E., Mark, D. F., Trappitsch, R., Crow, C. A., Wimpenny, J., Lee, M. R. & Smith, C. L. (2018) Chronology of martian breccia NWA 7034 and the formation of the martian crustal dichotomy. *Science Advances* **4**: eaap8306.
- Cayron, C., Douillard, T., Sibil, A., Fantozzi, G. & Sao-Jao, S. (2010) Reconstruction of the Cubic and Tetragonal Parent Grains from Electron Backscatter Diffraction Maps of Monoclinic Zirconia. *Journal of the American Ceramic Society* **93**: 2541-2544.
- Chamberlain, K. R., Schmitt, A. K., Swapp, S. M., Harrison, T. M., Swoboda-Colberg, N., Bleeker, W., Peterson, T. D., Jefferson, C. W. & Khudoley, A. K. (2010) In situ U-Pb SIMS (IN-SIMS) micro-baddeleyite dating of mafic rocks: method with examples. *Precambrian Research* **183**: 379-387.
- Charlier, B. L. A., Ginibre, C., Morgan, D., Nowell, G. M., Pearson, D. G., Davidson, J. P. & Ottley, C. J. (2006) Methods for the microsampling and high-precision analysis of strontium and rubidium isotopes at single crystal scale for petrological and geochronological applications. *Chemical Geology* **232**: 114-133.
- Chen J. H., and Wasserburg G. J. 1993. LEW88516 and SNC Meteorites. pp. 275.
- Chen, J. H. & Wasserburg, G. J. (1986) Formation ages and evolution of Shergotty and its parent planet from U-Th-Pb systematics. *Geochimica et Cosmochimica Acta* **50**: 955-968.
- Chu, Z., Chen, F., Yang, Y. & Guo, J. (2009) Precise determination of Sm, Nd concentrations and Nd isotopic compositions at the nanogram level in geological samples by thermal ionization mass spectrometry. *Journal of Analytical Atomic Spectrometry* **24**: 1534-1544.
- Clifford, S. M. (1993) A model for the hydrologic and climatic behavior of water on Mars. *Journal of Geophysical Research: Planets* **98**: 10973-11016.

- Cohen, B. E., Mark, D. F., Cassata, W. S., Lee, M. R., Tomkinson, T. & Smith, C. L. (2017) Taking the pulse of Mars via dating of a plume-fed volcano. *Nature Communications* **8**: 640.
- Combs, L. M., Udry, A., Howarth, G. H., Righter, M., Lapen, T. J., Gross, J., Ross, D. K., Rahib, R. R. & Day, J. M. D. (2019) Petrology of the enriched poikilitic shergottite Northwest Africa 10169: Insight into the martian interior. *Geochimica et Cosmochimica Acta* **266**: 435-462.
- Cook, D. L., Wadhwa, M., Clayton, R. N., Dauphas, N., Janney, P. E. & Davis, A. M. (2007) Mass-dependent fractionation of nickel isotopes in meteoritic metal. *Meteoritics & Planetary Science* **42**: 2067-2077.
- Costa, M. M., Jensen, N. K., Bouvier, L. C., Connelly, J. N., Mikouchi, T., Horstwood, M. S. A., Suuronen, J., Moynier, F., Deng, Z., Agranier, A., Martin, L. A. J., Johnson, T. E., Nemchin, A. A. & Bizzarro, M. (2020) The internal structure and geodynamics of Mars inferred from a 4.2-Gyr zircon record. *Proceedings of the National Academy of Sciences* **117**: 30973-30979.
- Cox M. A., Daly L., Cavosie A. J., Bland P. A., Lee M. R., Cohen B. E., Cairney J. M., Eder K., and Yang L. 2018. Complex Twinning in Baddeleyite from the Martian Meteorite North West Africa (NWA) 11522; Preliminary Results. pp. 6257.
- Crozaz, G. & Wadhwa, M. (2001) The terrestrial alteration of saharan shergottites dar al gani 476 and 489: a case study of weathering in a hot desert environment. *Geochimica et Cosmochimica Acta* **65**: 971-977.
- Crozaz, G., Floss, C. & Wadhwa, M. (2003) Chemical alteration and REE mobilization in meteorites from hot and cold deserts. *Geochimica et Cosmochimica Acta* **67**: 4727-4741.
- Darling, J. R., Moser, D. E., Barker, I. R., Tait, K. T., Chamberlain, K. R., Schmitt, A. K. & Hyde, B. C. (2016) Variable microstructural response of baddeleyite to shock metamorphism in young basaltic shergottite NWA 5298 and improved U-Pb dating of Solar System events. *Earth and Planetary Science Letters* **444**: 1-12.
- Darling, J. R., White, L. F., Kizovski, T., Černok, A., Moser, D. E., Tait, K. T., Dunlop, J., Langelier, B., Douglas, J. O., Zhao, X., Franchi, I. A. & Anand, M. (2021) The shocking state of apatite and merrillite in shergottite Northwest Africa 5298 and extreme nanoscale chlorine isotope variability revealed by atom probe tomography. *Geochimica et Cosmochimica Acta* **293**: 422-437.
- Debaille, V., Yin, Q. -, Brandon, A. D. & Jacobsen, B. (2008) Martian mantle mineralogy investigated by the ^{176}Lu - ^{176}Hf and ^{147}Sm - ^{143}Nd systematics of shergottites. *Earth and Planetary Science Letters* **269**: 186-199.
- Debaille V., Roland J., Goderis S., Hublet G., and Pourkhorsandi H. 2022. Asuka 12325: Expanding the Chemical Variety of the Martian Mantle Sampled by Shergottites. pp. 2433.

- Deutsch, A. & Schärer, U. (1990) Isotope systematics and shock-wave metamorphism: I. U-Pb in zircon, titanite and monazite, shocked experimentally up to 59 GPa. *Geochimica et Cosmochimica Acta* **54**: 3427-3434.
- Edmunson, J., Borg, L. E., Shearer, C. K. & Papike, J. J. (2005) Defining the mechanisms that disturb the Sm-Nd isotopic systematics of the Martian meteorites: Examples from Dar al Gani 476 and Allan Hills 77005. *Meteoritics & Planetary Science* **40**: 1159-1174.
- Ehlmann, B. L. & Edwards, C. S. (2014) Mineralogy of the Martian Surface. *Annual Review of Earth and Planetary Sciences* **42**: 291-315.
- Ehlmann, B. L., Mustard, J. F., Murchie, S. L., Bibring, J., Meunier, A., Fraeman, A. A. & Langevin, Y. (2011) Subsurface water and clay mineral formation during the early history of Mars. *Nature* **479**: 53-60.
- El Goresy, A., Gillet, P., Miyahara, M., Ohtani, E., Ozawa, S., Beck, P. & Montagnac, G. (2013) Shock-induced deformation of Shergottites: Shock-pressure and perturbations of magmatic ages on Mars. *Geochimica et Cosmochimica Acta* **101**: 233-262.
- Farley, K. A., Malespin, C., Mahaffy, P., Grotzinger, J. P., Vasconcelos, P. M., Milliken, R. E., Malin, M., Edgett, K. S., Pavlov, A. A., Hurowitz, J. A., Grant, J. A., Miller, H. B., Arvidson, R., Beegle, L., Calef, F., Conrad, P. G., Dietrich, W. E., Eigenbrode, J., Gellert, R., Gupta, S., Hamilton, V., Hassler, D. M., Lewis, K. W., McLennan, S. M., Ming, D., Navarro-González, R., Schwenger, S. P., Steele, A., Stolper, E. M., Sumner, D. Y., Vaniman, D., Vasavada, A., Williford, K., Wimmer-Schweingruber, R., null, n., Blake, D. F., Bristow, T., DesMarais, D., Edwards, L., Haberle, R., Hoehler, T., Hollingsworth, J., Kahre, M., Keely, L., McKay, C., Wilhelm, M. B., Bleacher, L., Brinckerhoff, W., Choi, D., Dworkin, J. P., Floyd, M., Freissinet, C., Garvin, J., Glavin, D., Harpold, D., Martin, D. K., McAdam, A., Raaen, E., Smith, M. D., Stern, J., Tan, F., Trainer, M., Meyer, M., Posner, A., Voytek, M., Anderson, R. C., Aubrey, A., Behar, A., Blaney, D., Brinza, D., Christensen, L., Crisp, J. A., DeFlores, L., Feldman, J., Feldman, S., Flesch, G., Hurowitz, J., Jun, I., Keymeulen, D., Maki, J., Mischna, M., Morookian, J. M., Parker, T., Pavri, B., Schoppers, M., Sengstacken, A., Simmonds, J. J., Spanovich, N., Juarez, Manuel de la Torre, Webster, C. R., Yen, A., Archer, P. D., Cucinotta, F., Jones, J. H., Morris, R. V., Niles, P., Rampe, E., Nolan, T., Fisk, M., Radziemski, L., Barraclough, B., Bender, S., Berman, D., Dobrea, E. N., Tokar, R., Williams, R. M. E., Yingst, A., Leshin, L., Cleghorn, T., Huntress, W., Manhès, G., Hudgins, J., Olson, T., Stewart, N., Sarrazin, P., Vicenzi, E., Wilson, S. A., Bullock, M., Ehresmann, B., Peterson, J., Rafkin, S., Zeitlin, C., Fedosov, F., Golovin, D., Karpushkina, N., Kozyrev, A., Litvak, M., Malakhov, A., Mitrofanov, I., Mokrousov, M., Nikiforov, S., Prokhorov, V., Sanin, A., Tretyakov, V., Varenikov, A., Vostrukhin, A., Kuzmin, R., Clark, B., Wolff, M., Botta, O., Drake, D., Bean, K.,

Lemmon, M., Anderson, R. B., Herkenhoff, K., Lee, E. M., Sucharski, R., Hernández, M. Á, de Pablo, Ávalos, J. J. B., Ramos, M., Kim, M., Plante, I., Muller, J., Ewing, R., Boynton, W., Downs, R., Fitzgibbon, M., Harshman, K., Morrison, S., Kortmann, O., Palucis, M., Williams, A., Lugmair, G., Wilson, M. A., Rubin, D., Jakosky, B., Balic-Zunic, T., Frydenvang, J., Jensen, J. K., Kinch, K., Koefoed, A., Madsen, M. B., Stipp, S. L. S., Boyd, N., Campbell, J. L., Perrett, G., Pradler, I., VanBommel, S., Jacob, S., Owen, T., Rowland, S., Savijärvi, H., Boehm, E., Böttcher, S., Burmeister, S., Guo, J., Köhler, J., García, C. M., Mueller-Mellin, R., Bridges, J. C., McConnochie, T., Benna, M., Franz, H., Bower, H., Brunner, A., Blau, H., Boucher, T., Carmosino, M., Atreya, S., Elliott, H., Halleaux, D., Rennó, N., Wong, M., Pepin, R., Elliott, B., Spray, J., Thompson, L., Gordon, S., Newsom, H., Ollila, A., Williams, J., Bentz, J., Nealson, K., Popa, R., Kah, L. C., Moersch, J., Tate, C., Day, M., Kocurek, G., Hallet, B., Sletten, R., Francis, R., McCullough, E., Cloutis, E., ten Kate, I. L., Kuzmin, R., Fraeman, A., Scholes, D., Slavney, S., Stein, T., Ward, J., Berger, J. & Moores, J. E. (2014) In Situ Radiometric and Exposure Age Dating of the Martian Surface. *Science* **343**: 1247166.

Ferdous J., and Brandon A. D. (2020). Crystallization Age of Enriched Poikilitic Shergottite Northwest Africa 7397 Determined from Sm-Nd Isotope Systematics. pp. 1064.

Ferdous, J., Brandon, A. D., Peslier, A. H. & Pirotte, Z. (2017) Evaluating crustal contributions to enriched shergottites from the petrology, trace elements, and Rb-Sr and Sm-Nd isotope systematics of Northwest Africa 856. *Geochimica et Cosmochimica Acta* **211**: 280-306.

Filiberto, J., Gross, J., Udry, A., Trela, J., Wittmann, A., Cannon, K. M., Penniston-Dorland, S., Ash, R., Hamilton, V. E., Meado, A. L., Carpenter, P., Jolliff, B. & Ferré, E. C. (2018) Shergottite Northwest Africa 6963: A Pyroxene-Cumulate Martian Gabbro. *Journal of Geophysical Research: Planets* **123**: 1823-1841.

Fisher, C. M., McFarlane, C. R. M., Hanchar, J. M., Schmitz, M. D., Sylvester, P. J., Lam, R. & Longerich, H. P. (2011) Sm–Nd isotope systematics by laser ablation-multicollector-inductively coupled plasma mass spectrometry: Methods and potential natural and synthetic reference materials. *Chemical Geology* **284**: 1-20.

Foley, C. N., Wadhwa, M., Borg, L. E., Janney, P. E., Hines, R. & Grove, T. L. (2005) The early differentiation history of Mars from 182W-142Nd isotope systematics in the SNC meteorites. *Geochimica et Cosmochimica Acta* **69**: 4557-4571.

French, J. E. & Heaman, L. M. (2010) Precise U–Pb dating of Paleoproterozoic mafic dyke swarms of the Dharwar craton, India: implications for the existence of the Neoarchean supercraton Sclavia. *Precambrian Research* **183**: 416-441.

- Fritz, J., Greshake, A. & Stöffler, D. (2005) Micro-Raman spectroscopy of plagioclase and maskelynite in Martian meteorites: Evidence of progressive shock metamorphism. *Antarctic Meteorite Research* **18**: 96.
- Fritz, J., Greshake, A. & Fernandes, V. A. (2017) Revising the shock classification of meteorites. *Meteoritics & Planetary Science* **52**: 1216-1232.
- Fritz J., Fernandes V. A., Greshake A., Holzwarth A., and Böttger U. (2019) On the formation of diaplectic glass: Shock and thermal experiments with plagioclase of different chemical compositions. *Meteoritics and Planetary Science* **54**: 1533-1547.
- Gaffney, A. M., Borg, L. E. & Connelly, J. N. (2007) Uranium–lead isotope systematics of Mars inferred from the basaltic shergottite QUE 94201. *Geochimica et Cosmochimica Acta* **71**: 5016-5031.
- Gaffney, A. M., Borg, L. E., Asmerom, Y., Shearer, C. K. & Burger, P. V. (2011) Disturbance of isotope systematics during experimental shock and thermal metamorphism of a lunar basalt with implications for Martian meteorite chronology. *Meteoritics & Planetary Science* **46**: 35-52.
- Gao, S., Liu, X., Yuan, H., Hattendorf, B., Günther, D., Chen, L. & Hu, S. (2002) Determination of Forty Two Major and Trace Elements in USGS and NIST SRM Glasses by Laser Ablation-Inductively Coupled Plasma-Mass Spectrometry. *Geostandards Newsletter* **26**: 181-196.
- Gattacceca, J., McCubbin, F. M., Bouvier, A. & Grossman, J. (2020) The Meteoritical Bulletin, No. 107. *Meteoritics & Planetary Science* **55**: 460-462.
- Geiss, J. & Rossi, A. P. (2013) On the chronology of lunar origin and evolution. *The Astronomy and Astrophysics Review* **21**: 68.
- Ghiorso, M. S. & Evans, B. W. (2008) Thermodynamics of rhombohedral oxide solid solutions and a revision of the Fe-Ti two-oxide geothermometer and oxygen-barometer. *American Journal of Science* **308**: 957-1039.
- Goodrich, C. A. (2002) Olivine-phyric martian basalts: A new type of shergottite. *Meteoritics & Planetary Science* **37**: B31-B34.
- Goodrich, C. A. (2003) Petrogenesis of olivine-phyric shergottites Sayh al Uhaymir 005 and Elephant Moraine A79001 lithology A. *Geochimica et Cosmochimica Acta* **67**: 3735-3772.
- Goodrich, C. A., Herd, C. D. K. & Taylor, L. A. (2003) Spinel and oxygen fugacity in olivine-phyric and Iherzolitic shergottites. *Meteoritics & Planetary Science* **38**: 1773-1792.
- Goodwin, A., Garwood, R. J. & Tartèse, R. (2022) A Review of the “Black Beauty” Martian Regolith Breccia and Its Martian Habitability Record. *Astrobiology* **22**: 755-767.

- Greshake, A., Fritz, J., Böttger, U. & Goran, D. (2013) Shear-induced ringwoodite formation in the Martian shergottite Dar al Gani 670. *Earth and Planetary Science Letters* **375**: 383-394.
- Gross, J., Treiman, A. H., Filiberto, J. & Herd, C. D. K. (2011) Primitive olivine-phyric shergottite NWA 5789: Petrography, mineral chemistry, and cooling history imply a magma similar to Yamato-980459. *Meteoritics & Planetary Science* **46**: 116-133.
- Hamilton J. S., Herd C. D. K., Walton E. L., and Tornabene L. L. 2020. Prioritizing Candidate Source Craters for Martian Meteorites. pp. 2607.
- Harlou, R., Pearson, D. G., Nowell, G. M., Ottley, C. J. & Davidson, J. P. (2009) Combined Sr isotope and trace element analysis of melt inclusions at sub-ng levels using micro-milling, TIMS and ICPMS. *Chemical Geology* **260**: 254-268.
- Harper, C. L., Nyquist, L. E., Bansal, B., Wiesmann, H. & Chi-Yu Shih (1995) Rapid Accretion and Early Differentiation of Mars Indicated by $^{142}\text{Nd}/^{144}\text{Nd}$ in SNC Meteorites. *Science* **267**: 213-217.
- Hartmann, W. K. (2005) Martian cratering 8: Isochron refinement and the chronology of Mars. *Icarus* **174**: 294-320.
- Hartmann, W. K. (1973) Martian Cratering, 4, Mariner 9 initial analysis of cratering chronology. *Journal of Geophysical Research (1896-1977)* **78**: 4096-4116.
- Hartmann W. K., and Neukum G. 2001. Cratering Chronology and the Evolution of Mars. Chronology and Evolution of. pp. 165-194.
- Hartmann, W. K. & Berman, D. C. (2000) Elysium Planitia lava flows: Crater count chronology and geological implications. *Journal of Geophysical Research: Planets* **105**: 15011-15025.
- Harvey, J. & Baxter, E. F. (2009) An improved method for TIMS high precision neodymium isotope analysis of very small aliquots (1–10 ng). *Chemical Geology* **258**: 251-257.
- Harvey, R. P., Wadhwa, M., McSween, H. Y. & Crozaz, G. (1993) Petrography, mineral chemistry, and petrogenesis of Antarctic Shergottite LEW88516. *Geochimica et Cosmochimica Acta* **57**: 4769-4783.
- Hays, N. R., Drake M. J., and Gehrels G. G. 2011. U-Th-Pb Analysis of Baddeleyites in Shergottite Meteorites. 42nd Annual Lunar and Planetary Science Conference. pp. 1243.
- Head, J. N., Jay Melosh, H. & Ivanov, B. A. (2002) Martian Meteorite Launch: High-Speed Ejecta from Small Craters. *Science* **298**: 1752-1756.
- Heaman, L. M. (2009) The application of U–Pb geochronology to mafic, ultramafic and alkaline rocks: An evaluation of three mineral standards. *Chemical Geology* **261**: 43-52.
- Heaman, L. M. & LeCheminant, A. N. (1993) Paragenesis and U-Pb systematics of baddeleyite (ZrO_2). *Chemical Geology; Geochemistry of Accessory Minerals* **110**: 95-126.

- Herd, C. D. (2006) Insights into the redox history of the NWA 1068/1110 martian basalt from mineral equilibria and vanadium oxybarometry. *American Mineralogist* **91**: 1616-1627.
- Herd, C. (2019) Reconciling redox: making spatial and temporal sense of oxygen fugacity variations in martian igneous rocks. *LPI*: 2746.
- Herd, C. D. K., Walton, E. L., Agee, C. B., Muttik, N., Ziegler, K., Shearer, C. K., Bell, A. S., Santos, A. R., Burger, P. V., Simon, J. I., Tappa, M. J., McCubbin, F. M., Gattaccea, J., Lagroix, F., Sanborn, M. E., Yin, Q., Cassata, W. S., Borg, L. E., Lindvall, R. E., Kruijer, T. S., Brennecka, G. A., Kleine, T., Nishiizumi, K. & Caffee, M. W. (2017) The Northwest Africa 8159 martian meteorite: Expanding the martian sample suite to the early Amazonian. *Geochimica et Cosmochimica Acta* **218**: 1-26.
- Herd, C. D. K., Moser, D. E., Tait, K., Darling, J. R., Shaulis, B. J. & McCoy, T. J. (2018a) Crystallization of Baddeleyite in Basaltic Rocks from Mars, and Comparisons with the Earth, Moon, and Vesta. *Microstructural Geochronology*: 137-166.
- Herd C. D. K., Tornabene L. L., Bowling T. J., Walton E. L., Sharp T. G., Melosh H. J., Hamilton J. S., Viviano C. E., and Ehlmann B. L. (2018b). Constraining the Source Craters of the Martian Meteorites: Implications for Prioritization of Returned Samples from Mars. pp. 6097.
- Herzog G. F., and Caffee M. W. 2014. Cosmic-Ray Exposure Ages of Meteorites. In: , edited by Davis A. M. pp. 419-454.
- Hoffmann, D. L., Spötl, C. & Mangini, A. (2009) Micromill and in situ laser ablation sampling techniques for high spatial resolution MC-ICPMS U-Th dating of carbonates. *Chemical Geology* **259**: 253-261.
- Howarth, G. H. & Udry, A. (2017) Trace elements in olivine and the petrogenesis of the intermediate, olivine-phyric shergottite NWA 10170. *Meteoritics & Planetary Science* **52**: 391-409.
- Howarth, G. H., Pernet-Fisher, J., Balta, J. B., Barry, P. H., Bodnar, R. J. & Taylor, L. A. (2014) Two-stage polybaric formation of the new enriched, pyroxene-oikocrystic, Iherzolitic shergottite, NWA 7397. *Meteoritics & Planetary Science* **49**: 1812-1830.
- Hu, J. & Sharp, T. G. (2022) Formation, preservation and extinction of high-pressure minerals in meteorites: temperature effects in shock metamorphism and shock classification. *Progress in Earth and Planetary Science* **9**: 6.
- Huang, K., Blusztajn, J., Oppo, D. W., Curry, W. B. & Peucker-Ehrenbrink, B. (2012) High-precision and accurate determinations of neodymium isotopic compositions at nanogram levels in natural materials by MC-ICP-MS. *Journal of Analytical Atomic Spectrometry* **27**: 1560-1567.

- Hui, H., Peslier, A. H., Lapen, T. J., Shafer, J. T., Brandon, A. D. & Irving, A. J. (2011) Petrogenesis of basaltic shergottite Northwest Africa 5298: Closed-system crystallization of an oxidized mafic melt. *Meteoritics & Planetary Science* **46**: 1313-1328.
- Ibanez-Mejia, M., Gehrels, G. E., Ruiz, J., Vervoort, J. D., Eddy, M. P. & Li, C. (2014) Small-volume baddeleyite (ZrO₂) U-Pb geochronology and Lu-Hf isotope geochemistry by LA-ICP-MS. Techniques and applications. *Chemical Geology* **384**: 149-167.
- Ikeda, Y. (1994) Petrography and petrology of the ALH-77005 shergottite. *Antarctic Meteorite Research* **7**: 9.
- Irving A. J., Kuehner S. M., Lapen T. J., Righter M., Busemann H., Wieler R., and Nishiizumi K. 2017. Keeping Up with the Martian Meteorites and Constraining the Number of Separate Launch Sites on Mars. pp. 2068.
- Ivanov, B. A., Jay Melosh, H. & Head, J. N. (2002) Martian Meteorite Launch: High-Speed Ejecta from Small Craters. *Science* **298**: 1752-1756.
- Jagoutz, E. (1989) Sr and Nd isotopic systematics in ALHA 77005: Age of shock metamorphism in shergottites and magmatic differentiation on Mars. *Geochimica et Cosmochimica Acta* **53**: 2429-2441.
- Jagoutz, E. & Wänke, H. (1986) Sr and Nd isotopic systematics of Shergotty meteorite. *Geochimica et Cosmochimica Acta* **50**: 939-953.
- Jakosky, B. M., Pepin, R. O., Johnson, R. E. & Fox, J. L. (1994) Mars Atmospheric Loss and Isotopic Fractionation by Solar-Wind-Induced Sputtering and Photochemical Escape. *Icarus* **111**: 271-288.
- Jambon, A., Barrat, J. A., Sautter, V., Gillet, P., Göpel, C., Javoy, M., Joron, J. L. & Lesourd, M. (2002) The basaltic shergottite Northwest Africa 856: Petrology and chemistry. *Meteoritics & Planetary Science* **37**: 1147-1164.
- Jean, M. M., Howarth, G. H., Bodnar, B., Klyukin, Y. & Taylor, L. A. (2016) Petrogenesis of the New Basaltic Shergottite Northwest Africa 10299: fO₂ Consistent with an Intermediate to Depleted Geochemical Source. *LPI*: 2698.
- Jiang, Y. & Hsu, W. (2012) Petrogenesis of Grove Mountains 020090: An enriched “Iherzolitic” shergottite. *Meteoritics & Planetary Science* **47**: 1419-1435.
- Jones, J. H. (1989) Isotopic relationships among the shergottites, the nakhlites and Chassigny. *Lunar and Planetary Science Conference Proceedings* **19**: 465-474.
- Kelly, P. M. & Francis Rose, L. R. (2002) The martensitic transformation in ceramics — its role in transformation toughening. *Progress in Materials Science* **47**: 463-557.

- Kerschhofer, L., Schärer, U. & Deutsch, A. (2000) Evidence for crystals from the lower mantle: baddeleyite megacrysts of the Mbuji Mayi kimberlite. *Earth and Planetary Science Letters* **179**: 219-225.
- Kizovski, T. V., Izawa, M. R. M., Tait, K. T., Moser, D. E., Day, J. M. D., Hyde, B. C., White, L. F., Kovarik, L., Taylor, S. D., Perea, D. E., Barker, I. R. & Joy, B. R. (2020) Petrogenesis, alteration, and shock history of intermediate shergottite Northwest Africa 7042: Evidence for hydrous magmatism on Mars? *Geochimica et Cosmochimica Acta* **283**: 103-123.
- Košler, J., Fonneland, H., Sylvester, P., Tubrett, M. & Pedersen, R. (2002) U-Pb dating of detrital zircons for sediment provenance studies—a comparison of laser ablation ICPMS and SIMS techniques. *Chemical Geology* **182**: 605-618.
- Krietsch, D. (2020) Alteration on asteroids, diversity of primordial volatiles and their carriers in carbonaceous chondrites, and martian shergottite sampling sites - studied by meteoritic noble gases. *Ph.D. Thesis*.
- Kring, D. A., Gleason, J. D., Swindle, T. D., Nishiizumi, K., Caffee, M. W., Hill, D. H., Jull, A. T. & Boynton, W. V. (2003) Composition of the first bulk melt sample from a volcanic region of Mars: Queen Alexandra Range 94201. *Meteoritics & Planetary Science* **38**: 1833-1848.
- Kuchka, C. R., Herd, C. D. K., Walton, E. L., Guan, Y. & Liu, Y. (2017) Martian low-temperature alteration materials in shock-melt pockets in Tissint: Constraints on their preservation in shergottite meteorites. *Geochimica et Cosmochimica Acta* **210**: 228-246.
- Lagain, A., Benedix, G. K., Servis, K., Baratoux, D., Doucet, L. S., Rajšić, A., Devillepoix, H. A. R., Bland, P. A., Towner, M. C., Sansom, E. K. & Miljković, K. (2021) The Tharsis mantle source of depleted shergottites revealed by 90 million impact craters. *Nature Communications* **12**: 6352.
- Lagain, A., Bouley, S., Zanda, B., Miljković, K., Rajšić, A., Baratoux, D., Payré, V., Doucet, L. S., Timms, N. E., Hewins, R., Benedix, G. K., Malarewic, V., Servis, K. & Bland, P. A. (2022) Early crustal processes revealed by the ejection site of the oldest martian meteorite. *Nature Communications* **13**: 3782.
- Lapen, T. J., Righter, M., Brandon, A. D., Debaille, V., Beard, B. L., Shafer, J. T. & Peslier, A. H. (2010) A Younger Age for ALH84001 and Its Geochemical Link to Shergottite Sources in Mars. *Science* **328**: 347-351.
- Lapen, T. J., Righter, M., Andreasen, R., Irving, A. J., Satkoski, A. M., Beard, B. L., Nishiizumi, K., Timothy Jull, A. J. & Caffee, M. W. (2017) Two billion years of magmatism recorded from a single Mars meteorite ejection site. *Science Advances* **3**: e1600922.
- Lapen, T. J., Righter, M., Gao, Y. & Irving, A. J. (2018) Representative Bulk Elemental Compositions for a Suite of Shergottites. *LPI*: 2773.

- Lentz, R. C. F. & McSween Jr., H. Y. (2000) Crystallization of the basaltic shergottites: Insights from crystal size distribution (CSD) analysis of pyroxenes. *Meteoritics & Planetary Science* **35**: 919-927.
- Li, C., Chen, F. & Li, X. (2007) Precise isotopic measurements of sub-nanogram Nd of standard reference material by thermal ionization mass spectrometry using the NdO⁺ technique. *International Journal of Mass Spectrometry* **266**: 34-41.
- Li, Q., Li, X., Liu, Y., Tang, G., Yang, J. & Zhu, W. (2010) Precise U-Pb and Pb-Pb dating of Phanerozoic baddeleyite by SIMS with oxygen flooding technique. *Journal of Analytical Atomic Spectrometry* **25**: 1107-1113.
- Liu, T., Li, C. & Lin, Y. (2011) Rb-Sr and Sm-Nd isotopic systematics of the Iherzolitic shergottite GRV 99027. *Meteoritics & Planetary Science* **46**: 681-689.
- Lindner M., Hezel D. C., Gerdes A., Marschall H. R., and Brenker F. E. 2022. Age of enriched gabbroic shergottite Northwest Africa 6963 and its Si-rich mesostasis (abstract). *88th Annual Meeting of the Meteoritical Society 2022*:Abstract #6137 (LPI Contrib. No. 2695).
- Lindsley, D. H. (1983) Pyroxene thermometry. *American Mineralogist* **68**: 477-493.
- Llorca, J., Roszjar, J., Cartwright, J. A., Bischoff, A., Ott, U., Pack, A., Merchel, S., Rugel, G., Fimiani, L. & Ludwig, P. (2013) The Ksar Ghilane 002 shergottite—the 100th registered Martian meteorite fragment. *Meteoritics & Planetary Science* **48**: 493-513.
- Lodders, K. (1998) A survey of shergottite, nakhlite and chassigny meteorites whole-rock compositions. *Meteoritics & Planetary Science* **33**: A183-A190.
- Lodders K., Palme H., and Gail H. 2009. 4.4 Abundances of the elements in the Solar System. In: *Solar system*, edited by Anonymous : Springer. pp. 712-770.
- Lorenz, C. A., Ivanova, M. A., Teplyakova, S. N., Korochantsev, A. V., Franchi, I. A. & Ott, U. (2010) Basaltic Shergottite, Jiddat Al Harasis 479. *Meteoritics & Planetary Science* **73**: 5228.
- Lovering J. F., and Wark D. A. 1971. Uranium-enriched phases in Apollo 11 and Apollo 12 basaltic rocks. *Lunar and Planetary Science Conference Proceedings*. pp. 151.
- Ludwig, K. R. (2003) User's manual for isoplot 3.00, a geochronological toolkit for microsoft excel. *Berkeley Geochronl.Cent.Spec.Publ.* **4**: 25-32.
- Marchi, S. (2021) A New Martian Crater Chronology: Implications for Jezero Crater. *The Astronomical Journal* **161**: 187.
- Mathew, K. J., Marty, B., Marti, K. & Zimmermann, L. (2003) Volatiles (nitrogen, noble gases) in recently discovered SNC meteorites, extinct radioactivities and evolution. *Earth and Planetary Science Letters* **214**: 27-42.

- McCoy, T. J., Taylor, G. J. & Keil, K. (1992) Zagami: Product of a two-stage magmatic history. *Geochimica et Cosmochimica Acta* **56**: 3571-3582.
- McCubbin, F. M., Shearer, C. K., Burger, P. V., Hauri, E. H., Wang, J., Elardo, S. M. & Papike, J. J. (2014) Volatile abundances of coexisting merrillite and apatite in the martian meteorite Shergotty: Implications for merrillite in hydrous magmas. *American Mineralogist* **99**: 1347-1354.
- McCubbin, F. M., Boyce, J. W., Novák-Szabó, T., Santos, A. R., Tartèse, R., Muttik, N., Domokos, G., Vazquez, J., Keller, L. P., Moser, D. E., Jerolmack, D. J., Shearer, C. K., Steele, A., Elardo, S. M., Rahman, Z., Anand, M., Delhaye, T. & Agee, C. B. (2016) Geologic history of Martian regolith breccia Northwest Africa 7034: Evidence for hydrothermal activity and lithologic diversity in the Martian crust. *Journal of Geophysical Research: Planets* **121**: 2120-2149.
- McFarlane, C. R. M. & Spray, J. G. (2022) The Los Angeles martian diabase: Phosphate U-Th-Pb geochronology and mantle source constraints. *Geochimica et Cosmochimica Acta* **326**: 166-179.
- McSween Jr., H. Y. (1994) What we have learned about Mars from SNC meteorites. *Meteoritics* **29**: 757-779.
- McSween, H. Y., Eisenhour, D. D., Taylor, L. A., Wadhwa, M. & Crozaz, G. (1996) QUE94201 shergottite: Crystallization of a Martian basaltic magma. *Geochimica et Cosmochimica Acta* **60**: 4563-4569.
- Melosh, H. J. (1984) Impact ejection, spallation, and the origin of meteorites. *Icarus* **59**: 234-260.
- Melosh, H. J. (1985) Ejection of rock fragments from planetary bodies. *Geology* **13**: 144-148.
- Meteoritical Bulletin Database. URL: <https://www.lpi.usra.edu/meteor/about.php>. Last updated on August 19, 2022. Accessed on August 23, 2022.
- MEPAG E2E-iSAG (2012) Planning for Mars Returned Sample Science: Final Report of the MSR End-to-End International Science Analysis Group (E2E-iSAG). *Astrobiology* **12**: 175-230.
- Millonig, L. J., Gerdes, A. & Groat, L. A. (2013) The effect of amphibolite facies metamorphism on the U-Th-Pb geochronology of accessory minerals from meta-carbonatites and associated meta-alkaline rocks. *Chemical Geology* **353**: 199-209.
- Min, K., Farah, A. E., Lee, S. R. & Lee, J. I. (2017) (U-Th)/He ages of phosphates from Zagami and ALHA77005 Martian meteorites: Implications to shock temperatures. *Geochimica et Cosmochimica Acta* **196**: 160-178.
- Misawa, K. & Yamaguchi, A. (2007) U-Pb ages of NWA 856 baddeleyite. *M&PSA* **42**: 5228.
- Misawa, K., Yamada, K., Nakamura, N., Morikawa, N., Yamashita, K. & Premo, W. R. (2006) Sm-Nd isotopic systematics of lherzolitic shergottite Yamato-793605. *Antarctic Meteorite Research*: 45-57.

- Misawa, K., Park, J., Shih, C. -, Reese, Y., Bogard, D. D. & Nyquist, L. E. (2008) Rb–Sr, Sm–Nd, and Ar–Ar isotopic systematics of Iherzolitic shergottite Yamato 000097. *Polar Science* **2**: 163-174.
- Misawa, K., Nakamura, N., Premo, W. R. & Tatsumoto, M. (1997) U-Th-Pb isotopic systematics of Iherzolitic shergottite Yamato-793605. *Antarctic Meteorite Research* **10**: 95.
- Morikawa, N., Misawa, K., Kondorosi, G., Premo, W. R., Tatsumoto, M. & Nakamura, N. (2001) Rb-Sr isotopic systematics of Iherzolitic shergottite Yamato-793605. *Antarctic Meteorite Research* **14**: 47-60.
- Moser, D. E., Chamberlain, K. R., Tait, K. T., Schmitt, A. K., Darling, J. R., Barker, I. R. & Hyde, B. C. (2013) Solving the Martian meteorite age conundrum using micro-baddeleyite and launch-generated zircon. *Nature* **499**: 454-457.
- Nakanishi, N., Yokoyama, T., Okabayashi, S., Iwamori, H. & Hirata, T. (2022) Geochemical constraints on the formation of chondrules: Implication from Os and Fe isotopes and HSE abundances in metals from CR chondrites. *Geochimica et Cosmochimica Acta* **319**: 254-270.
- Neukum, G. & Hiller, K. (1981) Martian ages. *Journal of Geophysical Research: Solid Earth* **86**: 3097-3121.
- Neukum, G. & Wise, D. U. (1976) Mars: A Standard Crater Curve and Possible New Time Scale. *Science* **194**: 1381-1387.
- Neukum G., Ivanov B. A., and Hartmann W. K. 2001. Cratering Records in the Inner Solar System in Relation to the Lunar Reference System. Chronology and Evolution of. pp. 55-86.
- Nicklas, R. W., Day, J. M. D., Vaci, Z., Udry, A., Liu, Y. & Tait, K. T. (2021) Uniform oxygen fugacity of shergottite mantle sources and an oxidized martian lithosphere. *Earth and Planetary Science Letters* **564**: 116876.
- Nielsen, R.,H., Schleiwitz, J.,H., Nielsen, H. & Updated, b. S. (2013) Zirconium and Zirconium Compounds. *Kirk-Othmer Encyclopedia of Chemical Technology*: 1-46.
- Niihara, T. (2011) Uranium-lead age of baddeleyite in shergottite Roberts Massif 04261: Implications for magmatic activity on Mars. *Journal of Geophysical Research: Planets* **116**.
- Niihara, T., Kaiden, H., Misawa, K., Sekine, T. & Mikouchi, T. (2012) U–Pb isotopic systematics of shock-loaded and annealed baddeleyite: Implications for crystallization ages of Martian meteorite shergottites. *Earth and Planetary Science Letters* **341-344**: 195-210.
- Nishiizumi K., Hillegonds D. J., McHargue L. R., and Jull A. J. T. 2004. Exposure and Terrestrial Histories of New Lunar and Martian Meteorites. pp. 1130.
- Nyquist L. E., Bogard D. D., Shih C. -, Greshake A., Stöffler D., and Eugster O. (2001a). Ages and Geologic Histories of Martian Meteorites. Chronology and Evolution of. pp. 105-164.

- Nyquist L. E., Reese Y., Wiesmann H., and Shih C. (2001b). Age of EET79001B and implications for shergottite origins. *Lunar and Planetary Science Conference*. pp. 1407.
- Nyquist L. E., Ikeda Y., Shih C., Reese Y. D., Nakamura N., and Takeda H. (2006). Sm-Nd age and Nd-and Sr-isotopic evidence for the petrogenesis of Dhofar 378. *30th Symposium on antarctic Meteorites*.
- Nyquist, L. E., Bogard, D. D., Shih, C. -, Park, J., Reese, Y. D. & Irving, A. J. (2009) Concordant Rb-Sr, Sm-Nd, and Ar-Ar ages for Northwest Africa 1460: A 346Ma old basaltic shergottite related to "Iherzolitic" shergottites. *Geochimica et Cosmochimica Acta* **73**: 4288-4309.
- Ohtaka, O., Fukui, H., Kunisada, T., Fujisawa, T., Funakoshi, K., Utsumi, W., Irifune, T., Kuroda, K. & Kikegawa, T. (2001) Phase relations and equations of state of ZrO₂ under high temperature and high pressure. *Physical Review B* **63**: 174108.
- O'Neal E. W., Ostwald A. M., Udry A., Gross J., Righter M., McQuaig D. R., Lapen T. J., Howarth G. H., and Johnsen R. 2022. Melt Inclusion, Trace Element, and Isotopic Analyses of a Poikilitic Shergottite Suite: Implications for Martian Magmatism. pp. 2449.
- Ottley C. J., Pearson D. G., and Irvine G. J. 2003. A routine method for the dissolution of geological samples for the analysis of REE and trace elements via ICP-MS. In: *Plasma Source Mass Spectrometry: Applications and Emerging Technologies*, edited by Holland G. and Tanner S. D.: The Royal Society of Chemistry. pp. 221-230.
- Palme, H., Lodders, K. & Jones, A. (2014) Solar system abundances of the elements. *Planets, Asteroids, Comets and The Solar System, Volume 2 of Treatise on Geochemistry (Second Edition)*. Edited by Andrew M. Davis. Elsevier, 2014., p.15-36 2.
- Park, J., Bogard, D. D., Mikouchi, T. & McKay, G. A. (2008) Dhofar 378 Martian shergottite: Evidence of early shock melting. *Journal of Geophysical Research: Planets* **113**.
- Park, J., Bogard, D. D., Nyquist, L. E., Garrison, D. H. & Mikouchi, T. (2013) Ar-Ar ages and trapped Ar components in Martian shergottites RBT 04262 and LAR 06319. *Geochimica et Cosmochimica Acta* **121**: 546-570.
- Park, J., Bogard D. D., Nyquist L. E. & Herzog, G. F. (2014) Issues in dating young rocks from another planet: Martian shergottites. *Geological Society, London, Special Publications* **378**: 297-316.
- Pepin, R. O. (1994) Evolution of the Martian Atmosphere. *Icarus* **111**: 289-304.
- Plescia, J. B. (1990) Recent flood lavas in the Elysium region of Mars. *Icarus* **88**: 465-490.
- Pollington, A. D. & Baxter, E. F. (2011) High precision microsampling and preparation of zoned garnet porphyroblasts for Sm-Nd geochronology. *Chemical Geology* **281**: 270-282.

- Reinhard A., Inglis J. D., Steiner R., LaMont S., and Jackson M. G. 2019. Isotopic Analysis of Sub-Nanogram Nd Samples Using New ATONA Amplifiers. AGU Fall Meeting Abstracts. pp. V11D-0111.
- Returned Sample Science Board, Carrier B. L., Beaty D. W., McSween H. Y., Czaja A. D., Goreva Y. S., Hausrath E. M., Herd C. D. K., Humayun M., McCubbin F. M., McLennan S. M., Pratt L. M., Sephton M. A., Steele A., and Weiss B. P. 2017. Strategies for Investigation Early Mars Using Returned Samples. pp. 3051.
- Righter, M., Andreasen, R., Lapen, T. J. & Irving, A. J. (2014) The age and source composition for depleted shergottite Northwest Africa 7635: A 2.3 Ga magmatic rock from early Amazonian Mars. *LPI*: 2550.
- Righter M., Lapen T. J., and Irving A. J. (2018). Extending the Range in Ages and Source Compositions of Shergottites: Lu-Hf and Sm-Nd Age and Isotope Systematics of Northwest Africa 4480. pp. 2609.
- Schmitt, A. K., Chamberlain, K. R., Swapp, S. M. & Harrison, T. M. (2010) In situ U-Pb dating of micro-baddeleyite by secondary ion mass spectrometry. *Chemical Geology* **269**: 386-395.
- Schoene B. (2014). 4.10 - U-Th-Pb Geochronology. In: *Treatise on Geochemistry (Second Edition)*, edited by Holland H. D. and Turekian K. K. Oxford: Elsevier. pp. 341-378.
- Schulz, T., Povinec, P. P., Ferrière, L., Jull, A. J. T., Kováčik, A., Sýkora, I., Tusch, J., Münker, C., Topa, D. & Koeberl, C. (2020) The history of the Tissint meteorite, from its crystallization on Mars to its exposure in space: New geochemical, isotopic, and cosmogenic nuclide data. *Meteoritics & Planetary Science* **55**: 294-311.
- Shafer, J. T., Brandon, A. D., Lapen, T. J., Righter, M., Peslier, A. H. & Beard, B. L. (2010) Trace element systematics and ^{147}Sm - ^{143}Nd and ^{176}Lu - ^{176}Hf ages of Larkman Nunatak 06319: Closed-system fractional crystallization of an enriched shergottite magma. *Geochimica et Cosmochimica Acta* **74**: 7307-7328.
- Sharp T. G., and de Carli P. S. (2006). Shock Effects in Meteorites. In: , edited by Lauretta D. S. and McSween H. Y. pp. 653.
- Sharp, T. G., Walton, E. L., Hu, J. & Agee, C. (2019) Shock conditions recorded in NWA 8159 martian augite basalt with implications for the impact cratering history on Mars. *Geochimica et Cosmochimica Acta* **246**: 197-212.
- Shaulis, B. J., Righter, M., Lapen, T. J., Jolliff, B. J. & Irving, A.J. (2017) 3.1 Ga crystallization age for magnesian and ferroan gabbro lithologies in the Northwest Africa 773 clan of lunar meteorites. *Geochimica et Cosmochimica Acta* **213**: 435-456.

- Shearer, C. K., Burger, P. V., Papike, J. J., McCubbin, F. M. & Bell, A. S. (2015) Crystal chemistry of merrillite from Martian meteorites: Mineralogical recorders of magmatic processes and planetary differentiation. *Meteoritics & Planetary Science* **50**: 649-673.
- Sheen, A. I., Herd, C. D. K., Hamilton, J. & Walton, E. L. (2021) Petrographic controls on baddeleyite occurrence in a suite of eight basaltic shergottites. *Meteoritics & Planetary Science* **56**: 1502-1530.
- Shih, C. -, Nyquist, L. E., Bogard, D. D., McKay, G. A., Wooden, J. L., Bansal, B. M. & Wiesmann, H. (1982) Chronology and petrogenesis of young achondrites, Shergotty, Zagami, and ALHA77005: late magmatism on a geologically active planet. *Geochimica et Cosmochimica Acta* **46**: 2323-2344.
- Shih C. -, Nyquist L. E., Wiesmann H., and Barrat J. A. (2003). Age and Petrogenesis of Picritic Shergottite NWA1068: Sm-Nd and Rb-Sr Isotopic Studies. pp. 1439.
- Shih, C., Nyquist, L. E., Wiesmann, H., Reese, Y. & Misawa, K. (2005) Rb-Sr and Sm-Nd dating of olivine-phryic shergottite Yamato 980459: Petrogenesis of depleted shergottites. *Antarctic meteorite research* **18**: 46-65.
- Shih, C. -, Nyquist, L. E., Reese, Y. & Misawa, K. (2011) Sm-Nd and Rb-Sr studies of lherzolitic shergottite Yamato 984028. *Polar Science* **4**: 515-529.
- Sikdar, J. & Rai, V. K. (2020) Si-Mg isotopes in enstatite chondrites and accretion of reduced planetary bodies. *Scientific Reports* **10**: 1273.
- Smith, D. K. & Newkirk, W. (1965) The crystal structure of baddeleyite (monoclinic ZrO₂) and its relation to the polymorphism of ZrO₂. *Acta Crystallographica* **18**: 983-991.
- Soderblom, L. A., Condit, C. D., West, R. A., Herman, B. M. & Kreidler, T. J. (1974) Martian planetwide crater distributions: Implications for geologic history and surface processes. *Icarus* **22**: 239-263.
- Söderlund, U., Isachsen, C. E., Bylund, G., Heaman, L. M., Patchett, P. J., Vervoort, J. D. & Andersson, U. B. (2005) U-Pb baddeleyite ages and Hf, Nd isotope chemistry constraining repeated mafic magmatism in the Fennoscandian Shield from 1.6 to 0.9 Ga. *Contributions to Mineralogy and Petrology* **150**: 174.
- Stacey, J. S. & Kramers, J. D. (1975) Approximation of terrestrial lead isotope evolution by a two-stage model. *Earth and Planetary Science Letters* **26**: 207-221.
- Staddon L. G., Darling J. R., Stephen N. R., Dunlop J., and Tait K. T. (2020). Baddeleyite Microstructures in Variably Shocked Martian Meteorites: An Opportunity to Link Shock Barometry and Robust Geochronology. 51st Annual Lunar and Planetary Science Conference, pp. 2302.

- Staddon L., Darling J., Schwarz W., Stephen N., Schuindt S., Dunlop J., and Tait K. (2021a). Combined microstructural analysis and in-situ U-Pb chronology of baddeleyite within shergottites. *Goldschmidt* 2021. doi: 10.7185/gold2021.7956
- Staddon, L. G., Darling, J. R., Schwarz, W. H., Stephen, N. R., Schuindt, S., Dunlop, J. & Tait, K. T. (2021b) Dating martian mafic crust; microstructurally constrained baddeleyite geochronology of enriched shergottites Northwest Africa (NWA) 7257, NWA 8679 and Zagami. *Geochimica et Cosmochimica Acta* **315**: 73-88.
- Stanjek, H., Glasemann, R. & Hellmann, A. (2013) Smectite contents of road aggregates derived from crushed volcanic rocks and their impact on the durability of road pavements. *Clay Minerals* **48**: 463-471.
- Stolper, E. & McSween Jr, H. Y. (1979) Petrology and origin of the shergottite meteorites. *Geochimica et Cosmochimica Acta* **43**: 1475-1498.
- Stöffler, D., Ostertag, R., Jammes, C., Pfannschmidt, G., Gupta, P. R. S., Simon, S. B., Papike, J. J. & Beauchamp, R. H. (1986) Shock metamorphism and petrography of the Shergotty achondrite. *Geochimica et Cosmochimica Acta* **50**: 889-903.
- Storey, C. D., Jeffries, T. E. & Smith, M. (2006) Common lead-corrected laser ablation ICP-MS U-Pb systematics and geochronology of titanite. *Chemical Geology* **227**: 37-52.
- Symes, S. J. K., Borg, L. E., Shearer, C. K. & Irving, A. J. (2008) The age of the martian meteorite Northwest Africa 1195 and the differentiation history of the shergottites. *Geochimica et Cosmochimica Acta* **72**: 1696-1710.
- Takagi, S., Kyono, A., Nozawa, S., Kawai, N., Inukai, K., Fukaya, R., Funamori, N., Adachi, S. & Ichiyangagi, K. (2020) In Situ Observation of the Phase Transition Behavior of Shocked Baddeleyite. *Geophysical Research Letters* **47**: e2020GL089592.
- Taylor, G. J. (2013) The bulk composition of Mars. *Geochemistry* **73**: 401-420.
- Timms, N. E., Erickson, T. M., Zanetti, M. R., Pearce, M. A., Cayron, C., Cavausie, A. J., Reddy, S. M., Wittmann, A. & Carpenter, P. K. (2017) Cubic zirconia in >2370 °C impact melt records Earth's hottest crust. *Earth and Planetary Science Letters* **477**: 52-58.
- Tornabene, L. L., Moersch, J. E., McSween Jr., H. Y., McEwen, A. S., Piatek, J. L., Milam, K. A. & Christensen, P. R. (2006) Identification of large (2–10 km) rayed craters on Mars in THEMIS thermal infrared images: Implications for possible Martian meteorite source regions. *Journal of Geophysical Research: Planets* **111**.

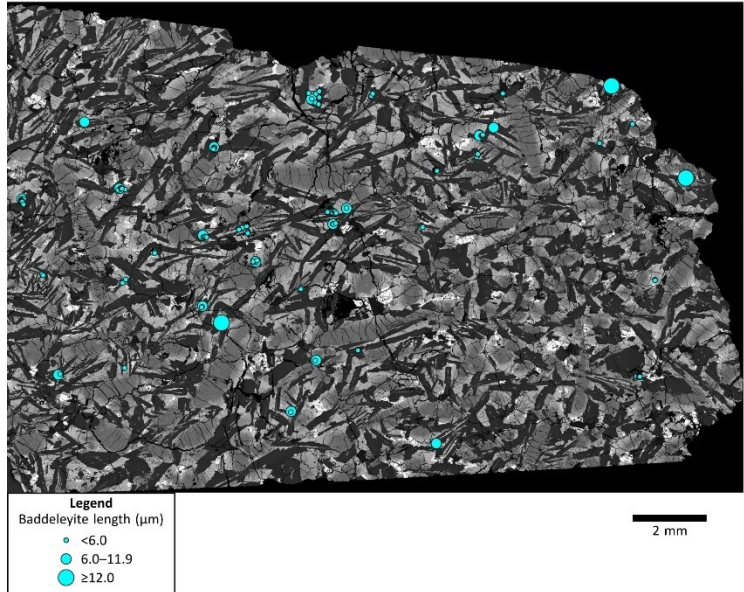
- Treiman, A. H. (2005) The nakhlite meteorites: Augite-rich igneous rocks from Mars. *Geochemistry* **65**: 203-270.
- Treiman, A. H., Gleason, J. D. & Bogard, D. D. (2000) The SNC meteorites are from Mars. *Planetary and Space Science* **48**: 1213-1230.
- Treiman, A. H., Barrett, R. A. & Gooding, J. L. (1993) Preterrestrial aqueous alteration of the Lafayette (SNC) meteorite. *Meteoritics* **28**: 86-97.
- Udry, A. & Day, J. M. D. (2018) 1.34 billion-year-old magmatism on Mars evaluated from the co-genetic nakhlite and chassignite meteorites. *Geochimica et Cosmochimica Acta* **238**: 292-315.
- Udry, A., Howarth, G. H., Herd, C. D. K., Day, J. M. D., Lapen, T. J. & Filiberto, J. (2020) What Martian Meteorites Reveal About the Interior and Surface of Mars. *Journal of Geophysical Research: Planets* **125**: e2020JE006523.
- Usui, T., McSween, H. Y. & Floss, C. (2008) Petrogenesis of olivine-phyric shergottite Yamato 980459, revisited. *Geochimica et Cosmochimica Acta* **72**: 1711-1730.
- Usui, T., Sanborn, M., Wadhwa, M. & McSween, H. Y. (2010) Petrology and trace element geochemistry of Robert Massif 04261 and 04262 meteorites, the first examples of geochemically enriched Iherzolitic shergottites. *Geochimica et Cosmochimica Acta* **74**: 7283-7306.
- Usui, T., Alexander, C. M. O., Wang, J., Simon, J. I. & Jones, J. H. (2012) Origin of water and mantle–crust interactions on Mars inferred from hydrogen isotopes and volatile element abundances of olivine-hosted melt inclusions of primitive shergottites. *Earth and Planetary Science Letters* **357-358**: 119-129.
- Váci, Z. & Agee, C. (2020) Constraints on Martian Chronology from Meteorites. *Geosciences* **10**.
- Vasconcelos, P. M., Farley, K. A., Malespin, C. A., Mahaffy, P., Ming, D., McLennan, S. M., Hurowitz, J. A. & Rice, M. S. (2016) Discordant K-Ar and young exposure dates for the Windjana sandstone, Kimberley, Gale Crater, Mars. *Journal of Geophysical Research: Planets* **121**: 2176-2192.
- Volkert, C. A. & Minor, A. M. (2007) Focused Ion Beam Microscopy and Micromachining. *MRS Bulletin* **32**: 389-399.
- Wadhwa, M. (2001) Redox State of Mars' Upper Mantle and Crust from Eu Anomalies in Shergottite Pyroxenes. *Science* **291**: 1527-1530.
- Wadhwa, M., McSween, H. Y. & Crozaz, G. (1994) Petrogenesis of shergottite meteorites inferred from minor and trace element microdistributions. *Geochimica et Cosmochimica Acta* **58**: 4213-4229.

- Wadhwa, M., Crozaz, G., Taylor, L. A. & McSween Jr, H. Y. (1998) Martian basalt (shergottite) Queen Alexandra Range 94201 and lunar basalt 15555: A tale of two pyroxenes. *Meteoritics & Planetary Science* **33**: 321-328
- Wakaki, S. & Ishikawa, T. (2018) Isotope analysis of nanogram to sub-nanogram sized Nd samples by total evaporation normalization thermal ionization mass spectrometry. *International Journal of Mass Spectrometry* **424**: 40-48.
- Walton, E. L., Kelley, S. P. & Herd, C. D. K. (2008) Isotopic and petrographic evidence for young Martian basalts. *Geochimica et Cosmochimica Acta* **72**: 5819-5837.
- Walton, E. L., Irving, A. J., Bunch, T. E. & Herd, C. (2012) Northwest Africa 4797: A strongly shocked ultramafic poikilitic shergottite related to compositionally intermediate Martian meteorites. *Meteoritics & Planetary Science* **47**: 1449-1474.
- Weisberg, M. K., Smith, C., Herd, C., Haack, H., Yamaguchi, A., Chennaoui Aoudjehane, H., Welzenbach, L. & Grossman, J. N. (2010) The Meteoritical Bulletin, No. 98, September 2010. *Meteoritics & Planetary Science* **45**: 1530-1551.
- Werner, S. C., Ody, A. & Poulet, F. (2014) The Source Crater of Martian Shergottite Meteorites. *Science* **343**: 1343-1346.
- White, L. F., Darling, J. R., Moser, D. E., Reinhard, D. A., Prosa, T. J., Bullen, D., Olson, D., Larson, D. J., Lawrence, D. & Martin, I. (2017) Atomic-scale age resolution of planetary events. *Nature Communications* **8**: 15597.
- White, L. F., Darling, J. R., Moser, D. E., Cayron, C., Barker, I., Dunlop, J. & Tait, K. T. (2018) Baddeleyite as a widespread and sensitive indicator of meteorite bombardment in planetary crusts. *Geology* **46**: 719-722.
- White, L. F., Tait, K. T., Kamo, S. L., Moser, D. E. & Darling, J. R. (2020) Highly accurate dating of micrometre-scale baddeleyite domains through combined focused ion beam extraction and U-Pb thermal ionization mass spectrometry (FIB-TIMS). *Geochronology* **2**: 177-186.
- Wieler, R., Huber, L., Busemann, H., Seiler, S., Leya, I., Maden, C., Masarik, J., Meier, M. M. M., Nagao, K., Trappitsch, R. & Irving, A. J. (2016) Noble gases in 18 Martian meteorites and angrite Northwest Africa 7812—Exposure ages, trapped gases, and a re-evaluation of the evidence for solar cosmic ray-produced neon in shergottites and other achondrites. *Meteoritics & Planetary Science* **51**: 407-428.
- Wingate, M. T. D. & Compston, W. (2000) Crystal orientation effects during ion microprobe U-Pb analysis of baddeleyite. *Chemical Geology* **168**: 75-97.

- Wittmann, A., Kenkemann, T., Schmitt, R. T. & Stöffler, D. (2006) Shock-metamorphosed zircon in terrestrial impact craters. *Meteoritics & Planetary Science* **41**: 433-454.
- Wones, D. R. & Gilbert, M. C. (1969) The fayalite-magnetite-quartz assemblage between 600 and 800 °C. *American Journal of Science* **267**: 480-488.
- Wu, Y. & Hsu, W. (2019) Trace Element Geochemistry and U-Pb Chronology of the Basaltic Shergottite Northwest Africa 8653. *LPICo* **82**: 6282.
- Wu, Y., 徐伟彪, Li, Q., Che, X. & Liao, S. (2021) Heterogeneous martian mantle: Evidence from petrology, mineral chemistry, and in situ U-Pb chronology of the basaltic shergottite Northwest Africa 8653. *Geochimica et Cosmochimica Acta* **309**: 352-365.
- Yin, A. (2012) An episodic slab-rollback model for the origin of the Tharsis rise on Mars: Implications for initiation of local plate subduction and final unification of a kinematically linked global plate-tectonic network on Earth. *Lithosphere* **4**: 553-593.
- Zack, T. & Hogmalm, K. J. (2016) Laser ablation Rb/Sr dating by online chemical separation of Rb and Sr in an oxygen-filled reaction cell. *Chemical Geology* **437**: 120-133.
- Zhou, Q., Herd, C. D. K., Yin, Q., Li, X., Wu, F., Li, Q., Liu, Y., Tang, G. & McCoy, T. J. (2013) Geochronology of the Martian meteorite Zagami revealed by U-Pb ion probe dating of accessory minerals. *Earth and Planetary Science Letters* **374**: 156-163.
- Zipfel, J., Scherer, P., Spettel, B., Dreibus, G. & Schultz, L. (2000) Petrology and chemistry of the new shergottite Dar al Gani 476. *Meteoritics & Planetary Science* **35**: 95-106.

APPENDIX 1

JaH 479-1



JaH 479-2

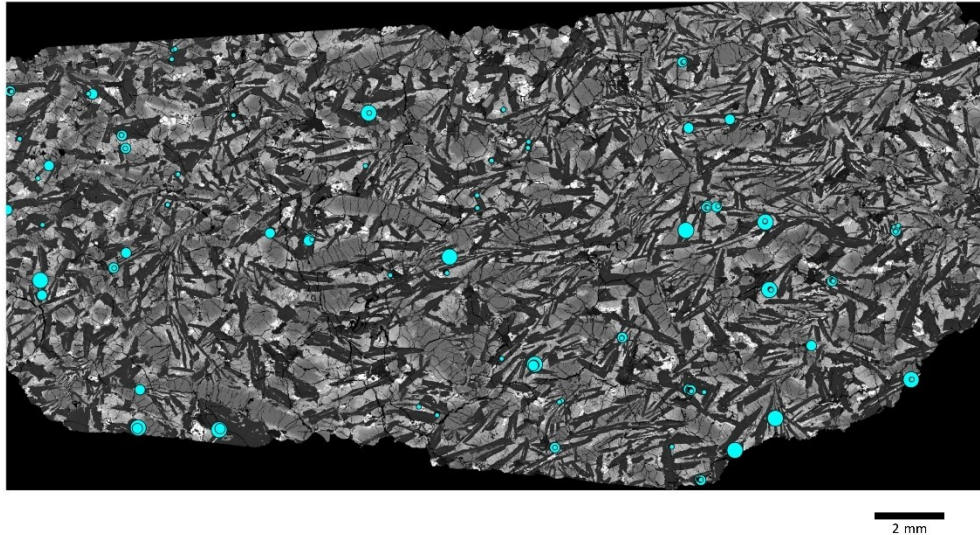


Fig. A1.1. Full BSE map of baddeleyite occurrences in JaH 479.

KG 002

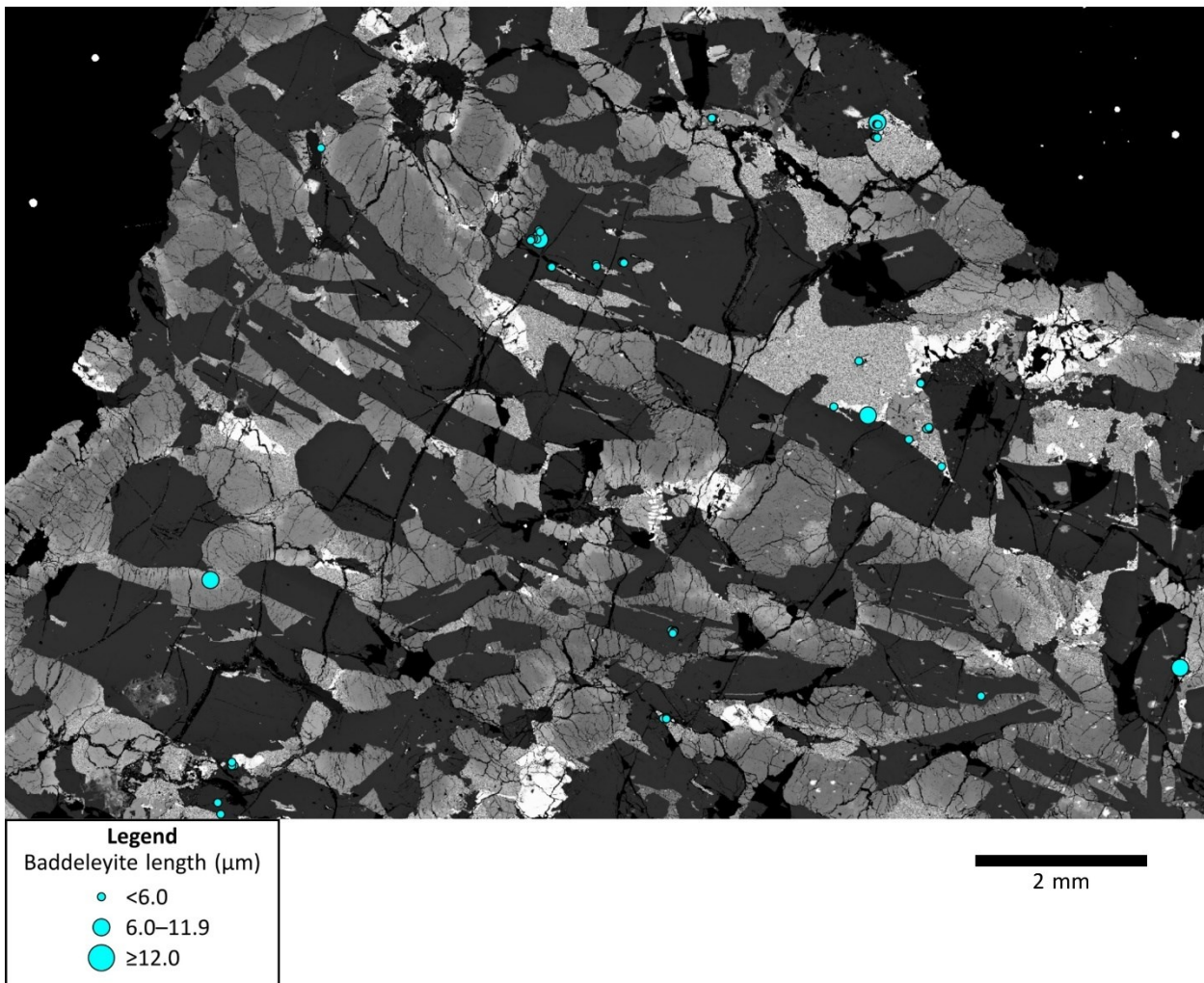


Fig. A1.2. Full BSE map of baddeleyite occurrences in KG 002.

NWA 10299

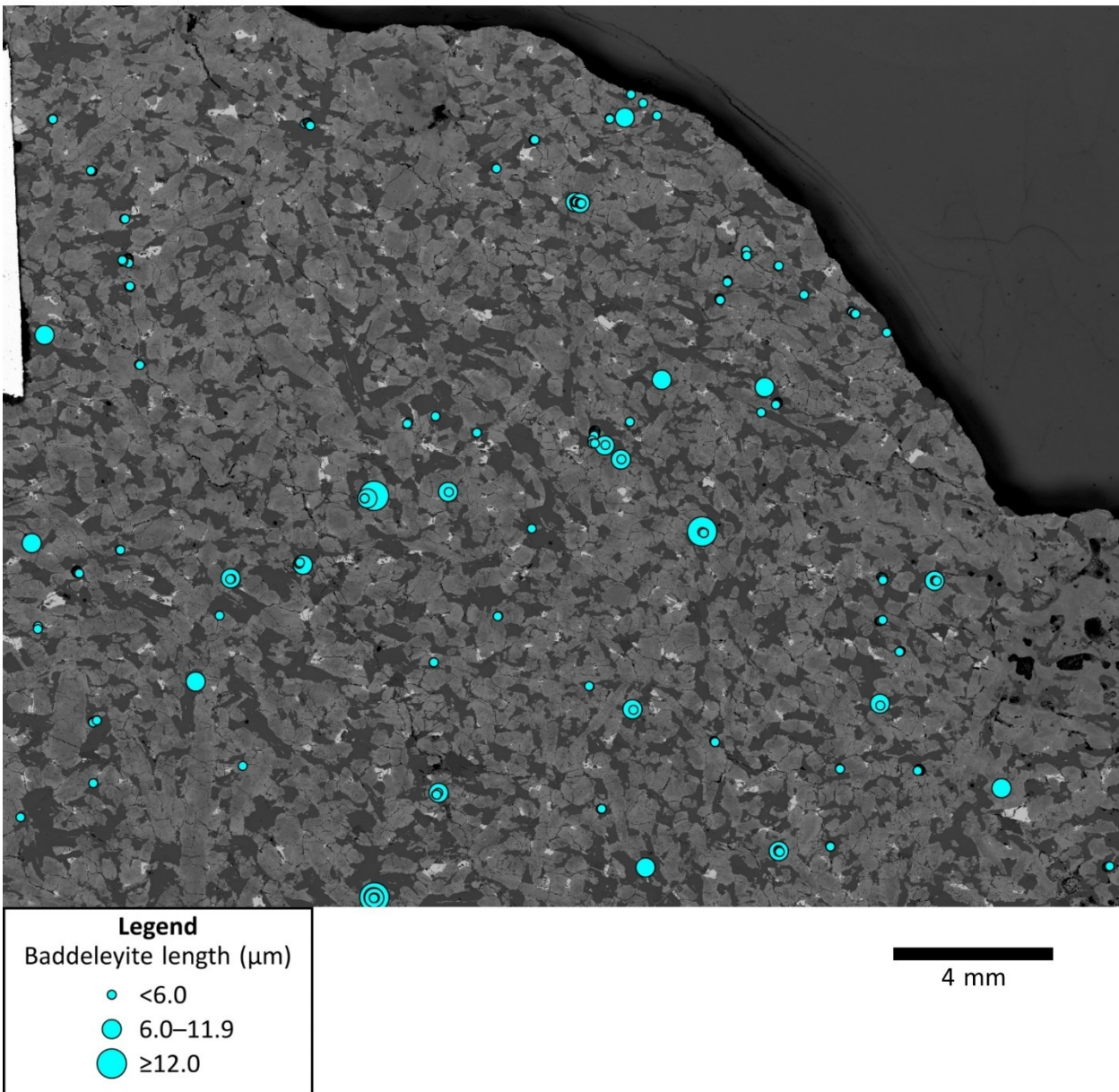


Fig. A1.3. Full BSE map of baddeleyite occurrences in NWA 10299.

NWA 11057

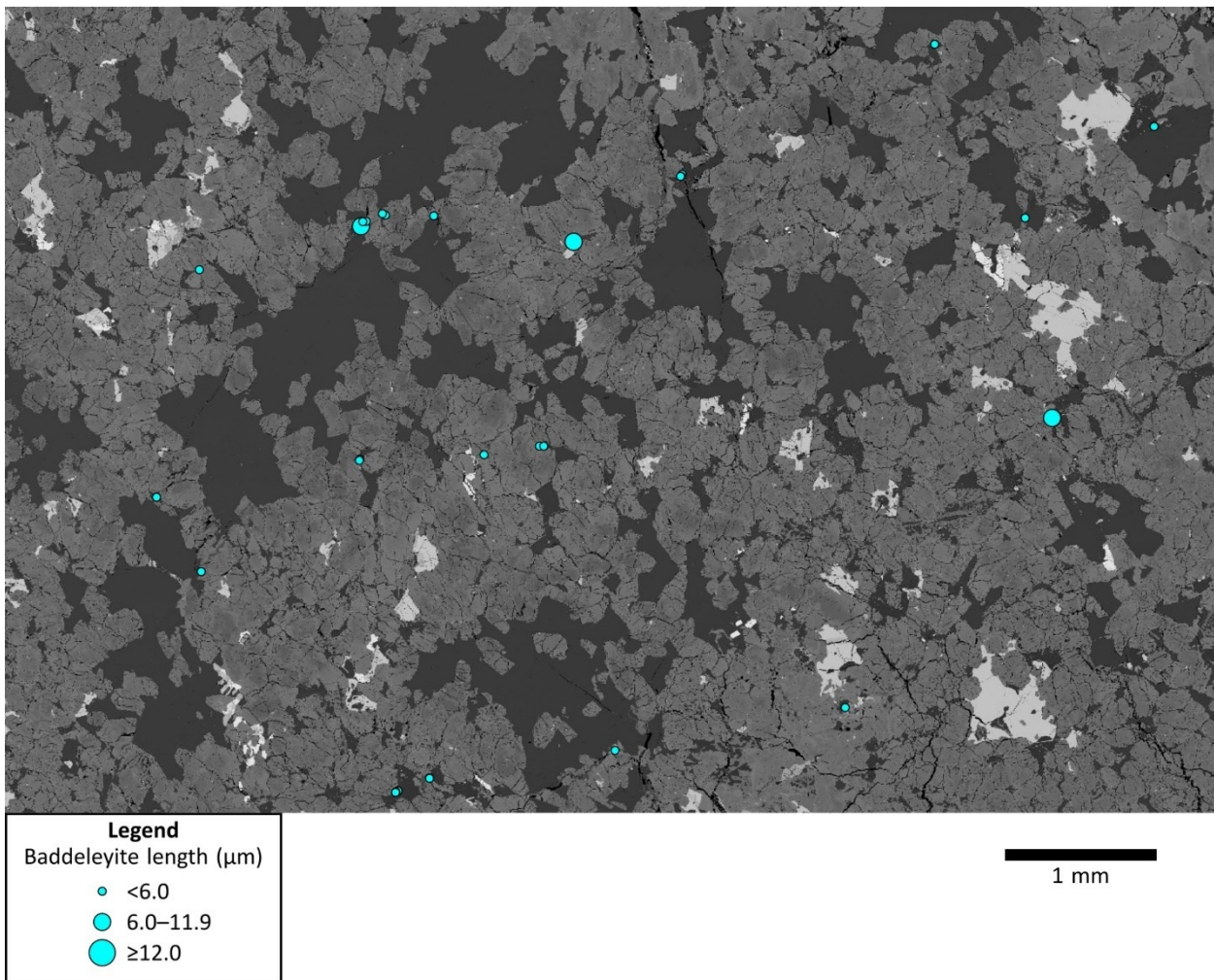


Fig. A1.4. Full BSE map of baddeleyite occurrences in NWA 11057.

NWA 11073

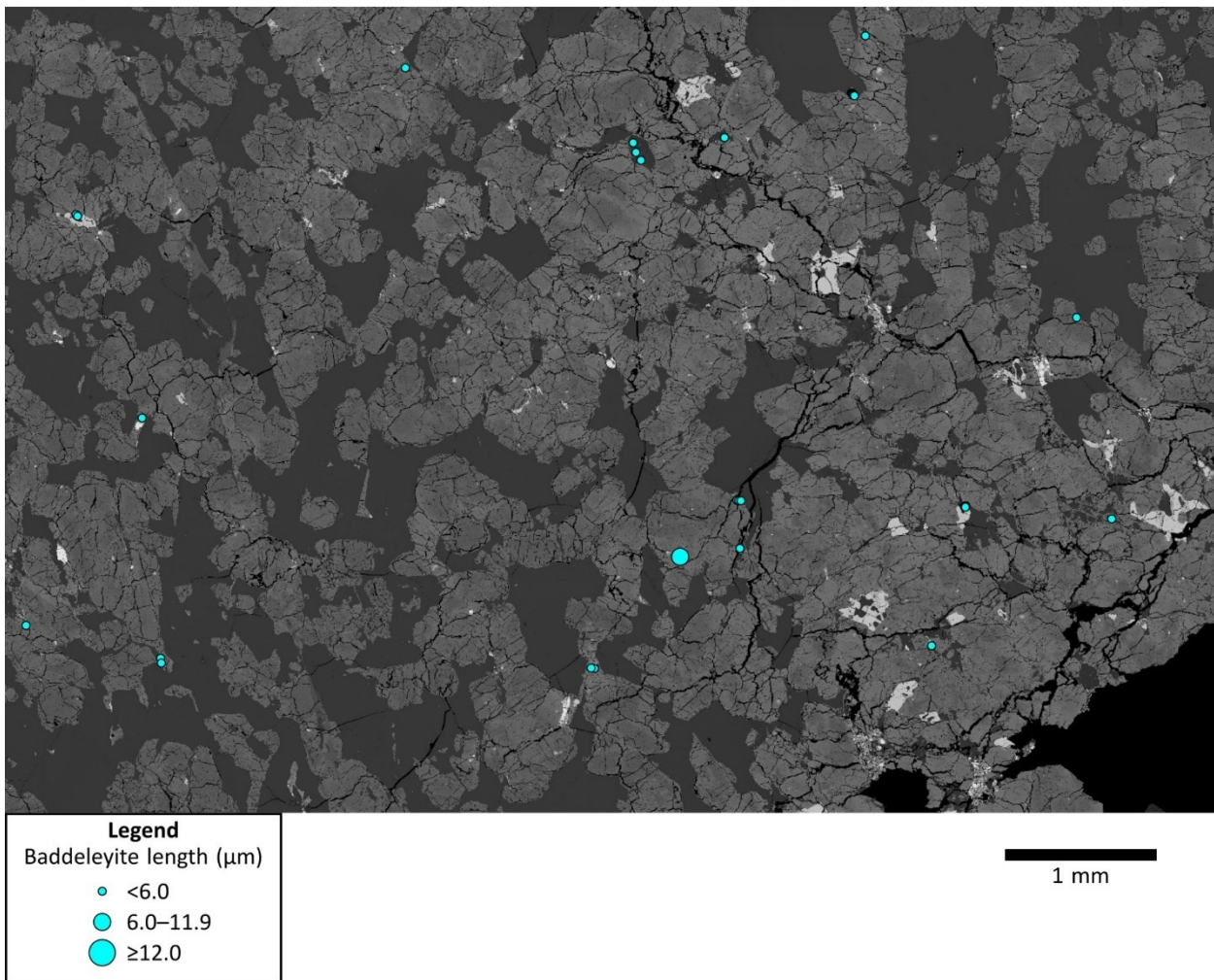


Fig. A1.5. Full BSE map of baddeleyite occurrences in NWA 11073.

NWA 11255

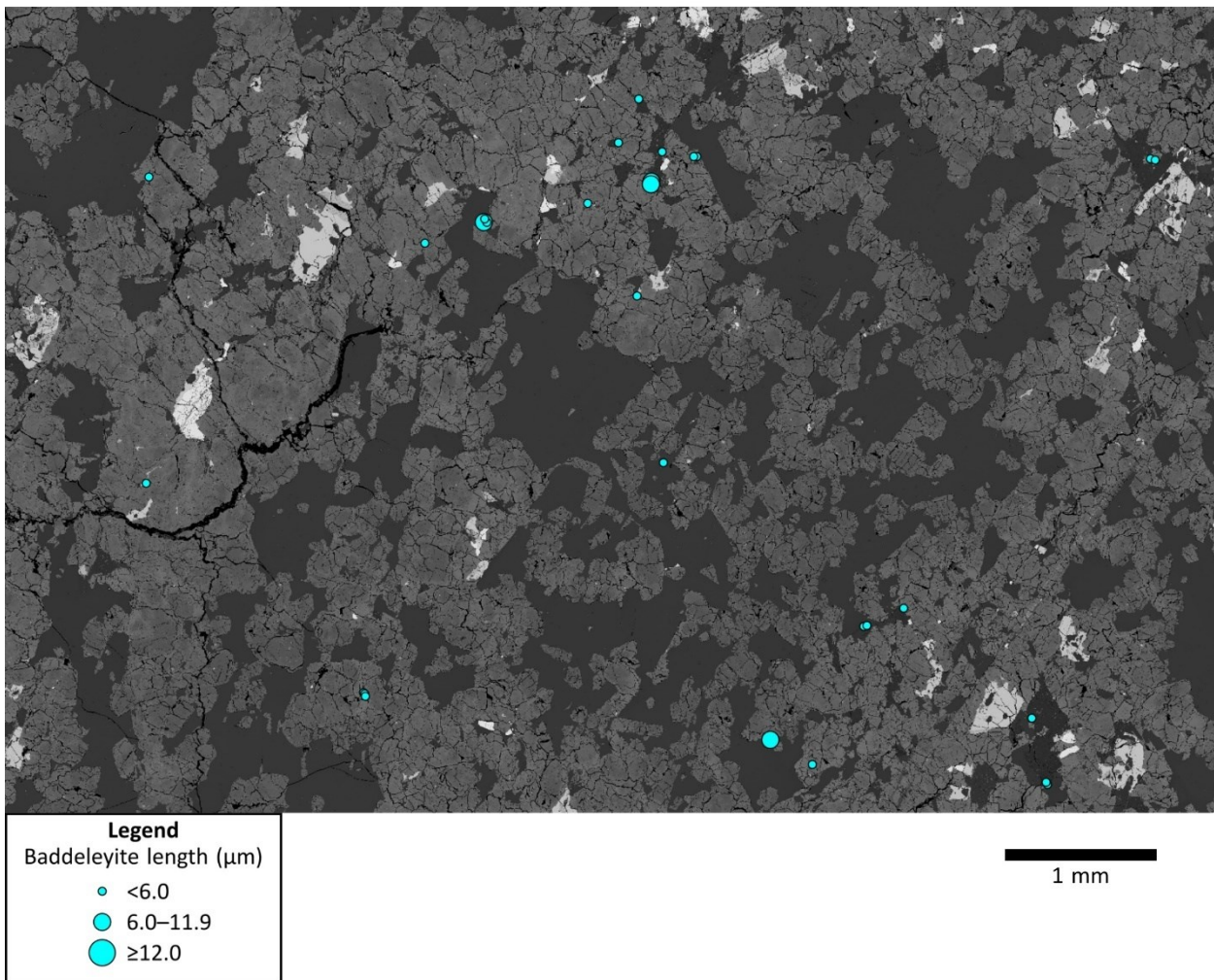


Fig. A1.6. Full BSE map of baddeleyite occurrences in NWA 11255.

NWA 12262

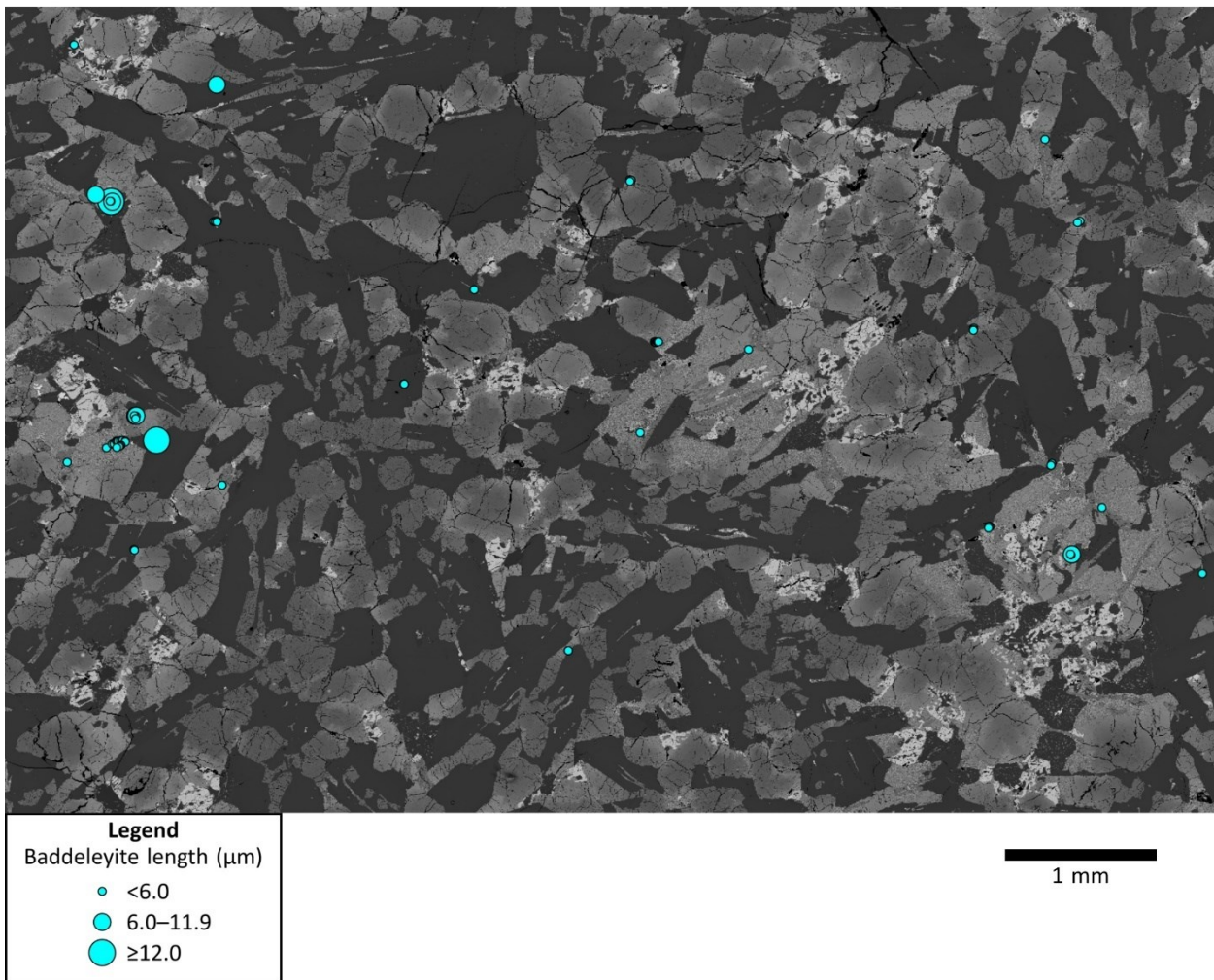


Fig. A1.7. Full BSE map of baddeleyite occurrences in NWA 12262.

NWA 12919

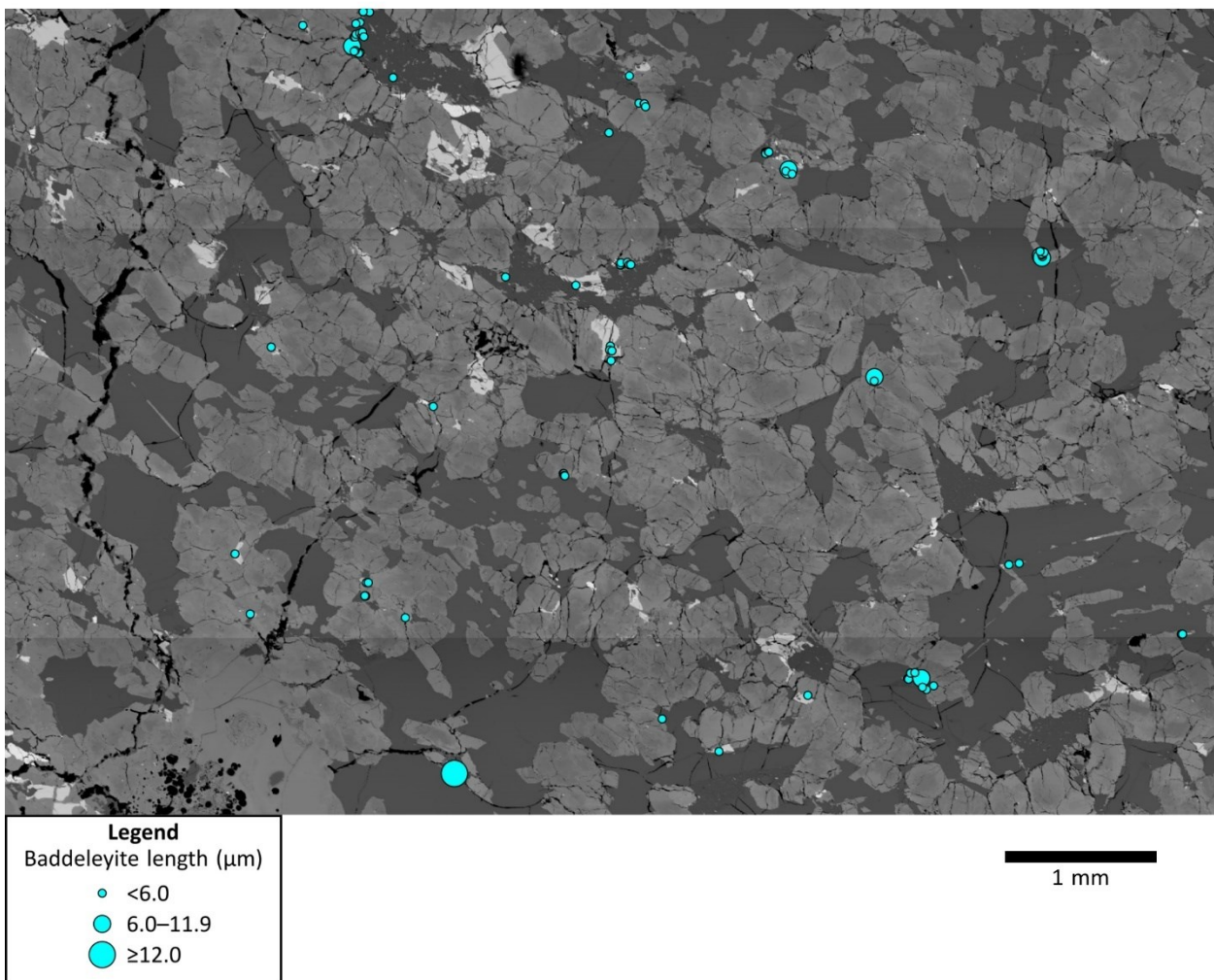


Fig. A1.8. Full BSE map of baddeleyite occurrences in NWA 12919.

Table A1.1. EPMA analysis of pyroxenes.

SAMPLE	SiO ₂	TiO ₂	Al ₂ O ₃	V ₂ O ₃	Cr ₂ O ₃	FeO	NiO	MnO	MgO	CaO	Na ₂ O	K ₂ O	TOTAL	NOTES
JaH479-1_px01-1	51.68	0.31	1.47	0.10	0.33	14.02	0.00	0.48	13.96	17.02	0.15	0.00	99.52	
JaH479-1_px01-2	51.45	0.33	1.59	0.11	0.27	13.86	0.00	0.45	13.66	17.17	0.20	0.01	99.10	
JaH479-1_px01-3	51.29	0.36	1.68	0.10	0.16	14.08	0.02	0.47	13.03	17.92	0.21	0.00	99.32	
JaH479-1_px01-4	50.18	0.44	1.04	0.08	0.03	22.90	0.00	0.66	10.35	13.99	0.13	0.00	99.80	
JaH479-1_px01-5	46.85	0.46	0.49	0.00	0.00	39.79	0.00	0.97	3.71	7.45	0.06	0.00	99.78	
JaH479-1_px02-1	51.77	0.30	1.71	0.10	0.51	16.59	0.03	0.56	15.72	12.24	0.13	0.00	99.66	
JaH479-1_px02-2	51.79	0.34	1.57	0.10	0.24	14.06	0.00	0.48	13.49	17.55	0.19	0.00	99.81	
JaH479-1_px02-3	50.82	0.31	1.20	0.07	0.04	23.66	0.02	0.74	14.91	7.38	0.10	0.02	99.27	
JaH479-1_px02-4	50.80	0.35	1.02	0.07	0.03	22.45	0.02	0.71	12.62	11.44	0.10	0.00	99.61	
JaH479-1_px02-5	49.46	0.38	0.72	0.04	0.00	30.57	0.03	0.82	9.86	8.11	0.04	0.00	100.03	
JaH479-1_px02-6	46.99	0.63	0.66	0.00	0.00	39.72	0.00	0.96	3.00	8.12	0.05	0.00	100.13	
JaH479-1_px03-1	49.77	0.39	1.05	0.07	0.13	22.64	0.00	0.65	10.60	13.81	0.16	0.01	99.28	
JaH479-1_px03-2	51.36	0.33	1.62	0.10	0.38	14.38	0.02	0.50	14.37	16.15	0.17	0.00	99.38	
JaH479-1_px03-3	51.15	0.35	1.68	0.11	0.15	15.30	0.02	0.48	13.08	17.05	0.16	0.00	99.53	
JaH479-1_px03-4	50.29	0.35	0.85	0.06	0.00	24.84	0.00	0.75	11.60	10.99	0.09	0.00	99.82	
JaH479-1_px03-5	48.02	0.57	0.76	0.05	0.00	34.30	0.00	0.88	6.02	9.65	0.08	0.00	100.33	
JaH479-1_px04-1	51.64	0.34	1.61	0.10	0.46	16.31	0.03	0.58	15.40	13.24	0.13	0.00	99.84	
JaH479-1_px04-2	51.51	0.32	1.55	0.10	0.40	15.79	0.00	0.57	14.97	14.23	0.14	0.00	99.58	
JaH479-1_px04-3	51.54	0.33	1.60	0.09	0.19	16.97	0.00	0.56	14.29	14.29	0.13	0.00	99.99	
JaH479-1_px04-4	51.02	0.24	0.76	0.05	0.03	26.70	0.02	0.77	14.78	5.55	0.05	0.00	99.97	
JaH479-1_px04-5	47.44	0.45	0.51	0.01	0.00	39.24	0.00	0.97	4.07	7.41	0.06	0.00	100.16	
JaH479-1_px05-1	50.55	0.32	1.61	0.09	0.58	16.42	0.00	0.56	15.81	12.49	0.16	0.00	98.59	
JaH479-1_px05-2	50.63	0.33	1.59	0.09	0.45	15.62	0.02	0.53	14.98	14.23	0.16	0.00	98.63	
JaH479-1_px05-3	50.53	0.33	1.53	0.09	0.16	17.25	0.00	0.60	14.24	14.13	0.12	0.00	98.98	
JaH479-1_px05-4	49.38	0.43	0.99	0.08	0.02	23.26	0.00	0.67	10.37	13.73	0.15	0.00	99.08	
JaH479-1_px05-5	47.52	0.60	0.76	0.04	0.00	33.35	0.00	0.86	5.94	10.25	0.08	0.00	99.40	
JaH479-1_px06-1	51.23	0.38	1.85	0.11	0.71	15.45	0.00	0.55	15.19	13.62	0.17	0.00	99.26	
JaH479-1_px06-2	51.56	0.29	1.41	0.09	0.29	16.03	0.00	0.54	14.64	14.41	0.16	0.01	99.43	
JaH479-1_px06-3	50.61	0.36	1.12	0.08	0.00	21.45	0.00	0.64	11.79	13.22	0.14	0.01	99.42	
JaH479-1_px06-4	49.06	0.48	0.87	0.06	0.00	28.61	0.00	0.77	8.33	11.53	0.12	0.00	99.83	
JaH479-1_px06-5	46.51	0.58	0.75	0.00	0.00	41.25	0.00	1.06	2.40	7.57	0.05	0.00	100.17	
JaH479-1_px07-1	51.13	0.27	1.34	0.08	0.37	17.15	0.00	0.56	15.96	11.89	0.15	0.01	98.91	
JaH479-1_px07-2	51.55	0.27	1.20	0.08	0.31	14.43	0.00	0.52	14.67	16.06	0.18	0.00	99.27	
JaH479-1_px07-3	50.19	0.35	1.09	0.07	0.02	21.70	0.00	0.64	11.62	13.29	0.16	0.01	99.14	
JaH479-1_px07-4	49.24	0.43	0.85	0.06	0.00	24.95	0.00	0.67	9.06	13.68	0.14	0.01	99.09	
JaH479-1_px07-5	47.07	0.48	0.55	0.00	0.00	38.30	0.00	0.93	4.37	7.84	0.05	0.00	99.59	
JaH479-1_px08-1	52.40	0.14	0.65	0.04	0.23	20.94	0.00	0.71	18.45	5.81	0.06	0.00	99.43	
JaH479-1_px08-2	51.95	0.25	1.10	0.08	0.20	16.39	0.00	0.56	14.79	13.95	0.15	0.00	99.42	
JaH479-1_px08-3	50.68	0.24	0.64	0.04	0.00	27.17	0.00	0.79	13.20	6.96	0.08	0.00	99.80	

Table A1.1.(continued) EPMA analysis of pyroxenes.

SAMPLE	SiO ₂	TiO ₂	Al ₂ O ₃	V ₂ O ₃	Cr ₂ O ₃	FeO	NiO	MnO	MgO	CaO	Na ₂ O	K ₂ O	TOTAL	NOTES
JaH479-1_px08-4	48.27	0.59	0.71	0.04	0.00	31.79	0.00	0.79	5.18	12.56	0.11	0.00	100.04	
JaH479-1_px08-5	47.08	0.60	0.65	0.00	0.00	39.26	0.00	1.01	3.40	8.00	0.06	0.00	100.06	
JaH479-1_px09-1	50.77	0.37	1.91	0.12	0.51	12.94	0.00	0.44	13.81	17.67	0.21	0.00	98.75	
JaH479-1_px09-2	51.05	0.36	1.57	0.11	0.21	13.67	0.02	0.45	13.17	18.15	0.20	0.00	98.96	
JaH479-1_px09-3	49.77	0.39	0.97	0.07	0.03	23.17	0.00	0.68	11.24	12.68	0.13	0.00	99.13	
JaH479-1_px09-4	47.41	0.65	0.94	0.02	0.00	31.16	0.00	0.75	4.98	13.65	0.13	0.00	99.69	
JaH479-1_px09-5	45.47	0.33	0.32	0.00	0.00	45.22	0.00	1.35	1.39	5.31	0.00	0.00	99.39	
JaH479-1_px10-1	51.68	0.31	1.47	0.10	0.30	14.50	0.03	0.50	14.07	16.20	0.15	0.00	99.31	
JaH479-1_px10-2	50.83	0.27	1.02	0.06	0.04	23.91	0.00	0.74	14.31	7.95	0.07	0.00	99.20	
JaH479-1_px10-3	50.46	0.35	0.86	0.05	0.03	25.75	0.00	0.76	12.19	9.16	0.07	0.00	99.68	
JaH479-1_px10-4	49.07	0.47	0.78	0.06	0.00	30.72	0.00	0.80	8.46	9.28	0.09	0.00	99.73	
JaH479-1_px10-5	47.21	0.54	0.67	0.00	0.00	38.74	0.00	0.96	4.03	7.70	0.05	0.00	99.90	
JaH479-1_px11-1	49.22	0.44	0.78	0.05	0.03	30.65	0.00	0.82	8.96	8.91	0.10	0.01	99.97	
JaH479-1_px11-2	47.81	0.53	0.68	0.01	0.00	36.68	0.00	0.92	4.76	8.84	0.07	0.00	100.30	
JaH479-1_px11-3	46.63	0.26	0.29	0.00	0.00	44.53	0.00	1.15	1.95	5.48	0.00	0.00	100.29	Adjacent to baddeleyite
KG002_bdp01-1	29.79	0.20	0.04	0.00	0.00	66.74	0.00	1.46	1.39	0.30	0.00	0.00	99.92	
KG002_bdp02-1	50.65	0.33	1.06	0.07	0.06	20.71	0.00	0.64	12.98	12.13	0.13	0.00	98.76	
KG002_bdp02-2	50.62	0.29	0.80	0.04	0.03	26.12	0.00	0.77	13.70	6.73	0.07	0.00	99.17	
KG002_bdp02-3	47.85	0.48	0.63	0.03	0.00	36.31	0.00	0.92	5.40	8.06	0.06	0.00	99.74	
KG002_bdp02-4	47.41	0.56	0.59	0.02	0.00	38.45	0.00	0.95	4.22	7.74	0.04	0.00	99.98	Adjacent to baddeleyite
NWA10299_px1-1	52.88	0.15	0.77	0.04	0.38	19.90	0.02	0.66	19.59	5.95	0.06	0.00	100.40	
NWA10299_px1-2	53.11	0.14	0.76	0.04	0.39	20.05	0.02	0.67	19.79	5.52	0.06	0.00	100.55	
NWA10299_px1-3	50.64	0.29	0.79	0.04	0.19	27.86	0.00	0.77	13.26	6.68	0.07	0.00	100.59	
NWA10299_px1-4	49.95	0.37	0.68	0.04	0.14	30.59	0.00	0.86	11.73	6.16	0.06	0.00	100.58	
NWA10299_px1-5	48.71	0.56	0.64	0.00	0.03	34.73	0.00	0.91	6.80	8.24	0.08	0.00	100.70	
NWA10299_px2-1	52.54	0.23	1.23	0.07	0.50	14.40	0.02	0.52	15.60	15.10	0.15	0.00	100.36	
NWA10299_px2-2	52.40	0.23	1.19	0.08	0.56	15.25	0.02	0.50	14.91	15.38	0.17	0.00	100.69	
NWA10299_px2-3	49.13	0.46	1.09	0.07	0.24	24.09	0.00	0.60	9.94	14.14	0.17	0.01	99.94	
NWA10299_px2-4	48.63	0.76	0.94	0.03	0.04	28.12	0.00	0.75	7.21	13.55	0.13	0.00	100.16	
NWA10299_px2-5	48.92	0.65	0.81	0.03	0.05	32.68	0.00	0.86	7.94	8.66	0.08	0.00	100.68	
NWA10299_px3-1	50.73	0.44	1.12	0.08	0.26	21.53	0.00	0.63	10.80	14.91	0.16	0.00	100.66	
NWA10299_px3-2	50.31	0.47	0.94	0.07	0.20	23.96	0.00	0.68	10.37	13.21	0.15	0.00	100.36	
NWA10299_px3-3	49.67	0.61	0.81	0.05	0.05	27.46	0.00	0.71	8.32	12.87	0.11	0.00	100.66	
NWA10299_px3-4	49.24	0.64	0.88	0.03	0.04	29.08	0.00	0.75	7.42	12.69	0.11	0.00	100.88	
NWA10299_px3-5	48.81	0.42	0.46	0.02	0.00	36.87	0.02	0.94	7.60	5.73	0.05	0.00	100.92	
NWA10299_px4-1	52.66	0.23	1.19	0.08	0.65	13.50	0.02	0.48	15.47	15.80	0.17	0.00	100.25	
NWA10299_px4-2	52.19	0.26	1.28	0.09	0.37	15.12	0.00	0.51	14.30	16.13	0.16	0.00	100.41	
NWA10299_px4-3	50.98	0.40	1.11	0.07	0.27	21.84	0.02	0.63	11.30	13.86	0.15	0.00	100.63	
NWA10299_px4-4	49.82	0.53	0.89	0.05	0.16	26.98	0.00	0.72	9.12	12.36	0.13	0.00	100.76	

Table A1.1.(continued) EPMA analysis of pyroxenes.

SAMPLE	SiO ₂	TiO ₂	Al ₂ O ₃	V ₂ O ₃	Cr ₂ O ₃	FeO	NiO	MnO	MgO	CaO	Na ₂ O	K ₂ O	TOTAL	NOTES
NWA10299_px4-5	48.79	0.61	0.68	0.02	0.02	34.39	0.00	0.91	6.88	8.45	0.07	0.00	100.82	
NWA10299_px5-1	52.79	0.21	1.13	0.07	0.46	14.04	0.02	0.52	15.40	15.73	0.16	0.00	100.53	
NWA10299_px5-2	52.78	0.24	1.22	0.08	0.54	13.51	0.02	0.47	15.17	16.31	0.17	0.00	100.51	
NWA10299_px5-3	51.34	0.34	1.07	0.07	0.27	19.47	0.00	0.58	11.92	15.22	0.16	0.00	100.44	
NWA10299_px5-4	50.14	0.37	0.73	0.05	0.14	30.40	0.00	0.83	11.29	6.79	0.06	0.00	100.80	
NWA10299_px5-5	48.65	0.56	0.65	0.01	0.00	36.59	0.00	0.98	6.94	6.77	0.04	0.00	101.19	
NWA10299_px6-1	52.93	0.17	0.86	0.05	0.35	19.95	0.02	0.69	18.63	6.74	0.06	0.00	100.45	
NWA10299_px6-2	53.09	0.15	0.78	0.04	0.40	20.38	0.02	0.70	19.18	5.98	0.05	0.00	100.77	
NWA10299_px6-3	51.32	0.38	1.16	0.09	0.26	19.42	0.00	0.58	11.82	15.28	0.17	0.00	100.48	
NWA10299_px6-4	49.40	0.64	0.80	0.02	0.03	29.40	0.00	0.76	7.31	12.25	0.10	0.00	100.71	
NWA10299_px6-5	48.66	0.54	0.65	0.00	0.00	36.08	0.00	0.95	6.73	7.31	0.05	0.00	100.97	
NWA10299_px7-1	51.90	0.29	1.29	0.09	0.25	16.42	0.00	0.55	13.44	15.76	0.16	0.00	100.15	
NWA10299_px7-2	50.84	0.38	1.11	0.08	0.28	20.96	0.00	0.64	11.68	13.92	0.14	0.00	100.03	
NWA10299_px7-3	50.66	0.45	1.11	0.07	0.28	21.77	0.00	0.63	10.84	14.41	0.15	0.00	100.37	
NWA10299_px7-4	49.04	0.58	0.70	0.02	0.00	30.62	0.00	0.81	6.53	12.17	0.10	0.00	100.57	
NWA10299_px7-5	48.71	0.48	0.53	0.01	0.03	36.59	0.00	0.93	6.93	6.38	0.03	0.00	100.62	
NWA10299_px8-1	52.81	0.17	0.84	0.04	0.32	20.48	0.02	0.67	19.00	5.84	0.05	0.00	100.24	
NWA10299_px8-2	52.49	0.23	1.16	0.09	0.46	15.00	0.02	0.50	14.63	15.55	0.17	0.00	100.30	
NWA10299_px8-3	51.67	0.32	1.23	0.09	0.22	17.59	0.00	0.55	12.87	15.45	0.15	0.00	100.14	
NWA10299_px8-4	50.49	0.49	1.01	0.06	0.19	23.57	0.00	0.65	9.54	14.18	0.14	0.00	100.32	
NWA10299_px8-5	48.63	0.61	0.64	0.02	0.05	35.12	0.00	0.91	6.98	7.58	0.06	0.00	100.60	Adjacent to baddeleyite
NWA10299_px9-1	52.67	0.22	1.17	0.09	0.53	14.69	0.03	0.51	15.45	14.96	0.14	0.00	100.46	
NWA10299_px9-2	51.73	0.30	1.20	0.08	0.28	18.31	0.02	0.59	13.20	14.80	0.14	0.00	100.65	
NWA10299_px9-3	50.39	0.40	0.87	0.05	0.17	27.15	0.00	0.75	10.77	10.07	0.09	0.00	100.71	
NWA10299_px9-4	48.59	0.80	0.74	0.02	0.03	31.37	0.00	0.77	5.60	12.75	0.10	0.00	100.77	
NWA10299_px9-5	47.84	0.46	0.50	0.00	0.00	39.25	0.00	1.02	4.95	6.74	0.04	0.00	100.80	Adjacent to baddeleyite
NWA10299_px10-1	51.82	0.39	1.33	0.08	0.46	16.92	0.00	0.52	13.21	15.62	0.17	0.00	100.52	
NWA10299_px10-2	51.35	0.36	1.13	0.08	0.29	20.15	0.00	0.60	12.08	14.36	0.15	0.00	100.55	
NWA10299_px10-3	50.92	0.43	1.16	0.08	0.30	21.75	0.00	0.63	11.36	13.75	0.14	0.00	100.52	
NWA10299_px10-4	49.55	0.42	0.75	0.03	0.12	32.94	0.00	0.88	9.53	6.58	0.07	0.00	100.87	
NWA10299_px10-5	48.47	0.55	0.58	0.01	0.05	35.89	0.00	0.89	6.97	7.29	0.06	0.00	100.76	Adjacent to baddeleyite
NWA11057_px01-1	51.92	0.30	1.54	0.08	0.32	14.02	0.00	0.48	14.27	16.15	0.16	0.01	99.25	
NWA11057_px01-2	52.15	0.25	1.34	0.08	0.33	14.28	0.02	0.51	14.64	15.71	0.17	0.00	99.48	
NWA11057_px01-3	51.22	0.27	1.33	0.08	0.24	17.17	0.00	0.53	12.98	15.47	0.15	0.00	99.44	
NWA11057_px01-4	50.33	0.35	0.80	0.06	0.11	29.24	0.00	0.85	12.11	6.10	0.08	0.00	100.03	
NWA11057_px01-5	50.36	0.42	0.94	0.05	0.12	26.90	0.00	0.76	11.40	8.75	0.08	0.00	99.78	
NWA11057_px02-1	52.33	0.18	0.86	0.05	0.13	22.16	0.02	0.72	17.85	5.52	0.06	0.01	99.89	
NWA11057_px02-2	51.75	0.23	0.81	0.04	0.17	24.77	0.00	0.73	15.65	5.66	0.06	0.00	99.87	
NWA11057_px02-3	50.57	0.22	0.73	0.05	0.09	28.36	0.00	0.79	13.57	5.45	0.05	0.00	99.88	

Table A1.1.(continued) EPMA analysis of pyroxenes.

SAMPLE	SiO ₂	TiO ₂	Al ₂ O ₃	V ₂ O ₃	Cr ₂ O ₃	FeO	NiO	MnO	MgO	CaO	Na ₂ O	K ₂ O	TOTAL	NOTES
NWA11057_px02-4	49.87	0.45	0.72	0.05	0.11	30.45	0.00	0.81	10.90	6.56	0.08	0.00	100.00	
NWA11057_px02-5	49.72	0.44	0.65	0.04	0.06	31.58	0.00	0.83	10.75	5.90	0.07	0.00	100.04	
NWA11057_px03-1	51.79	0.26	1.45	0.08	0.28	15.30	0.00	0.49	14.58	14.73	0.16	0.01	99.13	
NWA11057_px03-2	52.07	0.26	1.40	0.09	0.31	14.50	0.00	0.48	13.90	16.49	0.16	0.00	99.66	
NWA11057_px03-3	50.95	0.35	1.11	0.08	0.15	20.69	0.00	0.60	11.44	14.39	0.14	0.00	99.90	
NWA11057_px03-4	49.76	0.35	0.71	0.04	0.09	31.55	0.00	0.84	10.59	6.08	0.05	0.00	100.06	
NWA11057_px03-5	49.06	0.59	0.72	0.01	0.03	32.11	0.00	0.84	8.21	8.40	0.08	0.00	100.05	
NWA11057_px04-1	51.68	0.36	1.82	0.12	0.46	13.21	0.03	0.43	13.82	17.37	0.19	0.00	99.49	
NWA11057_px04-2	51.22	0.27	1.26	0.07	0.29	17.61	0.00	0.53	12.92	14.90	0.16	0.00	99.23	
NWA11057_px04-3	51.79	0.27	1.39	0.08	0.35	15.71	0.03	0.52	14.43	14.64	0.13	0.01	99.35	
NWA11057_px04-4	50.21	0.29	0.72	0.05	0.09	27.91	0.00	0.79	12.24	6.82	0.05	0.00	99.17	
NWA11057_px04-5	50.44	0.27	0.64	0.04	0.09	28.64	0.00	0.82	12.99	5.54	0.08	0.00	99.55	
NWA11057_px05-1	52.39	0.16	0.88	0.04	0.18	21.50	0.02	0.70	18.03	5.75	0.06	0.00	99.71	
NWA11057_px05-2	52.04	0.17	0.90	0.04	0.15	22.22	0.02	0.69	17.67	5.45	0.06	0.01	99.42	
NWA11057_px05-3	51.86	0.18	0.84	0.05	0.13	22.78	0.02	0.71	17.29	5.58	0.06	0.00	99.50	
NWA11057_px05-4	51.26	0.36	0.72	0.04	0.11	25.88	0.00	0.75	15.29	5.30	0.06	0.00	99.77	
NWA11057_px05-5	48.61	0.52	0.64	0.01	0.00	34.00	0.00	0.91	8.10	6.70	0.06	0.00	99.55	
NWA11057_px05-6	49.62	0.64	0.65	0.03	0.04	32.24	0.00	0.86	9.71	6.71	0.05	0.01	100.56	
NWA11057_px06-1	51.35	0.31	1.55	0.09	0.36	16.06	0.00	0.48	12.72	16.35	0.18	0.01	99.46	
NWA11057_px06-2	50.94	0.31	1.27	0.08	0.17	19.57	0.00	0.56	11.62	14.75	0.15	0.00	99.42	
NWA11057_px06-3	50.39	0.47	1.06	0.07	0.19	21.86	0.00	0.62	10.40	14.57	0.17	0.00	99.80	
NWA11057_px06-4	48.90	0.50	0.63	0.03	0.03	33.89	0.00	0.90	8.40	6.70	0.06	0.00	100.04	
NWA11057_px06-5	48.85	0.55	0.64	0.02	0.00	32.41	0.00	0.88	8.58	7.68	0.06	0.00	99.67	
NWA11057_px07-1	51.86	0.25	1.29	0.07	0.34	15.06	0.00	0.50	14.47	15.18	0.17	0.00	99.19	
NWA11057_px07-2	51.63	0.30	1.33	0.10	0.21	15.92	0.00	0.52	13.49	15.63	0.16	0.00	99.29	
NWA11057_px07-3	50.16	0.44	1.06	0.08	0.16	22.68	0.00	0.63	9.84	14.07	0.14	0.00	99.26	
NWA11057_px07-4	49.85	0.58	1.21	0.08	0.25	22.55	0.00	0.63	9.39	14.78	0.19	0.00	99.51	
NWA11057_px07-5	49.20	0.57	0.72	0.02	0.03	32.07	0.00	0.87	8.71	7.78	0.07	0.00	100.04	
NWA11057_px08-1	51.94	0.36	1.78	0.11	0.37	14.06	0.02	0.49	14.10	16.28	0.17	0.00	99.68	
NWA11057_px08-2	51.97	0.25	1.34	0.08	0.29	15.25	0.00	0.50	14.14	15.50	0.16	0.01	99.49	
NWA11057_px08-3	51.17	0.38	1.15	0.08	0.15	19.92	0.00	0.60	11.69	14.74	0.15	0.00	100.03	
NWA11057_px08-4	49.94	0.41	0.67	0.04	0.10	30.53	0.00	0.85	11.02	6.46	0.08	0.00	100.10	
NWA11057_px08-5	49.49	0.41	0.55	0.03	0.04	32.11	0.00	0.85	10.27	5.78	0.05	0.00	99.58	
NWA11057_px08-6	49.53	0.42	0.53	0.03	0.02	32.72	0.03	0.86	9.84	6.25	0.06	0.00	100.29	Adjacent to baddeleyite
NWA11057_px09-1	50.75	0.37	1.14	0.08	0.17	20.40	0.00	0.61	11.16	14.98	0.15	0.00	99.81	
NWA11057_px09-2	49.86	0.58	0.95	0.04	0.07	25.50	0.00	0.69	8.66	13.79	0.13	0.00	100.27	
NWA11057_px09-3	48.84	0.87	0.75	0.03	0.03	32.72	0.00	0.85	7.61	8.67	0.09	0.00	100.46	
NWA11057_px10-1	52.34	0.24	1.35	0.07	0.33	14.19	0.00	0.52	14.49	15.96	0.16	0.01	99.66	
NWA11057_px10-2	51.57	0.27	1.24	0.08	0.30	16.86	0.00	0.52	12.65	16.08	0.16	0.00	99.73	

Table A1.1.(continued) EPMA analysis of pyroxenes.

SAMPLE	SiO ₂	TiO ₂	Al ₂ O ₃	V ₂ O ₃	Cr ₂ O ₃	FeO	NiO	MnO	MgO	CaO	Na ₂ O	K ₂ O	TOTAL	NOTES
NWA11057_px10-3	50.34	0.50	1.14	0.08	0.16	21.96	0.00	0.63	10.20	14.56	0.17	0.01	99.75	
NWA11057_px10-4	49.52	0.42	0.55	0.03	0.03	32.57	0.00	0.88	9.94	6.06	0.05	0.00	100.05	
NWA11057_px10-5	49.16	0.48	0.58	0.01	0.02	33.11	0.00	0.87	8.89	6.71	0.06	0.00	99.89	Adjacent to baddeleyite
NWA11073_px01-1	51.24	0.33	1.50	0.09	0.25	15.47	0.00	0.55	14.11	15.17	0.15	0.00	98.86	
NWA11073_px01-2	51.70	0.23	1.23	0.08	0.32	15.11	0.00	0.52	14.78	14.86	0.15	0.00	98.98	
NWA11073_px01-3	51.52	0.27	1.30	0.08	0.28	15.62	0.02	0.52	14.08	15.38	0.15	0.00	99.22	
NWA11073_px01-4	51.34	0.16	0.58	0.04	0.08	25.07	0.03	0.74	16.15	5.14	0.05	0.00	99.38	
NWA11073_px01-5	50.92	0.20	0.63	0.04	0.10	27.34	0.00	0.75	14.56	4.78	0.04	0.00	99.36	
NWA11073_px02-1	51.41	0.29	1.42	0.08	0.29	14.68	0.00	0.50	14.14	15.81	0.18	0.00	98.80	
NWA11073_px02-2	51.42	0.32	1.44	0.11	0.24	14.17	0.00	0.49	13.93	16.59	0.17	0.00	98.88	
NWA11073_px02-3	51.02	0.38	1.75	0.12	0.28	14.96	0.03	0.51	14.02	15.75	0.17	0.00	98.99	
NWA11073_px02-4	51.27	0.18	0.82	0.04	0.16	23.12	0.03	0.71	16.00	6.64	0.06	0.00	99.03	
NWA11073_px02-5	51.20	0.19	0.67	0.05	0.11	25.14	0.00	0.75	15.06	6.10	0.06	0.00	99.33	
NWA11073_px03-1	51.83	0.24	1.31	0.08	0.33	14.69	0.02	0.51	14.46	15.57	0.16	0.00	99.20	
NWA11073_px03-2	49.77	0.43	1.06	0.07	0.16	21.23	0.00	0.60	10.81	13.98	0.15	0.00	98.26	
NWA11073_px03-3	49.75	0.55	1.03	0.07	0.15	22.30	0.00	0.61	9.59	14.85	0.18	0.00	99.08	
NWA11073_px03-4	49.82	0.35	0.66	0.03	0.08	30.85	0.02	0.80	11.69	5.49	0.05	0.00	99.84	
NWA11073_px03-5	49.32	0.46	0.66	0.03	0.05	32.03	0.00	0.86	9.83	6.55	0.06	0.00	99.85	
NWA11073_px04-1	52.27	0.16	0.83	0.05	0.20	21.10	0.03	0.68	16.91	7.59	0.08	0.00	99.90	
NWA11073_px04-2	51.77	0.16	0.81	0.05	0.20	22.03	0.03	0.68	17.85	5.43	0.06	0.00	99.07	
NWA11073_px04-3	50.02	0.30	0.81	0.05	0.09	26.67	0.00	0.78	12.72	7.55	0.08	0.00	99.07	
NWA11073_px04-4	49.58	0.35	0.69	0.03	0.09	29.37	0.00	0.82	11.66	6.26	0.07	0.00	98.92	
NWA11073_px04-5	49.09	0.49	0.64	0.03	0.02	31.84	0.00	0.84	9.65	7.05	0.06	0.00	99.71	
NWA11073_px05-1	51.92	0.27	1.23	0.08	0.28	15.78	0.00	0.52	14.45	14.83	0.14	0.00	99.50	
NWA11073_px05-2	52.01	0.25	1.24	0.08	0.36	14.70	0.02	0.53	14.62	15.59	0.16	0.00	99.56	
NWA11073_px05-3	50.74	0.33	0.90	0.05	0.13	24.66	0.00	0.76	12.95	9.01	0.09	0.00	99.62	
NWA11073_px05-4	48.31	0.54	0.62	0.01	0.00	33.72	0.00	0.91	8.17	6.78	0.04	0.00	99.10	
NWA11073_px05-5	48.10	0.53	0.52	0.01	0.03	34.98	0.00	0.95	7.96	6.21	0.05	0.00	99.34	Adjacent to baddeleyite
NWA11073_px06-1	52.10	0.18	0.90	0.05	0.20	21.52	0.02	0.70	17.87	6.13	0.06	0.00	99.73	
NWA11073_px06-2	51.41	0.27	0.82	0.04	0.16	23.46	0.02	0.73	16.97	5.37	0.04	0.00	99.29	
NWA11073_px06-3	50.83	0.35	0.73	0.04	0.12	27.20	0.00	0.77	14.44	5.35	0.05	0.00	99.88	
NWA11073_px06-4	49.63	0.40	0.66	0.04	0.06	31.39	0.00	0.82	10.92	6.04	0.07	0.00	100.03	
NWA11073_px06-5	49.17	0.60	0.78	0.03	0.00	30.56	0.00	0.82	8.67	9.25	0.08	0.00	99.96	
NWA11073_px07-1	51.49	0.33	1.54	0.09	0.25	15.16	0.02	0.51	13.83	15.35	0.16	0.01	98.74	
NWA11073_px07-2	51.66	0.27	1.46	0.08	0.37	14.96	0.02	0.51	14.50	15.51	0.14	0.00	99.48	
NWA11073_px07-3	51.64	0.28	1.16	0.07	0.27	16.98	0.03	0.56	13.71	14.43	0.15	0.00	99.28	
NWA11073_px07-4	50.98	0.21	0.69	0.04	0.12	27.05	0.00	0.80	14.41	5.45	0.05	0.00	99.80	
NWA11073_px07-5	50.98	0.19	0.68	0.05	0.09	25.54	0.00	0.73	15.10	5.36	0.06	0.01	98.79	
NWA11073_px08-1	51.56	0.37	1.63	0.11	0.25	15.98	0.02	0.52	13.83	15.64	0.15	0.00	100.06	

Table A1.1.(continued) EPMA analysis of pyroxenes.

SAMPLE	SiO ₂	TiO ₂	Al ₂ O ₃	V ₂ O ₃	Cr ₂ O ₃	FeO	NiO	MnO	MgO	CaO	Na ₂ O	K ₂ O	TOTAL	NOTES
NWA11073_px08-2	50.44	0.55	1.04	0.06	0.16	21.98	0.00	0.61	10.39	14.85	0.16	0.00	100.24	
NWA11073_px08-3	49.50	0.50	0.66	0.02	0.03	32.66	0.02	0.87	9.43	6.78	0.06	0.00	100.53	
NWA11073_px08-4	49.75	0.39	0.74	0.05	0.10	29.80	0.00	0.81	11.00	7.09	0.08	0.00	99.81	
NWA11073_px08-5	49.00	0.55	0.72	0.03	0.03	32.67	0.00	0.88	8.94	6.82	0.06	0.00	99.70	
NWA11073_px09-1	51.92	0.25	1.30	0.08	0.34	15.49	0.00	0.53	15.11	14.27	0.15	0.00	99.44	
NWA11073_px09-2	50.98	0.37	1.22	0.06	0.27	20.51	0.02	0.61	12.22	13.08	0.16	0.00	99.50	
NWA11073_px09-3	49.98	0.69	1.33	0.05	0.19	23.00	0.00	0.65	9.92	13.78	0.16	0.00	99.75	
NWA11073_px09-4	48.92	0.54	0.72	0.03	0.07	29.62	0.02	0.80	8.85	10.32	0.11	0.00	100.00	
NWA11073_px09-5	48.86	0.50	0.65	0.02	0.03	33.03	0.00	0.87	8.79	6.68	0.07	0.00	99.50	
NWA11073_px10-1	51.72	0.25	1.28	0.08	0.30	15.52	0.03	0.50	14.10	15.76	0.14	0.00	99.68	
NWA11073_px10-2	51.83	0.19	0.89	0.04	0.16	22.18	0.00	0.70	17.61	5.63	0.06	0.00	99.29	
NWA11073_px10-3	51.80	0.19	0.88	0.05	0.19	22.73	0.00	0.72	16.99	5.85	0.06	0.00	99.46	
NWA11073_px10-4	51.15	0.28	1.00	0.06	0.13	23.34	0.00	0.70	14.79	7.82	0.09	0.00	99.36	
NWA11073_px10-5	49.72	0.41	0.70	0.04	0.08	30.48	0.00	0.82	10.97	6.54	0.06	0.00	99.82	
NWA11255_px01-1	52.04	0.27	1.48	0.09	0.45	13.46	0.02	0.47	14.60	16.70	0.18	0.00	99.76	
NWA11255_px01-2	52.19	0.30	1.49	0.09	0.43	13.16	0.00	0.45	14.33	17.04	0.18	0.00	99.66	
NWA11255_px01-3	52.25	0.25	1.32	0.09	0.32	14.54	0.02	0.48	14.22	16.18	0.15	0.00	99.82	
NWA11255_px01-4	50.69	0.41	1.09	0.07	0.14	20.48	0.00	0.60	11.15	14.60	0.15	0.00	99.38	
NWA11255_px01-5	49.45	0.50	0.68	0.04	0.03	30.92	0.00	0.84	9.56	7.94	0.07	0.01	100.04	
NWA11255_px02-1	51.53	0.34	1.83	0.11	0.48	15.56	0.00	0.50	13.78	15.46	0.18	0.00	99.77	
NWA11255_px02-2	52.22	0.26	1.36	0.07	0.30	14.33	0.02	0.50	14.65	15.78	0.15	0.01	99.65	
NWA11255_px02-3	50.08	0.30	1.08	0.07	0.21	23.56	0.00	0.65	10.09	13.70	0.13	0.00	99.87	
NWA11255_px02-4	49.81	0.45	0.63	0.03	0.04	31.54	0.00	0.87	10.60	6.16	0.07	0.00	100.20	
NWA11255_px02-5	49.50	0.47	0.60	0.01	0.00	32.66	0.00	0.88	9.91	5.87	0.07	0.00	99.97	
NWA11255_px03-1	51.86	0.30	1.51	0.09	0.39	15.33	0.00	0.49	14.38	15.16	0.16	0.00	99.67	
NWA11255_px03-2	52.15	0.29	1.28	0.08	0.33	15.59	0.00	0.51	14.28	14.90	0.16	0.01	99.58	
NWA11255_px03-3	52.13	0.25	1.34	0.10	0.35	14.86	0.00	0.49	14.31	15.72	0.16	0.00	99.71	
NWA11255_px03-4	50.94	0.54	1.45	0.08	0.31	19.32	0.00	0.58	12.36	13.91	0.16	0.00	99.65	
NWA11255_px03-5	49.51	0.55	0.64	0.03	0.04	32.36	0.00	0.83	9.63	6.55	0.06	0.00	100.20	
NWA11255_px04-1	52.06	0.27	1.48	0.08	0.28	15.56	0.02	0.52	14.31	14.76	0.16	0.01	99.51	
NWA11255_px04-2	51.81	0.27	1.45	0.09	0.33	15.61	0.00	0.50	14.67	14.37	0.15	0.00	99.25	
NWA11255_px04-3	50.87	0.33	0.75	0.05	0.10	26.83	0.00	0.79	13.38	6.49	0.06	0.00	99.65	
NWA11255_px04-4	50.06	0.38	0.69	0.04	0.10	30.06	0.00	0.83	11.55	6.10	0.05	0.00	99.86	
NWA11255_px04-5	49.59	0.43	0.66	0.04	0.06	31.53	0.00	0.83	10.73	5.90	0.06	0.01	99.84	
NWA11255_px05-1	52.04	0.32	1.53	0.09	0.35	14.07	0.02	0.49	14.05	16.49	0.17	0.00	99.62	
NWA11255_px05-2	50.56	0.31	1.20	0.07	0.25	20.52	0.00	0.58	10.65	15.23	0.16	0.00	99.53	
NWA11255_px05-3	50.15	0.32	0.69	0.04	0.09	28.91	0.00	0.82	12.32	6.37	0.06	0.00	99.77	
NWA11255_px05-4	49.03	0.53	0.62	0.02	0.02	32.77	0.00	0.92	9.02	6.75	0.06	0.00	99.74	
NWA11255_px05-5	49.34	0.42	0.48	0.01	0.03	33.07	0.00	0.91	9.82	5.86	0.05	0.00	99.99	

Table A1.1.(continued) EPMA analysis of pyroxenes.

SAMPLE	SiO ₂	TiO ₂	Al ₂ O ₃	V ₂ O ₃	Cr ₂ O ₃	FeO	NiO	MnO	MgO	CaO	Na ₂ O	K ₂ O	TOTAL	NOTES
NWA11255_px06-1	52.20	0.25	1.24	0.07	0.28	15.17	0.00	0.52	15.06	14.59	0.14	0.00	99.52	
NWA11255_px06-2	51.60	0.25	1.24	0.07	0.33	16.07	0.02	0.55	13.69	15.25	0.15	0.00	99.22	
NWA11255_px06-3	50.91	0.28	0.81	0.05	0.09	25.16	0.00	0.76	13.24	8.07	0.07	0.00	99.44	
NWA11255_px06-4	50.99	0.27	0.80	0.04	0.10	26.02	0.02	0.80	14.30	6.27	0.07	0.00	99.68	
NWA11255_px06-5	50.67	0.23	0.71	0.05	0.07	27.14	0.00	0.78	13.56	6.12	0.06	0.00	99.39	
NWA11255_px07-1	52.14	0.27	1.34	0.08	0.32	14.08	0.00	0.50	14.52	16.21	0.13	0.00	99.59	
NWA11255_px07-2	52.11	0.26	1.33	0.08	0.32	14.15	0.00	0.48	14.61	16.13	0.16	0.00	99.63	
NWA11255_px07-3	51.86	0.31	1.52	0.09	0.45	13.82	0.03	0.46	14.34	16.49	0.17	0.00	99.54	
NWA11255_px07-4	51.54	0.31	1.19	0.07	0.15	17.89	0.02	0.60	13.32	14.36	0.15	0.01	99.61	
NWA11255_px07-5	50.82	0.24	0.72	0.05	0.09	26.75	0.00	0.79	13.86	6.21	0.05	0.00	99.58	
NWA11255_px08-1	51.72	0.31	1.62	0.10	0.35	15.34	0.00	0.52	14.48	14.87	0.16	0.00	99.47	
NWA11255_px08-2	51.89	0.31	1.54	0.09	0.36	13.89	0.02	0.45	14.01	16.91	0.17	0.00	99.64	
NWA11255_px08-3	52.19	0.28	1.44	0.09	0.32	15.03	0.00	0.52	14.94	15.36	0.14	0.00	100.31	
NWA11255_px08-4	51.14	0.26	0.93	0.06	0.15	24.41	0.02	0.73	14.24	7.78	0.07	0.00	99.79	
NWA11255_px08-5	50.99	0.24	0.78	0.05	0.10	25.88	0.00	0.74	14.61	6.07	0.05	0.00	99.51	
NWA11255_px09-1	50.04	0.63	1.17	0.07	0.17	22.28	0.00	0.63	9.72	14.96	0.16	0.00	99.83	
NWA11255_px09-2	49.48	0.70	1.01	0.05	0.05	24.26	0.02	0.64	8.71	14.61	0.16	0.00	99.69	
NWA11255_px09-3	49.16	0.46	0.62	0.02	0.02	33.08	0.00	0.89	9.43	6.13	0.05	0.00	99.86	Adjacent to baddeleyite
NWA11255_px10-1	51.49	0.31	1.20	0.07	0.16	17.99	0.00	0.57	12.69	15.23	0.14	0.00	99.85	
NWA11255_px10-2	50.23	0.45	1.02	0.07	0.17	23.28	0.02	0.66	10.42	13.35	0.12	0.00	99.79	
NWA11255_px10-3	49.34	0.54	0.63	0.02	0.02	31.69	0.02	0.88	9.47	7.39	0.07	0.00	100.07	Adjacent to baddeleyite
NWA11255_px11-1	51.83	0.25	1.33	0.08	0.36	14.76	0.02	0.48	13.96	16.02	0.16	0.00	99.25	
NWA11255_px11-2	51.12	0.29	1.22	0.08	0.26	18.18	0.02	0.54	12.65	14.68	0.15	0.00	99.19	
NWA11255_px11-3	50.36	0.43	1.02	0.08	0.16	22.17	0.00	0.64	10.89	13.53	0.15	0.00	99.43	
NWA11255_px11-4	50.28	0.35	1.27	0.08	0.25	21.12	0.00	0.59	10.40	14.70	0.15	0.00	99.19	
NWA11255_px11-5	48.71	0.64	0.84	0.03	0.11	33.84	0.00	0.92	9.45	5.15	0.03	0.00	99.72	Adjacent to baddeleyite
NWA12262_px01-1	51.28	0.46	1.90	0.12	0.22	14.74	0.00	0.47	12.73	17.74	0.16	0.00	99.82	
NWA12262_px01-2	51.60	0.23	0.80	0.06	0.15	20.68	0.03	0.67	15.49	9.97	0.09	0.00	99.77	
NWA12262_px01-3	50.29	0.27	0.58	0.04	0.00	30.35	0.00	0.84	11.17	6.86	0.07	0.00	100.47	
NWA12262_px01-4	47.49	0.63	0.69	0.01	0.00	38.02	0.00	0.93	3.83	8.88	0.06	0.00	100.54	
NWA12262_px01-5	47.05	0.58	0.61	0.00	0.00	42.20	0.00	1.05	2.24	7.26	0.06	0.00	101.05	
NWA12262_px01-6	46.60	0.29	0.39	0.00	0.00	45.03	0.00	1.24	1.15	5.83	0.00	0.00	100.53	
NWA12262_px02-1	50.45	0.30	0.70	0.04	0.00	27.39	0.03	0.79	12.05	8.42	0.07	0.00	100.24	
NWA12262_px02-2	50.51	0.37	0.96	0.06	0.03	26.20	0.00	0.77	11.75	9.65	0.08	0.00	100.38	
NWA12262_px02-3	48.99	0.46	0.71	0.04	0.00	32.79	0.00	0.86	8.35	8.05	0.08	0.00	100.33	
NWA12262_px02-4	47.73	0.66	0.73	0.02	0.00	37.77	0.00	0.96	4.09	8.88	0.06	0.00	100.90	
NWA12262_px02-5	46.96	0.64	0.68	0.00	0.00	41.81	0.00	1.02	2.26	7.49	0.05	0.00	100.91	
NWA12262_px03-1	51.59	0.31	1.47	0.09	0.39	17.12	0.02	0.57	15.03	12.76	0.13	0.00	99.48	
NWA12262_px03-2	51.61	0.33	1.56	0.09	0.30	18.36	0.02	0.61	15.34	11.52	0.11	0.00	99.85	

Table A1.1.(continued) EPMA analysis of pyroxenes.

SAMPLE	SiO ₂	TiO ₂	Al ₂ O ₃	V ₂ O ₃	Cr ₂ O ₃	FeO	NiO	MnO	MgO	CaO	Na ₂ O	K ₂ O	TOTAL	NOTES
NWA12262_px03-3	51.06	0.45	2.00	0.11	0.33	17.28	0.02	0.59	14.11	13.70	0.16	0.00	99.81	
NWA12262_px03-4	50.89	0.36	1.09	0.07	0.06	21.36	0.00	0.63	12.22	13.16	0.14	0.00	99.98	
NWA12262_px03-5	49.48	0.35	0.63	0.04	0.00	32.02	0.00	0.85	9.23	7.97	0.08	0.00	100.65	
NWA12262_px03-6	47.39	0.57	0.77	0.02	0.00	40.17	0.00	0.97	2.61	8.36	0.06	0.00	100.92	
NWA12262_px04-1	52.15	0.24	1.22	0.07	0.18	22.59	0.03	0.70	17.31	5.80	0.05	0.00	100.34	
NWA12262_px04-2	50.97	0.39	2.03	0.11	0.24	17.74	0.02	0.58	13.67	13.90	0.15	0.00	99.80	
NWA12262_px04-3	50.90	0.35	1.12	0.07	0.06	21.09	0.00	0.63	12.62	12.97	0.13	0.00	99.94	
NWA12262_px04-4	50.37	0.27	0.72	0.05	0.03	25.16	0.00	0.72	12.71	9.26	0.10	0.00	99.39	
NWA12262_px04-5	49.68	0.31	0.52	0.03	0.00	32.47	0.00	0.88	9.88	6.45	0.06	0.00	100.28	
NWA12262_px04-6	48.59	0.48	0.55	0.04	0.02	35.14	0.00	0.86	6.36	8.20	0.06	0.00	100.30	
NWA12262_px05-1	51.29	0.48	1.97	0.13	0.28	14.49	0.00	0.46	13.05	17.34	0.18	0.00	99.67	
NWA12262_px05-2	51.26	0.37	1.75	0.09	0.25	17.61	0.00	0.55	13.87	13.94	0.15	0.00	99.84	
NWA12262_px05-3	51.72	0.33	1.55	0.09	0.22	17.39	0.00	0.59	14.47	13.50	0.13	0.00	99.99	
NWA12262_px05-4	49.61	0.35	0.72	0.04	0.00	29.90	0.00	0.82	9.82	8.41	0.07	0.00	99.74	
NWA12262_px05-5	48.39	0.55	0.64	0.03	0.00	34.21	0.00	0.83	5.00	10.95	0.09	0.00	100.69	
NWA12262_px06-1	50.69	0.43	1.82	0.12	0.27	14.80	0.00	0.44	12.77	17.93	0.18	0.00	99.45	
NWA12262_px06-2	50.53	0.42	1.53	0.09	0.11	20.54	0.00	0.62	12.69	13.07	0.14	0.00	99.74	
NWA12262_px06-3	50.51	0.42	1.22	0.08	0.05	19.85	0.00	0.58	11.35	15.55	0.15	0.00	99.76	
NWA12262_px06-4	48.12	0.46	0.49	0.03	0.00	37.57	0.00	0.94	5.88	6.84	0.05	0.00	100.38	
NWA12262_px06-5	46.74	0.42	0.36	0.00	0.00	43.90	0.00	1.10	2.41	5.57	0.03	0.00	100.53	
NWA12262_px07-1	51.01	0.50	2.02	0.12	0.19	16.66	0.03	0.54	13.18	15.46	0.16	0.00	99.87	
NWA12262_px07-2	51.15	0.40	2.01	0.10	0.16	18.03	0.00	0.58	13.67	13.46	0.14	0.00	99.70	
NWA12262_px07-3	50.50	0.27	0.83	0.04	0.03	26.32	0.00	0.78	14.15	6.61	0.07	0.00	99.60	
NWA12262_px07-4	50.19	0.24	0.56	0.03	0.03	29.39	0.02	0.82	12.94	5.77	0.05	0.00	100.04	
NWA12262_px07-5	48.20	0.51	0.65	0.04	0.00	37.16	0.00	0.89	6.42	6.61	0.06	0.00	100.54	
NWA12262_px08-1	51.28	0.34	1.56	0.09	0.20	18.35	0.02	0.59	14.35	12.93	0.13	0.00	99.84	
NWA12262_px08-2	50.85	0.40	1.78	0.10	0.22	18.06	0.00	0.55	13.70	13.84	0.15	0.00	99.65	
NWA12262_px08-3	50.81	0.23	0.66	0.04	0.03	26.63	0.03	0.81	14.12	6.59	0.05	0.00	100.00	
NWA12262_px08-4	49.67	0.32	0.48	0.02	0.00	33.33	0.00	0.90	9.52	6.18	0.05	0.00	100.47	
NWA12262_px08-5	46.76	0.43	0.45	0.00	0.00	44.44	0.00	1.10	1.91	5.03	0.04	0.00	100.16	
NWA12262_px09-1	49.71	0.52	0.97	0.06	0.00	27.84	0.00	0.75	8.14	12.22	0.13	0.00	100.34	
NWA12262_px09-2	51.15	0.38	1.18	0.08	0.07	20.02	0.00	0.61	12.35	14.12	0.14	0.00	100.10	
NWA12262_px09-3	51.07	0.32	1.54	0.08	0.23	18.00	0.02	0.60	14.59	12.99	0.16	0.00	99.60	
NWA12262_px09-4	50.64	0.35	1.13	0.07	0.07	20.68	0.02	0.61	12.51	13.26	0.14	0.01	99.49	
NWA12262_px09-5	47.31	0.50	0.57	0.00	0.00	40.76	0.00	1.00	2.89	7.35	0.07	0.00	100.45	Adjacent to baddeleyite
NWA12262_px10-1	51.16	0.42	2.15	0.12	0.31	16.42	0.00	0.54	13.81	14.76	0.16	0.00	99.85	
NWA12262_px10-2	51.14	0.33	1.57	0.10	0.28	18.02	0.00	0.56	14.46	13.14	0.14	0.00	99.74	
NWA12262_px10-3	50.70	0.38	1.84	0.10	0.22	19.14	0.00	0.61	14.56	12.10	0.14	0.00	99.79	
NWA12262_px10-4	49.23	0.31	0.54	0.03	0.00	33.87	0.00	0.89	9.42	6.00	0.06	0.00	100.35	

Table A1.1.(continued) EPMA analysis of pyroxenes.

SAMPLE	SiO ₂	TiO ₂	Al ₂ O ₃	V ₂ O ₃	Cr ₂ O ₃	FeO	NiO	MnO	MgO	CaO	Na ₂ O	K ₂ O	TOTAL	NOTES
NWA12262_px10-5	47.64	0.47	0.44	0.01	0.00	38.25	0.00	0.91	4.94	7.58	0.06	0.00	100.30	
NWA12262_px10-6	46.01	0.35	0.34	0.00	0.00	45.30	0.00	1.07	1.71	5.21	0.00	0.00	99.99	
AA-1(NWA12919)_px001-1	51.44	0.24	1.33	0.08	0.43	14.26	0.00	0.49	14.77	15.97	0.16	0.00	99.17	
AA-1(NWA12919)_px001-2	51.62	0.24	1.36	0.08	0.47	14.07	0.00	0.48	15.06	15.82	0.17	0.00	99.37	
AA-1(NWA12919)_px001-3	51.26	0.18	0.61	0.05	0.11	25.17	0.02	0.75	15.82	5.48	0.04	0.01	99.50	
AA-1(NWA12919)_px001-4	50.63	0.27	0.72	0.04	0.13	26.32	0.00	0.76	14.32	6.21	0.06	0.00	99.46	
AA-1(NWA12919)_px001-5	50.05	0.32	0.66	0.02	0.14	29.25	0.00	0.82	12.40	6.21	0.05	0.00	99.92	
AA-1(NWA12919)_px001-6	49.38	0.40	0.62	0.03	0.11	31.17	0.00	0.84	10.86	6.29	0.08	0.00	99.78	
AA-1(NWA12919)_px001-7	48.83	0.46	0.48	0.01	0.00	34.10	0.00	0.88	8.54	6.78	0.06	0.00	100.14	
AA-1(NWA12919)_px002-1	51.93	0.25	1.46	0.08	0.66	13.54	0.00	0.49	15.56	15.29	0.16	0.01	99.43	
AA-1(NWA12919)_px002-2	51.74	0.30	1.54	0.09	0.71	12.79	0.00	0.43	15.11	16.50	0.18	0.00	99.39	
AA-1(NWA12919)_px002-3	51.43	0.27	1.42	0.09	0.64	14.76	0.03	0.50	14.99	15.18	0.17	0.00	99.48	
AA-1(NWA12919)_px002-4	51.08	0.24	1.09	0.07	0.41	20.07	0.00	0.60	13.97	12.20	0.14	0.00	99.87	
AA-1(NWA12919)_px002-5	51.40	0.18	0.73	0.04	0.16	24.80	0.02	0.72	16.31	5.21	0.04	0.00	99.61	
AA-1(NWA12919)_px002-6	49.38	0.40	0.70	0.03	0.12	30.18	0.00	0.80	11.21	6.44	0.07	0.00	99.33	
AA-1(NWA12919)_px003-1	51.26	0.21	1.17	0.06	0.43	14.73	0.00	0.50	15.20	14.88	0.14	0.01	98.59	
AA-1(NWA12919)_px003-2	51.27	0.27	1.35	0.08	0.44	14.48	0.00	0.47	14.38	15.92	0.15	0.01	98.82	
AA-1(NWA12919)_px003-3	51.41	0.24	1.31	0.08	0.46	13.84	0.00	0.47	14.97	15.65	0.15	0.00	98.58	
AA-1(NWA12919)_px003-4	50.24	0.40	1.07	0.07	0.24	19.57	0.00	0.61	11.66	14.79	0.15	0.00	98.80	
AA-1(NWA12919)_px003-5	50.66	0.21	0.67	0.04	0.11	24.82	0.02	0.74	15.60	5.68	0.06	0.00	98.61	
AA-1(NWA12919)_px003-6	50.61	0.24	0.67	0.04	0.12	26.42	0.02	0.78	14.70	5.55	0.06	0.00	99.21	
AA-1(NWA12919)_px003-7	49.63	0.34	0.67	0.05	0.14	28.17	0.00	0.78	12.10	6.93	0.05	0.00	98.86	
AA-1(NWA12919)_px003-8	49.04	0.41	0.60	0.04	0.11	30.43	0.00	0.80	11.55	5.66	0.02	0.00	98.66	
AA-1(NWA12919)_px004-1	49.23	0.47	0.93	0.06	0.18	23.97	0.02	0.66	10.46	12.73	0.14	0.00	98.85	
AA-1(NWA12919)_px004-2	49.14	0.68	0.85	0.04	0.05	24.99	0.00	0.65	8.33	14.56	0.14	0.00	99.43	
AA-1(NWA12919)_px004-3	48.65	0.69	0.82	0.03	0.02	26.02	0.00	0.71	7.65	14.23	0.14	0.00	98.96	
AA-1(NWA12919)_px004-4	49.65	0.36	0.64	0.03	0.13	29.79	0.00	0.83	11.63	6.46	0.07	0.00	99.59	
AA-1(NWA12919)_px004-5	48.65	0.47	0.58	0.02	0.00	31.43	0.00	0.85	9.71	7.12	0.07	0.00	98.90	
AA-1(NWA12919)_px004-6	48.26	0.65	0.71	0.02	0.00	31.92	0.02	0.86	7.17	9.77	0.09	0.00	99.47	
AA-1(NWA12919)_px004-7	47.44	0.71	0.76	0.00	0.00	34.02	0.00	0.92	5.88	9.16	0.08	0.00	98.97	
AA-1(NWA12919)_px005-1	51.80	0.25	1.42	0.09	0.72	11.88	0.02	0.43	15.09	17.19	0.19	0.00	99.08	
AA-1(NWA12919)_px005-2	51.11	0.26	1.44	0.09	0.66	13.27	0.02	0.47	15.35	15.93	0.19	0.00	98.79	
AA-1(NWA12919)_px005-3	51.53	0.28	1.39	0.09	0.34	15.12	0.03	0.50	14.38	15.50	0.15	0.02	99.33	
AA-1(NWA12919)_px005-4	50.56	0.47	1.42	0.07	0.38	18.22	0.00	0.55	12.93	14.70	0.15	0.00	99.45	
AA-1(NWA12919)_px005-5	50.04	0.67	1.26	0.04	0.22	20.76	0.00	0.60	10.98	14.75	0.15	0.00	99.47	
AA-1(NWA12919)_px005-6	50.80	0.25	0.86	0.06	0.13	24.37	0.00	0.72	15.14	6.75	0.06	0.00	99.14	
AA-1(NWA12919)_px005-7	48.02	0.53	0.51	0.00	0.00	35.56	0.00	0.93	7.28	6.22	0.05	0.00	99.10	
AA-1(NWA12919)_px006-1	51.85	0.22	1.15	0.07	0.45	13.50	0.00	0.48	15.47	15.69	0.16	0.00	99.04	
AA-1(NWA12919)_px006-2	51.33	0.24	1.15	0.07	0.44	16.50	0.00	0.54	14.33	14.47	0.15	0.00	99.22	

Table A1.1.(continued) EPMA analysis of pyroxenes.

SAMPLE	SiO ₂	TiO ₂	Al ₂ O ₃	V ₂ O ₃	Cr ₂ O ₃	FeO	NiO	MnO	MgO	CaO	Na ₂ O	K ₂ O	TOTAL	NOTES
AA-1(NWA12919)_px006-3	51.35	0.26	1.32	0.08	0.46	14.32	0.00	0.48	14.85	15.70	0.16	0.00	98.98	
AA-1(NWA12919)_px006-4	50.89	0.20	0.70	0.04	0.12	24.86	0.00	0.77	15.83	5.63	0.06	0.00	99.10	
AA-1(NWA12919)_px006-5	51.00	0.22	0.72	0.04	0.10	24.82	0.00	0.75	15.37	6.17	0.06	0.00	99.25	
AA-1(NWA12919)_px006-6	50.38	0.27	0.67	0.04	0.13	26.30	0.00	0.79	13.98	6.31	0.06	0.00	98.93	
AA-1(NWA12919)_px006-7	48.75	0.53	0.59	0.02	0.06	31.63	0.00	0.84	9.03	7.77	0.07	0.00	99.29	
AA-1(NWA12919)_px006-8	48.32	0.36	0.51	0.02	0.08	35.08	0.00	0.93	8.36	5.66	0.03	0.00	99.35	
AA-1(NWA12919)_px007-1	51.02	0.29	1.52	0.10	0.79	11.53	0.00	0.42	14.68	17.74	0.20	0.00	98.29	
AA-1(NWA12919)_px007-2	50.99	0.26	1.43	0.09	0.67	12.55	0.02	0.45	15.17	16.70	0.19	0.00	98.52	
AA-1(NWA12919)_px007-3	51.32	0.27	1.44	0.09	0.70	12.84	0.02	0.44	15.09	16.52	0.18	0.00	98.91	
AA-1(NWA12919)_px007-4	51.19	0.26	1.36	0.08	0.51	13.63	0.00	0.48	14.57	16.44	0.15	0.00	98.67	
AA-1(NWA12919)_px007-5	50.33	0.36	1.10	0.09	0.23	17.68	0.00	0.52	12.21	15.83	0.16	0.00	98.51	
AA-1(NWA12919)_px007-6	49.49	0.51	1.10	0.08	0.25	20.56	0.00	0.58	10.60	15.35	0.16	0.00	98.68	
AA-1(NWA12919)_px007-7	49.34	0.52	1.09	0.08	0.24	20.97	0.00	0.57	10.37	15.16	0.17	0.00	98.51	
AA-1(NWA12919)_px007-8	48.79	0.29	0.69	0.04	0.15	31.93	0.00	0.87	10.44	5.77	0.06	0.00	99.03	
AA-1(NWA12919)_px007-9	48.91	0.55	0.74	0.03	0.13	27.67	0.02	0.74	9.06	11.19	0.10	0.00	99.14	
AA-1(NWA12919)_px007-10	48.33	0.45	0.47	0.02	0.04	32.98	0.00	0.89	8.95	6.64	0.04	0.00	98.81	
AA-1(NWA12919)_px008-1	51.57	0.26	1.40	0.09	0.60	14.30	0.00	0.47	14.76	15.64	0.16	0.00	99.25	
AA-1(NWA12919)_px008-2	51.23	0.31	1.69	0.11	0.74	12.31	0.02	0.42	14.50	17.25	0.19	0.00	98.77	
AA-1(NWA12919)_px008-3	51.44	0.26	1.30	0.08	0.40	14.76	0.00	0.48	14.38	15.83	0.16	0.00	99.09	
AA-1(NWA12919)_px008-4	50.52	0.32	1.17	0.08	0.25	18.04	0.02	0.54	12.66	14.96	0.15	0.00	98.71	
AA-1(NWA12919)_px008-5	49.82	0.32	0.71	0.04	0.15	27.79	0.02	0.76	12.61	6.53	0.05	0.00	98.80	
AA-1(NWA12919)_px008-6	50.12	0.29	0.66	0.04	0.14	27.73	0.00	0.81	13.33	5.94	0.06	0.00	99.12	
AA-1(NWA12919)_px008-7	49.73	0.27	0.62	0.04	0.14	28.41	0.00	0.77	12.79	5.77	0.05	0.00	98.59	
AA-1(NWA12919)_px008-8	49.58	0.29	0.65	0.04	0.12	28.61	0.00	0.80	12.34	5.81	0.06	0.00	98.30	
AA-1(NWA12919)_px009-1	51.45	0.25	1.31	0.08	0.48	13.89	0.00	0.47	14.77	16.04	0.16	0.00	98.90	
AA-1(NWA12919)_px009-2	50.60	0.26	1.26	0.08	0.42	16.35	0.00	0.51	13.03	16.11	0.18	0.00	98.80	
AA-1(NWA12919)_px009-3	50.51	0.35	1.15	0.08	0.21	17.77	0.00	0.55	12.17	15.69	0.16	0.00	98.64	
AA-1(NWA12919)_px009-4	50.15	0.41	1.06	0.08	0.22	19.86	0.00	0.53	10.94	15.60	0.16	0.00	99.01	
AA-1(NWA12919)_px009-5	49.20	0.56	1.00	0.07	0.21	22.39	0.00	0.63	9.49	14.90	0.14	0.02	98.61	
AA-1(NWA12919)_px009-6	48.77	0.68	0.83	0.03	0.05	25.95	0.00	0.68	7.82	14.18	0.13	0.00	99.12	
AA-1(NWA12919)_px009-7	48.78	0.74	0.92	0.03	0.05	24.94	0.00	0.67	7.67	15.06	0.15	0.00	99.01	
AA-1(NWA12919)_px009-8	48.64	0.75	0.94	0.03	0.05	25.28	0.00	0.67	7.74	14.76	0.15	0.00	99.01	
AA-1(NWA12919)_px009-9	48.30	0.52	0.56	0.00	0.03	32.60	0.00	0.87	8.21	7.77	0.06	0.00	98.92	
AA-1(NWA12919)_px010-1	51.64	0.26	1.44	0.10	0.70	12.18	0.02	0.41	15.10	16.98	0.19	0.00	99.02	
AA-1(NWA12919)_px010-2	51.30	0.26	1.38	0.08	0.64	13.83	0.00	0.46	14.88	15.83	0.17	0.00	98.83	
AA-1(NWA12919)_px010-3	51.88	0.20	1.05	0.06	0.46	14.34	0.03	0.49	15.24	15.37	0.16	0.00	99.28	
AA-1(NWA12919)_px010-4	49.77	0.34	0.72	0.04	0.14	28.68	0.00	0.80	12.30	6.37	0.07	0.00	99.23	
AA-1(NWA12919)_px010-5	48.99	0.47	0.77	0.04	0.10	30.52	0.00	0.80	10.45	7.16	0.06	0.00	99.36	
AA-1(NWA12919)_px010-6	48.00	0.56	0.60	0.02	0.00	33.09	0.00	0.87	7.58	8.17	0.05	0.00	98.94	

Table A1.1.(continued) EPMA analysis of pyroxenes.

SAMPLE	SiO ₂	TiO ₂	Al ₂ O ₃	V ₂ O ₃	Cr ₂ O ₃	FeO	NiO	MnO	MgO	CaO	Na ₂ O	K ₂ O	TOTAL	NOTES
AA-1(NWA12919)_px011-1	51.51	0.32	1.66	0.12	0.65	14.15	0.03	0.51	15.37	14.96	0.18	0.00	99.46	
AA-1(NWA12919)_px011-2	51.12	0.33	1.79	0.10	0.67	15.75	0.02	0.53	15.71	13.11	0.15	0.00	99.28	
AA-1(NWA12919)_px011-3	51.59	0.24	1.24	0.08	0.46	14.51	0.00	0.49	15.44	14.92	0.15	0.01	99.13	
AA-1(NWA12919)_px011-4	51.81	0.23	1.26	0.08	0.45	13.97	0.00	0.47	15.36	15.62	0.16	0.00	99.41	
AA-1(NWA12919)_px011-5	51.09	0.29	1.03	0.06	0.16	22.72	0.02	0.68	14.73	8.87	0.09	0.00	99.74	
AA-1(NWA12919)_px011-6	49.62	0.45	0.72	0.05	0.16	28.29	0.00	0.81	11.43	7.72	0.07	0.00	99.32	
AA-1(NWA12919)_px011-7	48.75	0.51	0.57	0.03	0.09	32.25	0.00	0.84	9.18	6.91	0.05	0.00	99.18	
AA-1(NWA12919)_px011-8	48.55	0.57	1.43	0.00	0.02	32.57	0.00	0.85	7.44	7.93	0.31	0.03	99.70	
AA-1(NWA12919)_px012-1	51.87	0.25	1.47	0.09	0.57	13.21	0.00	0.46	15.19	16.19	0.17	0.00	99.47	
AA-1(NWA12919)_px012-2	51.75	0.26	1.41	0.08	0.61	13.41	0.00	0.46	15.37	15.81	0.18	0.00	99.34	
AA-1(NWA12919)_px012-3	51.59	0.27	1.30	0.09	0.46	14.30	0.02	0.48	14.45	16.43	0.16	0.00	99.55	
AA-1(NWA12919)_px012-4	50.99	0.35	1.12	0.07	0.21	17.82	0.00	0.56	12.54	15.65	0.16	0.00	99.47	
AA-1(NWA12919)_px012-5	50.55	0.27	0.67	0.05	0.13	27.53	0.00	0.79	13.73	6.07	0.05	0.00	99.84	
AA-1(NWA12919)_px012-6	50.08	0.29	0.66	0.04	0.14	28.90	0.02	0.79	13.05	5.47	0.06	0.00	99.50	
AA-1(NWA12919)_px012-7	49.19	0.43	0.59	0.03	0.07	31.28	0.00	0.81	10.66	6.24	0.06	0.00	99.36	
AA-1(NWA12919)_px012-8	48.01	0.61	0.63	0.00	0.00	34.71	0.00	0.94	6.97	7.47	0.05	0.00	99.39	
AA-1(NWA12919)_px013-1	51.40	0.27	1.40	0.08	0.57	14.22	0.00	0.51	14.57	16.21	0.19	0.00	99.42	
AA-1(NWA12919)_px013-2	52.01	0.16	0.85	0.04	0.27	20.51	0.02	0.70	18.67	5.95	0.07	0.00	99.25	
AA-1(NWA12919)_px013-3	51.61	0.17	0.83	0.03	0.27	22.60	0.02	0.71	17.81	5.38	0.05	0.00	99.48	
AA-1(NWA12919)_px013-4	51.51	0.24	0.97	0.04	0.26	22.65	0.00	0.68	17.47	5.54	0.06	0.00	99.42	
AA-1(NWA12919)_px013-5	49.06	0.51	0.60	0.03	0.09	31.97	0.00	0.86	10.03	6.72	0.07	0.00	99.94	
AA-1(NWA12919)_px013-6	48.63	0.68	0.76	0.01	0.02	29.81	0.00	0.77	7.34	11.79	0.10	0.00	99.91	
AA-1(NWA12919)_px013-7	48.16	0.57	0.59	0.02	0.00	35.73	0.00	0.94	7.24	6.73	0.05	0.00	100.03	
AA-1(NWA12919)_px013-8	48.29	0.58	0.65	0.01	0.00	34.72	0.00	0.89	6.86	8.03	0.07	0.00	100.10	
AA-1(NWA12919)_px014-1	49.73	0.54	1.02	0.07	0.23	21.81	0.00	0.59	9.83	15.49	0.16	0.00	99.47	
AA-1(NWA12919)_px014-2	48.01	0.52	0.58	0.02	0.06	33.33	0.00	0.88	8.01	7.59	0.06	0.00	99.06	
AA-1(NWA12919)_px014-3	48.32	0.49	0.55	0.02	0.00	34.22	0.00	0.92	8.33	6.43	0.04	0.00	99.32	
AA-1(NWA12919)_px014-4	48.69	0.48	0.53	0.02	0.00	33.67	0.00	0.87	9.11	6.29	0.05	0.00	99.71	
AA-1(NWA12919)_px014-5	49.18	0.45	0.57	0.03	0.04	32.13	0.00	0.83	10.16	6.29	0.05	0.00	99.73	
AA-1(NWA12919)_px014-6	48.43	0.54	0.58	0.02	0.03	33.65	0.02	0.91	8.51	6.83	0.05	0.00	99.57	
AA-1(NWA12919)_px015-1	51.49	0.25	1.32	0.08	0.53	14.81	0.00	0.51	15.17	14.86	0.15	0.00	99.17	
AA-1(NWA12919)_px015-2	51.39	0.27	1.39	0.08	0.55	14.80	0.00	0.51	15.16	14.82	0.16	0.01	99.14	
AA-1(NWA12919)_px015-3	50.75	0.28	1.32	0.09	0.39	16.81	0.00	0.49	12.58	16.27	0.18	0.00	99.16	
AA-1(NWA12919)_px015-4	50.70	0.31	1.24	0.07	0.19	22.26	0.00	0.71	15.20	8.45	0.09	0.00	99.22	
AA-1(NWA12919)_px015-5	49.34	0.52	0.76	0.04	0.11	28.49	0.00	0.81	11.28	7.71	0.07	0.00	99.13	
AA-1(NWA12919)_px015-6	49.80	0.33	0.65	0.04	0.12	29.07	0.00	0.82	12.21	6.32	0.04	0.00	99.40	
AA-1(NWA12919)_px015-7	49.34	0.44	0.64	0.04	0.13	30.42	0.00	0.83	10.87	6.60	0.06	0.00	99.37	
AA-1(NWA12919)_px015-8	49.11	0.47	0.64	0.04	0.09	30.96	0.00	0.81	10.39	6.65	0.06	0.00	99.22	
AA-1(NWA12919)_px016-1	51.48	0.25	1.30	0.08	0.43	14.09	0.02	0.51	14.92	15.86	0.15	0.00	99.09	

Table A1.1.(continued) EPMA analysis of pyroxenes.

SAMPLE	SiO ₂	TiO ₂	Al ₂ O ₃	V ₂ O ₃	Cr ₂ O ₃	FeO	NiO	MnO	MgO	CaO	Na ₂ O	K ₂ O	TOTAL	NOTES
AA-1(NWA12919)_px016-2	51.61	0.25	1.27	0.08	0.50	14.26	0.00	0.48	14.63	16.04	0.15	0.00	99.27	
AA-1(NWA12919)_px016-3	49.72	0.49	1.11	0.07	0.26	22.16	0.02	0.64	10.29	14.14	0.17	0.00	99.07	
AA-1(NWA12919)_px016-4	50.33	0.46	1.10	0.07	0.21	20.74	0.00	0.59	11.28	14.38	0.17	0.00	99.33	
AA-1(NWA12919)_px016-5	48.84	0.69	0.75	0.02	0.05	26.12	0.00	0.71	7.78	14.12	0.12	0.00	99.20	
AA-1(NWA12919)_px016-6	48.57	0.55	0.52	0.02	0.00	33.15	0.00	0.89	8.23	7.50	0.06	0.00	99.49	
AA-1(NWA12919)_px016-7	48.80	0.50	0.55	0.03	0.00	33.76	0.00	0.85	9.20	6.24	0.06	0.00	99.99	
AA-1(NWA12919)_px017-1	51.81	0.27	1.37	0.08	0.59	14.80	0.00	0.48	15.77	14.17	0.14	0.00	99.48	
AA-1(NWA12919)_px017-2	52.11	0.22	1.18	0.08	0.43	13.77	0.00	0.48	15.54	15.52	0.17	0.00	99.50	
AA-1(NWA12919)_px017-3	52.26	0.22	1.08	0.07	0.44	13.76	0.02	0.47	15.56	15.76	0.17	0.00	99.81	
AA-1(NWA12919)_px017-4	50.09	0.42	1.12	0.07	0.33	20.82	0.00	0.61	11.22	14.21	0.16	0.00	99.05	
AA-1(NWA12919)_px017-5	50.29	0.27	0.81	0.05	0.11	28.15	0.00	0.75	13.53	5.59	0.06	0.00	99.61	
AA-1(NWA12919)_px018-1	52.00	0.24	1.30	0.07	0.52	13.77	0.00	0.48	15.49	15.22	0.17	0.00	99.26	
AA-1(NWA12919)_px018-2	51.93	0.23	1.15	0.07	0.47	13.80	0.02	0.50	15.23	15.60	0.17	0.00	99.17	
AA-1(NWA12919)_px018-3	51.85	0.25	1.30	0.08	0.45	13.64	0.00	0.45	15.11	15.92	0.16	0.00	99.21	
AA-1(NWA12919)_px018-4	51.49	0.30	1.41	0.09	0.35	14.71	0.00	0.48	14.06	16.45	0.14	0.00	99.48	
AA-1(NWA12919)_px018-5	50.90	0.22	0.75	0.03	0.11	24.82	0.00	0.75	15.43	6.02	0.05	0.00	99.08	
AA-1(NWA12919)_px018-6	50.43	0.27	0.72	0.05	0.14	27.09	0.00	0.78	13.65	6.19	0.07	0.00	99.39	
AA-1(NWA12919)_px018-7	49.38	0.37	0.58	0.04	0.12	30.63	0.00	0.83	11.21	5.80	0.06	0.00	99.02	
AA-1(NWA12919)_px018-8	49.32	0.42	0.60	0.04	0.06	31.06	0.00	0.81	10.54	6.56	0.06	0.00	99.47	
AA-1(NWA12919)_px018-9	48.60	0.49	0.55	0.03	0.02	32.22	0.00	0.85	9.42	6.49	0.05	0.00	98.72	
AA-1(NWA12919)_px018-10	48.73	0.47	0.51	0.02	0.02	32.33	0.00	0.85	9.29	6.54	0.04	0.00	98.80	
AA-1(NWA12919)_px018-11	48.57	0.46	0.49	0.02	0.06	32.27	0.02	0.85	8.71	7.57	0.07	0.00	99.09	
AA-1(NWA12919)_px019-1	51.07	0.25	1.21	0.07	0.43	16.44	0.00	0.49	13.42	15.73	0.16	0.00	99.27	
AA-1(NWA12919)_px019-2	50.40	0.42	0.98	0.07	0.26	21.05	0.00	0.61	11.15	14.49	0.15	0.00	99.58	
AA-1(NWA12919)_px019-3	50.43	0.38	1.20	0.07	0.34	19.33	0.00	0.56	11.56	15.44	0.16	0.00	99.47	
AA-1(NWA12919)_px019-4	49.00	0.61	0.86	0.04	0.13	25.98	0.00	0.69	8.08	13.76	0.12	0.00	99.27	
AA-1(NWA12919)_px019-5	48.49	0.45	0.58	0.03	0.04	34.06	0.00	0.88	8.42	6.35	0.04	0.00	99.34	
AA-1(NWA12919)_px019-6	48.25	0.51	0.57	0.01	0.00	35.21	0.00	0.95	7.19	6.83	0.05	0.00	99.57	Adjacent to baddeleyite
AA-1(NWA12919)_px020-1	51.48	0.26	1.29	0.09	0.47	14.24	0.00	0.50	14.88	15.75	0.17	0.00	99.13	
AA-1(NWA12919)_px020-2	51.12	0.33	1.25	0.08	0.23	16.81	0.00	0.54	13.60	15.40	0.15	0.00	99.51	
AA-1(NWA12919)_px020-3	50.36	0.25	0.72	0.04	0.14	26.24	0.00	0.77	14.22	6.22	0.05	0.00	99.01	
AA-1(NWA12919)_px020-4	50.21	0.29	0.68	0.04	0.13	27.92	0.00	0.79	13.36	5.98	0.06	0.00	99.46	
AA-1(NWA12919)_px020-5	49.21	0.44	0.74	0.05	0.13	29.19	0.00	0.78	11.11	7.57	0.07	0.00	99.29	
AA-1(NWA12919)_px020-6	48.24	0.54	0.58	0.01	0.03	34.23	0.00	0.90	7.39	7.50	0.05	0.00	99.47	Adjacent to baddeleyite
AA-1(NWA12919)_px021-1	48.43	0.69	0.70	0.02	0.07	29.53	0.00	0.78	7.34	11.57	0.10	0.00	99.23	
AA-1(NWA12919)_px021-2	48.42	0.59	0.58	0.01	0.07	32.47	0.00	0.86	7.74	8.48	0.07	0.00	99.29	Adjacent to baddeleyite
AA-1(NWA12919)_px022-1	51.10	0.30	1.39	0.08	0.34	15.71	0.00	0.50	13.44	16.31	0.16	0.00	99.33	
AA-1(NWA12919)_px022-2	50.08	0.42	1.03	0.07	0.22	20.73	0.00	0.60	11.05	14.79	0.17	0.00	99.16	
AA-1(NWA12919)_px022-3	49.03	0.44	0.52	0.02	0.04	31.45	0.00	0.83	9.93	6.86	0.05	0.00	99.17	

Table A1.1.(continued) EPMA analysis of pyroxenes.

SAMPLE	SiO ₂	TiO ₂	Al ₂ O ₃	V ₂ O ₃	Cr ₂ O ₃	FeO	NiO	MnO	MgO	CaO	Na ₂ O	K ₂ O	TOTAL	NOTES
AA-1(NWA12919)_px022-4	48.75	0.53	0.58	0.02	0.05	32.07	0.00	0.83	9.14	7.32	0.05	0.00	99.34	
AA-1(NWA12919)_px022-5	48.47	0.58	0.64	0.02	0.04	32.75	0.00	0.86	8.33	7.46	0.05	0.00	99.20	
AA-1(NWA12919)_px022-6	48.59	0.51	0.58	0.02	0.02	32.73	0.00	0.87	8.99	6.89	0.06	0.00	99.26	
AA-1(NWA12919)_px022-7	48.28	0.48	0.53	0.01	0.00	35.54	0.00	0.92	7.32	6.39	0.05	0.00	99.52	Adjacent to baddeleyite
AA-1(NWA12919)_px023-1	51.50	0.22	1.15	0.07	0.46	14.45	0.00	0.47	15.24	14.96	0.15	0.02	98.69	
AA-1(NWA12919)_px023-2	49.64	0.64	0.89	0.06	0.10	22.07	0.02	0.58	10.11	14.94	0.14	0.00	99.19	
AA-1(NWA12919)_px023-3	49.12	0.52	0.88	0.07	0.12	25.45	0.00	0.68	9.46	12.61	0.12	0.00	99.03	
AA-1(NWA12919)_px023-4	47.42	0.57	0.53	0.00	0.04	35.18	0.03	0.90	7.26	6.75	0.04	0.00	98.72	Adjacent to baddeleyite
AA-1(NWA12919)_px023-5	48.72	0.42	0.61	0.04	0.09	31.99	0.00	0.85	9.72	6.28	0.04	0.00	98.76	
AA-1(NWA12919)_px024-1	48.16	0.44	0.61	0.03	0.07	31.63	0.00	0.81	9.96	6.44	0.06	0.01	98.22	
AA-1(NWA12919)_px024-2	47.41	0.64	0.65	0.00	0.00	33.13	0.00	0.90	6.38	9.37	0.09	0.01	98.58	
AA-1(NWA12919)_px024-3	46.97	0.50	0.55	0.00	0.00	36.82	0.00	0.99	5.06	7.74	0.05	0.00	98.68	
AA-1(NWA12919)_px024-4	46.89	0.70	0.65	0.00	0.00	35.11	0.00	0.93	4.78	9.48	0.08	0.00	98.62	
AA-1(NWA12919)_px024-5	46.55	0.75	0.51	0.00	0.00	37.63	0.00	0.97	4.85	7.13	0.06	0.00	98.45	Adjacent to baddeleyite

Table A1.2. EPMA analysis of former igneous plagioclase.

SAMPLE	SiO ₂	TiO ₂	Al ₂ O ₃	V ₂ O ₃	Cr ₂ O ₃	FeO	NiO	MnO	MgO	CaO	Na ₂ O	K ₂ O	TOTAL	%Ab	%An	%Or
NWA10299_plag01-1	56.28	0.04	27.17	0.00	0.00	0.67	0.00	0.00	0.06	9.88	5.67	0.42	100.19	50%	48%	2%
NWA10299_plag01-2	54.69	0.04	27.83	0.01	0.00	0.73	0.00	0.00	0.06	10.84	5.22	0.32	99.74	46%	52%	2%
NWA10299_plag01-3	56.78	0.06	26.38	0.00	0.00	0.82	0.00	0.02	0.05	9.30	5.68	0.65	99.74	51%	46%	4%
NWA10299_plag02-1	55.24	0.04	28.01	0.00	0.00	0.65	0.00	0.00	0.07	10.62	5.45	0.37	100.45	47%	51%	2%
NWA10299_plag02-2	54.93	0.04	28.38	0.00	0.00	0.76	0.00	0.00	0.07	10.81	5.34	0.34	100.67	46%	52%	2%
NWA10299_plag02-3	55.63	0.03	27.98	0.00	0.00	0.97	0.00	0.02	0.05	10.22	5.58	0.40	100.88	49%	49%	2%
NWA10299_plag03-1	54.60	0.04	28.70	0.00	0.00	0.73	0.00	0.00	0.05	11.15	5.20	0.22	100.69	45%	54%	1%
NWA10299_plag03-2	54.70	0.03	28.61	0.00	0.00	0.57	0.00	0.00	0.08	10.98	5.31	0.29	100.57	46%	52%	2%
NWA10299_plag03-3	57.39	0.06	26.68	0.00	0.00	0.90	0.00	0.00	0.05	8.67	5.99	1.21	100.95	52%	41%	7%
NWA10299_plag04-1	55.07	0.04	28.06	0.00	0.00	0.76	0.00	0.00	0.10	11.10	5.25	0.27	100.65	45%	53%	2%
NWA10299_plag04-2	55.79	0.03	27.81	0.00	0.00	0.60	0.00	0.02	0.07	10.42	5.36	0.60	100.70	47%	50%	3%
NWA10299_plag04-3	57.98	0.04	26.02	0.00	0.00	0.60	0.00	0.00	0.03	8.17	5.43	2.34	100.61	47%	39%	13%
NWA10299_plag05-1	56.93	0.05	27.16	0.00	0.00	0.71	0.00	0.00	0.05	9.59	5.80	0.49	100.78	51%	46%	3%
NWA10299_plag05-2	58.50	0.06	26.27	0.00	0.00	0.64	0.00	0.00	0.04	8.43	6.17	0.83	100.94	54%	41%	5%
NWA10299_plag05-3	58.46	0.06	25.95	0.00	0.00	1.16	0.00	0.02	0.05	7.64	6.15	1.10	100.59	55%	38%	7%
NWA11057_plag01-1	56.79	0.05	27.07	0.00	0.00	0.61	0.00	0.00	0.07	9.77	5.73	0.29	100.38	51%	48%	2%
NWA11057_plag01-2	57.46	0.06	26.78	0.00	0.00	0.56	0.00	0.00	0.07	9.20	5.96	0.36	100.45	53%	45%	2%
NWA11057_plag01-3	57.89	0.06	26.76	0.00	0.00	0.58	0.00	0.00	0.03	8.83	5.99	0.50	100.64	53%	44%	3%
NWA11057_plag02-1	55.57	0.04	27.88	0.00	0.00	0.53	0.00	0.00	0.08	10.48	5.40	0.18	100.16	48%	51%	1%
NWA11057_plag02-2	55.65	0.04	27.78	0.00	0.00	0.56	0.00	0.00	0.09	10.54	5.42	0.24	100.32	48%	51%	1%
NWA11057_plag02-3	58.36	0.05	26.70	0.00	0.00	0.63	0.00	0.00	0.03	8.34	6.18	0.70	100.99	55%	41%	4%
NWA11057_plag03-1	57.98	0.06	26.24	0.01	0.00	0.58	0.00	0.00	0.05	8.54	6.11	0.53	100.10	55%	42%	3%
NWA11057_plag03-2	58.17	0.06	26.37	0.00	0.00	0.55	0.02	0.02	0.05	8.41	6.13	0.51	100.29	55%	42%	3%
NWA11057_plag03-3	58.12	0.05	26.36	0.00	0.00	0.65	0.00	0.00	0.05	8.37	6.14	0.54	100.28	55%	42%	3%
NWA11057_plag04-1	58.30	0.06	26.39	0.00	0.00	0.57	0.00	0.00	0.04	8.51	6.23	0.43	100.53	56%	42%	2%
NWA11057_plag04-2	58.31	0.05	26.59	0.00	0.00	0.67	0.00	0.00	0.04	8.50	6.22	0.45	100.83	55%	42%	3%
NWA11057_plag04-3	58.33	0.06	26.60	0.00	0.00	0.66	0.00	0.00	0.04	8.35	6.23	0.49	100.76	56%	41%	3%
NWA11057_plag05-1	57.65	0.05	26.68	0.00	0.00	0.54	0.00	0.00	0.05	8.99	6.00	0.37	100.33	54%	44%	2%
NWA11057_plag05-2	57.90	0.06	26.69	0.00	0.00	0.57	0.00	0.00	0.06	8.78	6.11	0.42	100.59	54%	43%	2%
NWA11057_plag05-3	58.40	0.07	26.63	0.00	0.00	0.77	0.00	0.00	0.05	8.49	6.15	0.56	101.12	55%	42%	3%
NWA11073_plag01-1	54.36	0.03	28.09	0.00	0.00	0.47	0.00	0.02	0.10	11.04	5.10	0.14	99.35	45%	54%	1%
NWA11073_plag01-2	54.55	0.03	27.94	0.00	0.00	0.52	0.00	0.00	0.12	11.14	5.13	0.14	99.57	45%	54%	1%
NWA11073_plag01-3	53.50	0.03	28.28	0.00	0.00	0.58	0.00	0.02	0.09	11.57	4.81	0.23	99.11	42%	56%	1%
NWA11073_plag02-1	56.70	0.05	26.48	0.00	0.00	0.59	0.00	0.00	0.07	9.14	5.98	0.40	99.41	53%	45%	2%
NWA11073_plag02-2	56.68	0.05	26.49	0.00	0.00	0.61	0.00	0.00	0.05	9.27	5.91	0.39	99.45	52%	45%	2%
NWA11073_plag02-3	56.51	0.05	26.56	0.00	0.00	0.79	0.00	0.00	0.05	9.22	5.94	0.40	99.52	53%	45%	2%
NWA11073_plag03-1	54.32	0.03	28.31	0.00	0.00	0.55	0.00	0.00	0.09	11.15	5.06	0.24	99.75	44%	54%	1%
NWA11073_plag03-2	56.20	0.04	27.28	0.00	0.00	0.56	0.00	0.00	0.07	9.85	5.67	0.32	99.99	50%	48%	2%
NWA11073_plag03-3	57.70	0.05	26.55	0.00	0.00	0.66	0.02	0.02	0.04	8.50	6.23	0.46	100.23	55%	42%	3%

Table A1.2.(continued) EPMA analysis of former igneous plagioclase.

SAMPLE	SiO ₂	TiO ₂	Al ₂ O ₃	V ₂ O ₃	Cr ₂ O ₃	FeO	NiO	MnO	MgO	CaO	Na ₂ O	K ₂ O	TOTAL	%Ab	%An	%Or
NWA11073_plag04-1	56.16	0.05	27.32	0.00	0.00	0.52	0.00	0.00	0.07	9.96	5.66	0.28	100.02	50%	49%	2%
NWA11073_plag04-2	58.36	0.05	26.52	0.00	0.00	0.53	0.00	0.00	0.04	8.32	6.31	0.50	100.63	56%	41%	3%
NWA11073_plag04-3	58.37	0.05	26.53	0.00	0.00	0.69	0.00	0.02	0.04	8.33	6.34	0.57	100.94	56%	41%	3%
NWA11073_plag04-4	57.63	0.05	26.47	0.00	0.00	0.81	0.00	0.01	0.04	8.60	6.15	0.63	100.39	54%	42%	4%
NWA11073_plag05-1	54.17	0.04	28.26	0.00	0.00	0.48	0.00	0.00	0.10	11.20	4.99	0.16	99.40	44%	55%	1%
NWA11073_plag05-2	54.18	0.03	28.44	0.00	0.00	0.53	0.00	0.00	0.08	11.29	4.97	0.19	99.71	44%	55%	1%
NWA11073_plag05-3	55.08	0.04	27.79	0.00	0.00	0.73	0.00	0.00	0.05	10.64	5.25	0.26	99.84	46%	52%	2%
NWA11255_plag01-1	55.90	0.03	28.35	0.00	0.00	0.59	0.00	0.00	0.08	10.37	5.52	0.26	101.10	48%	50%	2%
NWA11255_plag01-2	58.05	0.05	27.01	0.00	0.00	0.57	0.00	0.00	0.05	8.86	6.20	0.43	101.22	54%	43%	2%
NWA11255_plag01-3	56.93	0.04	27.63	0.00	0.00	0.68	0.00	0.00	0.06	9.38	5.95	0.34	101.01	52%	46%	2%
NWA11255_plag02-1	53.78	0.03	29.00	0.00	0.00	0.49	0.02	0.00	0.12	11.64	4.89	0.13	100.10	43%	56%	1%
NWA11255_plag02-2	53.93	0.03	28.82	0.00	0.00	0.51	0.00	0.01	0.13	11.45	4.98	0.13	99.99	44%	56%	1%
NWA11255_plag02-3	53.57	0.03	28.97	0.00	0.00	0.60	0.00	0.00	0.10	11.58	4.86	0.20	99.91	43%	56%	1%
NWA11255_plag03-1	55.45	0.05	28.15	0.00	0.00	0.58	0.00	0.02	0.07	10.42	5.49	0.26	100.49	48%	50%	2%
NWA11255_plag03-2	55.19	0.04	28.32	0.00	0.00	0.54	0.00	0.02	0.07	10.65	5.38	0.24	100.45	47%	52%	1%
NWA11255_plag03-3	57.65	0.06	26.70	0.00	0.00	0.65	0.00	0.00	0.04	8.60	6.24	0.51	100.45	55%	42%	3%
NWA11255_plag04-1	53.92	0.03	28.56	0.00	0.00	0.46	0.00	0.02	0.12	11.10	5.05	0.12	99.38	45%	54%	1%
NWA11255_plag04-2	53.58	0.03	28.53	0.00	0.00	0.50	0.00	0.00	0.13	11.52	4.97	0.12	99.38	44%	56%	1%
NWA11255_plag04-3	52.58	0.03	29.02	0.00	0.00	0.64	0.00	0.00	0.08	11.91	4.67	0.14	99.07	41%	58%	1%
NWA11255_plag05-1	55.82	0.05	27.97	0.00	0.00	0.55	0.02	0.00	0.07	10.15	5.63	0.31	100.57	49%	49%	2%
NWA11255_plag05-2	56.08	0.04	27.79	0.00	0.00	0.53	0.00	0.00	0.07	9.98	5.69	0.33	100.51	50%	48%	2%
NWA11255_plag05-3	57.43	0.07	26.67	0.00	0.00	0.71	0.00	0.00	0.04	8.63	6.13	0.64	100.32	54%	42%	4%
AA-1(NWA12919)_plag001-1	53.55	0.03	28.26	0.00	0.00	0.57	0.00	0.02	0.07	11.94	4.80	0.24	99.48	42%	57%	1%
AA-1(NWA12919)_plag001-2	54.14	0.03	28.06	0.00	0.00	0.52	0.00	0.00	0.06	11.35	5.04	0.25	99.45	44%	55%	1%
AA-1(NWA12919)_plag001-3	54.39	0.04	28.00	0.00	0.00	0.53	0.02	0.00	0.07	11.32	5.11	0.20	99.68	44%	54%	1%
AA-1(NWA12919)_plag001-4	57.96	0.05	26.37	0.00	0.00	0.53	0.00	0.00	0.05	8.78	6.17	0.44	100.35	55%	43%	3%
AA-1(NWA12919)_plag001-5	58.62	0.05	26.25	0.01	0.00	0.58	0.00	0.00	0.04	8.24	6.31	0.64	100.74	56%	40%	4%
AA-1(NWA12919)_plag002-1	55.74	0.04	27.16	0.00	0.00	0.50	0.00	0.00	0.07	10.28	5.56	0.21	99.56	49%	50%	1%
AA-1(NWA12919)_plag002-2	55.87	0.04	27.18	0.00	0.00	0.54	0.00	0.00	0.08	10.42	5.54	0.23	99.90	48%	50%	1%
AA-1(NWA12919)_plag002-3	56.06	0.04	27.20	0.00	0.00	0.52	0.00	0.00	0.07	10.22	5.57	0.29	99.97	49%	49%	2%
AA-1(NWA12919)_plag002-4	56.45	0.04	27.05	0.00	0.00	0.55	0.00	0.00	0.07	9.98	5.70	0.34	100.18	50%	48%	2%
AA-1(NWA12919)_plag003-1	55.90	0.04	26.95	0.00	0.00	0.50	0.00	0.00	0.08	10.19	5.60	0.22	99.48	49%	50%	1%
AA-1(NWA12919)_plag003-2	56.39	0.04	26.95	0.00	0.00	0.50	0.00	0.00	0.07	9.94	5.69	0.25	99.83	50%	48%	1%
AA-1(NWA12919)_plag003-3	56.51	0.05	26.82	0.00	0.00	0.48	0.00	0.00	0.07	9.68	5.77	0.26	99.64	51%	47%	2%
AA-1(NWA12919)_plag003-4	56.80	0.05	26.93	0.00	0.00	0.51	0.00	0.00	0.07	9.80	5.82	0.28	100.26	51%	47%	2%
AA-1(NWA12919)_plag004-1	54.05	0.03	28.32	0.00	0.00	0.53	0.00	0.00	0.08	11.69	4.94	0.17	99.81	43%	56%	1%
AA-1(NWA12919)_plag004-2	54.87	0.03	27.72	0.00	0.00	0.52	0.00	0.00	0.09	10.98	5.28	0.19	99.68	46%	53%	1%
AA-1(NWA12919)_plag004-3	58.45	0.06	26.13	0.00	0.00	0.52	0.00	0.00	0.03	8.27	6.34	0.45	100.25	57%	41%	3%
AA-1(NWA12919)_plag005-1	57.71	0.06	26.53	0.00	0.00	0.54	0.00	0.00	0.06	8.96	6.16	0.48	100.50	54%	43%	3%

Table A1.2.(continued) EPMA analysis of former igneous plagioclase.

SAMPLE	SiO ₂	TiO ₂	Al ₂ O ₃	V ₂ O ₃	Cr ₂ O ₃	FeO	NiO	MnO	MgO	CaO	Na ₂ O	K ₂ O	TOTAL	%Ab	%An	%Or
AA-1(NWA12919)_plag006-1	58.50	0.04	26.61	0.01	0.00	0.55	0.00	0.00	0.02	8.58	6.23	0.56	101.10	55%	42%	3%
AA-1(NWA12919)_plag007-1	57.49	0.05	26.44	0.00	0.00	0.53	0.00	0.00	0.04	8.86	6.14	0.44	99.99	54%	43%	3%
AA-1(NWA12919)_plag008-1	54.57	0.04	28.05	0.00	0.00	0.51	0.00	0.02	0.09	11.41	5.08	0.20	99.97	44%	55%	1%
AA-1(NWA12919)_plag008-2	57.86	0.06	26.27	0.00	0.00	0.56	0.00	0.00	0.06	8.75	6.14	0.41	100.11	55%	43%	2%

Table A1.3. EPMA analysis of pyroxenes and olivine in three-phase symplectite. Reconstructed bulk composition is calculated assuming pure SiO₂ composition for the silica phase.

SAMPLE	SiO ₂	TiO ₂	Al ₂ O ₃	V ₂ O ₃	Cr ₂ O ₃	FeO	NiO	MnO	MgO	CaO	Na ₂ O	K ₂ O	TOTAL	Mode
JaH479-1_sym01px-1	47.22	0.62	0.81	0.01	0.00	31.35	0.00	0.88	3.32	15.65	0.15	0.01	100.02	37
JaH479-1_sym01px-2	47.88	0.79	0.91	0.00	0.00	29.99	0.00	0.80	3.42	16.64	0.15	0.00	100.58	
JaH479-1_sym01px-3	46.41	0.68	1.20	0.00	0.00	34.05	0.00	0.84	2.69	13.06	0.10	0.01	99.04	
JaH479-1_sym01px-4	46.80	0.90	0.51	0.00	0.00	35.15	0.00	0.98	1.63	13.88	0.12	0.01	99.98	
JaH479-1_sym01px-5	46.96	0.87	0.95	0.00	0.00	31.06	0.00	0.72	1.44	17.35	0.14	0.01	99.50	
JaH479-1_sym01px-6	47.13	0.89	0.68	0.00	0.00	32.38	0.00	0.80	1.18	17.00	0.13	0.00	100.19	
JaH479-1_sym01ol-1	29.47	0.11	0.10	0.00	0.00	66.63	0.00	1.44	1.48	0.29	0.00	0.00	99.52	36
JaH479-1_sym01ol-2	29.98	0.10	0.12	0.00	0.00	67.18	0.00	1.47	1.15	0.28	0.00	0.01	100.29	
JaH479-1_sym01ol-3	29.79	0.11	0.02	0.00	0.00	67.80	0.00	1.47	1.15	0.23	0.00	0.00	100.57	
JaH479-1_sym01ol-4	29.86	0.09	0.25	0.00	0.00	64.50	0.00	1.49	1.86	0.67	0.00	0.02	98.74	
JaH479-1_sym01ol-5	29.63	0.07	0.22	0.00	0.00	63.39	0.00	1.43	2.85	0.58	0.00	0.01	98.18	
JaH479-1_sym01ol-6	29.60	0.09	0.02	0.00	0.00	66.91	0.00	1.51	1.36	0.41	0.00	0.00	99.90	
JaH479-1_sym01bulk	55.11	0.33	0.36	0.00	0.00	35.75	0.00	0.84	1.43	5.92	0.05	0.00	99.79	
JaH479-1_sym02px-1	47.75	0.76	0.90	0.02	0.00	30.25	0.00	0.83	4.07	15.55	0.13	0.00	100.26	41
JaH479-1_sym02px-2	46.15	0.54	0.96	0.02	0.00	34.46	0.00	0.89	4.24	13.34	0.12	0.03	100.75	
JaH479-1_sym02px-3	47.34	0.72	1.11	0.01	0.00	28.73	0.00	0.74	4.21	15.70	0.15	0.02	98.73	
JaH479-1_sym02px-4	47.52	0.76	0.84	0.02	0.00	28.76	0.00	0.73	3.50	17.53	0.16	0.00	99.82	
JaH479-1_sym02px-5	46.34	0.66	0.93	0.01	0.00	31.68	0.00	0.78	3.59	15.58	0.11	0.01	99.69	
JaH479-1_sym02ol-1	35.35	0.15	0.57	0.00	0.00	61.40	0.00	1.27	2.53	1.14	0.08	0.06	102.55	27
JaH479-1_sym02ol-2	44.04	0.26	0.76	0.00	0.00	52.60	0.00	1.08	1.99	0.55	0.11	0.10	101.49	
JaH479-1_sym02ol-3	42.87	0.25	1.13	0.00	0.00	40.52	0.00	0.84	3.61	4.32	0.13	0.15	93.82	
JaH479-1_sym02ol-4	34.41	0.93	1.28	0.00	0.00	39.26	0.00	0.86	5.39	5.33	0.07	0.08	87.61	
JaH479-1_sym02ol-5	23.78	0.06	0.74	0.00	0.00	52.22	0.00	1.06	4.15	6.96	0.37	0.05	89.39	
JaH479-1_sym02bulk	62.00	0.34	0.57	0.01	0.00	28.01	0.00	0.64	2.22	6.60	0.08	0.03	100.48	
KG002_sym01px-1	47.50	0.64	0.91	0.00	0.00	29.80	0.00	0.87	2.23	16.48	0.14	0.03	98.60	37
KG002_sym01px-2	47.34	0.52	0.52	0.00	0.00	35.12	0.00	1.04	2.23	14.25	0.12	0.01	101.15	
KG002_sym01px-3	47.80	0.56	0.76	0.00	0.00	30.18	0.00	0.84	2.09	14.98	0.14	0.03	97.38	
KG002_sym01px-4	47.82	0.68	0.57	0.00	0.00	30.18	0.00	0.89	2.27	17.17	0.13	0.00	99.71	
KG002_sym01px-5	47.20	0.55	0.70	0.00	0.00	34.77	0.00	0.96	2.33	14.39	0.13	0.02	101.05	
KG002_sym01px-6	47.75	0.67	0.61	0.00	0.00	30.02	0.00	0.88	2.27	17.25	0.12	0.01	99.58	
KG002_sym01ol-1	31.10	0.07	0.04	0.00	0.00	64.35	0.00	1.71	1.80	0.42	0.00	0.00	99.49	37
KG002_sym01ol-2	33.36	0.09	0.11	0.00	0.00	63.27	0.00	1.61	1.65	0.54	0.00	0.00	100.63	
KG002_sym01ol-3	36.81	0.09	0.14	0.00	0.00	58.56	0.00	1.46	1.51	0.50	0.03	0.01	99.11	
KG002_sym01ol-4	37.91	0.14	0.52	0.00	0.00	55.34	0.00	1.35	1.63	1.67	0.05	0.04	98.65	
KG002_sym01ol-5	32.60	0.13	0.22	0.00	0.00	61.55	0.00	1.61	1.97	2.01	0.03	0.01	100.13	
KG002_sym01ol-6	34.51	0.08	0.16	0.00	0.00	63.27	0.00	1.66	1.79	0.41	0.03	0.00	101.91	

Table A1.3.(continued)

SAMPLE	SiO ₂	TiO ₂	Al ₂ O ₃	V ₂ O ₃	Cr ₂ O ₃	FeO	NiO	MnO	MgO	CaO	Na ₂ O	K ₂ O	TOTAL	Mode
KG002_sym01bulk	56.27	0.26	0.32	0.00	0.00	34.43	0.00	0.92	1.46	6.11	0.06	0.01	99.84	
KG002_sym02px-1	47.87	0.65	0.56	0.00	0.00	30.53	0.00	0.80	2.15	16.82	0.15	0.01	99.54	35
KG002_sym02px-2	45.95	0.53	1.11	0.00	0.00	32.74	0.00	0.77	2.22	14.97	0.13	0.06	98.48	
KG002_sym02px-3	48.03	0.68	0.58	0.00	0.00	29.53	0.00	0.72	2.44	17.46	0.14	0.00	99.58	
KG002_sym02px-4	48.61	0.63	0.65	0.00	0.00	29.77	0.00	0.70	2.14	16.39	0.13	0.02	99.04	
KG002_sym02px-5	47.72	0.66	0.58	0.00	0.00	29.84	0.00	0.70	2.16	17.66	0.14	0.00	99.46	
KG002_sym02px-6	47.90	0.64	0.65	0.00	0.00	30.03	0.00	0.74	2.07	17.36	0.12	0.01	99.52	
KG002_sym02ol-1	32.47	0.17	0.32	0.00	0.00	61.27	0.00	1.27	1.62	2.77	0.00	0.02	99.91	40
KG002_sym02ol-2	39.27	0.12	0.24	0.00	0.00	56.85	0.02	1.21	1.38	1.21	0.05	0.03	100.38	
KG002_sym02ol-3	33.55	0.14	0.18	0.00	0.00	60.20	0.00	1.29	1.68	2.11	0.02	0.01	99.18	
KG002_sym02ol-4	31.24	0.08	0.09	0.00	0.00	65.14	0.02	1.41	1.69	0.36	0.00	0.00	100.03	
KG002_sym02ol-5	40.06	0.08	0.33	0.00	0.00	54.50	0.00	1.16	1.41	0.46	0.04	0.04	98.08	
KG002_sym02ol-6	36.87	0.10	0.18	0.00	0.00	59.11	0.02	1.28	1.89	0.86	0.03	0.03	100.37	
KG002_sym02bulk	55.92	0.27	0.33	0.00	0.00	34.45	0.00	0.77	1.41	6.39	0.06	0.01	99.61	
NWA12262_sym01px-1	47.59	0.73	0.89	0.00	0.02	32.01	0.00	0.83	2.93	14.53	0.13	0.00	99.66	56
NWA12262_sym01px-2	48.13	0.78	0.94	0.01	0.00	31.01	0.00	0.80	3.07	14.69	0.14	0.01	99.58	
NWA12262_sym01px-3	47.62	0.69	0.87	0.00	0.00	33.86	0.00	0.90	2.94	12.36	0.09	0.01	99.34	
NWA12262_sym01px-4	48.25	0.67	0.81	0.01	0.00	33.54	0.00	0.94	3.08	12.91	0.11	0.00	100.32	
NWA12262_sym01px-5	47.74	0.73	0.78	0.00	0.00	33.71	0.00	0.86	1.32	14.34	0.13	0.01	99.62	
NWA12262_sym01px-6	47.27	0.72	0.81	0.00	0.00	34.97	0.00	0.87	2.03	12.19	0.11	0.00	98.97	
NWA12262_sym01px-7	46.38	0.74	0.98	0.00	0.00	34.61	0.00	0.87	1.18	14.70	0.13	0.02	99.61	
NWA12262_sym01ol-1	30.95	0.14	0.14	0.00	0.00	64.85	0.00	1.80	1.41	1.28	0.00	0.00	100.57	24
NWA12262_sym01ol-2	40.85	0.17	0.31	0.00	0.00	52.03	0.00	1.25	1.44	1.31	0.06	0.05	97.47	
NWA12262_sym01ol-3	31.26	0.29	0.42	0.00	0.00	63.77	0.00	1.44	2.00	0.80	0.06	0.07	100.11	
NWA12262_sym01bulk	54.88	0.45	0.56	0.00	0.00	33.15	0.00	0.84	1.71	7.93	0.08	0.01	99.62	
NWA12262_sym03px-1	45.88	0.71	0.87	0.00	0.00	34.35	0.00	0.77	2.13	14.42	0.13	0.01	99.27	49
NWA12262_sym03px-2	48.35	0.63	0.86	0.01	0.00	32.89	0.00	0.80	2.17	12.75	0.13	0.03	98.62	
NWA12262_sym03px-3	46.85	0.90	1.06	0.00	0.00	32.24	0.00	0.71	0.83	17.27	0.13	0.01	100.00	
NWA12262_sym03px-4	48.47	0.86	0.97	0.02	0.00	29.50	0.00	0.69	2.57	16.50	0.12	0.03	99.73	
NWA12262_sym03ol-1	42.51	0.48	0.33	0.00	0.00	55.01	0.02	1.42	1.84	0.65	0.04	0.05	102.35	26
NWA12262_sym03ol-2	34.64	0.09	0.11	0.00	0.02	62.62	0.00	1.52	2.00	0.35	0.04	0.01	101.40	
NWA12262_sym03ol-3	34.79	0.18	0.12	0.00	0.00	60.22	0.00	1.57	1.52	0.72	0.00	0.02	99.14	
NWA12262_sym03ol-4	36.95	0.25	0.35	0.00	0.00	54.17	0.00	1.47	1.04	3.66	0.05	0.02	97.96	
NWA12262_sym02bulk	57.33	0.39	0.47	0.00	0.00	31.77	0.00	0.77	1.58	7.27	0.07	0.02	99.68	

Table A1.4. EPMA analysis of titanomagnetite-ilmenite pairs. Data excluded from calculating f_{O_2} are denoted in red.

SAMPLE	SiO ₂	TiO ₂	Al ₂ O ₃	V ₂ O ₃	Cr ₂ O ₃	FeO(T)	NiO	MnO	MgO	CaO	Na ₂ O	K ₂ O	ZnO	ZrO ₂	TOTAL	NOTES
JaH479-1_tmex01-1	0.19	24.22	1.94	0.04	0.00	70.30	0.00	0.51	0.07	0.05	0.00	0.00	0.00	0.00	97.32	
JaH479-1_tmex01-2	0.11	24.58	1.76	0.03	0.03	70.33	0.00	0.48	0.05	0.02	0.00	0.00	0.00	0.00	97.39	
JaH479-1_tmex01-3	0.14	24.24	1.90	0.04	0.00	70.43	0.02	0.48	0.04	0.03	0.00	0.00	0.00	0.00	97.32	
JaH479-1_tmex01-4	0.15	25.69	1.75	0.02	0.00	69.27	0.00	0.48	0.05	0.01	0.00	0.00	0.00	0.00	97.42	
JaH479-1_tmex01-5	0.10	25.77	1.56	0.02	0.03	69.33	0.00	0.51	0.07	0.04	0.00	0.00	0.00	0.00	97.43	
JaH479-1_tmex01-6	0.10	17.45	2.32	0.11	0.02	76.78	0.00	0.42	0.04	0.00	0.00	0.00	0.00	97.24		
JaH479-1_ilm01-1	0.05	50.45	0.05	0.00	0.00	48.08	0.00	0.78	0.10	0.04	0.00	0.00	0.00	0.00	99.55	
JaH479-1_ilm01-2	0.06	50.21	0.05	0.00	0.03	48.37	0.00	0.78	0.08	0.08	0.00	0.00	0.00	0.00	99.66	
JaH479-1_ilm01-3	0.05	50.93	0.04	0.00	0.00	48.11	0.00	0.80	0.10	0.04	0.00	0.00	0.00	0.00	100.07	
JaH479-1_tmex02-1	0.10	25.60	1.76	0.12	0.03	69.27	0.00	0.49	0.07	0.03	0.00	0.00	0.00	0.00	97.47	
JaH479-1_tmex02-2	0.08	23.89	2.29	0.17	0.03	70.32	0.00	0.50	0.08	0.01	0.00	0.00	0.00	0.00	97.37	
JaH479-1_tmex02-3	0.09	25.88	1.91	0.11	0.00	68.75	0.00	0.51	0.08	0.00	0.00	0.00	0.00	0.00	97.33	
JaH479-1_tmex02-4	0.09	24.69	1.92	0.08	0.00	70.06	0.00	0.49	0.07	0.02	0.00	0.00	0.00	0.00	97.42	
JaH479-1_tmex02-5	0.08	27.28	1.73	0.03	0.02	67.97	0.00	0.52	0.07	0.02	0.00	0.00	0.00	0.00	97.72	
JaH479-1_tmex02-6	0.10	25.56	1.78	0.05	0.00	68.95	0.00	0.49	0.06	0.07	0.00	0.00	0.00	0.00	97.06	
JaH479-1_tmex02-7	0.13	28.32	1.59	0.04	0.00	65.69	0.00	0.55	0.10	0.09	0.00	0.00	0.00	0.00	96.51	
JaH479-1_tmex02-8	0.10	25.40	1.85	0.09	0.00	69.14	0.00	0.50	0.06	0.00	0.00	0.00	0.00	0.00	97.14	
JaH479-1_ilm02-1	0.08	50.75	0.04	0.00	0.00	48.24	0.00	0.79	0.12	0.02	0.00	0.00	0.00	0.00	100.04	
JaH479-1_ilm02-2	0.08	50.72	0.04	0.00	0.00	48.13	0.00	0.78	0.13	0.01	0.00	0.00	0.00	0.00	99.89	
JaH479-1_ilm02-3	0.06	50.73	0.02	0.00	0.00	47.96	0.00	0.83	0.12	0.03	0.00	0.00	0.00	0.00	99.75	
JaH479-1_ilm02-4	0.10	50.36	0.04	0.00	0.00	48.24	0.00	0.80	0.10	0.10	0.00	0.00	0.00	0.00	99.74	
															Tmt portion of exsolved tmt; 30% modal	
JaH 479 Int_1 Lt_1	0.12	11.11	2.67	0.39	0.06	80.94	0.00	0.34	0.08	0.02	0.17	0.00	95.90	proportion. Analysis by Nick Castle		
JaH 479 Int_1 Lt_2	0.13	14.45	2.50	0.34	0.06	78.15	0.01	0.39	0.08	0.03	0.07	0.00	96.20	Analysis by Nick Castle		
JaH 479 Int_1 Lt_3	0.12	9.80	2.70	0.42	0.06	81.01	0.00	0.33	0.05	0.08	0.11	0.00	94.67	Analysis by Nick Castle		
JaH 479 Int_1 Lt_4	0.11	13.67	2.65	0.35	0.07	78.71	0.00	0.38	0.07	0.03	0.05	0.01	96.09	Analysis by Nick Castle		
JaH 479 Int_1 Lt_5	0.11	13.31	2.73	0.36	0.06	79.09	0.00	0.38	0.06	0.03	0.19	0.00	96.31	Analysis by Nick Castle		
JaH 479 Int_1 Lt_6	0.13	13.92	2.75	0.38	0.06	77.87	0.00	0.38	0.07	0.05	0.15	0.05	95.80	Analysis by Nick Castle		
JaH 479 Int_1 Lt_7	0.10	9.61	2.94	0.43	0.06	81.18	0.00	0.35	0.05	0.07	0.12	0.02	94.94	Analysis by Nick Castle		
JaH 479 Int_1 Lt_8	0.11	10.20	3.00	0.45	0.08	80.39	0.00	0.38	0.02	0.09	0.13	0.00	94.84	Analysis by Nick Castle		
JaH 479 Int_1 Lt_9	0.10	10.34	3.00	0.44	0.07	80.64	0.00	0.34	0.06	0.02	0.06	0.00	95.06	Analysis by Nick Castle		
JaH 479 Int_1 Lt_10	0.13	10.51	2.53	0.40	0.07	80.60	0.01	0.34	0.07	0.03	0.05	0.04	94.78	Analysis by Nick Castle		
															Ilm portion of exsolved tmt; 70% modal	
JaH 479 Int_1 Dk_1	0.26	26.56	1.01	0.13	0.05	65.43	0.00	0.53	0.26	0.11	0.08	0.05	94.48	proportion. Analysis by Nick Castle		
JaH 479 Int_1 Dk_2	0.20	26.22	1.13	0.16	0.04	66.71	0.00	0.52	0.15	0.05	0.00	0.04	95.22	Analysis by Nick Castle		
JaH 479 Int_1 Dk_3	0.42	33.00	0.89	0.02	0.06	60.27	0.00	0.59	0.37	0.07	0.05	0.04	95.78	Analysis by Nick Castle		
JaH 479 Int_1 Dk_4	0.18	21.71	1.49	0.27	0.04	69.83	0.00	0.49	0.11	0.10	0.07	0.01	94.29	Analysis by Nick Castle		
JaH 479 Int_1 Dk_5	0.21	34.24	0.66	0.07	0.03	59.12	0.00	0.63	0.19	0.13	0.00	0.07	95.34	Analysis by Nick Castle		
JaH 479 Int_1 Dk_6	0.19	32.23	0.83	0.13	0.06	61.48	0.00	0.60	0.17	0.04	0.00	0.04	95.76	Analysis by Nick Castle		

Table A1.4.(continued) EPMA analysis of titanomagnetite-ilmenite pairs. Data excluded from calculating f_{O_2} are denoted in red.

SAMPLE	SiO ₂	TiO ₂	Al ₂ O ₃	V ₂ O ₃	Cr ₂ O ₃	FeO(T)	NiO	MnO	MgO	CaO	Na ₂ O	K ₂ O	ZnO	ZrO ₂	TOTAL	NOTES
JaH 479 Int_1 Dk_7	0.17	43.46	0.50	0.00	0.02	52.12	0.00	0.73	0.14	0.17			0.05	0.02	97.39	Analysis by Nick Castle
JaH 479 Int_1 Dk_8	0.44	42.93	0.54	0.00	0.02	52.41	0.00	0.67	0.41	0.15			0.00	0.09	97.66	Analysis by Nick Castle
JaH 479 Int_1 Dk_9	1.30	33.01	1.10	0.06	0.05	57.65	0.00	0.58	0.93	0.31			0.01	0.00	94.99	Analysis by Nick Castle Ilm inclusion within exsolved tmt. Analysis by
JaH 479 Int_1 Inc_1	0.15	50.44	0.04	0.00	0.01	47.05	0.00	0.79	0.19	0.05			0.00	0.03	98.75	Nick Castle
JaH 479 Int_1 Inc_2	0.10	51.30	0.04	0.00	0.02	46.69	0.00	0.80	0.16	0.06			0.00	0.08	99.25	Analysis by Nick Castle
JaH 479 Int_1 Inc_3	0.08	51.52	0.04	0.00	0.00	47.10	0.00	0.80	0.15	0.05			0.00	0.06	99.80	Analysis by Nick Castle
JaH 479 Int_1 Inc_4	0.26	51.06	0.15	0.00	0.02	47.02	0.00	0.81	0.23	0.08			0.00	0.00	99.63	Analysis by Nick Castle
JaH 479 Int_1 Inc_5	0.09	35.13	1.03	0.00	0.02	59.94	0.01	0.57	0.12	0.04			0.01	0.60	97.57	Analysis by Nick Castle
JaH 479 Int_1 Inc_6	0.23	50.26	0.09	0.00	0.01	47.23	0.01	0.77	0.30	0.04			0.00	0.02	98.96	Analysis by Nick Castle Exsolved tmt, same as Int_1 Lt and Int_1 Dk, but analyzed with a defocused beam.
JaH 479 Int 1 TMT_1	0.16	23.15	1.88	0.27	0.05	69.27	0.00	0.48	0.11	0.10			0.00	0.01	95.47	Analysis by Nick Castle
JaH 479 Int 1 TMT_2	0.22	24.77	1.67	0.25	0.05	67.93	0.00	0.50	0.15	0.08			0.04	0.01	95.66	Analysis by Nick Castle
JaH 479 Int 1 TMT_3	0.24	27.53	1.41	0.18	0.05	65.08	0.00	0.51	0.17	0.12			0.11	0.05	95.45	Analysis by Nick Castle
JaH 479 Int 1 TMT_4	0.12	25.16	1.82	0.26	0.08	67.52	0.00	0.52	0.10	0.06			0.14	0.06	95.82	Analysis by Nick Castle
JaH 479 Int 1 TMT_5	0.19	21.82	2.07	0.29	0.06	70.43	0.00	0.48	0.10	0.06			0.12	0.02	95.64	Analysis by Nick Castle
JaH 479 Int 1 Ilmn_1	1.94	45.87	0.57	0.00	0.00	44.73	0.01	0.78	0.53	0.21			0.00	0.11	94.73	Only one analysis. Analysis by Nick Castle
JaH 479 Int 2 TMT 1	0.35	24.29	1.66	0.26	0.05	67.38	0.01	0.49	0.25	0.12			0.17	0.01	95.04	Analysis by Nick Castle
JaH 479 Int 2 TMT 2	0.18	25.17	1.72	0.32	0.04	67.51	0.00	0.51	0.11	0.08			0.10	0.04	95.78	Analysis by Nick Castle
JaH 479 Int 2 TMT 3	0.23	25.58	1.77	0.31	0.03	66.87	0.00	0.52	0.16	0.06			0.02	0.03	95.58	Analysis by Nick Castle
JaH 479 Int 2 TMT 4	0.26	24.69	1.73	0.23	0.04	68.12	0.01	0.52	0.21	0.11			0.06	0.03	95.98	Analysis by Nick Castle
JaH 479 Int 2 TMT 5	0.20	25.78	1.56	0.21	0.02	67.14	0.00	0.51	0.15	0.09			0.01	0.01	95.66	Analysis by Nick Castle
JaH 479 Int 2 TMT_6	0.33	24.19	1.48	0.19	0.01	68.14	0.00	0.46	0.22	0.13			0.08	0.01	95.23	Analysis by Nick Castle
JaH 479 Int 2 Ilmn_1	0.14	49.79	0.05	0.00	0.01	47.11	0.00	0.79	0.18	0.02			0.02	0.08	98.18	Analysis by Nick Castle
JaH 479 Int 2 Ilmn_2	1.55	47.68	0.19	0.00	0.00	47.04	0.00	0.82	0.47	0.07			0.02	0.04	97.87	Analysis by Nick Castle
JaH 479 Int 2 Ilmn_3	0.69	48.18	0.16	0.00	0.01	46.61	0.00	0.77	0.61	0.09			0.00	0.07	97.19	Analysis by Nick Castle
JaH 479 Int 2 Ilmn_4	0.09	50.01	0.05	0.00	0.00	47.15	0.00	0.79	0.19	0.06			0.02	0.12	98.50	Analysis by Nick Castle
JaH 479 Int 2 Ilmn_5	0.12	49.65	0.05	0.00	0.00	47.23	0.00	0.77	0.19	0.07			0.00	0.11	98.18	Analysis by Nick Castle
JaH 479 Int 4 Ilmn 1	8.92	35.38	0.16	0.00	0.00	52.38	0.01	1.06	0.73	0.08			0.00	0.08	98.79	Analysis by Nick Castle
JaH 479 Int 4 Ilmn 2	0.10	49.74	0.03	0.00	0.00	47.39	0.00	0.81	0.17	0.03			0.01	0.13	98.42	Analysis by Nick Castle
JaH 479 Int 4 TMT 1	0.17	25.45	1.57	0.11	0.02	67.81	0.00	0.52	0.12	0.04			0.06	0.00	95.87	Analysis by Nick Castle
JaH 479 Int 4 TMT 2	0.18	25.13	1.64	0.14	0.03	68.06	0.00	0.52	0.12	0.05			0.12	0.01	95.99	Analysis by Nick Castle
JaH 479 Int 4 TMT 3	0.19	21.79	1.79	0.20	0.04	70.42	0.01	0.48	0.12	0.14			0.10	0.01	95.29	Analysis by Nick Castle
JaH 479 Int 4 TMT 4	0.28	22.69	1.58	0.10	0.01	69.53	0.00	0.48	0.11	0.27			0.04	0.00	95.09	Analysis by Nick Castle
JaH 479 Int 4 TMT 5	0.15	26.48	1.65	0.12	0.01	66.94	0.01	0.56	0.10	0.06			0.03	0.06	96.16	Analysis by Nick Castle
JaH 479 Int 4 TMT 6	0.11	12.12	2.42	0.20	0.02	79.56	0.01	0.38	0.07	0.02			0.10	0.01	95.00	Analysis by Nick Castle
KG002_tm01-1	0.09	23.15	1.81	0.02	0.04	72.41	0.00	0.56	0.15	0.03	0.00	0.00			98.26	
KG002_tm01-2	0.12	23.31	1.77	0.01	0.03	72.37	0.00	0.56	0.15	0.04	0.00	0.00			98.36	

Table A1.4.(continued) EPMA analysis of titanomagnetite-ilmenite pairs. Data excluded from calculating f_{O_2} are denoted in red.

SAMPLE	SiO ₂	TiO ₂	Al ₂ O ₃	V ₂ O ₃	Cr ₂ O ₃	FeO(T)	NiO	MnO	MgO	CaO	Na ₂ O	K ₂ O	ZnO	ZrO ₂	TOTAL	NOTES
KG002_tm01-3	0.09	24.63	1.58	0.00	0.03	71.65	0.00	0.61	0.14	0.03	0.00	0.00	0.00	0.00	98.76	
KG002_ilm01-1	0.12	50.08	0.09	0.00	0.00	47.28	0.00	0.62	0.26	0.22	0.00	0.01	0.00	0.00	98.68	
KG002_ilm01-2	0.13	50.27	0.05	0.00	0.00	47.66	0.00	0.67	0.27	0.08	0.00	0.00	0.00	0.00	99.13	
KG002_ilm01-3	0.08	50.35	0.04	0.00	0.00	47.59	0.00	0.66	0.27	0.10	0.00	0.00	0.00	0.00	99.09	
KG002_tm02-1	0.06	23.04	1.80	0.02	0.00	72.45	0.00	0.67	0.08	0.06	0.00	0.00	0.00	0.00	98.18	
KG002_tm02-2	0.07	23.45	1.78	0.00	0.03	72.42	0.00	0.67	0.09	0.00	0.00	0.00	0.00	0.00	98.51	
KG002_tm02-3	0.07	23.70	1.70	0.00	0.02	71.86	0.00	0.65	0.07	0.08	0.00	0.00	0.00	0.00	98.15	
KG002_ilm02a-1	0.04	50.01	0.06	0.00	0.00	47.45	0.00	0.91	0.14	0.57	0.00	0.00	0.00	0.00	99.18	A and b denote different grains of ilm inclusion within the same exsolved tmt grain
KG002_ilm02a-2	0.15	49.99	0.10	0.00	0.00	47.36	0.00	0.91	0.13	0.44	0.00	0.00	0.00	0.00	99.08	
KG002_ilm02a-3	0.02	50.36	0.05	0.00	0.00	47.49	0.00	0.85	0.13	0.32	0.00	0.00	0.00	0.00	99.22	
KG002_ilm02b-1	1.54	47.17	0.56	0.00	0.00	45.19	0.00	0.73	0.12	0.28	0.00	0.04	0.00	0.00	95.63	
KG002_ilm02b-2	0.51	49.39	0.28	0.00	0.00	47.49	0.00	0.80	0.13	0.09	0.00	0.01	0.00	0.00	98.70	
KG002_ilm02b-3	0.42	49.46	0.20	0.00	0.00	47.87	0.00	0.86	0.16	0.08	0.00	0.01	0.00	0.00	99.06	
KG002_tm03-1	0.07	24.25	1.77	0.48	0.04	71.30	0.00	0.57	0.17	0.02	0.00	0.00	0.00	0.00	98.67	
KG002_tm03-2	0.07	23.61	1.96	0.56	0.04	71.68	0.00	0.59	0.16	0.02	0.00	0.00	0.00	0.00	98.69	
KG002_tm03-3	0.06	22.32	2.23	0.68	0.10	72.41	0.00	0.59	0.15	0.02	0.00	0.00	0.00	0.00	98.56	
KG002_ilm03-1	0.03	50.66	0.06	0.00	0.00	47.80	0.00	0.69	0.26	0.04	0.00	0.00	0.00	0.00	99.54	
KG002_ilm03-2	0.00	50.89	0.04	0.00	0.00	47.88	0.00	0.69	0.28	0.03	0.00	0.00	0.00	0.00	99.81	
KG002_ilm03-3	0.02	50.94	0.05	0.00	0.00	47.76	0.00	0.69	0.30	0.04	0.00	0.00	0.00	0.00	99.80	
KG002_tm04-1	0.08	22.82	1.67	0.00	0.00	72.64	0.00	0.57	0.07	0.00	0.00	0.00	0.00	0.00	97.85	
KG002_tm04-2	0.06	23.16	1.68	0.00	0.00	72.41	0.00	0.61	0.07	0.00	0.00	0.00	0.00	0.00	97.99	
KG002_tm04-3	0.06	23.11	1.71	0.00	0.00	72.39	0.00	0.61	0.06	0.03	0.00	0.00	0.00	0.00	97.97	
KG002_ilm04-1	0.00	50.02	0.05	0.00	0.00	47.96	0.00	0.73	0.11	0.01	0.00	0.00	0.00	0.00	98.88	
KG002_ilm04-2	0.04	50.26	0.05	0.00	0.00	48.06	0.00	0.68	0.12	0.00	0.00	0.00	0.00	0.00	99.21	
KG002_ilm04-3	0.02	50.37	0.04	0.00	0.00	47.77	0.03	0.71	0.13	0.02	0.00	0.00	0.00	0.00	99.09	
KG002_tm05-1	0.07	22.45	1.88	0.19	0.05	71.96	0.00	0.55	0.16	0.16	0.00	0.00	0.00	0.00	97.47	
KG002_tm05-2	0.07	22.71	1.90	0.19	0.03	71.91	0.00	0.56	0.16	0.11	0.00	0.00	0.00	0.00	97.64	
KG002_tm05-3	0.08	23.01	1.90	0.20	0.06	71.86	0.00	0.54	0.15	0.10	0.00	0.00	0.00	0.00	97.90	
KG002_ilm05-1	0.12	48.69	0.15	0.00	0.00	47.40	0.00	0.61	0.26	0.38	0.00	0.00	0.00	0.00	97.61	
KG002_ilm05-2	0.04	49.35	0.04	0.00	0.00	47.68	0.00	0.65	0.24	0.19	0.00	0.00	0.00	0.00	98.19	
KG002_ilm05-3	0.04	49.27	0.05	0.00	0.00	47.64	0.00	0.63	0.25	0.20	0.00	0.00	0.00	0.00	98.08	
NWA10299_tm01-1	0.07	25.14	1.82	0.52	1.53	69.81	0.00	0.55	0.40	0.00	0.00	0.00	0.00	0.00	99.84	
NWA10299_tm01-2	0.08	25.33	1.80	0.56	1.52	69.75	0.00	0.56	0.39	0.00	0.00	0.00	0.00	0.00	99.99	
NWA10299_tm01-3	0.08	25.00	2.00	0.66	1.10	70.17	0.02	0.54	0.35	0.00	0.00	0.00	0.00	0.00	99.92	
NWA10299_ilm01-1	0.02	52.05	0.03	0.00	0.04	47.52	0.00	0.59	0.55	0.00	0.00	0.00	0.00	0.00	100.80	
NWA10299_ilm01-2	0.04	51.91	0.04	0.00	0.07	47.45	0.00	0.60	0.54	0.01	0.00	0.00	0.00	0.00	100.66	
NWA10299_ilm01-3	0.03	51.74	0.04	0.00	0.10	47.22	0.00	0.62	0.57	0.00	0.00	0.00	0.00	0.00	100.32	
NWA10299_tm02-1	0.06	25.31	1.71	0.64	1.33	69.21	0.00	0.54	0.42	0.03	0.00	0.00	0.00	0.00	99.25	

Table A1.4.(continued) EPMA analysis of titanomagnetite-ilmenite pairs. Data excluded from calculating f_{O_2} are denoted in red.

SAMPLE	SiO ₂	TiO ₂	Al ₂ O ₃	V ₂ O ₃	Cr ₂ O ₃	FeO(T)	NiO	MnO	MgO	CaO	Na ₂ O	K ₂ O	ZnO	ZrO ₂	TOTAL	NOTES
NWA10299_tm02-2	0.07	24.95	1.81	0.72	1.68	69.14	0.00	0.52	0.41	0.05	0.00	0.00			99.35	
NWA10299_tm02-3	0.08	23.72	2.02	0.76	1.72	69.72	0.00	0.49	0.42	0.06	0.00	0.00			98.99	
NWA10299_ilm02-1	0.00	51.36	0.06	0.00	0.11	47.24	0.00	0.62	0.65	0.03	0.00	0.00			100.07	
NWA10299_ilm02-2	0.02	51.75	0.05	0.00	0.11	47.07	0.00	0.61	0.66	0.02	0.00	0.00			100.29	
NWA10299_ilm02-3	0.03	51.55	0.04	0.00	0.12	47.06	0.00	0.62	0.68	0.04	0.00	0.00			100.14	
NWA10299_tm03-1	0.08	25.00	1.75	0.40	1.27	69.73	0.00	0.55	0.43	0.02	0.00	0.00			99.23	
NWA10299_tm03-2	0.07	24.94	1.74	0.40	1.27	69.62	0.00	0.55	0.45	0.04	0.00	0.00			99.08	
NWA10299_tm03-3	0.11	23.05	2.18	0.52	1.98	69.66	0.00	0.52	0.43	0.09	0.00	0.00			98.54	
NWA10299_ilm03-1	0.15	50.05	0.08	0.00	0.15	47.30	0.00	0.64	0.78	0.14	0.00	0.00			99.29	
NWA10299_ilm03-2	0.09	50.57	0.04	0.00	0.09	47.23	0.00	0.65	0.75	0.19	0.00	0.00			99.61	
NWA10299_ilm03-3	0.08	50.55	0.04	0.00	0.13	47.36	0.00	0.61	0.75	0.17	0.00	0.00			99.69	
NWA10299_tm04-1	0.05	25.86	1.63	0.56	2.03	68.38	0.00	0.58	0.48	0.05	0.00	0.00			99.62	
NWA10299_tm04-2	0.09	25.83	1.71	0.59	2.04	68.49	0.00	0.56	0.48	0.00	0.00	0.00			99.79	
NWA10299_tm04-3	0.06	25.40	1.73	0.61	2.03	68.61	0.00	0.59	0.50	0.02	0.00	0.00			99.55	
NWA10299_ilm04-1	0.14	47.57	0.20	0.01	0.83	49.23	0.00	0.61	0.76	0.04	0.00	0.00			99.39	
NWA10299_ilm04-2	0.33	48.75	0.10	0.00	0.25	46.68	0.07	0.63	0.93	0.08	0.04	0.00			97.86	
NWA10299_ilm04-3	0.05	48.44	0.15	0.00	0.89	48.52	0.00	0.64	0.74	0.10	0.00	0.00			99.53	
NWA10299_ilm04-4	0.20	49.67	0.07	0.00	0.25	47.08	0.02	0.62	0.88	0.10	0.00	0.00			98.89	
NWA10299_tm06-1	0.10	25.36	1.95	0.56	1.10	69.52	0.02	0.56	0.43	0.03	0.00	0.00			99.63	
NWA10299_tm06-2	0.07	25.38	1.73	0.52	0.88	69.78	0.00	0.56	0.42	0.04	0.00	0.00			99.38	
NWA10299_tm06-3	0.07	25.49	1.64	0.47	0.77	69.84	0.00	0.58	0.42	0.04	0.00	0.00			99.32	
NWA10299_ilm06-1	0.06	51.24	0.05	0.00	0.09	47.31	0.00	0.65	0.68	0.08	0.00	0.00			100.16	
NWA10299_ilm06-2	0.00	51.28	0.04	0.00	0.08	47.00	0.00	0.65	0.70	0.15	0.00	0.00			99.90	
NWA10299_ilm06-3	0.03	51.10	0.03	0.00	0.10	47.16	0.00	0.64	0.68	0.39	0.00	0.00			100.13	
NWA10299_tm07-1	0.08	24.36	1.78	0.40	0.48	71.21	0.00	0.53	0.42	0.03	0.00	0.00			99.29	
NWA10299_tm07-2	0.08	24.85	1.71	0.40	0.50	70.67	0.00	0.55	0.45	0.03	0.00	0.00			99.24	
NWA10299_tm07-3	0.06	23.59	1.94	0.47	0.53	71.48	0.00	0.54	0.42	0.03	0.00	0.00			99.06	
NWA10299_ilm07-1	0.06	50.24	0.09	0.00	0.15	48.41	0.00	0.63	0.66	0.00	0.00	0.00			100.24	
NWA10299_ilm07-2	0.06	50.56	0.08	0.00	0.10	48.34	0.00	0.64	0.67	0.02	0.00	0.00			100.47	
NWA10299_ilm07-3	0.02	50.59	0.08	0.00	0.08	48.11	0.00	0.67	0.68	0.00	0.00	0.00			100.23	
NWA11057_tm01-1	0.06	24.57	2.48	0.29	0.46	70.08	0.00	0.54	0.46	0.05	0.00	0.00			98.99	
NWA11057_tm01-2	0.07	24.88	2.35	0.26	0.45	70.21	0.02	0.56	0.47	0.00	0.00	0.00			99.27	
NWA11057_tm01-3	0.04	23.08	2.58	0.30	0.43	71.25	0.00	0.50	0.44	0.07	0.00	0.00			98.69	
NWA11057_ilm01-1	0.00	51.12	0.05	0.00	0.08	47.37	0.00	0.57	0.76	0.03	0.00	0.00			99.98	
NWA11057_ilm01-2	0.17	50.91	0.14	0.00	0.08	46.95	0.00	0.61	0.76	0.03	0.00	0.01			99.66	
NWA11057_ilm01-3	0.02	51.31	0.06	0.00	0.08	46.98	0.00	0.61	0.74	0.02	0.00	0.00			99.82	
NWA11057_tm02-1	0.06	22.01	2.27	0.46	1.25	70.54	0.00	0.50	0.45	0.31	0.00	0.00			97.85	
NWA11057_tm02-2	0.07	23.52	1.99	0.41	1.12	69.81	0.00	0.53	0.45	0.09	0.00	0.00			97.99	
NWA11057_tm02-3	0.06	23.83	1.89	0.39	0.83	69.83	0.00	0.51	0.46	0.07	0.00	0.00			97.87	

Table A1.4.(continued) EPMA analysis of titanomagnetite-ilmenite pairs. Data excluded from calculating f_{O_2} are denoted in red.

SAMPLE	SiO ₂	TiO ₂	Al ₂ O ₃	V ₂ O ₃	Cr ₂ O ₃	FeO(T)	NiO	MnO	MgO	CaO	Na ₂ O	K ₂ O	ZnO	ZrO ₂	TOTAL	NOTES
NWA11057_ilm02-1	0.00	50.80	0.05	0.00	0.06	47.03	0.00	0.57	0.73	0.08	0.00	0.00	0.00	0.00	99.32	
NWA11057_ilm02-2	0.00	50.67	0.05	0.00	0.08	46.99	0.00	0.59	0.71	0.11	0.00	0.00	0.00	0.00	99.20	
NWA11057_ilm02-3	0.17	50.94	0.06	0.00	0.08	46.94	0.00	0.58	0.75	0.10	0.00	0.00	0.00	0.00	99.62	
NWA11057_tm03-1	0.07	24.19	2.08	0.51	1.34	69.96	0.00	0.50	0.49	0.00	0.00	0.00	0.00	0.00	99.14	
NWA11057_tm03-2	0.08	24.16	2.09	0.52	1.16	70.13	0.02	0.53	0.45	0.00	0.00	0.00	0.00	0.00	99.14	
NWA11057_tm03-3	0.08	24.79	1.94	0.44	0.92	69.74	0.00	0.54	0.47	0.02	0.00	0.00	0.00	0.00	98.94	
NWA11057_tm03-4	0.07	25.21	1.73	0.37	0.83	69.48	0.00	0.57	0.46	0.07	0.00	0.00	0.00	0.00	98.79	
NWA11057_ilm03-1	0.02	51.28	0.05	0.00	0.11	47.09	0.00	0.60	0.77	0.03	0.00	0.00	0.00	0.00	99.95	
NWA11057_ilm03-2	0.04	51.32	0.05	0.00	0.12	47.20	0.00	0.58	0.78	0.00	0.00	0.00	0.00	0.00	100.09	
NWA11057_ilm03-3	0.04	50.93	0.06	0.00	0.10	47.03	0.00	0.58	0.79	0.06	0.00	0.00	0.00	0.00	99.59	
NWA11057_tm04-1	0.07	23.58	2.01	0.67	1.21	69.51	0.02	0.52	0.60	0.05	0.00	0.00	0.00	0.00	98.24	
NWA11057_tm04-2	0.06	23.63	2.18	0.71	1.53	69.19	0.00	0.54	0.59	0.08	0.00	0.00	0.00	0.00	98.51	
NWA11057_tm04-3	0.06	24.26	1.93	0.62	1.37	68.72	0.02	0.54	0.60	0.08	0.00	0.01	0.00	0.00	98.21	
NWA11057_ilm04-1	0.06	51.23	0.05	0.00	0.15	46.48	0.00	0.58	1.00	0.07	0.00	0.00	0.00	0.00	99.62	
NWA11057_ilm04-2	0.03	51.35	0.05	0.00	0.10	46.46	0.00	0.54	1.02	0.08	0.00	0.00	0.00	0.00	99.63	
NWA11057_ilm04-3	0.02	51.29	0.04	0.00	0.08	46.13	0.00	0.57	1.02	0.17	0.00	0.00	0.00	0.00	99.32	
NWA11057_tm05-1	0.06	24.67	2.02	0.65	1.42	69.10	0.02	0.53	0.63	0.00	0.00	0.00	0.00	0.00	99.10	
NWA11057_tm05-2	0.05	24.75	1.92	0.62	1.44	68.91	0.00	0.54	0.61	0.04	0.00	0.00	0.00	0.00	98.88	
NWA11057_tm05-3	0.05	24.28	2.15	0.68	1.55	68.87	0.00	0.53	0.61	0.11	0.00	0.00	0.00	0.00	98.83	
NWA11057_ilm05-1	0.03	51.14	0.05	0.00	0.07	46.61	0.00	0.58	1.00	0.23	0.00	0.00	0.00	0.00	99.71	
NWA11057_ilm05-2	0.03	50.93	0.04	0.00	0.07	46.49	0.00	0.59	1.01	0.40	0.00	0.00	0.00	0.00	99.56	
NWA11057_ilm05-3	0.05	51.21	0.05	0.00	0.07	46.71	0.00	0.57	0.98	0.13	0.00	0.01	0.00	0.00	99.78	
NWA11057_ilm05-4	0.03	51.30	0.04	0.00	0.07	46.21	0.00	0.59	0.99	0.15	0.00	0.01	0.00	0.00	99.39	
NWA11057_tm06-1	0.08	22.86	1.98	0.49	0.88	70.74	0.00	0.52	0.50	0.05	0.00	0.00	0.00	0.00	98.10	
NWA11057_tm06-2	0.06	23.41	1.77	0.45	0.55	70.98	0.00	0.54	0.54	0.08	0.00	0.00	0.00	0.00	98.38	
NWA11057_tm06-3	0.06	22.99	1.67	0.42	0.65	70.64	0.00	0.58	0.52	0.09	0.00	0.00	0.00	0.00	97.62	
NWA11057_ilm06-1	0.03	50.75	0.04	0.03	0.05	46.54	0.00	0.61	0.88	0.17	0.00	0.00	0.00	0.00	99.10	
NWA11057_ilm06-2	0.00	50.77	0.04	0.03	0.05	46.34	0.00	0.65	0.87	0.12	0.00	0.00	0.00	0.00	98.87	
NWA11057_ilm06-3	0.00	50.69	0.04	0.03	0.04	46.55	0.00	0.63	0.88	0.17	0.00	0.00	0.00	0.00	99.03	
NWA11057_tm07-1	0.07	22.30	2.06	0.26	0.46	71.46	0.02	0.49	0.33	0.23	0.00	0.00	0.00	0.00	97.68	
NWA11057_tm07-2	0.07	22.78	1.93	0.23	0.37	71.50	0.00	0.51	0.34	0.10	0.00	0.00	0.00	0.00	97.83	
NWA11057_tm07-3	0.09	22.47	1.93	0.24	0.38	71.19	0.00	0.53	0.35	0.19	0.00	0.00	0.00	0.00	97.37	
NWA11057_ilm07-1	0.00	50.17	0.06	0.00	0.06	47.15	0.00	0.54	0.56	0.25	0.00	0.00	0.00	0.00	98.79	
NWA11057_ilm07-2	0.03	50.07	0.06	0.00	0.03	47.09	0.00	0.59	0.58	0.22	0.00	0.00	0.00	0.00	98.67	
NWA11057_ilm07-3	0.02	50.40	0.05	0.00	0.04	47.20	0.00	0.60	0.58	0.11	0.00	0.00	0.00	0.00	99.00	
NWA11073_tm01-1	0.07	22.85	1.86	0.38	0.48	71.39	0.00	0.50	0.55	0.02	0.00	0.00	0.00	0.00	98.10	
NWA11073_tm01-2	0.08	23.07	1.78	0.36	0.43	71.09	0.02	0.52	0.57	0.02	0.00	0.00	0.00	0.00	97.94	
NWA11073_tm01-3	0.08	22.70	1.89	0.35	0.49	71.41	0.02	0.50	0.55	0.02	0.00	0.00	0.00	0.00	98.01	
NWA11073_ilm01-1	0.03	51.11	0.06	0.00	0.05	46.75	0.00	0.59	0.95	0.05	0.00	0.00	0.00	0.00	99.59	

Table A1.4.(continued) EPMA analysis of titanomagnetite-ilmenite pairs. Data excluded from calculating f_{O_2} are denoted in red.

SAMPLE	SiO ₂	TiO ₂	Al ₂ O ₃	V ₂ O ₃	Cr ₂ O ₃	FeO(T)	NiO	MnO	MgO	CaO	Na ₂ O	K ₂ O	ZnO	ZrO ₂	TOTAL	NOTES
NWA11073_ilm01-2	0.00	50.99	0.04	0.00	0.06	47.09	0.00	0.59	0.92	0.06	0.00	0.00	0.00	0.00	99.75	
NWA11073_ilm01-3	0.00	50.83	0.05	0.00	0.09	46.91	0.00	0.58	0.91	0.07	0.00	0.00	0.00	0.00	99.44	
NWA11073_tm02-1	0.07	21.53	1.93	0.23	0.37	72.55	0.00	0.52	0.32	0.08	0.00	0.00	0.00	0.00	97.60	
NWA11073_tm02-2	0.10	21.86	1.97	0.27	0.39	72.23	0.00	0.51	0.35	0.10	0.00	0.00	0.00	0.00	97.78	
NWA11073_tm02-3	0.10	24.43	1.38	0.15	0.27	70.60	0.00	0.58	0.35	0.25	0.00	0.00	0.00	0.00	98.11	
NWA11073_ilm02-1	0.02	50.22	0.04	0.00	0.00	47.23	0.00	0.60	0.64	0.09	0.00	0.00	0.00	0.00	98.84	
NWA11073_ilm02-2	0.09	49.57	0.04	0.00	0.00	46.97	0.00	0.58	0.66	0.15	0.00	0.00	0.00	0.00	98.06	
NWA11073_ilm02-3	0.55	47.85	0.21	0.00	0.05	45.29	0.00	0.59	0.65	0.23	0.00	0.03	0.00	0.00	95.45	
NWA11073_tm03-1	0.08	18.07	2.71	0.59	1.08	73.42	0.00	0.47	0.40	0.11	0.00	0.00	0.00	0.00	96.93	
NWA11073_tm03-2	0.10	19.47	2.55	0.62	0.90	72.30	0.00	0.51	0.41	0.12	0.00	0.00	0.00	0.00	96.98	
NWA11073_tm03-3	0.08	20.15	2.33	0.51	0.81	72.80	0.00	0.50	0.42	0.09	0.00	0.00	0.00	0.00	97.69	
NWA11073_ilm03-1	0.33	49.55	0.11	0.00	0.05	46.26	0.00	0.59	0.83	0.11	0.00	0.01	0.00	0.00	97.84	
NWA11073_ilm03-2	0.24	50.23	0.07	0.00	0.07	46.82	0.00	0.61	0.80	0.13	0.00	0.00	0.00	0.00	98.97	
NWA11073_ilm03-3	0.22	49.61	0.10	0.00	0.05	46.53	0.00	0.63	0.87	0.13	0.00	0.01	0.00	0.00	98.15	
NWA11073_tm04-1	0.06	23.54	2.18	0.40	0.67	70.73	0.00	0.52	0.37	0.07	0.00	0.00	0.00	0.00	98.54	
NWA11073_tm04-2	0.06	23.15	2.13	0.40	0.56	71.26	0.00	0.51	0.35	0.00	0.00	0.00	0.00	0.00	98.42	
NWA11073_tm04-3	0.07	22.21	2.09	0.37	0.45	71.82	0.00	0.51	0.29	0.31	0.00	0.00	0.00	0.00	98.12	
NWA11073_ilm04-1	0.04	50.79	0.04	0.00	0.07	47.24	0.00	0.57	0.63	0.06	0.00	0.00	0.00	0.00	99.44	
NWA11073_ilm04-2	0.04	50.79	0.05	0.00	0.10	47.21	0.00	0.57	0.62	0.04	0.00	0.00	0.00	0.00	99.42	
NWA11073_ilm04-3	0.02	51.03	0.04	0.00	0.09	47.00	0.00	0.57	0.61	0.00	0.00	0.00	0.00	0.00	99.36	
NWA11073_tm05-1	0.06	23.82	2.10	0.52	0.65	70.19	0.00	0.56	0.36	0.05	0.00	0.00	0.00	0.00	98.31	
NWA11073_tm05-2	0.06	23.81	2.05	0.53	0.72	69.70	0.00	0.53	0.39	0.12	0.00	0.00	0.00	0.00	97.91	
NWA11073_tm05-3	0.08	24.49	1.89	0.43	0.61	69.79	0.00	0.55	0.42	0.07	0.00	0.00	0.00	0.00	98.33	
NWA11073_ilm05-1	0.02	51.15	0.03	0.00	0.11	46.77	0.00	0.64	0.67	0.02	0.00	0.00	0.00	0.00	99.41	
NWA11073_ilm05-2	0.03	51.03	0.04	0.00	0.10	46.90	0.00	0.59	0.67	0.07	0.00	0.00	0.00	0.00	99.43	
NWA11073_ilm05-3	0.00	51.06	0.04	0.00	0.10	47.04	0.00	0.59	0.69	0.06	0.00	0.00	0.00	0.00	99.58	
NWA11073_tm06-1	0.06	22.43	2.37	0.66	0.67	70.86	0.00	0.51	0.30	0.24	0.00	0.00	0.00	0.00	98.10	
NWA11073_tm06-2	0.06	22.56	2.50	0.67	0.61	70.84	0.00	0.50	0.29	0.07	0.00	0.00	0.00	0.00	98.10	
NWA11073_tm06-3	0.07	22.33	2.57	0.72	0.89	70.22	0.00	0.52	0.28	0.36	0.00	0.00	0.00	0.00	97.96	
NWA11073_ilm06-1	0.02	51.03	0.05	0.00	0.07	47.45	0.00	0.57	0.52	0.06	0.00	0.00	0.00	0.00	99.77	
NWA11073_ilm06-2	0.05	50.62	0.06	0.00	0.07	47.08	0.00	0.59	0.51	0.12	0.00	0.00	0.00	0.00	99.10	
NWA11073_ilm06-3	0.03	50.77	0.05	0.00	0.07	47.06	0.00	0.62	0.45	0.22	0.00	0.00	0.00	0.00	99.27	
NWA11073_tm07-1	0.07	24.24	2.06	0.61	0.82	69.88	0.00	0.51	0.46	0.01	0.00	0.00	0.00	0.00	98.66	
NWA11073_tm07-2	0.06	23.20	2.41	0.74	0.81	70.48	0.00	0.51	0.43	0.00	0.00	0.00	0.00	0.00	98.64	
NWA11073_tm07-3	0.08	22.83	2.46	0.66	0.97	70.45	0.00	0.49	0.41	0.06	0.00	0.00	0.00	0.00	98.41	
NWA11073_tm07-4	0.07	23.88	2.14	0.66	0.78	70.21	0.00	0.50	0.44	0.00	0.00	0.00	0.00	0.00	98.68	
NWA11073_tm07-5	0.06	23.00	2.15	0.58	0.77	70.89	0.00	0.50	0.44	0.00	0.00	0.00	0.00	0.00	98.39	
NWA11073_ilm07-1	0.00	51.25	0.05	0.00	0.15	46.77	0.00	0.59	0.73	0.02	0.00	0.00	0.00	0.00	99.56	
NWA11073_ilm07-2	0.69	51.27	0.07	0.00	0.13	46.71	0.00	0.59	0.72	0.00	0.00	0.00	0.00	0.00	100.18	

Table A1.4.(continued) EPMA analysis of titanomagnetite-ilmenite pairs. Data excluded from calculating f_{O_2} are denoted in red.

SAMPLE	SiO ₂	TiO ₂	Al ₂ O ₃	V ₂ O ₃	Cr ₂ O ₃	FeO(T)	NiO	MnO	MgO	CaO	Na ₂ O	K ₂ O	ZnO	ZrO ₂	TOTAL	NOTES
NWA11073_ilm07-3	0.06	51.27	0.06	0.00	0.11	46.85	0.00	0.58	0.74	0.01	0.00	0.00	0.00	0.00	99.68	
NWA11255_tm01-1	0.10	22.83	2.19	0.67	1.61	70.40	0.00	0.53	0.51	0.03	0.00	0.00	0.00	0.00	98.87	
NWA11255_tm01-2	0.06	23.14	2.08	0.62	1.44	70.65	0.00	0.52	0.51	0.03	0.00	0.00	0.00	0.00	99.05	
NWA11255_tm01-3	0.08	24.16	1.90	0.52	1.01	70.43	0.00	0.52	0.53	0.04	0.00	0.00	0.00	0.00	99.19	
NWA11255_ilm01-1	0.03	51.01	0.05	0.00	0.12	46.92	0.00	0.59	0.88	0.14	0.00	0.00	0.00	0.00	99.74	
NWA11255_ilm01-2	0.02	51.31	0.06	0.00	0.12	46.92	0.00	0.59	0.85	0.04	0.00	0.00	0.00	0.00	99.91	
NWA11255_ilm01-3	0.02	51.10	0.06	0.00	0.15	47.03	0.00	0.57	0.88	0.02	0.00	0.00	0.00	0.00	99.83	
NWA11255_tm02-1	0.07	21.70	2.12	0.55	1.06	71.20	0.04	0.55	0.47	0.09	0.00	0.00	0.00	0.00	97.85	
NWA11255_tm02-2	0.08	22.55	2.01	0.53	0.76	71.47	0.00	0.51	0.48	0.04	0.00	0.00	0.00	0.00	98.43	
NWA11255_tm02-3	0.07	22.31	2.01	0.56	0.99	71.33	0.00	0.51	0.46	0.00	0.00	0.00	0.00	0.00	98.24	
NWA11255_ilm02-1	0.04	50.69	0.03	0.00	0.05	46.82	0.00	0.55	0.86	0.03	0.00	0.02	0.00	0.00	99.09	
NWA11255_ilm02-2	0.10	50.81	0.04	0.00	0.07	46.98	0.00	0.59	0.84	0.03	0.00	0.00	0.00	0.00	99.46	
NWA11255_ilm02-3	0.02	50.66	0.03	0.00	0.06	47.19	0.00	0.58	0.82	0.00	0.00	0.00	0.00	0.00	99.36	
NWA11255_tm03-1	0.09	22.55	1.84	0.41	0.49	71.66	0.00	0.49	0.45	0.02	0.00	0.00	0.00	0.00	98.00	
NWA11255_tm03-2	0.08	22.61	1.88	0.41	0.50	71.50	0.00	0.52	0.45	0.00	0.00	0.00	0.00	0.00	97.95	
NWA11255_tm03-3	0.08	21.24	2.22	0.74	1.11	71.78	0.00	0.49	0.40	0.02	0.00	0.00	0.00	0.00	98.08	
NWA11255_ilm03-1	0.03	50.57	0.05	0.00	0.08	46.95	0.00	0.59	0.73	0.04	0.00	0.00	0.00	0.00	99.04	
NWA11255_ilm03-2	0.00	50.48	0.07	0.00	0.06	47.20	0.00	0.59	0.75	0.02	0.00	0.00	0.00	0.00	99.17	
NWA11255_ilm03-3	0.03	50.52	0.04	0.00	0.04	47.16	0.00	0.59	0.76	0.02	0.00	0.00	0.00	0.00	99.16	
NWA11255_tm04-1	0.06	23.41	2.15	0.32	0.52	70.73	0.00	0.57	0.42	0.00	0.00	0.00	0.00	0.00	98.18	
NWA11255_tm04-2	0.09	23.45	2.15	0.32	0.53	70.94	0.00	0.53	0.40	0.06	0.00	0.00	0.00	0.00	98.47	
NWA11255_tm04-3	0.09	23.02	2.34	0.37	0.68	70.80	0.00	0.53	0.40	0.02	0.00	0.00	0.00	0.00	98.25	
NWA11255_ilm04-1	0.02	50.45	0.05	0.00	0.08	47.21	0.00	0.60	0.65	0.02	0.00	0.00	0.00	0.00	99.08	
NWA11255_ilm04-2	0.15	50.54	0.10	0.00	0.09	46.94	0.00	0.65	0.65	0.06	0.00	0.00	0.00	0.00	99.18	
NWA11255_ilm04-3	0.56	49.35	0.15	0.00	0.08	46.85	0.00	0.61	0.78	0.18	0.00	0.00	0.00	0.00	98.56	
NWA11255_tm05-1	0.07	22.44	1.97	0.29	0.46	71.85	0.00	0.49	0.53	0.10	0.00	0.00	0.00	0.00	98.20	
NWA11255_tm05-2	0.10	22.59	2.00	0.33	0.46	71.72	0.00	0.52	0.53	0.05	0.00	0.00	0.00	0.00	98.30	
NWA11255_tm05-3	0.08	22.08	2.16	0.32	0.50	71.80	0.02	0.49	0.54	0.08	0.00	0.00	0.00	0.00	98.07	
NWA11255_ilm05-1	0.03	50.60	0.06	0.00	0.05	46.85	0.00	0.58	0.93	0.13	0.00	0.00	0.00	0.00	99.23	
NWA11255_ilm05-2	0.10	50.42	0.07	0.00	0.03	46.76	0.00	0.60	0.92	0.09	0.00	0.00	0.00	0.00	98.99	
NWA11255_ilm05-3	0.02	50.75	0.04	0.00	0.06	46.81	0.00	0.59	0.94	0.07	0.00	0.00	0.00	0.00	99.28	
NWA11255_tm06-1	0.09	22.99	1.79	0.41	0.62	70.96	0.02	0.52	0.51	0.02	0.00	0.00	0.00	0.00	97.93	
NWA11255_tm06-2	0.08	22.09	1.96	0.40	0.52	71.99	0.00	0.52	0.51	0.01	0.00	0.00	0.00	0.00	98.08	
NWA11255_tm06-3	0.07	22.47	1.83	0.38	0.44	71.57	0.03	0.52	0.51	0.00	0.00	0.00	0.00	0.00	97.82	
NWA11255_ilm06-1	0.04	50.63	0.06	0.00	0.06	47.06	0.00	0.60	0.83	0.03	0.00	0.00	0.00	0.00	99.31	
NWA11255_ilm06-2	0.03	50.54	0.07	0.00	0.06	46.94	0.00	0.59	0.83	0.00	0.00	0.00	0.00	0.00	99.06	
NWA11255_ilm06-3	0.03	50.47	0.05	0.00	0.08	46.96	0.00	0.60	0.86	0.03	0.00	0.00	0.00	0.00	99.08	
NWA12262_tmex01-1	0.08	27.84	1.27	0.00	0.03	68.16	0.00	0.66	0.12	0.02	0.00	0.00	0.00	0.00	98.18	
NWA12262_tmex01-2	0.10	27.33	1.26	0.00	0.00	68.58	0.00	0.66	0.10	0.00	0.00	0.00	0.00	0.00	98.03	

Table A1.4.(continued) EPMA analysis of titanomagnetite-ilmenite pairs. Data excluded from calculating f_{O_2} are denoted in red.

SAMPLE	SiO ₂	TiO ₂	Al ₂ O ₃	V ₂ O ₃	Cr ₂ O ₃	FeO(T)	NiO	MnO	MgO	CaO	Na ₂ O	K ₂ O	ZnO	ZrO ₂	TOTAL	NOTES
NWA12262_tmex01-3	0.10	25.08	1.46	0.06	0.00	70.41	0.03	0.62	0.11	0.02	0.00	0.00	0.00	0.00	97.89	
NWA12262_tmex01-4	0.08	24.06	1.44	0.10	0.00	71.26	0.00	0.59	0.12	0.00	0.00	0.00	0.00	0.00	97.65	
NWA12262_tmex01-5	0.10	27.31	1.35	0.03	0.00	68.14	0.00	0.64	0.15	0.00	0.00	0.00	0.00	0.00	97.72	
NWA12262_ilm01-1	0.06	47.95	0.08	0.00	0.00	49.56	0.00	0.81	0.20	0.04	0.00	0.01	0.00	0.00	98.71	
NWA12262_ilm01-2	0.06	48.04	0.06	0.00	0.00	49.88	0.00	0.82	0.18	0.02	0.00	0.00	0.00	0.00	99.06	
NWA12262_ilm01-3	0.11	48.43	0.08	0.00	0.00	49.55	0.00	0.82	0.17	0.01	0.00	0.00	0.00	0.00	99.17	
NWA12262_tmex02-1	0.12	22.82	1.49	0.17	0.00	71.76	0.00	0.63	0.19	0.03	0.00	0.00	0.00	0.00	97.21	
NWA12262_tmex02-2	0.06	26.63	1.36	0.16	0.04	68.62	0.00	0.70	0.24	0.03	0.00	0.00	0.00	0.00	97.84	
NWA12262_tmex02-3	0.09	25.06	1.49	0.23	0.00	69.61	0.00	0.66	0.21	0.09	0.00	0.00	0.00	0.00	97.44	
NWA12262_tmex02-4	0.06	25.18	1.42	0.27	0.05	69.57	0.00	0.65	0.22	0.02	0.00	0.00	0.00	0.00	97.44	
NWA12262_tmex02-5	0.07	24.10	1.47	0.25	0.04	70.69	0.00	0.63	0.21	0.09	0.00	0.00	0.00	0.00	97.55	
																A, b, and c denote different grains of ilm inclusion within the same exsolved tmt grain (tmex02)
NWA12262_ilm02a-1	0.08	49.03	0.06	0.00	0.00	48.91	0.00	0.89	0.38	0.04	0.00	0.00	0.00	0.00	99.39	
NWA12262_ilm02a-2	0.09	47.14	0.07	0.00	0.00	49.93	0.00	0.82	0.33	0.00	0.00	0.01	0.00	0.00	98.39	
NWA12262_ilm02a-3	0.07	47.83	0.06	0.00	0.00	49.74	0.00	0.85	0.31	0.02	0.00	0.00	0.00	0.00	98.88	
NWA12262_ilm02b-1	0.13	47.89	0.07	0.00	0.00	49.68	0.00	0.89	0.31	0.03	0.00	0.00	0.00	0.00	99.00	
NWA12262_ilm02b-2	0.14	47.92	0.15	0.00	0.00	49.73	0.00	0.84	0.31	0.04	0.00	0.02	0.00	0.00	99.15	
NWA12262_ilm02b-3	0.13	48.01	0.07	0.00	0.00	49.45	0.00	0.84	0.33	0.03	0.00	0.01	0.00	0.00	98.87	
NWA12262_ilm02c-1	0.05	47.39	0.07	0.00	0.00	49.27	0.00	0.89	0.35	0.11	0.00	0.00	0.00	0.00	98.13	
NWA12262_ilm02c-2	0.10	45.97	0.05	0.00	0.00	49.86	0.00	0.83	0.33	0.11	0.00	0.00	0.00	0.00	97.25	
NWA12262_ilm02c-3	2.03	45.21	0.74	0.00	0.00	48.86	0.00	0.85	0.35	0.27	0.06	0.05		98.42		
NWA12262_tmex03-1	0.08	28.03	1.38	0.02	0.04	67.53	0.00	0.63	0.20	0.02	0.00	0.00	0.00	0.00	97.93	
NWA12262_tmex03-2	0.09	25.49	1.62	0.06	0.03	70.18	0.00	0.59	0.19	0.02	0.00	0.00	0.00	0.00	98.27	
NWA12262_tmex03-3	0.10	24.06	1.64	0.08	0.00	70.96	0.00	0.56	0.16	0.07	0.00	0.00	0.00	0.00	97.63	
NWA12262_tmex03-4	0.10	22.26	1.69	0.08	0.03	72.79	0.00	0.56	0.14	0.00	0.00	0.00	0.00	0.00	97.65	
NWA12262_ilm03-1	0.06	48.20	0.06	0.00	0.00	49.50	0.00	0.79	0.26	0.03	0.00	0.00	0.00	0.00	98.90	
NWA12262_ilm03-2	0.12	47.73	0.10	0.00	0.00	49.54	0.00	0.81	0.26	0.06	0.00	0.00	0.00	0.00	98.62	
NWA12262_ilm03-3	0.06	48.43	0.08	0.00	0.00	49.59	0.00	0.80	0.27	0.04	0.00	0.00	0.00	0.00	99.27	
NWA12262_tmex04-1	0.09	25.60	1.44	0.09	0.00	69.38	0.00	0.61	0.17	0.06	0.00	0.00	0.00	0.00	97.44	
NWA12262_tmex04-2	0.11	27.20	1.35	0.13	0.00	68.27	0.00	0.65	0.19	0.02	0.00	0.00	0.00	0.00	97.92	
NWA12262_tmex04-3	0.08	27.38	1.29	0.12	0.02	68.01	0.00	0.65	0.16	0.01	0.00	0.00	0.00	0.00	97.72	
NWA12262_tmex04-4	0.06	27.27	1.27	0.11	0.00	67.79	0.00	0.66	0.17	0.00	0.00	0.00	0.00	0.00	97.33	
																A and b denote different grains of ilm inclusion within the same exsolved tmt grain
NWA12262_ilm04a-1	0.05	48.63	0.06	0.00	0.00	49.69	0.00	0.83	0.26	0.02	0.00	0.00	0.00	0.00	99.54	
NWA12262_ilm04a-2	0.13	48.32	0.08	0.00	0.00	49.85	0.00	0.80	0.27	0.02	0.00	0.00	0.00	0.00	99.47	
NWA12262_ilm04a-3	0.05	48.19	0.06	0.00	0.00	49.41	0.00	0.82	0.25	0.08	0.00	0.01	0.00	0.00	98.87	
NWA12262_ilm04b-1	0.02	48.66	0.06	0.00	0.00	49.56	0.00	0.83	0.27	0.05	0.00	0.00	0.00	0.00	99.45	
NWA12262_ilm04b-2	0.14	48.55	0.08	0.00	0.00	49.47	0.00	0.80	0.26	0.04	0.00	0.00	0.00	0.00	99.34	

Table A1.4.(continued) EPMA analysis of titanomagnetite-ilmenite pairs. Data excluded from calculating f_{O_2} are denoted in red.

SAMPLE	SiO ₂	TiO ₂	Al ₂ O ₃	V ₂ O ₃	Cr ₂ O ₃	FeO(T)	NiO	MnO	MgO	CaO	Na ₂ O	K ₂ O	ZnO	ZrO ₂	TOTAL	NOTES
NWA12262_ilm04b-3	0.04	48.47	0.06	0.00	0.00	49.55	0.00	0.84	0.26	0.03	0.00	0.00	0.00	0.00	99.25	
AA-1(NWA12919)_tm001-1	0.08	24.17	1.52	0.39	0.74	69.45	0.00	0.53	0.30	0.02	0.00	0.00	0.00	0.00	97.20	
AA-1(NWA12919)_tm001-2	0.07	24.15	1.50	0.39	0.72	69.20	0.00	0.49	0.30	0.02	0.00	0.00	0.00	0.00	96.84	
AA-1(NWA12919)_tm001-3	0.09	23.81	1.65	0.43	0.71	69.79	0.00	0.51	0.29	0.00	0.00	0.00	0.00	0.00	97.28	
AA-1(NWA12919)_tm001-4	0.08	23.49	1.70	0.44	0.66	69.77	0.02	0.49	0.28	0.00	0.00	0.00	0.00	0.00	96.93	
AA-1(NWA12919)_tm001-5	0.07	23.82	1.62	0.41	0.82	69.55	0.00	0.49	0.29	0.00	0.00	0.00	0.00	0.00	97.07	
AA-1(NWA12919)_ilm001-1	0.10	49.85	0.03	0.14	0.06	46.72	0.00	0.55	0.45	0.07	0.00	0.00	0.00	0.00	97.97	
AA-1(NWA12919)_ilm001-2	0.00	50.07	0.04	0.15	0.08	47.01	0.00	0.56	0.45	0.03	0.00	0.00	0.00	0.00	98.39	
AA-1(NWA12919)_ilm001-3	0.02	50.13	0.04	0.16	0.07	47.03	0.00	0.58	0.44	0.01	0.00	0.00	0.00	0.00	98.48	
AA-1(NWA12919)_ilm001-4	0.00	50.04	0.03	0.15	0.09	46.61	0.00	0.58	0.47	0.06	0.00	0.00	0.00	0.00	98.03	
AA-1(NWA12919)_ilm001-5	0.02	50.06	0.03	0.16	0.09	47.03	0.00	0.57	0.44	0.03	0.00	0.00	0.00	0.00	98.43	
AA-1(NWA12919)_tm002-1	0.06	24.30	1.64	0.34	0.71	69.57	0.00	0.55	0.46	0.00	0.00	0.00	0.00	0.00	97.63	
AA-1(NWA12919)_tm002-2	0.06	24.77	1.57	0.31	0.75	69.40	0.02	0.54	0.45	0.03	0.00	0.00	0.00	0.00	97.90	
AA-1(NWA12919)_tm002-3	0.08	24.26	1.59	0.33	0.71	69.40	0.00	0.53	0.45	0.03	0.00	0.00	0.00	0.00	97.38	
AA-1(NWA12919)_tm002-4	0.08	23.55	1.93	0.43	0.92	69.15	0.00	0.52	0.44	0.04	0.00	0.00	0.00	0.00	97.06	
AA-1(NWA12919)_tm002-5	0.10	23.30	2.09	0.46	1.49	68.78	0.00	0.52	0.45	0.07	0.00	0.00	0.00	0.00	97.26	
AA-1(NWA12919)_ilm002-1	0.09	47.95	0.26	0.13	0.35	47.82	0.00	0.59	0.72	0.21	0.00	0.00	0.00	0.00	98.12	
AA-1(NWA12919)_ilm002-2	0.02	49.92	0.05	0.11	0.11	46.29	0.00	0.59	0.72	0.27	0.00	0.00	0.00	0.00	98.08	
AA-1(NWA12919)_ilm002-3	0.00	50.14	0.04	0.10	0.09	46.15	0.00	0.56	0.72	0.09	0.00	0.00	0.00	0.00	97.89	
AA-1(NWA12919)_ilm002-4	0.02	49.73	0.03	0.11	0.10	45.77	0.00	0.61	0.71	0.23	0.00	0.00	0.00	0.00	97.31	
AA-1(NWA12919)_ilm002-5	0.21	46.89	0.09	0.09	0.09	44.16	0.00	0.57	0.72	0.75	0.00	0.01	0.00	0.00	93.58	
AA-1(NWA12919)_tm002-1	0.08	24.50	1.64	0.37	1.14	68.34	0.00	0.53	0.47	0.09	0.00	0.00	0.00	0.00	97.16	
AA-1(NWA12919)_tm002-2	0.08	24.46	1.69	0.37	1.14	68.33	0.00	0.55	0.47	0.07	0.00	0.00	0.00	0.00	97.16	
AA-1(NWA12919)_tm002-3	0.07	24.57	1.69	0.39	1.19	68.06	0.00	0.52	0.48	0.04	0.00	0.00	0.00	0.00	97.01	
AA-1(NWA12919)_tm002-4	0.08	24.38	1.66	0.38	1.19	68.21	0.00	0.53	0.45	0.09	0.00	0.00	0.00	0.00	96.97	
AA-1(NWA12919)_tm002-5	0.09	24.27	1.75	0.39	1.73	67.73	0.02	0.56	0.44	0.09	0.00	0.00	0.00	0.00	97.07	
AA-1(NWA12919)_ilm003-1	0.04	50.05	0.04	0.13	0.09	46.16	0.00	0.58	0.72	0.11	0.00	0.00	0.00	0.00	97.92	
AA-1(NWA12919)_ilm003-2	0.02	50.24	0.04	0.10	0.12	46.23	0.00	0.58	0.72	0.09	0.00	0.00	0.00	0.00	98.14	
AA-1(NWA12919)_ilm003-3	0.02	50.29	0.03	0.09	0.10	46.54	0.00	0.57	0.76	0.06	0.00	0.00	0.00	0.00	98.46	
AA-1(NWA12919)_ilm003-4	0.06	49.82	0.05	0.09	0.09	46.41	0.00	0.54	0.74	0.18	0.00	0.00	0.00	0.00	97.98	
AA-1(NWA12919)_ilm003-5	0.04	49.98	0.03	0.08	0.08	46.44	0.00	0.57	0.76	0.15	0.00	0.00	0.00	0.00	98.13	
AA-1(NWA12919)_tm004-1	0.10	22.02	1.84	0.22	0.31	71.27	0.00	0.50	0.22	0.16	0.00	0.00	0.00	0.00	96.64	
AA-1(NWA12919)_tm004-2	0.10	22.26	1.82	0.20	0.31	71.79	0.00	0.47	0.23	0.09	0.00	0.01	0.00	0.00	97.28	
AA-1(NWA12919)_tm004-3	0.09	22.16	1.82	0.21	0.29	71.48	0.00	0.50	0.24	0.10	0.00	0.00	0.00	0.00	96.89	
AA-1(NWA12919)_tm004-4	0.14	21.97	1.79	0.21	0.27	71.44	0.00	0.51	0.25	0.08	0.00	0.03	0.00	0.00	96.69	
AA-1(NWA12919)_tm004-5	0.12	21.90	1.85	0.19	0.25	71.28	0.00	0.49	0.25	0.12	0.00	0.01	0.00	0.00	96.46	
AA-1(NWA12919)_ilm004-1	0.04	49.29	0.04	0.05	0.00	47.18	0.00	0.59	0.41	0.39	0.00	0.03	0.00	0.00	98.02	
AA-1(NWA12919)_ilm004-2	0.04	49.37	0.03	0.07	0.00	47.00	0.00	0.57	0.43	0.37	0.00	0.02	0.00	0.00	97.90	
AA-1(NWA12919)_ilm004-3	0.05	49.06	0.06	0.06	0.00	46.78	0.00	0.60	0.44	0.51	0.00	0.02	0.00	0.00	97.58	

Table A1.4.(continued) EPMA analysis of titanomagnetite-ilmenite pairs. Data excluded from calculating f_{O_2} are denoted in red.

SAMPLE	SiO ₂	TiO ₂	Al ₂ O ₃	V ₂ O ₃	Cr ₂ O ₃	FeO(T)	NiO	MnO	MgO	CaO	Na ₂ O	K ₂ O	ZnO	ZrO ₂	TOTAL	NOTES
AA-1(NWA12919)_tm007-1	0.10	22.45	1.60	0.33	0.93	70.94	0.00	0.56	0.31	0.03	0.00	0.00	0.00	0.00	97.25	
AA-1(NWA12919)_tm007-2	0.08	22.88	1.73	0.35	0.88	70.18	0.00	0.51	0.33	0.02	0.00	0.00	0.00	0.00	96.96	
AA-1(NWA12919)_tm007-3	0.07	22.90	1.74	0.35	0.84	70.58	0.00	0.53	0.33	0.03	0.00	0.00	0.00	0.00	97.37	
AA-1(NWA12919)_ilm007-1	0.02	50.23	0.05	0.06	0.07	47.00	0.00	0.57	0.54	0.02	0.00	0.00	0.00	0.00	98.56	
AA-1(NWA12919)_ilm007-2	0.02	50.18	0.04	0.08	0.08	46.82	0.00	0.61	0.55	0.02	0.00	0.00	0.00	0.00	98.40	
AA-1(NWA12919)_ilm007-3	0.03	50.01	0.04	0.09	0.08	47.36	0.00	0.59	0.53	0.04	0.00	0.00	0.00	0.00	98.77	
AA-1(NWA12919)_tm008-1	0.08	22.71	1.68	0.30	0.76	71.11	0.00	0.48	0.33	0.04	0.00	0.00	0.00	0.00	97.49	
AA-1(NWA12919)_tm008-2	0.09	23.02	1.58	0.28	0.74	70.58	0.00	0.47	0.34	0.02	0.00	0.00	0.00	0.00	97.12	
AA-1(NWA12919)_tm008-3	0.10	23.18	1.49	0.24	0.72	70.02	0.00	0.46	0.34	0.06	0.00	0.02	0.00	0.00	96.63	
AA-1(NWA12919)_ilm008-1	0.06	49.74	0.05	0.07	0.13	46.63	0.02	0.55	0.57	0.12	0.00	0.00	0.00	0.00	97.94	
AA-1(NWA12919)_ilm008-2	0.10	49.94	0.03	0.07	0.09	46.64	0.00	0.55	0.55	0.10	0.00	0.01	0.00	0.00	98.08	
AA-1(NWA12919)_ilm008-3	0.00	50.14	0.03	0.05	0.13	46.75	0.00	0.56	0.56	0.05	0.00	0.00	0.00	0.00	98.27	
AA-1(NWA12919)_tm009-1	0.05	23.71	1.61	0.22	0.51	70.57	0.00	0.57	0.39	0.05	0.00	0.00	0.00	0.00	97.68	
AA-1(NWA12919)_tm009-2	0.08	23.60	1.60	0.23	0.53	70.95	0.00	0.56	0.37	0.02	0.00	0.00	0.00	0.00	97.94	
AA-1(NWA12919)_tm009-3	0.07	22.55	1.75	0.24	0.54	71.38	0.02	0.53	0.35	0.04	0.00	0.00	0.00	0.00	97.47	
AA-1(NWA12919)_ilm009-1	0.04	50.53	0.03	0.00	0.05	46.89	0.00	0.63	0.65	0.03	0.00	0.00	0.00	0.00	98.85	
AA-1(NWA12919)_ilm009-2	0.03	50.84	0.03	0.00	0.08	46.71	0.00	0.63	0.65	0.02	0.00	0.00	0.00	0.00	98.99	
AA-1(NWA12919)_ilm009-3	0.04	50.48	0.03	0.00	0.04	46.92	0.00	0.61	0.63	0.06	0.00	0.00	0.00	0.00	98.81	
AA-1(NWA12919)_tm010-1	0.06	24.85	1.45	0.51	1.17	68.38	0.00	0.51	0.47	0.00	0.00	0.00	0.00	0.00	97.40	
AA-1(NWA12919)_tm010-2	0.07	24.90	1.43	0.50	1.08	68.72	0.00	0.54	0.44	0.02	0.00	0.00	0.00	0.00	97.70	
AA-1(NWA12919)_tm010-3	0.06	25.38	1.45	0.54	1.02	67.95	0.00	0.56	0.46	0.01	0.00	0.00	0.00	0.00	97.43	
AA-1(NWA12919)_ilm010-1	8.68	21.59	2.86	0.41	0.73	60.45	0.00	0.53	0.86	1.12	0.23	0.39	0.00	0.00	97.85	
AA-1(NWA12919)_ilm010-2	8.78	21.59	2.96	0.41	0.76	60.94	0.00	0.54	0.90	1.16	0.22	0.39	0.00	0.00	98.65	
AA-1(NWA12919)_ilm010-3	8.71	21.48	2.98	0.42	0.76	61.14	0.00	0.54	0.86	1.15	0.20	0.40	0.00	0.00	98.64	
AA-1(NWA12919)_ilm010rerun-1	0.02	50.11	0.05	0.11	0.16	47.12	0.00	0.57	0.68	0.00	0.00	0.00	0.00	0.00	98.82	
AA-1(NWA12919)_ilm010rerun-2	0.14	50.05	0.04	0.10	0.10	47.11	0.00	0.57	0.70	0.04	0.00	0.00	0.00	0.00	98.85	
AA-1(NWA12919)_ilm010rerun-3	0.06	49.96	0.04	0.12	0.08	47.35	0.00	0.58	0.67	0.22	0.00	0.01	0.00	0.00	99.09	
AA-1(NWA12919)_tm012-1	0.08	23.94	1.63	0.25	0.72	70.86	0.00	0.56	0.36	0.00	0.00	0.00	0.00	0.00	98.40	
AA-1(NWA12919)_tm012-2	0.08	23.08	1.79	0.28	0.75	71.51	0.00	0.56	0.35	0.00	0.00	0.00	0.00	0.00	98.40	
AA-1(NWA12919)_tm012-3	0.08	22.61	1.86	0.31	0.87	71.44	0.00	0.54	0.35	0.00	0.00	0.00	0.00	0.00	98.06	
AA-1(NWA12919)_ilm012-1	0.04	50.16	0.06	0.05	0.06	47.39	0.00	0.68	0.59	0.02	0.00	0.00	0.00	0.00	99.05	
AA-1(NWA12919)_ilm012-2	0.09	49.94	0.06	0.04	0.06	47.42	0.00	0.66	0.59	0.00	0.00	0.00	0.00	0.00	98.86	
AA-1(NWA12919)_ilm012-3	0.25	47.63	0.15	0.05	0.05	46.24	0.00	0.67	0.56	0.06	0.00	0.01	0.00	0.00	95.67	
AA-1(NWA12919)_tm013-1	0.08	23.91	1.68	0.24	0.42	70.83	0.00	0.57	0.29	0.16	0.00	0.00	0.00	0.00	98.18	
AA-1(NWA12919)_tm013-2	0.09	23.78	1.74	0.26	0.39	71.21	0.00	0.56	0.30	0.09	0.00	0.00	0.00	0.00	98.42	
AA-1(NWA12919)_tm013-3	0.07	24.01	1.83	0.27	0.46	71.50	0.00	0.57	0.31	0.07	0.00	0.00	0.00	0.00	99.09	
AA-1(NWA12919)_ilm013-1	0.00	50.70	0.03	0.00	0.07	47.10	0.00	0.61	0.49	0.00	0.00	0.00	0.00	0.00	99.00	
AA-1(NWA12919)_ilm013-2	0.02	50.68	0.06	0.00	0.06	47.35	0.00	0.66	0.50	0.00	0.00	0.00	0.00	0.00	99.33	
AA-1(NWA12919)_ilm013-3	0.02	50.67	0.05	0.00	0.08	47.68	0.00	0.62	0.47	0.00	0.00	0.00	0.00	0.00	99.59	

Table A1.5. Averaged EPMA analysis of titanomagnetite-ilmenite pairs, with calculated FeO and Fe₂O₃ based on charge balancing. Data excluded from calculating f_{O_2} are denoted in red.

SAMPLE	Analysis	Pair	SiO ₂	TiO ₂	Al ₂ O ₃	V ₂ O ₃	Cr ₂ O ₃	FeO (Total)	NiO	MnO	MgO	CaO	Na ₂ O	K ₂ O	P ₂ O ₅	ZrO ₂	FeO	Fe ₂ O ₃	Total
JaH479	tmex01avg	1	0.14	24.90	1.78	0.03	0.01	69.93	0.00	0.49	0.06	0.03	0.00	0.00	0.00	54.40	17.26	99.10	
JaH479	ilm01avg	1	0.05	50.53	0.05	0.00	0.01	48.19	0.00	0.79	0.09	0.05	0.00	0.00	0.00	44.89	3.66	100.13	
JaH479	tmex02avg	2	0.10	25.83	1.85	0.09	0.01	68.77	0.00	0.51	0.07	0.03	0.00	0.00	0.00	54.93	15.38	98.79	
JaH479	ilm02avg	2	0.08	50.64	0.04	0.00	0.00	48.14	0.00	0.80	0.12	0.04	0.00	0.00	0.00	45.02	3.47	100.20	
JaH479	Int_1 avg_wted	3	0.18	25.05	1.48	0.21	0.05	67.65	0.00	0.52	0.14	0.08				0.03	54.03	15.13	96.89
JaH479	Int 1 TMT_avg*	3	0.19	24.48	1.77	0.25	0.06	68.04	0.00	0.50	0.13	0.08				0.03	53.73	15.91	97.12
JaH479	Int_1 Inc_avg	3	0.16	50.92	0.07	0.00	0.01	47.02	0.00	0.79	0.20	0.06				0.04	45.58	1.60	99.44
JaH479	Int 2 TMT_avg	4	0.26	24.95	1.65	0.25	0.03	67.53	0.00	0.50	0.18	0.10				0.02	54.32	14.67	96.94
JaH479	Int 2 Ilmn_avg	4	0.12	49.82	0.05	0.00	0.00	47.16	0.00	0.78	0.18	0.05				0.10	44.70	2.73	98.55
JaH479	Int 4 TMT_avg	5	0.16	22.19	1.81	0.15	0.02	70.56	0.01	0.49	0.11	0.06				0.02	51.55	21.12	97.70
JaH479	Int 4 Ilmn 2	5	0.10	49.74	0.03	0.00	0.00	47.39	0.00	0.81	0.17	0.03				0.13	44.57	3.14	98.72
KG002	tm01avg	1	0.10	23.70	1.72	0.01	0.03	72.14	0.00	0.58	0.15	0.03	0.00	0.00	0.00	53.28	20.96	100.56	
KG002	ilm01avg	1	0.11	50.23	0.06	0.00	0.00	47.51	0.00	0.65	0.27	0.13	0.00	0.00	0.00	44.92	2.88	99.25	
KG002	tm02avg	2	0.07	23.40	1.76	0.01	0.02	72.24	0.00	0.66	0.08	0.05	0.00	0.00	0.00	52.87	21.53	100.44	
KG002	ilm02avg	2	0.07	50.12	0.07	0.00	0.00	47.43	0.00	0.89	0.13	0.44	0.00	0.00	0.00	45.41	2.25	99.39	
KG002	tm03avg	3	0.07	23.39	1.99	0.57	0.06	71.80	0.00	0.58	0.16	0.02	0.00	0.00	0.00	52.90	20.99	100.74	
KG002	ilm03avg	3	0.02	50.83	0.05	0.00	0.00	47.81	0.00	0.69	0.28	0.04	0.00	0.00	0.00	44.70	3.46	100.06	
KG002	tm04avg	4	0.07	23.03	1.69	0.00	0.00	72.48	0.00	0.60	0.07	0.01	0.00	0.00	0.00	52.43	22.28	100.17	
KG002	ilm04avg	4	0.02	50.22	0.05	0.00	0.00	47.93	0.01	0.71	0.12	0.01	0.00	0.00	0.00	44.38	3.95	99.46	
KG002	tm05avg	5	0.07	22.72	1.89	0.19	0.05	71.91	0.00	0.55	0.16	0.12	0.00	0.00	0.00	52.29	21.80	99.85	
KG002	ilm05avg	5	0.04	49.31	0.05	0.00	0.00	47.66	0.00	0.64	0.25	0.20	0.00	0.00	0.00	43.98	4.09	98.54	
NWA10299	tm01avg	1	0.08	25.16	1.87	0.58	1.38	69.91	0.01	0.55	0.38	0.00	0.00	0.00	0.00	54.56	17.06	101.63	
NWA10299	ilm01avg	1	0.03	51.90	0.04	0.00	0.07	47.40	0.00	0.60	0.55	0.00	0.00	0.00	0.00	45.23	2.41	100.83	
NWA10299	tm02avg	2	0.07	24.66	1.85	0.71	1.58	69.36	0.00	0.52	0.42	0.05	0.00	0.00	0.00	53.93	17.14	100.91	
NWA10299	ilm02avg	2	0.02	51.55	0.05	0.00	0.11	47.12	0.00	0.62	0.66	0.03	0.00	0.00	0.00	44.72	2.67	100.43	
NWA10299	tm03avg	3	0.09	24.33	1.89	0.44	1.51	69.67	0.00	0.54	0.44	0.05	0.00	0.00	0.00	53.61	17.85	100.74	
NWA10299	ilm03avg	3	0.11	50.39	0.05	0.00	0.12	47.30	0.00	0.63	0.76	0.17	0.00	0.00	0.00	44.27	3.36	99.87	
NWA10299	tm04avg	4	0.07	25.70	1.69	0.59	2.03	68.49	0.00	0.58	0.49	0.02	0.00	0.00	0.00	54.71	15.32	101.19	
NWA10299	ilm04avg	4	0.13	48.56	0.14	0.00	0.66	48.28	0.01	0.62	0.79	0.08	0.00	0.00	0.00	42.54	6.38	99.91	
NWA10299	tm06avg	5	0.08	25.41	1.77	0.52	0.92	69.71	0.01	0.57	0.42	0.04	0.00	0.00	0.00	54.62	16.77	101.12	
NWA10299	ilm06avg	5	0.03	51.21	0.04	0.00	0.09	47.16	0.00	0.65	0.69	0.21	0.00	0.00	0.00	44.85	2.56	100.32	
NWA10299	tm07avg	6	0.07	24.27	1.81	0.42	0.50	71.12	0.00	0.54	0.43	0.03	0.00	0.00	0.00	53.50	19.58	101.16	
NWA10299	ilm07avg	6	0.05	50.46	0.08	0.00	0.11	48.29	0.00	0.65	0.67	0.01	0.00	0.00	0.00	43.82	4.97	100.81	
NWA11057	tm01avg	1	0.06	24.18	2.47	0.28	0.45	70.51	0.01	0.53	0.46	0.04	0.00	0.00	0.00	53.44	18.98	100.88	
NWA11057	ilm01avg	1	0.06	51.11	0.08	0.00	0.08	47.10	0.00	0.60	0.75	0.03	0.00	0.00	0.00	44.40	2.99	100.12	
NWA11057	tm02avg	2	0.06	23.12	2.05	0.42	1.07	70.06	0.00	0.51	0.45	0.16	0.00	0.00	0.00	52.33	19.71	99.88	
NWA11057	ilm02avg	2	0.06	50.80	0.05	0.00	0.07	46.99	0.00	0.58	0.73	0.10	0.00	0.00	0.00	44.33	2.96	99.68	
NWA11057	tm03avg	3	0.08	24.59	1.96	0.46	1.06	69.83	0.01	0.54	0.47	0.02	0.00	0.00	0.00	53.71	17.91	100.80	
NWA11057	ilm03avg	3	0.03	51.18	0.05	0.00	0.11	47.11	0.00	0.59	0.78	0.03	0.00	0.00	0.00	44.29	3.13	100.19	

*No appreciable difference in calculated FeO and Fe₂O₃ between Int_1 avg_wted and Int 1 TMT_avg. The latter is preferred to maintain consistency with other samples in the study where exsolved tmt was analyzed also with a defocused beam.

Table A1.5.(continued) Averaged EPMA analysis of titanomagnetite-ilmenite pairs, with calculated FeO and Fe₂O₃ based on charge balancing.
Data excluded from calculating f_{O_2} are denoted in red.

SAMPLE	Analysis	Pair	SiO ₂	TiO ₂	Al ₂ O ₃	V ₂ O ₃	Cr ₂ O ₃	FeO (Total)	NiO	MnO	MgO	CaO	Na ₂ O	K ₂ O	P ₂ O ₅	ZrO ₂	FeO	Fe ₂ O ₃	Total
NWA11057	tm04avg	4	0.06	23.82	2.04	0.67	1.37	69.14	0.01	0.53	0.60	0.07	0.00	0.00	0.00	0.00	52.69	18.28	100.15
NWA11057	ilm04avg	4	0.04	51.29	0.05	0.00	0.11	46.36	0.00	0.56	1.01	0.11	0.00	0.00	0.00	0.00	44.20	2.40	99.76
NWA11057	tm05avg	5	0.05	24.57	2.03	0.65	1.47	68.96	0.01	0.53	0.62	0.05	0.00	0.00	0.00	0.00	53.40	17.29	100.67
NWA11057	ilm05avg	5	0.04	51.15	0.05	0.00	0.07	46.51	0.00	0.58	1.00	0.23	0.00	0.01	0.00	0.00	44.39	2.35	99.85
NWA11057	tm06avg	6	0.07	23.09	1.81	0.45	0.69	70.79	0.00	0.55	0.52	0.07	0.00	0.00	0.00	0.00	52.01	20.87	100.12
NWA11057	ilm06avg	6	0.01	50.74	0.04	0.03	0.05	46.48	0.00	0.63	0.88	0.15	0.00	0.00	0.00	0.00	43.88	2.89	99.29
NWA11057	tm07avg	7	0.08	22.52	1.97	0.24	0.40	71.38	0.01	0.51	0.34	0.17	0.00	0.00	0.00	0.00	51.99	21.55	99.78
NWA11057	ilm07avg	7	0.02	50.21	0.06	0.00	0.04	47.15	0.00	0.58	0.57	0.19	0.00	0.00	0.00	0.00	44.14	3.34	99.15
NWA11073	tm01avg	1	0.08	22.87	1.84	0.36	0.47	71.30	0.01	0.51	0.56	0.02	0.00	0.00	0.00	0.00	51.74	21.73	100.19
NWA11073	ilm01avg	1	0.01	50.98	0.05	0.00	0.07	46.92	0.00	0.59	0.93	0.06	0.00	0.00	0.00	0.00	43.81	3.45	99.94
NWA11073	tm02avg	2	0.09	22.61	1.76	0.22	0.34	71.79	0.00	0.54	0.34	0.14	0.00	0.00	0.00	0.00	52.08	21.91	100.02
NWA11073	ilm02avg	2	0.06	49.90	0.04	0.00	0.00	47.10	0.00	0.59	0.65	0.12	0.00	0.00	0.00	0.00	43.71	3.77	98.83
NWA11073	tm03avg	3	0.09	19.23	2.53	0.57	0.93	72.84	0.00	0.49	0.41	0.11	0.00	0.00	0.00	0.00	48.89	26.61	99.86
NWA11073	ilm03avg	3	0.23	49.92	0.09	0.00	0.06	46.68	0.00	0.62	0.84	0.13	0.00	0.01	0.00	0.00	44.22	2.72	98.83
NWA11073	tm04avg	4	0.06	22.97	2.13	0.39	0.56	71.27	0.00	0.51	0.34	0.13	0.00	0.00	0.00	0.00	52.48	20.88	100.45
NWA11073	ilm04avg	4	0.03	50.87	0.04	0.00	0.09	47.15	0.00	0.57	0.62	0.03	0.00	0.00	0.00	0.00	44.32	3.14	99.72
NWA11073	tm05avg	5	0.07	24.04	2.01	0.49	0.66	69.89	0.00	0.55	0.39	0.08	0.00	0.00	0.00	0.00	53.18	18.57	100.04
NWA11073	ilm05avg	5	0.02	51.08	0.04	0.00	0.10	46.90	0.00	0.61	0.68	0.05	0.00	0.00	0.00	0.00	44.33	2.86	99.76
NWA11073	tm06avg	6	0.06	22.44	2.48	0.68	0.72	70.64	0.00	0.51	0.29	0.22	0.00	0.00	0.00	0.00	52.25	20.43	100.10
NWA11073	ilm06avg	6	0.03	50.81	0.05	0.00	0.07	47.20	0.00	0.59	0.49	0.13	0.00	0.00	0.00	0.00	44.72	2.75	99.66
NWA11073	tm07avg	7	0.07	23.43	2.24	0.65	0.83	70.38	0.00	0.50	0.44	0.01	0.00	0.00	0.00	0.00	52.58	19.78	100.54
NWA11073	ilm07avg	7	0.03	51.26	0.06	0.00	0.13	46.81	0.00	0.59	0.74	0.02	0.00	0.00	0.00	0.00	44.38	2.70	99.89
NWA11255	tm01avg	1	0.08	23.38	2.06	0.60	1.35	70.49	0.00	0.52	0.52	0.03	0.00	0.00	0.00	0.00	52.61	19.87	101.03
NWA11255	ilm01avg	1	0.02	51.14	0.06	0.00	0.13	46.96	0.00	0.58	0.87	0.07	0.00	0.00	0.00	0.00	44.14	3.13	100.14
NWA11255	tm02avg	2	0.07	22.19	2.05	0.55	0.94	71.33	0.01	0.52	0.47	0.04	0.00	0.00	0.00	0.00	51.37	22.19	100.40
NWA11255	ilm02avg	2	0.05	50.72	0.03	0.00	0.06	47.00	0.00	0.57	0.84	0.02	0.00	0.01	0.00	0.00	43.87	3.48	99.65
NWA11255	tm03avg	3	0.08	22.13	1.98	0.52	0.70	71.65	0.00	0.50	0.43	0.01	0.00	0.00	0.00	0.00	51.32	22.59	100.27
NWA11255	ilm03avg	3	0.02	50.52	0.05	0.00	0.06	47.10	0.00	0.59	0.75	0.03	0.00	0.00	0.00	0.00	43.69	3.79	99.50
NWA11255	tm04avg	4	0.08	23.29	2.21	0.34	0.58	70.82	0.00	0.54	0.41	0.03	0.00	0.00	0.00	0.00	52.47	20.40	100.34
NWA11255	ilm04avg	4	0.09	50.50	0.08	0.00	0.09	47.08	0.00	0.63	0.65	0.04	0.00	0.00	0.00	0.00	44.14	3.26	99.46
NWA11255	tm05avg	5	0.08	22.37	2.04	0.31	0.47	71.79	0.01	0.50	0.53	0.08	0.00	0.00	0.00	0.00	51.59	22.45	100.44
NWA11255	ilm05avg	5	0.05	50.59	0.06	0.00	0.05	46.81	0.00	0.59	0.93	0.10	0.00	0.00	0.00	0.00	43.74	3.41	99.51
NWA11255	tm06avg	6	0.08	22.52	1.86	0.40	0.53	71.51	0.02	0.52	0.51	0.01	0.00	0.00	0.00	0.00	51.46	22.28	100.17
NWA11255	ilm06avg	6	0.03	50.55	0.06	0.00	0.07	46.99	0.00	0.60	0.84	0.02	0.00	0.00	0.00	0.00	43.59	3.78	99.53
NWA12262	tmex01avg	1	0.09	26.32	1.36	0.04	0.01	69.31	0.01	0.63	0.12	0.01	0.00	0.00	0.00	0.00	55.24	15.63	99.46
NWA12262	ilm01avg	1	0.08	48.14	0.07	0.00	0.00	49.66	0.00	0.82	0.18	0.02	0.00	0.00	0.00	0.00	42.57	7.88	99.77
NWA12262	tmex02avg	2	0.08	24.76	1.45	0.22	0.03	70.05	0.00	0.65	0.21	0.05	0.00	0.00	0.00	0.00	53.67	18.20	99.32
NWA12262	ilm02aavg	2	0.08	48.00	0.06	0.00	0.00	49.53	0.00	0.85	0.34	0.02	0.00	0.00	0.00	0.00	42.14	8.21	99.71
NWA12262	ilm02bavg	2	0.13	47.94	0.10	0.00	0.00	49.62	0.00	0.86	0.32	0.03	0.00	0.01	0.00	0.00	42.42	8.00	99.81
NWA12262	ilm02cavg	2	0.08	46.68	0.06	0.00	0.00	49.57	0.00	0.86	0.34	0.11	0.00	0.00	0.00	0.00	41.15	9.36	98.63
NWA12262	tmex03avg	3	0.09	24.96	1.58	0.06	0.03	70.37	0.00	0.59	0.17	0.03	0.00	0.00	0.00	0.00	54.12	18.05	99.68
NWA12262	ilm03avg	3	0.08	48.12	0.08	0.00	0.00	49.54	0.00	0.80	0.26	0.04	0.00	0.00	0.00	0.00	42.63	7.69	99.70
NWA12262	tmex04avg	4	0.09	26.86	1.34	0.11	0.01	68.36	0.00	0.64	0.17	0.02	0.00	0.00	0.00	0.00	55.51	14.28	99.03
NWA12262	ilm04aavg	4	0.08	48.38	0.07	0.00	0.00	49.65	0.00	0.82	0.26	0.04	0.00	0.00	0.00	0.00	42.82	7.58	100.05
NWA12262	ilm04bavg	4	0.07	48.56	0.07	0.00	0.00	49.53	0.00	0.82	0.26	0.04	0.00	0.00	0.00	0.00	42.91	7.35	100.08
AA-1(NWA12919)	tm001avg	1	0.08	23.89	1.60	0.41	0.73	69.55	0.00	0.50	0.29	0.01	0.00	0.00	0.00	0.00	52.71	18.71	98.94

Table A1.5.(continued) Averaged EPMA analysis of titanomagnetite-ilmenite pairs, with calculated FeO and Fe₂O₃ based on charge balancing.
Data excluded from calculating f_{O_2} are denoted in red.

SAMPLE	Analysis	Pair	SiO ₂	TiO ₂	Al ₂ O ₃	V ₂ O ₃	Cr ₂ O ₃	FeO (Total)	NiO	MnO	MgO	CaO	Na ₂ O	K ₂ O	P ₂ O ₅	ZrO ₂	FeO	Fe ₂ O ₃	Total
AA-1(NWA12919)	ilm001avg	1	0.03	50.03	0.03	0.15	0.08	46.88	0.00	0.57	0.45	0.04	0.00	0.00	0.00	43.87	3.35	98.60	
AA-1(NWA12919)	tm002avg	2	0.08	24.04	1.76	0.37	0.92	69.26	0.00	0.53	0.45	0.03	0.00	0.00	0.00	52.76	18.34	99.28	
AA-1(NWA12919)	ilm002avg	2	0.03	49.44	0.10	0.11	0.16	46.51	0.00	0.59	0.72	0.20	0.00	0.00	0.00	43.27	3.60	98.21	
AA-1(NWA12919)	tm003avg	3	0.08	24.44	1.69	0.38	1.28	68.13	0.00	0.54	0.46	0.08	0.00	0.00	0.00	53.04	16.78	98.75	
AA-1(NWA12919)	ilm003avg	3	0.04	50.08	0.04	0.10	0.10	46.36	0.00	0.57	0.74	0.12	0.00	0.00	0.00	43.62	3.04	98.43	
AA-1(NWA12919)	tm004avg	4	0.11	22.06	1.82	0.21	0.29	71.45	0.00	0.49	0.24	0.11	0.00	0.01	0.00	51.49	22.18	99.01	
AA-1(NWA12919)	ilm004avg	4	0.04	49.24	0.04	0.06	0.00	46.99	0.00	0.59	0.43	0.42	0.00	0.02	0.00	44.26	3.02	98.14	
AA-1(NWA12919)	tm007avg	5	0.08	22.74	1.69	0.34	0.88	70.57	0.00	0.53	0.32	0.03	0.00	0.00	0.00	51.70	20.97	99.29	
AA-1(NWA12919)	ilm007avg	5	0.02	50.14	0.04	0.08	0.08	47.06	0.00	0.59	0.54	0.03	0.00	0.00	0.00	43.73	3.70	98.95	
AA-1(NWA12919)	tm008avg	6	0.09	22.97	1.58	0.27	0.74	70.57	0.00	0.47	0.34	0.04	0.00	0.01	0.00	51.96	20.68	99.15	
AA-1(NWA12919)	ilm008avg	6	0.05	49.94	0.04	0.06	0.12	46.67	0.01	0.55	0.56	0.09	0.00	0.00	0.00	43.85	3.13	98.41	
AA-1(NWA12919)	tm009avg	7	0.07	23.29	1.65	0.23	0.53	70.97	0.01	0.55	0.37	0.04	0.00	0.00	0.00	52.19	20.86	99.79	
AA-1(NWA12919)	ilm009avg	7	0.04	50.62	0.03	0.00	0.06	46.84	0.00	0.62	0.64	0.04	0.00	0.00	0.00	44.02	3.13	99.20	
AA-1(NWA12919)	tm010avg	8	0.06	25.04	1.44	0.52	1.09	68.35	0.00	0.54	0.46	0.01	0.00	0.00	0.00	53.46	16.54	99.17	
AA-1(NWA12919)	ilm010rerunavg	8	0.07	50.04	0.04	0.11	0.11	47.19	0.00	0.57	0.68	0.09	0.00	0.00	0.00	43.80	3.77	99.30	
AA-1(NWA12919)	tm012avg	9	0.08	23.21	1.76	0.28	0.78	71.27	0.00	0.55	0.35	0.00	0.00	0.00	0.00	52.34	21.04	100.39	
AA-1(NWA12919)	ilm012avg	9	0.07	50.05	0.06	0.05	0.06	47.41	0.00	0.67	0.59	0.01	0.00	0.00	0.00	43.65	4.18	99.37	
AA-1(NWA12919)	tm013avg	10	0.08	23.90	1.75	0.26	0.42	71.18	0.00	0.57	0.30	0.11	0.00	0.00	0.00	53.34	19.83	100.55	
AA-1(NWA12919)	ilm013avg	10	0.01	50.68	0.05	0.00	0.07	47.38	0.00	0.63	0.49	0.00	0.00	0.00	0.00	44.16	3.58	99.67	

Table A1.6. Fe-Ti temperature and f_{O_2} (Δ NNO) as determined by the [Ghiorso and Evans \(2008\)](#) Fe-Ti oxide geothermobarometer online server, with conversion to Δ IW and Δ QFM based on [Wones and Gilbert \(1969\)](#).

SAMPLE	PAIR	Tmt	Ilm	T (C) Fe-Ti	delta NNO	logfO2	logfO2(N NO@200 MPa)	logfO2 (Rel to IW)	logfO2 (Rel to QFM)	Avg logfO2 (Rel to QFM)	σ
JaH479	1	tmex01avg	ilm01avg	880.15	-2.11	-14.4	-12.2	2.8	-1.0	-1.2	0.4
JaH479	2	tmex02avg	ilm02avg	907.81	-2.12	-13.9	-11.7	2.7	-1.1		
JaH479	3	Int 1 TMT_avg	Int_1 Ilm_avg	759.2	-3.12	-17.8	-14.7	2.1	-1.9		
JaH479	4 ^a	Int 2 TMT_avg	Int 2 Ilmn_avg	882.71	-2.2	-14.4	-12.2	2.7	-1.1		
JaH479	5	Int 4 TMT_avg	Int 4 Ilmn 2	832.07	-2.07	-15.2	-13.2	2.9	-0.9		
KG002	1	tm01avg	ilm01avg	821.68	-2.28	-15.7	-13.4	2.8	-1.1	-1.0	0.2
KG002	2	tm02avg	ilm02avg	819.72	-2.27	-15.7	-13.4	2.8	-1.1		
KG002	3	tm03avg	ilm03avg	804.32	-2.4	-16.1	-13.7	2.7	-1.2		
KG002	4	tm04avg	ilm04avg	827.01	-2.14	-15.4	-13.3	2.9	-1.0		
KG002	5	tm05avg	ilm05avg	874.87	-1.73	-14.1	-12.3	3.2	-0.6		
NWA10299	1	tm01avg	ilm01avg	749.98	-3.19	-18.1	-14.9	2.1	-2.0	-1.1	0.7
NWA10299	2	tm02avg	ilm02avg	775.31	-2.92	-17.3	-14.4	2.3	-1.7		
NWA10299	3	tm03avg	ilm03avg	894.61	-1.92	-13.9	-12.0	2.9	-0.9		
NWA10299	4 ^b	tm04avg	ilm04avg	1117.88	-0.89	-9.5	-8.6	3.5	0.0		
NWA10299	5	tm06avg	ilm06avg	824.5	-2.59	-15.9	-13.3	2.4	-1.5		
NWA10299	6	tm07avg	ilm07avg	922.87	-1.62	-13.1	-11.5	3.2	-0.6		
NWA11057	1	tm01avg	ilm01avg	806.12	-2.53	-16.2	-13.7	2.6	-1.4	-1.4	0.2
NWA11057	2	tm02avg	ilm02avg	802.41	-2.44	-16.2	-13.8	2.7	-1.3		
NWA11057	3	tm03avg	ilm03avg	816.19	-2.53	-16.0	-13.5	2.5	-1.4		
NWA11057	4	tm04avg	ilm04avg	761.36	-2.93	-17.6	-14.7	2.3	-1.7		
NWA11057	5	tm05avg	ilm05avg	804.44	-2.66	-16.4	-13.7	2.4	-1.5		
NWA11057	6	tm06avg	ilm06avg	779.62	-2.59	-16.9	-14.3	2.6	-1.4		
NWA11057	7	tm07avg	ilm07avg	815.89	-2.19	-15.7	-13.5	2.9	-1.0		
NWA11073	1	tm01avg	ilm01avg	792.1	-2.42	-16.4	-14.0	2.7	-1.3	-1.3	0.3
NWA11073	2	tm02avg	ilm02avg	840.19	-1.99	-15.0	-13.0	3.0	-0.9		
NWA11073	3	tm03avg	ilm03avg	790.22	-1.98	-16.0	-14.0	3.1	-0.8		
NWA11073	4	tm04avg	ilm04avg	783.81	-2.54	-16.7	-14.2	2.6	-1.4		
NWA11073	5	tm05avg	ilm05avg	780.56	-2.76	-17.0	-14.2	2.4	-1.6		
NWA11073	6	tm06avg	ilm06avg	775.75	-2.58	-16.9	-14.3	2.6	-1.4		
NWA11073	7	tm07avg	ilm07avg	753.76	-2.91	-17.8	-14.8	2.3	-1.7		
NWA11255	1	tm01avg	ilm01avg	795.84	-2.51	-16.4	-13.9	2.6	-1.3	-1.1	0.1
NWA11255	2	tm02avg	ilm02avg	799.85	-2.29	-16.1	-13.8	2.8	-1.1		
NWA11255	3	tm03avg	ilm03avg	807.84	-2.2	-15.9	-13.7	2.9	-1.0		
NWA11255	4	tm04avg	ilm04avg	822.37	-2.26	-15.6	-13.4	2.8	-1.1		
NWA11255	5	tm05avg	ilm05avg	804.06	-2.25	-16.0	-13.7	2.8	-1.1		
NWA11255	6	tm06avg	ilm06avg	811.9	-2.2	-15.8	-13.6	2.9	-1.1		
NWA12262	1 ^c	tmex01avg	ilm01avg	1140.47	-0.79	-9.1	-8.3	3.6	0.1	0.1	0.1
NWA12262	2	tmex02avg	ilm02avg	1094.63	-0.73	-9.6	-8.9	3.7	0.2		
NWA12262	2	tmex02avg	ilm02avg	1098.95	-0.71	-9.6	-8.9	3.7	0.2		
NWA12262	2	tmex02avg	ilm02cavg	1138.68	-0.51	-8.9	-8.4	3.9	0.4		
NWA12262	3	tmex03avg	ilm03avg	1089.8	-0.78	-9.8	-9.0	3.7	0.1		
NWA12262	4	tmex04avg	ilm04avg	1167.09	-0.81	-8.8	-8.0	3.5	0.0		
NWA12262	4	tmex04avg	ilm04bavg	1155.25	-0.87	-9.0	-8.2	3.5	0.0		
AA-1(NWA12919)	1	tm001avg	ilm001avg	826.79	-2.36	-15.6	-13.3	2.7	-1.2	-1.1	0.2
AA-1(NWA12919)	2	tm002avg	ilm002avg	886.08	-1.95	-14.1	-12.1	2.9	-0.9		
AA-1(NWA12919)	3	tm003avg	ilm003avg	844.69	-2.37	-15.3	-12.9	2.6	-1.3		
AA-1(NWA12919)	4	tm004avg	ilm004avg	844.9	-1.9	-14.8	-12.9	3.1	-0.8		
AA-1(NWA12919)	5	tm007avg	ilm007avg	821.02	-2.22	-15.6	-13.4	2.8	-1.1		
AA-1(NWA12919)	6	tm008avg	ilm008avg	808.33	-2.35	-16.0	-13.6	2.7	-1.2		
AA-1(NWA12919)	7	tm009avg	ilm009avg	786.07	-2.56	-16.7	-14.1	2.6	-1.4		
AA-1(NWA12919)	8	tm010avg	ilm010rerunavg	915.53	-1.92	-13.5	-11.6	2.9	-0.9		
AA-1(NWA12919)	9	tm012avg	ilm012avg	866.33	-1.89	-14.4	-12.5	3.0	-0.8		
AA-1(NWA12919)	10	tm013avg	ilm013avg	815.1	-2.39	-15.9	-13.5	2.7	-1.2		

a. ~96 wt% total for tmt analysis.

b. High Cr₂O₃ in ilm.

c. No appreciable difference in average f_{O_2} if all pair 2 and pair 4 values are averaged first before being averaged with pairs 1 and 3.

APPENDIX 2

Table A2.1. Counting times for SIMS U–Pb baddeleyite analysis.

Mass	$^{90}\text{Zr}_{2}^{16}\text{O}$	203.5	^{204}Pb	^{206}Pb	^{207}Pb	^{208}Pb	^{232}Th	^{238}U	$^{238}\text{U}^{16}\text{O}$	$^{238}\text{U}^{16}\text{O}_2$
Counting Time (s)	2	4	12	16.96	22	10	8	20	2.96	4.96

Table A2.2. SIMS U–Pb analysis of the Phalaborwa baddeleyite reference material.

Analysis	Date	^{204}Pb	^{206}Pb	^{207}Pb	^{208}Pb	^{232}Th	^{238}U	UO_2/U	$^{206}\text{Pb}/^{204}\text{Pb}$	$^{238}\text{U}/^{206}\text{Pb}$	1s	$^{207}\text{Pb}/^{206}\text{Pb}$	1s
PH_1	2021-11-22	0.025	4415	563.90	9.97	2.65	492	13.30	168400	2.64541	0.04979	0.12765	0.00031
PH_2	2021-11-22	0.011	1918	244.10	3.21	0.98	204	13.40	160300	2.56153	0.05748	0.12716	0.00035
PH_3	2021-11-22	0.019	3286	419.40	5.16	1.34	348	13.76	178700	2.67526	0.06977	0.12756	0.00029
PH_4	2021-11-22	0.009	3267	417.40	5.08	1.30	355	13.34	345000	2.59243	0.06252	0.12775	0.00029
PH_5	2021-11-22	0.013	3508	447.60	9.68	2.20	386	13.56	251000	2.71121	0.05512	0.12754	0.00025
PH_6	2021-11-22	0.007	3820	485.80	9.30	2.16	424	13.41	519600	2.67902	0.05247	0.12717	0.00027
PH_7	2021-11-22	0.004	4021	511.20	9.74	2.37	452	13.32	869600	2.67167	0.05714	0.12708	0.00027
PH_8	2021-11-22	0.013	3766	479.50	9.04	2.20	422	13.29	277100	2.65643	0.05598	0.12731	0.00031
PH_9	2021-11-23	0.000	1973	251.60	7.15	2.06	230	11.41	19680000	2.67811	0.05131	0.12749	0.00046
PH_10	2021-11-23	0.006	2091	265.70	7.82	1.91	242	11.35	329200	2.65324	0.05209	0.12697	0.00033
PH_11	2021-11-23	0.006	2986	379.50	9.31	2.52	319	12.68	537200	2.63391	0.04564	0.12707	0.00042
PH_12	2021-11-23	0.012	2895	367.70	9.84	1.97	318	12.26	242300	2.64997	0.04671	0.12700	0.00042
PH_13	2021-11-23	0.016	2955	376.50	11.63	3.37	329	12.19	185700	2.67443	0.04788	0.12741	0.00039
PH_14	2021-11-23	0.000	1064	135.70	6.47	0.71	115	13.22	10620000	2.74094	0.04755	0.12747	0.00051
PH_15	2021-11-23	0.012	1094	140.80	3.50	0.74	119	13.22	91340	2.74862	0.04738	0.12844	0.00068
PH_16	2021-11-23	0.006	1370	172.90	4.56	1.29	147	13.15	249200	2.71825	0.04763	0.12610	0.00043
PH_17	2021-11-24	0.009	4981	633.20	19.70	6.31	685	10.37	550600	2.64807	0.05314	0.12709	0.00042
PH_18	2021-11-24	0.000	1445	184.30	4.42	1.69	211	10.23	14440000	2.76696	0.06063	0.12756	0.00035
PH_19	2021-11-24	0.006	933	119.40	2.44	0.90	134	10.28	164800	2.73587	0.05742	0.12811	0.00074
PH_20	2021-11-24	0.006	5641	718.10	22.61	7.54	813	9.81	998400	2.60336	0.05789	0.12735	0.00020
PH_21	2021-11-24	0.000	5164	657.30	19.83	6.55	722	10.06	51610000	2.59734	0.05720	0.12729	0.00033
PH_22	2021-01-20	0.188	1782	226.60	16.94	4.54	216	12.98	9568	2.84618	0.19620	0.12582	0.00079
PH_23	2021-01-20	0.255	2066	264.40	11.64	2.90	265	11.81	8122	2.69078	0.20748	0.12631	0.00078
PH_24	2021-01-20	0.098	8131	1035.00	44.59	11.45	967	13.29	82570	2.86928	0.19181	0.12709	0.00040
PH_25	2021-01-20	0.120	3047	389.50	17.65	5.33	369	12.96	25490	2.83851	0.19543	0.12732	0.00060
PH_26	2021-01-20	0.086	3376	428.40	11.63	3.34	417	12.65	38860	2.81239	0.19938	0.12655	0.00073
PH_27	2021-01-20	0.089	4952	630.00	7.97	2.54	615	12.64	54430	2.82201	0.19997	0.12694	0.00049
PH_28	2021-01-20	0.107	4791	609.50	13.24	3.61	596	12.20	44330	2.71078	0.20055	0.12690	0.00038
PH_29	2021-01-20	0.039	2891	364.90	9.82	2.76	362	12.15	72480	2.71735	0.20240	0.12603	0.00065
PH_30	2021-01-20	0.199	3410	437.20	33.50	5.97	427	12.33	16840	2.76673	0.20325	0.12741	0.00041
PH_31	2021-01-20	0.055	4318	548.70	20.23	5.81	514	13.26	79770	2.86282	0.19175	0.12692	0.00055
PH_32	2021-01-21	0.025	3717	474.90	10.85	3.48	486	11.20	150600	2.52279	0.10370	0.12769	0.00028

Table A2.2.(continued) SIMS U–Pb analysis of the Phalaborwa baddeleyite reference material.

Analysis	$^{206}\text{Pb}/^{238}\text{U}$	1s	$^{207}\text{Pb}/^{235}\text{U}$	1s	Rho	$^{207}\text{Pb}-^{206}\text{Pb}$ Age (Ma)	1s	$^{206}\text{Pb}-^{238}\text{U}$ Age (Ma)	1s	$^{207}\text{Pb}-^{235}\text{U}$ Age (Ma)	1s	Concordance (%)*
PH_1	0.37801	0.00712	6.65290	0.12586	0.99	2066	4.3	2067	33	2066	17	100.0
PH_2	0.39039	0.00876	6.84458	0.15360	0.99	2059	4.8	2125	41	2092	20	103.2
PH_3	0.37380	0.00975	6.57449	0.17155	1.00	2065	4.1	2047	46	2056	23	99.1
PH_4	0.38574	0.00930	6.79446	0.16632	1.00	2067	4	2103	43	2085	22	101.7
PH_5	0.36884	0.00750	6.48629	0.13313	1.00	2064	3.5	2024	35	2044	18	98.1
PH_6	0.37327	0.00731	6.54507	0.13072	0.99	2059	3.7	2045	34	2052	18	99.3
PH_7	0.37430	0.00801	6.55831	0.14058	1.00	2058	3.8	2050	38	2054	19	99.6
PH_8	0.37645	0.00793	6.60776	0.14295	0.99	2061	4.3	2060	37	2060	19	100.0
PH_9	0.37340	0.00715	6.56389	0.12468	0.98	2064	6.3	2045	34	2055	17	99.1
PH_10	0.37690	0.00740	6.59803	0.13502	0.99	2056	4.6	2062	35	2059	18	100.3
PH_11	0.37966	0.00658	6.65190	0.11800	0.98	2058	5.8	2075	31	2066	16	100.8
PH_12	0.37736	0.00665	6.60796	0.11856	0.98	2057	5.8	2064	31	2060	16	100.3
PH_13	0.37391	0.00669	6.56851	0.11961	0.99	2063	5.4	2048	31	2055	16	99.3
PH_14	0.36484	0.00633	6.41239	0.11211	0.97	2063	7.1	2005	30	2034	15	97.2
PH_15	0.36382	0.00627	6.44290	0.11155	0.95	2077	9.3	2000	30	2038	15	96.3
PH_16	0.36788	0.00645	6.39607	0.11130	0.98	2044	6	2019	30	2032	15	98.8
PH_17	0.37763	0.00758	6.61756	0.13311	0.99	2058	5.8	2065	35	2062	18	100.3
PH_18	0.36141	0.00792	6.35616	0.13982	0.99	2065	4.8	1989	37	2026	19	96.3
PH_19	0.36551	0.00767	6.45630	0.13905	0.96	2072	10	2008	36	2040	19	96.9
PH_20	0.38412	0.00854	6.74450	0.14943	1.00	2062	2.7	2095	40	2078	20	101.6
PH_21	0.38501	0.00848	6.75716	0.14993	0.99	2061	4.6	2100	39	2080	20	101.9
PH_22	0.35135	0.02422	6.09515	0.42391	1.00	2040	11	1941	##	1990	61	95.1
PH_23	0.37164	0.02866	6.47225	0.50078	1.00	2047	11	2037	##	2042	68	99.5
PH_24	0.34852	0.02330	6.10716	0.40897	1.00	2058	5.6	1928	##	1991	58	93.7
PH_25	0.35230	0.02426	6.18436	0.42654	1.00	2061	8.3	1946	##	2002	60	94.4
PH_26	0.35557	0.02521	6.20435	0.44130	1.00	2051	10	1961	##	2005	62	95.6
PH_27	0.35436	0.02511	6.20217	0.44027	1.00	2056	6.9	1955	##	2005	62	95.1
PH_28	0.36890	0.02729	6.45462	0.47775	1.00	2055	5.3	2024	##	2040	65	98.5
PH_29	0.36801	0.02741	6.39471	0.47682	1.00	2043	9.1	2020	##	2032	65	98.9
PH_30	0.36144	0.02655	6.34941	0.46720	1.00	2063	5.7	1989	##	2025	65	96.4
PH_31	0.34931	0.02340	6.11293	0.41075	1.00	2056	7.7	1931	##	1992	59	93.9
PH_32	0.39639	0.01629	6.97850	0.28580	1.00	2066	3.9	2152	75	2109	36	104.2

Table A2.2.(continued) SIMS U–Pb analysis of the Phalaborwa baddeleyite reference material.

Analysis	Date	^{204}Pb	^{206}Pb	^{207}Pb	^{208}Pb	^{232}Th	^{238}U	UO_2/U	$^{206}\text{Pb}/^{204}\text{Pb}$	$^{238}\text{U}/^{206}\text{Pb}$	1s	$^{207}\text{Pb}/^{206}\text{Pb}$	1s
PH_33	2021-01-21	0.080	7036	900.90	21.61	6.62	927	11.44	86770	2.61531	0.10379	0.12788	0.00036
PH_34	2021-01-21	0.091	2667	340.80	10.93	2.50	421	9.55	29470	2.42063	0.12447	0.12739	0.00049
PH_35	2021-01-21	0.027	2641	334.60	7.68	2.19	386	10.25	94550	2.48813	0.11502	0.12662	0.00059
PH_36	2021-01-21	0.078	2238	284.10	11.62	3.06	365	9.75	28120	2.57281	0.12992	0.12651	0.00073
PH_37	2021-01-21	0.101	13990	1776.00	66.61	22.53	2073	10.80	138400	2.71339	0.11592	0.12685	0.00022
PH_38	2021-01-21	0.018	14100	1796.00	64.73	21.17	2071	10.80	764100	2.69166	0.11491	0.12738	0.00017
PH_39	2021-01-21	0.033	12460	1582.00	55.98	18.04	1802	10.94	384300	2.69685	0.11287	0.12693	0.00022
PH_40	2021-01-21	0.033	2332	298.70	7.37	2.39	321	11.35	68710	2.70507	0.10868	0.12789	0.00049
PH_41	2021-01-21	0.049	29410	3737.00	59.36	18.16	3838	11.46	588000	2.59902	0.10328	0.12705	0.00028
PH_42	2021-01-21	0.064	9989	1269.00	26.71	7.84	1336	11.23	158500	2.58726	0.10558	0.12691	0.00039
PH_43	2021-01-21	0.037	13900	1775.00	76.24	23.19	1867	11.87	383400	2.80403	0.10512	0.12764	0.00044
PH_44	2021-01-21	0.107	18280	2330.00	76.63	23.79	2445	11.89	168400	2.80057	0.10461	0.12745	0.00015

Table A2.2.(continued) SIMS U–Pb analysis of the Phalaborwa baddeleyite reference material.

Analysis	$^{206}\text{Pb}/^{238}\text{U}$	1s	$^{207}\text{Pb}/^{235}\text{U}$	1s	Rho	$^{207}\text{Pb}-^{206}\text{Pb}$ Age (Ma)	1s	$^{206}\text{Pb}-^{238}\text{U}$ Age (Ma)	1s	$^{207}\text{Pb}-^{235}\text{U}$ Age (Ma)	1s	Concordance (%)*
PH_33	0.38236	0.01517	6.74188	0.26751	1.00	2069	4.9	2087	71	2078	35	100.9
PH_34	0.41312	0.02124	7.25613	0.37702	1.00	2062	6.8	2229	97	2143	46	108.1
PH_35	0.40191	0.01858	7.01660	0.32628	0.99	2052	8.3	2178	85	2114	41	106.1
PH_36	0.38868	0.01963	6.77963	0.34994	0.99	2050	10	2117	91	2083	46	103.3
PH_37	0.36854	0.01574	6.44577	0.27550	1.00	2055	3	2023	74	2039	38	98.4
PH_38	0.37152	0.01586	6.52485	0.27844	1.00	2062	2.3	2037	75	2049	38	98.8
PH_39	0.37080	0.01552	6.48929	0.27203	1.00	2056	3.1	2033	73	2044	37	98.9
PH_40	0.36968	0.01485	6.51878	0.26490	1.00	2069	6.8	2028	70	2048	36	98.0
PH_41	0.38476	0.01529	6.74030	0.26738	1.00	2058	3.9	2098	71	2078	35	101.9
PH_42	0.38651	0.01577	6.76333	0.27633	1.00	2056	5.4	2107	73	2081	36	102.5
PH_43	0.35663	0.01337	6.27643	0.23588	1.00	2066	6.1	1966	64	2015	33	95.2
PH_44	0.35707	0.01334	6.27458	0.23466	1.00	2063	2	1968	63	2015	33	95.4

* Concordance is calculated as $(^{206}\text{Pb}-^{238}\text{U} \text{ Age}) / (^{207}\text{Pb}-^{206}\text{Pb} \text{ age}) \times 100\%$.

Table A2.3. SIMS U–Pb analysis of the FC4b baddeleyite reference material.

Analysis	Date	^{204}Pb	^{206}Pb	^{207}Pb	^{208}Pb	^{232}Th	^{238}U	UO_2/U	$^{206}\text{Pb}/^{204}\text{Pb}$	$^{238}\text{U}/^{206}\text{Pb}$	1s	$^{207}\text{Pb}/^{206}\text{Pb}$	1s
FC4b_1	2021-11-22	0.028	1650	127.00	3.74	1.44	308	14.65	57200	5.27476	0.09726	0.07675	0.00025
FC4b_2	2021-11-22	0.009	1328	101.30	3.59	1.29	251	14.71	142300	5.37063	0.10740	0.07625	0.00067
FC4b_3	2021-11-22	0.007	1048	80.20	2.86	1.21	196	14.94	135700	5.46093	0.10256	0.07644	0.00038
FC4b_4	2021-11-22	0.013	1151	88.91	2.81	1.10	218	14.79	88770	5.43095	0.10680	0.07714	0.00035
FC4b_5	2021-11-22	0.010	1270	97.23	2.81	1.27	242	14.69	121000	5.40009	0.11475	0.07646	0.00043
FC4b_6	2021-11-22	0.010	1119	85.74	2.63	1.10	207	15.10	115200	5.49481	0.10107	0.07654	0.00046
FC4b_7	2021-11-22	0.000	1247	94.32	2.94	1.52	235	14.69	12400000	5.34631	0.10595	0.07561	0.00043
FC4b_8	2021-11-22	0.013	1388	105.00	3.29	1.08	266	14.56	108800	5.36472	0.10721	0.07559	0.00034
FC4b_9	2021-11-23	0.009	2110	162.10	3.19	1.28	487	11.51	244200	5.33507	0.09912	0.07683	0.00026
FC4b_10	2021-11-23	0.000	3053	232.80	3.71	1.83	666	12.47	30450000	5.31697	0.09447	0.07628	0.00028
FC4b_11	2021-11-23	0.012	2991	228.10	3.71	1.76	665	12.37	255200	5.38837	0.09758	0.07622	0.00027
FC4b_12	2021-11-23	0.016	3009	230.20	4.16	2.05	676	12.38	189400	5.44998	0.09790	0.07647	0.00027
FC4b_13	2021-11-23	0.028	7864	601.60	8.72	3.94	1713	12.44	285700	5.29936	0.09388	0.07648	0.00013
FC4b_14	2021-11-23	0.018	4674	356.20	4.40	2.43	1015	12.50	253900	5.30091	0.09521	0.07619	0.00025
FC4b_15	2021-11-23	0.013	3094	235.30	4.21	2.01	682	12.33	221000	5.33129	0.09677	0.07600	0.00031
FC4b_16	2021-11-24	0.000	1118	85.44	3.59	2.00	331	9.90	11120000	5.41067	0.11464	0.07651	0.00036
FC4b_17	2021-11-24	0.000	1160	89.16	3.48	2.38	342	9.92	11560000	5.38857	0.11405	0.07692	0.00065
FC4b_18	2021-11-24	0.006	1230	93.77	4.33	2.97	397	9.09	204500	5.34005	0.13203	0.07617	0.00045
FC4b_19	2021-11-24	0.000	1255	95.75	5.06	2.92	403	9.15	12520000	5.35194	0.13180	0.07639	0.00055
FC4b_20	2021-11-24	0.018	1436	108.90	6.25	4.17	448	9.21	78550	5.24227	0.12971	0.07573	0.00043
FC4b_21	2021-11-24	0.026	1050	80.15	4.40	3.24	360	8.80	41180	5.46174	0.14786	0.07607	0.00057
FC4b_22	2021-11-24	0.002	1211	93.16	5.35	3.72	384	9.20	587500	5.31550	0.13279	0.07696	0.00043
FC4b_23	2021-11-24	0.008	1569	120.40	8.61	5.69	501	9.16	194400	5.33840	0.13004	0.07671	0.00035
FC4b_24	2021-01-20	0.179	2837	216.30	8.40	3.61	707	11.24	15650	4.92715	0.40198	0.07538	0.00045
FC4b_25	2021-01-20	0.077	941	71.66	5.78	3.32	237	10.91	12270	4.80681	0.40804	0.07500	0.00078
FC4b_26	2021-01-20	0.070	808	61.61	6.52	2.77	186	11.42	11370	4.63751	0.37317	0.07502	0.00066
FC4b_27	2021-01-20	0.097	592	45.05	3.62	2.21	147	11.12	6017	4.86325	0.40394	0.07380	0.00095
FC4b_28	2021-01-20	0.126	1679	128.70	5.60	2.91	416	11.02	13120	4.78494	0.39979	0.07561	0.00056
FC4b_29	2021-01-20	0.128	2119	162.80	4.91	2.73	531	11.13	16140	4.89481	0.40396	0.07601	0.00054
FC4b_30	2021-01-20	0.076	3033	232.80	9.60	4.97	785	11.95	39070	5.51007	0.41731	0.07639	0.00032
FC4b_31	2021-01-20	0.058	3392	257.80	24.00	6.19	849	12.19	58590	5.45545	0.40344	0.07579	0.00042
FC4b_32	2021-01-20	0.117	4285	321.50	425.70	84.91	891	14.44	37220	5.54007	0.33668	0.07486	0.00050

Table A2.3.(continued) SIMS U–Pb analysis of the FC4b baddeleyite reference material.

Analysis	$^{206}\text{Pb}/^{238}\text{U}$	1s	$^{207}\text{Pb}/^{235}\text{U}$	1s	Rho	$^{207}\text{Pb}-^{206}\text{Pb}$ Age (Ma)	1s	$^{206}\text{Pb}-^{238}\text{U}$ Age (Ma)	1s	$^{207}\text{Pb}-^{235}\text{U}$ Age (Ma)	1s	Concordance (%)*
FC4b_1	0.18958	0.00350	2.00610	0.03768	0.99	1115	6.4	1119	19	1118	13	100.4
FC4b_2	0.18620	0.00372	1.95767	0.04485	0.92	1102	18	1101	20	1101	15	99.9
FC4b_3	0.18312	0.00344	1.93007	0.03558	0.96	1107	9.9	1084	19	1092	12	97.9
FC4b_4	0.18413	0.00362	1.95842	0.03911	0.97	1125	9.2	1089	20	1101	13	96.8
FC4b_5	0.18518	0.00394	1.95236	0.04282	0.97	1107	11	1095	21	1099	15	98.9
FC4b_6	0.18199	0.00335	1.92051	0.03883	0.96	1109	12	1078	18	1088	14	97.2
FC4b_7	0.18705	0.00371	1.94989	0.03808	0.96	1085	11	1105	20	1098	13	101.8
FC4b_8	0.18640	0.00373	1.94285	0.03957	0.97	1084	9.1	1102	20	1096	14	101.7
FC4b_9	0.18744	0.00348	1.98570	0.03744	0.98	1117	6.9	1107	19	1111	13	99.1
FC4b_10	0.18808	0.00334	1.97800	0.03528	0.98	1102	7.2	1111	18	1108	12	100.8
FC4b_11	0.18559	0.00336	1.95034	0.03619	0.98	1101	7.1	1097	18	1099	12	99.6
FC4b_12	0.18349	0.00330	1.93468	0.03523	0.98	1107	7	1086	18	1093	12	98.1
FC4b_13	0.18870	0.00334	1.98975	0.03552	1.00	1108	3.5	1114	18	1112	12	100.5
FC4b_14	0.18865	0.00339	1.98174	0.03617	0.98	1100	6.5	1114	18	1109	12	101.3
FC4b_15	0.18757	0.00340	1.96567	0.03645	0.98	1095	8.1	1108	18	1104	12	101.2
FC4b_16	0.18482	0.00392	1.94961	0.04146	0.98	1108	9.3	1093	21	1098	14	98.6
FC4b_17	0.18558	0.00393	1.96828	0.04539	0.93	1119	17	1097	21	1105	16	98.0
FC4b_18	0.18726	0.00463	1.96662	0.04940	0.97	1099	12	1107	25	1104	17	100.7
FC4b_19	0.18685	0.00460	1.96791	0.05059	0.96	1105	14	1104	25	1105	17	99.9
FC4b_20	0.19076	0.00472	1.99178	0.05085	0.98	1088	11	1125	26	1113	17	103.4
FC4b_21	0.18309	0.00496	1.92039	0.05247	0.96	1097	15	1084	27	1088	18	98.8
FC4b_22	0.18813	0.00470	1.99617	0.05309	0.98	1120	11	1111	25	1114	18	99.2
FC4b_23	0.18732	0.00456	1.98124	0.05103	0.98	1114	9.2	1107	25	1109	17	99.4
FC4b_24	0.20296	0.01656	2.10934	0.17264	1.00	1079	12	1191	89	1152	56	110.4
FC4b_25	0.20804	0.01766	2.15142	0.18382	0.99	1069	21	1218	94	1166	59	113.9
FC4b_26	0.21563	0.01735	2.23056	0.18022	0.99	1069	18	1259	92	1191	57	117.8
FC4b_27	0.20562	0.01708	2.09242	0.17597	0.99	1036	26	1205	91	1146	58	116.3
FC4b_28	0.20899	0.01746	2.17880	0.18281	1.00	1085	15	1223	93	1174	58	112.7
FC4b_29	0.20430	0.01686	2.14102	0.17735	1.00	1095	14	1198	90	1162	57	109.4
FC4b_30	0.18149	0.01375	1.91155	0.14489	1.00	1105	8.3	1075	75	1085	51	97.3
FC4b_31	0.18330	0.01356	1.91561	0.14230	1.00	1090	11	1085	74	1087	50	99.5
FC4b_32	0.18050	0.01097	1.86307	0.11412	0.99	1065	13	1070	60	1068	40	100.5

Table A2.3.(continued) SIMS U–Pb analysis of the FC4b baddeleyite reference material.

Analysis	Date	^{204}Pb	^{206}Pb	^{207}Pb	^{208}Pb	^{232}Th	^{238}U	UO_2/U	$^{206}\text{Pb}/^{204}\text{Pb}$	$^{238}\text{U}/^{206}\text{Pb}$	1s	$^{207}\text{Pb}/^{206}\text{Pb}$	1s
FC4b_33	2021-01-20	0.049	1223	92.90	3.47	1.75	299	12.34	24860	5.40106	0.39512	0.07542	0.00068
FC4b_34	2021-01-20	0.040	1368	105.00	4.92	2.95	342	11.96	33960	5.32139	0.40481	0.07635	0.00073
FC4b_35	2021-01-20	0.012	1590	120.80	5.39	3.07	401	11.87	128200	5.32578	0.40723	0.07591	0.00040
FC4b_36	2021-01-20	0.117	3385	260.10	10.59	4.61	832	11.16	28880	4.81740	0.39669	0.07637	0.00041
FC4b_37	2021-01-21	0.046	1391	106.20	2.48	1.59	366	11.52	30720	5.26665	0.20613	0.07589	0.00051
FC4b_38	2021-01-21	0.049	1698	131.10	4.02	1.93	437	11.71	34700	5.27727	0.20276	0.07676	0.00049
FC4b_39	2021-01-21	0.070	877	67.54	3.56	2.02	244	11.30	12170	5.43617	0.22056	0.07594	0.00081
FC4b_40	2021-01-21	0.064	1227	93.01	4.96	2.59	336	11.21	18950	5.29106	0.21937	0.07509	0.00056
FC4b_41	2021-01-21	0.052	1474	113.50	4.55	2.55	398	11.42	28240	5.35048	0.21404	0.07651	0.00079
FC4b_42	2021-01-21	0.054	1295	99.16	4.93	2.39	354	10.98	23060	5.13186	0.21443	0.07598	0.00057
FC4b_43	2021-01-21	0.037	1211	92.87	5.09	2.42	331	10.90	32820	5.06727	0.21648	0.07629	0.00077
FC4b_44	2021-01-21	0.076	1107	82.58	4.85	2.77	300	11.08	14390	5.15246	0.21331	0.07363	0.00053

Table A2.3.(continued) SIMS U–Pb analysis of the FC4b baddeleyite reference material.

Analysis	$^{206}\text{Pb}/^{238}\text{U}$	1s	$^{207}\text{Pb}/^{235}\text{U}$	1s	Rho	$^{207}\text{Pb}-^{206}\text{Pb}$ Age (Ma)	1s	$^{206}\text{Pb}-^{238}\text{U}$ Age (Ma)	1s	$^{207}\text{Pb}-^{235}\text{U}$ Age (Ma)	1s	Concordance (%)*
FC4b_33	0.18515	0.01354	1.92540	0.14240	0.99	1080	18	1095	74	1090	49	101.4
FC4b_34	0.18792	0.01430	1.97814	0.15150	0.99	1104	19	1110	78	1108	52	100.5
FC4b_35	0.18777	0.01436	1.96515	0.15021	1.00	1093	11	1109	78	1104	51	101.5
FC4b_36	0.20758	0.01709	2.18594	0.18038	1.00	1105	11	1216	91	1177	57	110.0
FC4b_37	0.18987	0.00743	1.98688	0.07937	0.99	1092	13	1121	40	1111	27	102.7
FC4b_38	0.18949	0.00728	2.00560	0.07759	0.99	1115	13	1119	39	1117	26	100.4
FC4b_39	0.18395	0.00746	1.92599	0.08022	0.97	1093	21	1089	41	1090	28	99.6
FC4b_40	0.18900	0.00784	1.95676	0.08158	0.98	1071	15	1116	42	1101	28	104.2
FC4b_41	0.18690	0.00748	1.97165	0.08328	0.97	1108	21	1105	41	1106	28	99.7
FC4b_42	0.19486	0.00814	2.04139	0.08679	0.98	1095	15	1148	44	1129	29	104.8
FC4b_43	0.19735	0.00843	2.07583	0.09052	0.97	1103	20	1161	45	1141	30	105.3
FC4b_44	0.19408	0.00803	1.97043	0.08231	0.99	1031	15	1143	43	1105	28	110.9

* Concordance is calculated as $(^{206}\text{Pb}-^{238}\text{U} \text{ Age}) / (^{207}\text{Pb}-^{206}\text{Pb} \text{ age}) \times 100\%$.